SUPERSOLIDUS LIQUID PHASE SINTERING AND GRAIN GROWTH ACTIVATION IN A METAL INJECTION MOLDED NICKEL-BASE SUPERALLOY

by

Addison J. Rayner

Submitted in partial fulfilment of the requirements
for the degree of Doctor of Philosophy

at

Dalhousie University
Halifax, Nova Scotia
April 2020

Dedicated to

Kayleigh

TABLE OF CONTENTS

LIST OF TABLES

LIST OF FIGURES

ABSTRACT

Metal injection molding (MIM) is a technology that can be used to produce net-shape parts while reducing material waste and manufacturing costs. In the aerospace industry, the application of MIM to nickel superalloys (NiSAs) has been restricted to non-structural engine components due to their limited high temperature properties. State-of-the-art solid state sintering practices for MIM NiSAs generally lead to fine-grain microstructures, which have reduced creep resistance compared to coarser, cast, microstructures. Additionally, due to the use of fine pre-alloyed powders in the MIM process, carbon and oxygen can react with alloying elements such as W and other refractory metals (RMs) to form carbide and oxide phases which can restrict grain growth. In the present work, the behaviour of a MIM NiSA during both solid state sintering and supersolidus liquid phase sintering (SLPS) is evaluated using differential scanning calorimetry (DSC) and dilatometry (DIL). The influence of the sintering atmosphere, temperature, and time on the NiSA's grain growth, shape retention, and density are quantified. Comparative DSC analysis techniques were also developed to quantify the liquid fraction with time and temperature. Microstructural analysis performed using optical microscopy and scanning electron microscopy-energy dispersive spectroscopy (SEM-EDS) revealed the grain boundary evolution with time and temperature. The MIM NiSA was sensitive to the level of oxygen present in the sintering atmosphere and the formation of RM oxides at prior particle boundaries (PPBs) was found to inhibit grain growth and densification. It was also determined that RM-Ta mixed MC carbides situated at the PPBs in the MIM NiSA restricted grain growth during sintering. Time above the solidus temperature was found to dissolve the RM-Ta mixed MC carbides, enacting grain growth. Consequently, the dissolution of these MC carbides raised the equilibrium liquid fraction, leading to an increased liquid content, decreased part rigidity, and loss of alloy homogeneity. An existing SLPS model was modified to reflect the time dependency of the liquid phase. Similarly, liquid phase sintering with the commercial braze filler metal BNi-2 enacted grain growth in the MIM NiSA at lower temperatures, proving that grain growth can be activated by multiple means in the MIM NiSA.

LIST OF ABBREVIATIONS AND SYMBOLS USED

±	Plus or minus
°	Degrees
°C	Degrees Celsius
°C/min	Heating rate in degrees Celsius per minute
μA	Micro amps
μm	Microns
A	Grain surface area
Ag	Silver
Al	Aluminium
Al_2O_3	Alumina
Ar	Argon
ASTM	American Society for Testing and Materials
ASZ	Athermally solidified zone
Au	Gold
B	Boron
Bi	Bismuth
BNi-2	Nickel-based commercial brazing filler metal
Brown	State where binders have been removed, but the part has not been sintered
BSE	Back scatter electron
C	Carbon
Co	Cobalt
CO_2	Carbon dioxide
Cr	Chromium
C_{ss}	Contiguity
D	Average particle size
d_{10}	Particle size 10% of a powder's particles falls below
d_{50}	Average particle size of a powder

d_{90}	Particle size 90% of a powder's particles fall below
DIC	Differential interference contrast
DIL	Dilatometry
dL/Lo	Change in length relative to the initial length (strain)
DS	Diffusional solidification
DSC	Differential scanning calorimetry
EDS	Energy dispersive spectroscopy
F_c	Fractional grain coverage by liquid
FCC	Face centered cubic
Fe	Iron
f_L	Liquid fraction
f_S	Solid fraction
g	Grams
G	Average grain size
GCT	Grain coarsening temperature
Green	Initial, low-density state in which a powder compact contains binders
GS	Grain size
h	Sample height
H	Hydrogen
H_2O	Water
Hf	Hafnium
H_{fusion}	Heat of fusion for the complete melting of a material
hrs	Hours
H_T	Heat flow measured at the target temperature
In	Indium
IS	Isothermal solidification
J	Joules
J/g	Joules per gram

k	Partition coefficient
Kpm	Heating rate in degrees Kelvin per minute
kV	Kilovolts
L	Liquid
LC	Designation for “low carbon” containing Ni-superalloys
LCF	Low cycle fatigue
LPS	Liquid phase sintering
m/s	Meters per second (unit of velocity)
$M_{23}C_6$	Intermediate temperature FCC metal carbide phase where “M” stands for a variety of possible metallic elements.
mbar	Millibar
MC	High temperature FCC metal carbide phase with 1:1 metal to carbon stoichiometry where “M” stands for a variety of possible metallic elements.
mg	Milligrams
MIM	Metal injection molding
mins	Minutes
ml	Milliliters
ml/min	Milliliters per minute
mm	Millimeters
Mo	Molybdenum
MPa	Megapascals
mPa·s	MilliPascal-seconds (unit of viscosity)
MPD	Melting point depressant
mW	Milliwatts
mW/mg	Milliwatts per milligram
N	Nitrogen
Ni	Nickel
NiSA	Nickel superalloy

O_2	Oxygen
ODS	Oxide dispersion strengthened
PM	Powder metallurgy
ppb	Parts per billion
PPB	Prior particle boundary
ppm	Parts per million
PSD	Powder size distribution
Pt	Platinum
R	Resistance to movement between two grains
R^2	Coefficient of determination commonly referred to as an R-squared value
Re	Rhenium
REP	Rotating electrode process
RM	Refractory metal
rpm	Revolutions per minute
Ru	Ruthenium
S	Solid
S/L	Solid and liquid phase interface
SE	Secondary electron
sec	Seconds
SEM	Scanning electron microscopy
Si	Silicon
SiC	Silicon Carbide
SLPS	Supersolidus liquid phase sintering
Sn	Tin
t	Time
Ta	Tantalum
Ta-RM	Mix of Ta and a refractory metal element
TET	Turbine entry temperature

Ti	Titanium
TiC	Titanium carbide
T_L	Liquidus temperature
TLPB	Transient liquid phase bonding
T_m	Melting temperature
T_S	Solidus temperature
T_{SLPS}	Temperature of the SLPS process
V	Vanadium
VDT	Variable displacement transformer
V_L	Liquid fraction
V_S	Solid fraction
W	Tungsten
WC	Tungsten carbide
wt%	Weight percent
X_L	Composition of the liquid
X_{NiSA}	Composition of the NiSA
X_S	Composition of the solid
X_{S*}	Total solute content in the solid
Zn	Zinc
Zr	Zirconium
α	Velocity constant
γ	Gamma matrix phase constituted of an FCC Nickel solid solution
γ/γ'	Gamma-gamma prime phase mixture referring to a eutectic phase composition
γ'	Gamma prime precipitate phase constituted of ordered $L1_2$ structure $Ni_3(Al, Ti)$
γ_{LV}	Liquid-vapour surface energy
γ_{SL}	Solid-liquid interface energy
γ_{SS}	Solid-solid interface energy

γ-γ	Interface between two gamma phase grains (i.e. a gamma-gamma grain boundary)
δ	Liquid film thickness
ζ	Softening parameter of a semi-solid structure
ζ_{Dens}	Softening parameter at the onset of densification
ζ_{Dist}	Softening parameter at the onset of distortion
η_L	Liquid viscosity
θ	Wetting angle
ν	Relative velocity between two adjacent grains
π	Pi
ρ	Instantaneous sintered density
ρ_g	Green density
σ_{ss}	Strength of solid-solid bonds
φ	Dihedral angle

ACKNOWLEDGEMENTS

First, I would like to thank Dr. Ryan Clemmer for his guidance over the years. He helped and inspired me to embark on this journey and for that I am sincerely grateful.

I would like to thank my supervisory committee members, Dr. Paul Bishop and Dr. Andrew Warkentin, for their continual support and guidance over the past years. I must give a special thanks to my supervisor, Dr. Stephen Corbin, for his openness to questions, engagement in my research, and genuine care for my learning experience. His value of mentorship, experimentation, and growth has been a continual source of motivation to me and I will take these same values forward with me in my career.

Part of this work is based upon experiments I performed during a Mitacs Accelerate internship with Pratt and Whitney Canada (P&WC). I would like to thank Mitacs and P&WC for their financial support and for providing me with the opportunity to get involved with the aerospace industry. I would specifically like to thank Thomas Georges, Josianne Coulombe, Orlando Scalzo, Benoit Meulemeester, and Jessie Gagnon for their kindness, time, and mentorship during my term at P&WC. Their lasting confidence in my research efforts has made this work rewarding, and for that I extend my gratitude.

I have greatly benefited from the experience and friendship of my colleagues in our research group at Dalhousie University. I must thank Julian O'Flynn, Cathy Whitman, Clark Murray, and Dan Cluff for all of the research advice, discussions, and training over the years. Without them, this research would have been vastly more difficult. I would also like to thank my peers in the High Temperature Thermal Analysis Lab as well as many other faculty, staff, and students for their help, perspectives, and laughter over the course of this work.

I would like to acknowledge the financial support received from NSERC and P&WC through the NSERC Industrial Research Chair program. Their financial support made this research possible.

I must extend thanks to Martha & Kirby Brown for always treating me as a part of their family and for making Nova Scotia a place I call home. I must also thank my parents, Dave & Marie Rayner, for always encouraging me to challenge myself and follow my passion.

Finally, I must thank my wife, Kayleigh, for her unwavering support and patience throughout this journey. She has been here from the beginning and has always motivated me to do better and go further. Without her, this degree would not have been possible.

CHAPTER 1

INTRODUCTION

Nickel-based superalloys are heat resistant materials that retain exceptional strength at elevated temperatures [1,2]. For this reason, nickel-based superalloys (Ni-superalloys) are often the material of choice for the high temperature sections of aero engines [1,2]. However, conventionally cast superalloys are expensive to manufacture due to the demanding machining processes required to fabricate the complex part geometries found in the aerospace industry. In addition, the starting weight of a Ni-superalloy can be multiple times greater than the weight of the finished part, leading to a high buy-to-fly ratio and the generation of large amounts of waste material produced from machining or material removal [3]. Metal injection molding (MIM) is an alternative to manufacturing complex Ni-superalloy components without numerous machining steps [4]. Using MIM, Ni-superalloy powder can be formed into net-shaped parts that are then de-bound and sintered to full density. The MIM process only utilizes the volume of metallic material required to mold the part and involves little to no machining, decreasing raw material costs while significantly reducing the waste produced.

Despite the advantages of the MIM manufacturing route, MIM Ni-superalloys are currently restricted to non-structural applications in the aerospace industry. One reason for this restriction is the apparent inability to increase the grain size of some powder metallurgy (PM) Ni-superalloys [3]. Cast Ni-superalloys commonly contain grain sizes on the scale of 1-3 mm while the MIM Ni-superalloys exhibit much finer grain sizes ranging from 20-30 μm [3,5,6]. The dissimilar grain size between cast and MIM Ni-superalloys creates a difference in the grain boundary area, which impacts creep rupture life. In general, the higher grain boundary area associated with finer grain sizes causes a higher amount of grain boundary sliding during high temperature creep [2,3,5]. Therefore, it is desirable to increase the grain size of the MIM Ni-superalloys to improve their creep properties for structural applications in the high temperature sections of aero engines.

The present research focuses on various techniques for sintering a metal injection molded Ni-superalloy powder to achieve grain growth. Emphasis is also placed on the underlying mechanisms that prevent or allow grain growth to occur. This introductory chapter provides an overview of the nickel-based superalloys, metal injection molding process, and underlying sintering theory being applied. This is followed by a description of the thermal analysis methods used in this research.

1.1 Nickel-Based Superalloys

Nickel-based superalloys have been the subject of extensive research and development since their inception in the early 1940's and 1950's. As such, there is a significant body of literature on their properties, chemistry, and microstructure under a wide range of manufacturing and service conditions. It is not the objective of this work to explain the metallurgical development of the modern Ni-superalloy, but rather to study the fundamental microstructural behaviour of a MIM Ni-superalloy during the sintering process. Therefore, only the essential aspects of Ni-superalloy metallurgy and design are discussed in this section.

Ni-superalloys are commonly the material of choice when a part requires high strength under static, fatigue, and creep conditions at elevated temperatures [1,2]. This is the case for gas turbine engine components, which often operate at temperatures exceeding 800°C

[1,2]. Over the past decades, engine designers have significantly increased the turbine entry temperature (TET, the temperature at which the hot combustion gases enter the turbine section) to improve engine performance. This is clearly outlined in Figure 1-1, where the increase in engine TET has greatly outpaced the increase in material capability. These higher operating temperatures can effectively increase both the fuel efficiency and power output of the engine, but place stringent requirements on the materials used in the hot sections [1–3,7]. Prior to 1960, the maximum TETs were below 800°C while modern TETs can be above 1300°C [1]. Although blade cooling and coating materials in the modern engine prevent metal temperatures from reaching this extreme, alloy temperatures approaching 1100°C are a reality [1–3,7]. Increasing TETs have therefore driven, and continue to drive, improvements in both part design and Ni-superalloy metallurgy[1–3,7].

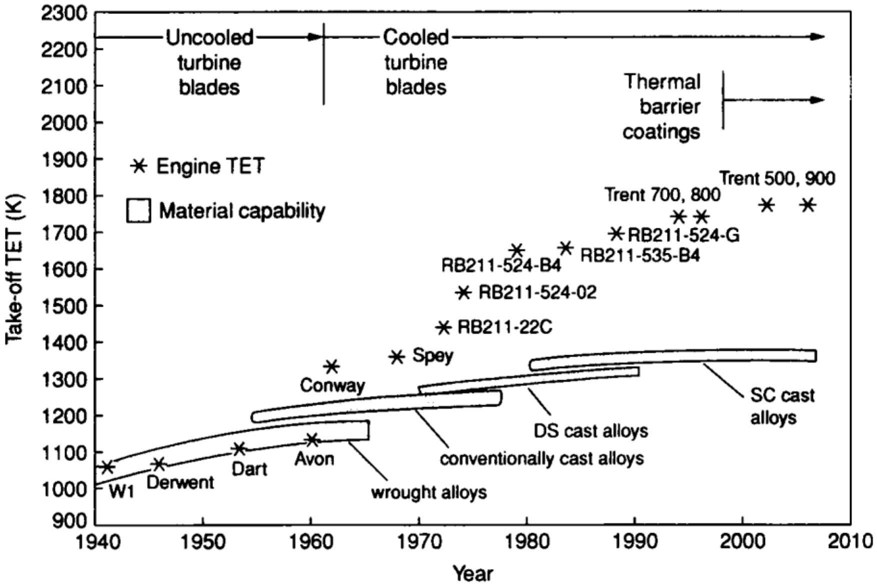

Figure 1-1. **Turbine entry temperature (TET) plotted with alloy temperature capability over recent decades [1].**

Reproduced with permission of Cambridge University press, from The Superalloys: Fundamentals and Applications, R.C. Reed, 2008, through PLSclear.

Compared to the Ni-superalloys, other metals such as titanium alloys and steels cannot match their strength at temperatures exceeding 1000°C [2]. Titanium alloys, although lighter, also display poor oxidation resistance above 700°C, limiting their application to the hot sections of the engine [1]. Some steels are low cost, high strength, and creep resistant, but do not exhibit the same creep rupture life at elevated temperatures [1,2]. In addition, both Ti and Fe exhibit a crystal structure transition above 700°C, which can lead to detrimental expansion or contraction of these alloys at elevated temperatures [1]. Ceramic materials such as silicon carbide and alumina are generally not used in these applications due to their poor toughness and ductility, despite their excellent resistance to creep [1]. Refractory metal alloys are generally too expensive along with other FCC structure elements such as Pt. Chromium is prone to brittleness and Co, although similar to Ni, is more expensive [1,2]. Evidently, the feasible options for suitable base elements in gas turbine alloys are limited. As a result, three main types of superalloys have been developed: Fe, Co, and Ni-based superalloys [1,2,8]. Of these, the Ni-superalloys are the most advanced and are used extensively in the hot sections of gas turbine engines, making them the focus of this discussion [1,2,8].

Before discussing the physical metallurgy of the Ni-superalloys in more detail, it is necessary to introduce the concept of creep. Creep is the slow deformation of a material over time at elevated temperatures under a sustained load [7]. In contrast to the behaviour of materials at low temperatures, where the strain is dependent on stress, the strain of materials at high temperatures is dependent on time and temperature in addition to stress [7]. The requirement for turbine engine materials to operate at high TETs for extended service lives makes creep a critical material property to consider for the Ni-superalloys.

There are three main stages of creep: primary, steady-state, and tertiary. A generalized constant-load creep response for metals is presented in Figure 1-2. Upon loading, there is an initial elastic deformation followed by the primary stage of creep. During primary creep, the strain rate continually decreases as the material either strain hardens or experiences an increase in creep resistance [9]. As the strain rate stabilizes, the material enters a stage of steady-state creep where the strain accumulates gradually over time. The rate of creep during this stage is determined by the stress applied at a given temperature as well as the balance between strain hardening and recovery processes in the material [9]. Over time, microstructural damage occurs and cavities form and accumulate at the start of the tertiary stage of creep. As the cavities accumulate and grow, the cross sectional area of the material is effectively decreased, resulting in an increasing creep rate leading up to final fracture [7]. The time to failure under various loading conditions is typically given as the creep-rupture life of a material.

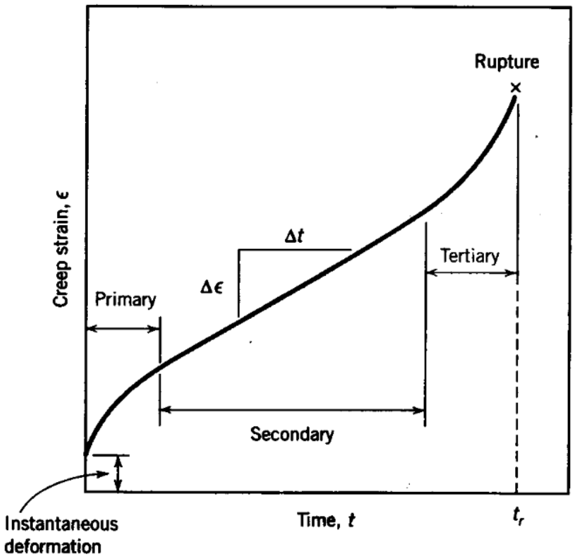

Figure 1-2. Generalized creep strain curve for metals under a constant load [9].

Republished with permission of John Wiley & Sons, from Materials Science and Engineering: An Introduction, W.D. Callister, D.G. Rethwisch, 8th edition, 2010. Permission conveyed through Copyright Clearance Center, Inc.

More relevant to the present research are the two mechanisms of creep: dislocation creep and diffusional creep. In crystalline materials, plastic deformation is a result of the dislocations overcoming the resistance of the lattice and any obstacles in their path [7]. These obstacles can include precipitates, solute atoms, and other dislocations which act to pin or lock dislocations in place by preventing them from gliding along their respective slip planes. However, the diffusion of atoms away from the bottom of the half plane located above a dislocation allows the dislocation to move upwards or "climb" [7]. If this occurs, the dislocation can climb over an obstacle in its path, becoming unlocked and gliding until it runs into another obstacle where it must climb once again. A mechanical force (i.e. a sustained load) can provide a driving force for the diffusion of atoms away from obstructed dislocations, enabling climb. This "glide-climb-glide" process repeats over time, leading to the slow, steady and time dependent deformation of creep [7]. Since dislocation climb requires diffusion, temperatures around 0.3-0.4 T_M (when diffusion becomes active) are generally required for dislocation creep to occur in metals. In addition, the dependence of creep rate on the applied stress is due to the climb force, which provides the driving force the diffusion of atoms away from the loaded dislocation. Larger applied stresses cause higher driving forces for the diffusion of atoms away from the dislocations, leading to faster rates of dislocation climb and, ultimately, higher strain rates [7].

In diffusional creep, the applied stress is relieved via grain elongation [7]. The mechanical force in this case provides the driving force for diffusion across the grains in the microstructure, leading to their elongation over time [7]. At high temperatures bulk diffusion allows this process to occur through the grain itself, but at lower temperatures grain boundary diffusion is dominant. In both cases, as is the case with dislocation creep, the creep rate is proportional to the stress. Grain boundary sliding occurs in conjunction with this process to prevent holes from opening up between grains [7].

To combat these creep mechanisms a number of design approaches are employed. For dislocation creep, the number of obstacles to dislocation motion are maximised by alloying to give a solid solution with stable precipitates. For diffusional creep, the grain size is maximised to make the diffusion distances large and limit the grain boundary area for grain boundary sliding and diffusion [7]. Precipitates such as carbides are also formed in the grain boundaries to resist grain boundary sliding [7].

The nickel-based superalloys are complicated alloys which rely on multiple strengthening mechanisms to retain strength and resist creep at high temperatures. Nickel, the primary constituent of the alloy, has an FCC structure that is stable from room temperature to its melting point [1]. It is this wide range of structural stability with temperature that makes Ni a suitable choice for elevated service temperatures [1]. The FCC structure imparts toughness and ductility to the alloy while also maintaining a relatively low diffusion rate of solute atoms, increasing high temperature stability of the alloy [1]. Ni also has a high solubility for alloying elements, making it suitable for high degrees of solid solution strengthening. Cr, Co, Fe, Mo, W, V, Ti, and Al are all commonly added to the Ni-superalloys in various quantities to provide solid solution strengthening [2]. The high levels of Cr used in these alloys serves to provide superior corrosion resistance, which is required for the high temperature, highly corrosive service environments found in gas turbine engines [2]. The solid solution of these solute elements in Ni constitutes the γ matrix phase of the Ni-superalloys.

Specific amounts of Al and Ti are added to the alloy to form an ordered Ni_3(Al, Ti) precipitate phase known as the gamma prime, γ’, phase [1,2,8]. The primary γ’ precipitates have a cuboidal morphology and are coherent with the γ matrix, exhibiting a lattice mismatch of less than 1.5% with the matrix [1,2,8]. Their coherency with γ matrix maintains a low interfacial energy, imparting long term thermal stability of the precipitate phase. Much finer secondary γ’ precipitates can also form as spherical particles in the γ matrix, increasing the degree of strengthening. The γ’ precipitates provide a large degree of precipitation hardening to the alloy and the Al: Ti ratio is typically controlled to maximize the γ’ volume fraction.

Refractory elements such as Ta, W, Re, and Ru are commonly added to the Ni-superalloys because they are potent solid solution strengtheners and have slow diffusion rates in Ni [1–3]. Although these elements have multiple effects on the alloy, they are typically added to increase creep resistance [1–3]. Hf and Zr are other alloying additions that can improve the high temperature performance of the Ni-superalloys. Not only is Hf a strong carbide former, but it is thought to segregate to the grain boundaries and fill vacancies, decreasing the grain boundary diffusion rate [1–3]. Hf can also enter the γ’ phase, causing it to precipitate with cellular or dendritic morphologies which serrate the grain boundaries, further improving the resistance to grain boundary sliding [1–3].

Carbide phases in the Ni-superalloys can also increase creep rupture life by resisting grain boundary sliding. Though, the formation of carbides removes solid solution strengthening elements from the γ matrix and can decrease ductility [1–3]. The formation of carbides depends on the alloy composition, temperature, and time, making the processing route critical to the final properties of the alloy[1–3].

Four types of carbide are observed in the Ni-superalloys: MC, $M_{23}C_6$, M_7C_3, and M_6C [1–3]. MC carbides are generally the most stable carbides at high temperatures and precipitate from the alloy melt. These carbides are most commonly Ti, W, Ta, and Hf carbides since these elements are strong carbide formers [1,2]. The MC carbides can have globular, script, or blocky morphology and can form in both the γ grains and grain boundaries. The $M_{23}C_6$ carbide forms in the grain boundaries and can contain Cr, Mo, and W, but is usually Cr rich [1,2]. The $M_{23}C_6$ carbides are stable at intermediate temperatures and have been found to form from the breakdown of MC carbides around 750°C [1,2]. M_6C and M_7C_3 are also observed in some alloys, though both commonly transform to $M_{23}C_6$ and are only stable at intermediate temperatures [1,2].

Carbon, along with boron, generally prefer locations along the grain boundaries and promote the formation of carbides and borides in the grain boundaries [1,2]. Carbon and boron are therefore considered grain boundary strengtheners, as these precipitate phases help combat grain boundary sliding during creep. The formation of controlled amounts of discontinuous MC and $M_{23}C_6$ carbide particles along the grain boundaries is considered essential to the creep rupture properties of the Ni-superalloys [1–3].

Despite their complexity, the overall design principle behind the Ni-superalloys is straight forward: place as many obstacles to dislocation movement in the alloy as possible and limit the diffusion rate of solute elements to promote high temperature stability [7]. These alloys derive their high temperature strength from a combination of solid solution strengthening, finely dispersed γ' precipitates, and discrete grain boundary carbide particles [1,2,7]. The slow diffusion of refractory elements in the γ matrix helps to retain alloy stability and strength while the presence of the discrete grain boundary carbides reduces grain sliding by pinning the grain boundaries, increasing the creep resistance [1,2,7].

For conventionally cast Ni-superalloys, the temperature at which rupture occurs at 1000hrs under a load of 137MPa ranges from about 930°C for IN738C to 950°C for MARM246 [1,3]. In general, the stress for 1000hr rupture decreases rapidly as the temperature is increased beyond 900°C. This behavior makes sense given the previous discussion on how the applied stress provides driving force for creep mechanisms to proceed. However, it is important to remember that the heat treatments and manufacturing processes applied to the Ni-superalloys can have a dramatic impact on the size, distribution, and morphology of both γ' precipitates and carbides, with various consequences on the rupture properties [1,2].

The creep properties outlined up to this point were for conventionally cast polycrystalline Ni-superalloys. Over past decades, alloy manufacturers have significantly improved the creep rupture properties of the Ni-superalloys, first by directional solidification and then followed by single crystal growth [1–3,7]. Directional solidification controls the growth direction of solid during the casting process, creating a columnar grain structure oriented along the axis of loading for the part. Single crystal growth controls the solidification process to maintain solid-liquid interface stability such that solid grows with a single crystallographic orientation. Directionally solidified alloys have a larger grain size than conventionally cast alloys while single crystals have no grain boundaries and are composed of a single grain. As the grain size increased and grain boundaries were eliminated from the Ni-superalloys, significant increases in creep rupture life were realized. Directionally solidified alloys can withstand temperatures in the range of 950-1000°C for the 1000hr/137MPa loading condition while single crystals can withstand temperatures approaching 1100°C under the same testing conditions [1,3]. The reduction of grain boundary area reduces the grain boundaries available for diffusion and grain sliding to occur, limiting diffusional creep. The removal of grain boundaries in the single crystal alloys also meant that grain boundary strengthening elements Hf, C, B, and Zr could be removed from the alloys, increasing the melting temperature and improving alloy segregation [1,3]. Modern single crystal superalloys typically contain additions of Re and Ru to improve the creep rupture properties of the alloys while Cr has generally been decreased to maintain temperature stability [1].

1.2 Powder Metallurgy of Nickel Superalloys

Powder metallurgy (PM) techniques offer a cost-effective manufacturing route for the Ni-superalloys [3]. More importantly, the fabrication of PM superalloys generates far less scrap material than the fabrication of cast alloys, reducing inventory requirements and recycling costs [3]. Not only does this decrease the buy-to-fly ratio of these alloys, but it aligns PM superalloys with current environmental concerns surrounding manufacturing. From this perspective, modern initiatives to curb carbon emissions, use energy more efficiently, and emit less waste make PM superalloys an attractive manufacturing route.

From a metallurgical perspective, PM Ni-superalloys offer better control over the microstructure as well as better microstructural and compositional homogeneity. Cast alloys can have non-uniform grain sizes, elemental segregation, and are prone to forming brittle eutectics which decrease their high temperature properties [3]. In addition, PM is the only available method to fabricate materials such as tungsten carbide cutting tools, porous filters, cermets, and oxide dispersion strengthened (ODS) alloys [3,10]. The ability of PM to produce materials with unique properties and microstructures makes it an advantageous technology across many sectors [3,10].

Powder metallurgy has been successfully applied to a number of Ni-superalloys in recent years [2,3,11]. For instance, Rene 95 produced via PM techniques has been used for turbine disks and compressor shafts in the F404 engine used in F-18 jets to reduce costs [2]. PM Rene 95, along with PM LC Astroloy and IN-100, have been applied to turbine disks because they combine high yield and tensile strengths with good creep and stress-rupture properties [2]. The PM version of these alloys also offers excellent low cycle fatigue (LCF) and crack propagation characteristics. The fine grain size associated with these PM alloys enables them to undergo superplastic forming while maintaining a homogenous solid solution containing a uniform distribution of γ' precipitates. The improved formability and properties in this case are unique to the PM processing route [2].

Advances in powder manufacturing techniques over the past decades has reduced the degree of powder contamination by C, O, H, and N, improving powder consolidation and compositional control [3]. However, challenges remain for the PM superalloys such as alloy design, grain size and contamination of the powder surface during production which become “prior particle boundary (PPB)” features in the sintered part. Powders can also become contaminated with ceramic inclusions (i.e. from degradation of the ceramic nozzles used to gas atomize the powder) and can contain entrapped gas, restricting densification of the material [3].

Powder contamination by C, O, H, and N remains problematic and preferential formation of stable carbides and oxides on particle free surfaces can restrict sintering [3]. To combat the PPB problem, many PM Ni-superalloys have a decreased carbon content to reduce carbide formation at PPBs. These alloys also tend to have an increased level of Ta and Hf which promote the formation of stable carbides within the powder particles instead of at the PPBs [3]. However, oxides at the PPBs can also act as nucleation sites for carbides, making oxidation critical to avoid as well [12].

The delineation of PPBs by oxides and carbides not only restricts densification, but it can also inhibit grain growth [3,12]. Given the fine grain size of the PM Ni-superalloys, the inability to increase the grain size means that the creep properties of the PM alloy are generally inferior to cast versions [2,3]. The PM Ni-superalloys are often very similar in composition to their cast versions, containing high amounts of refractory elements to help combat creep. These same elements generally act to form the PPB carbides that inhibit grain growth, resulting in their inferior creep properties.

1.3 Metal Injection Molding

Metal injection molding (MIM) is a powder metallurgy technique that combines the shaping capabilities of plastic injection molding with the engineering properties of metallic materials. It is a versatile technology that has been applied across multiple industrial sectors to manufacture items such as heat sinks, surgical tools, aero engine components, and automotive turbochargers [4]. MIM offers shape complexity, structural properties, tight tolerances, material flexibility, and low production costs making it an attractive manufacturing technique for small, complex parts across many industries [4].

In the MIM process, metal powders are mixed with binders to create a low melting temperature feedstock. This feedstock can then be injected into a mold of the desired shape under temperature and pressure. Once cooled, the molded part is comprised of metal powder in a solid binder matrix and is termed a “green part”. Green parts are oversized to account for the dimensional shrinkage that will later occur during powder consolidation and have a low strength due to the absence of any metallurgical bonds between powder particles. In order to increase the strength, the material must be consolidated at high temperatures via a sintering step. However, the binders must first be removed using a de-binding process, which leaves a porous metallic structure in the shape of the molded part. A pre-sintering step is typically applied after de-binding to start bonding the powder particles together and impart some mechanical strength to the porous structure. Following de-binding, the part is sintered to consolidate the metallic powder into a final, dense, material. Finishing treatments can subsequently be applied to the sintered parts, if required.

The MIM feedstock is typically designed to have a high packing density of powder. This increases the number of particle-particle contacts in the mixture while the binder fills the remaining inter-particle spaces. Ideally the powder itself has a wide particle size distribution (PSD) so that the packing density is high and has a spherical morphology for low inter-particle friction. Fine powder sizes also tend to improve feedstock flow and molding behaviour [4]. The binder is typically a multicomponent system of waxes and polymers. A surfactant may also be included to improve wetting of the binder on the powder and decrease the overall feedstock viscosity [4]. The feedstock is generally designed to behave as a viscous fluid at temperature and a solid at room temperature. A solids loading of about 60% is common in MIM [4].

During the injection molding stage, molten feedstock is injected into the mold cavity under pressure and is allowed to freeze in the mold cavity. At temperature, the binder system is designed to allow sufficient particle sliding during injection and fill voids in the mixture.

When frozen, binder system acts as a solid and holds the particles in their molded shape, providing some mechanical strength. Hydrostatic pressure during molding ensures uniform packing in the compact and prevents density gradients in the material [4].

De-binding can be accomplished numerous ways including solvent immersion, thermal evolution, and wicking methods. Wicking uses a powder bed to support the part and absorb the molten binders as they “wick” out of the porous part and is the most common de-binding method [4]. Slow heating rates are used to avoid evaporation of the binders, which can disrupt the powder structure and break the part. The multicomponent nature of the binder system also allows for individual phases of the binder to be removed separately, helping to retain strength as the binders are removed. Residual polymer often remains as a structural component of the de-bound part in the form of pendular bonds and the only way to practically remove the remaining binder is via thermal evolution at higher temperatures [4]. A subsequent pre-sintering step allows residual binders to burn off and causes the individual powder particles to form necks, increasing the mechanical properties of the part. If a wicking support media is used during de-binding, it must be removed before sintering, but pre-sintering can be done in the powder bed. Time and temperature of the pre-sinter stage can determine degree of bonding between particles (necking) and, therefore, dictates the pre-sinter strength.

Finally, a high temperature sintering process is applied to consolidate the part into a dense, structural material. A homogeneous, high packing density in the MIM part is required to obtain uniform shrinkage and good bonding during sintering [4]. Sintering cycles are designed to achieve specific properties and microstructures and heating rates are typically slow to avoid part distortion.

A number of Ni-superalloys have been successfully metal injection molded over recent years, including IN625, IN713, and IN718 [4,6,13–16]. However, the difficulties associated with sintering MIM Ni-superalloys to full density prevents the widespread use of MIM in critical aerospace components [4]. The number of reactive elements in the Ni-superalloys (i.e. Ti, Al, W) makes these powders sensitive to carbon and oxygen contamination during the MIM process, which is detrimental to sintering [2–4,6]. In addition, the fine grain sizes in some MIM Ni-superalloys limits their high temperature creep life [6]. Therefore, further advances in sintering and grain coarsening of the MIM Ni-superalloys is required before they can be employed in structural high temperature applications.

1.4 Sintering Theory

The present research applies solid state, liquid phase, and supersolidus liquid phase sintering techniques in attempts to achieve grain growth in a MIM nickel superalloy (NiSA). These sintering approaches are well established and are therefore only briefly discussed in this section.

1.4.1 Solid State Sintering

Sintering is a process that causes powder particles to bond together at elevated temperatures. The bonding between particles is driven by the removal of free surfaces to decrease the overall surface energy of the material [11]. This process is shown in Figure 1-3, where the formation and growth of particle bonds into necks and grain boundaries is caused by mass transport mechanisms which allow atoms to move to lower energy lattice sites in order to reduce surface energy. Heating the material to a high enough temperature provides the activation energy required for the atoms to break free from their initial lattice sites and diffuse to new, lower energy, locations [11]. Most materials require temperatures between 0.5 and 0.8 of their melting temperature to exhibit sintering.

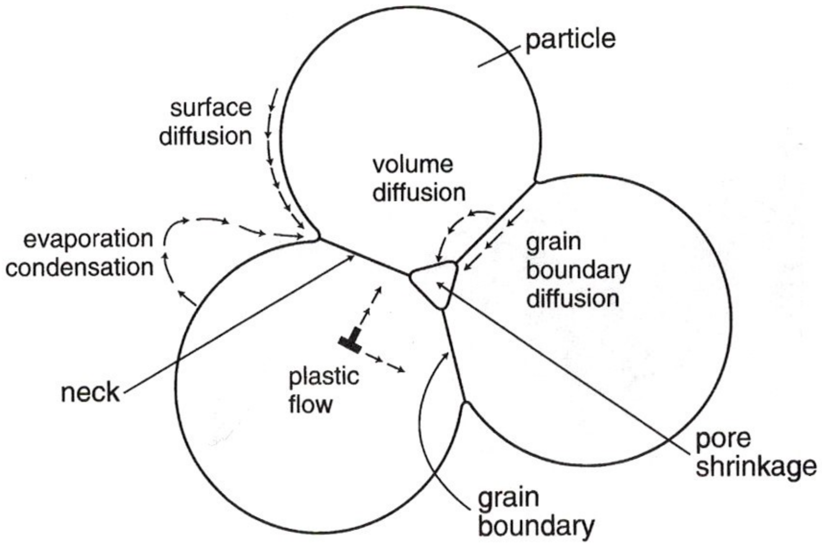

Figure 1-3. Schematic of the various diffusion mechanisms which contribute to sintering [10].
Reprinted with permission from R.M. German, A. Bose, Injection Molding of Metals and Ceramics Metal Powder Industries Federation, Princeton, New Jersey, USA, 1997.

The temperature, time, and particle size all influence the rate of bond growth between particles and are key variables in the sintering process. The time-temperature profile used to sinter a given powder compact significantly influences the final microstructure and properties of that material. Temperature governs the amount of energy available for mass transport to occur and inherently the rate at which it occurs. The time that energy is available for also influences the amount of mass transport, grain growth, and final density [11].

Surface and bulk transport are the two divisions of mass transport mechanisms during sintering. Both transport mechanisms relocate atoms into the bond (neck) between particles and contribute to particle bonding, however the source of atoms differs between the mechanisms. Surface transport moves atoms from surrounding pore surfaces while bulk transport moves atoms from nearby grain boundaries. In addition, bulk transport mechanisms contribute to both coarsening and densification, while surface transport mechanisms only cause coarsening [11].

Surface transport mechanisms include surface diffusion and evaporation-condensation and are typically active at lower temperatures during heating of the material. In this initial stage of sintering there is a large amount of neck growth between contacting particles. However, since the necks between particles have a small volume, the volume of mass transported to the neck is relatively small, and there is no significant contribution to densification or dimensional change during the necking stage [11]. There can be, however, a significant degree of microstructural coarsening as a result of surface transport. This can cause the strength and grain size to increase while the surface energy is significantly reduced. For sintering processes where densification and dimensional change are not the desired outcome, such as in casting cores and porous bearings, surface transport mechanisms are targeted [11].

Bulk transport mechanisms are responsible for densification and shrinkage of the material and generally dominate sintering at high temperatures [11]. Grain boundary diffusion and volume diffusion are two bulk transport mechanisms that generally dominate the sintering of metals. Both mechanisms involve the movement of vacancies from pores through the lattice or along grain boundaries causing mass transport into the pores. The vacancies are subsequently eliminated at microstructural interfaces such as grain boundaries, dislocations, or phase boundaries, leading to densification of the material. Generally, grain boundary diffusion has a lower activation energy than volume diffusion and so it is often the dominant bulk transport mechanism [11].

The sintering process commonly involves a combination of both bulk and surface transport mechanisms which are dominant at different stages of sintering. Cooperation between these mechanisms is also required for effective sintering. For instance, mass transport along a grain boundary requires surface diffusion to redistribute the atoms along the boundary [11]. Therefore, mass transport in sintering utilizes multiple mechanisms, making sintering of many materials a challenging process to fully understand and predict.

The sintering process can also be described using different stages which refer to its geometric progression. There are four main stages of sintering: point contact, initial stage, intermediate stage, and final stage [11]. A schematic of these stages is presented in Figure 1-4. The point contact stage describes the powder prior to any particle bonding where the powder is loosely packed together. In this stage, adhesion between particles occurs due to weak forces such as Van der Waals forces and agglomeration. The initial stage of sintering describes the growth of a bond between particles from an initial point contact and is only active for the beginning of neck growth. Aside from the necking observed between particles, the initial stage of sintering generally does not exhibit any densification over the point contact stage. In contrast, the intermediate stage is characterized by densification of the porous structure, grain growth, and pore rounding. The final stage of sintering primarily describes changes in pore structure when the pores have become spherical and closed. At the beginning of the final stage, pores are attached to grain boundaries, but will separate from them as the final stage progresses. There is also typically clear evidence of grain growth in the final stage of sintering and the grain size is larger than the initial particle size of the powder.

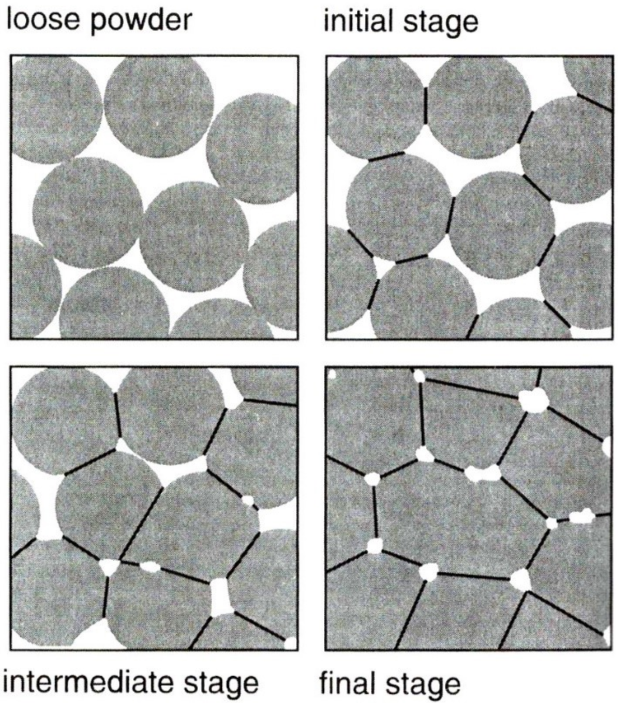

Figure 1-4. Schematic of the various stages of sintering [11].

Reproduced with permission of John Wiley & Sons, from Sintering Theory and Practice, R.M. German, 1996, [11]. Permission conveyed through Copyright Clearance Center, Inc.

1.4.2 Liquid Phase Sintering

Liquid phase sintering (LPS) is a sintering technique which can achieve high rates of densification in powder metallurgy (PM) components [11]. In LPS, a lower melting point additive is added to the primary powder to form a liquid phase during sintering. The mixed powders generally undergo densification from solid state sintering prior to the liquid phase forming. Once liquid forms, the three main parameters that effect the sintering behaviour are the solid solubility in the liquid, wetting of the liquid on the solid grains, and solid phase diffusion in the liquid [11]. The capillary force from the liquid phase helps eliminate pores and reduce surface area. The liquid phase also acts as a path for rapid diffusion and mass transport, aiding densification and bonding between particles. Three main stages of densification are generally observed once liquid forms: re-arrangement, solution-reprecipitation, and final-stage sintering [11]. A schematic of the liquid phase sintering process stages is presented in Figure 1-5.

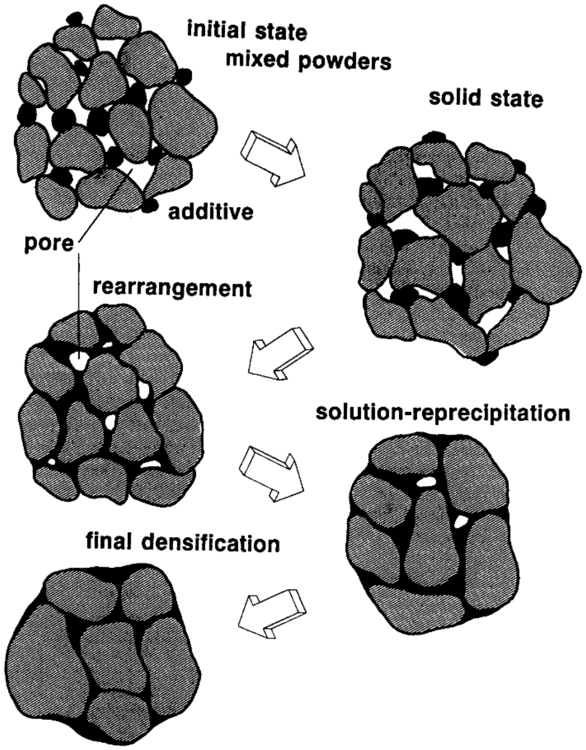

Figure 1-5. Schematic of the liquid phase sintering stages [11].
Reproduced with permission of John Wiley & Sons, from Sintering Theory and Practice, R.M. German, 1996. Permission conveyed through Copyright Clearance Center, Inc.

When the liquid first forms, there is a rapid densification due to the liquid phase dissolving the edges of solid grains and capillary forces causing grain re-arrangement. As the solid grains re-pack to a higher density during re-arrangement, liquid is released to fill pores in the structure. As this occurs, the viscosity of the semi-solid structure increases, resulting in a continuously decreasing densification rate [11]. In addition, any prior solid state sintering of the powder restricts the re-arrangement of the solid grains, further restricting densification.

As liquid phase sintering progresses, the initial rate of densification obtained by re-arrangement reduces considerably. At this point, solubility and diffusivity effects begin to dominate the sintering process and the solution-reprecipitation stage begins [11]. Smaller grains have higher energy and solubility in the liquid than larger ones, creating a concentration gradient in the liquid. This causes mass to be transported from the small grains to the larger ones via diffusion through the liquid in an Ostwald ripening process [11]. The coarsening of the grain size in solution-reprecipitation is accompanied by densification via grain shape accommodation where the reprecipitating grains can grow in custom shapes to obtain a higher packing density and reduce the overall surface energy.

The final stage of liquid phase sintering is primarily sintering of the solid phase. Microstructural coarsening continues during this stage and additional densification is slow due to the rigidity of the contacting solid grains [11]. In general, the sintering time during the final stage of sintering is kept low due to degrading material properties. For instance, alloys may display solute segregation, grain growth, and trapped gas in pores may cause swelling. Therefore, short sintering times are common in liquid phase sintering [11].

The volume of liquid formed is another critical parameter in liquid phase sintering. The degree of densification during the re-arrangement stage is influenced by how much liquid is present [11]. High amounts of liquid may be capable of reaching full density during re-arrangement while low amounts of liquid may require longer hold times in order to reach full density via the slower solution-reprecipitation stage. In addition, the liquid phase volume influences the structural rigidity of the material during sintering. If too much liquid is present, the structure of the material may not be able to withstand the force of gravity, leading to slumping and shape loss. In contrast, too little liquid may not provide sufficient capillary force, solution of solid grains, or liquid grain coverage to enact grain re-arrangement, preventing effective use of the liquid phase. Therefore, the volume fraction of the low melting point additive must be properly selected to form a liquid fraction which will effectively sinter the material to full density while avoiding shape loss [11,17,18].

1.4.3 Supersolidus Liquid Phase Sintering

Supersolidus liquid phase sintering (SLPS) has emerged as a specialized sintering technique which can achieve rapid densification of powder metallurgy (PM) components [11]. In SLPS, pre-alloyed powder is heated above its solidus temperature to form a liquid phase within the powder particles. The liquid phase causes each particle to fragment into individual grains which subsequently re-arrange and re-pack under capillary force from the liquid. The liquid phase also migrates through the porous structure quickly under capillary force and acts as a path for fast diffusion and mass transport. The net effect of the grain re-arrangement is rapid densification of the powder compact while solution-reprecipitation and grain shape accommodation contribute to the elimination of the remaining porosity [11]. The general progression of SLPS is illustrated in Figure 1-6.

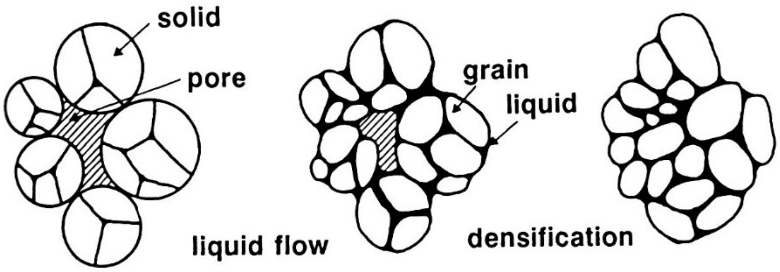

Figure 1-6. Progression of SLPS from left) initial powder, middle) liquid formation and particle fragmentation, and right) grain re-arrangement and densification [11].
Reproduced with permission of John Wiley & Sons, from Sintering Theory and Practice, R.M. German, 1996. Permission conveyed through Copyright Clearance Center, Inc.

SLPS causes liquid to form at particle contacts and in the grain boundaries within the powder particles [11]. The liquid formed within the powder particles causes them to soften, enabling densification in response to the capillary forces which develop at the particle contacts [17]. The average capillary force throughout the material acts as a net hydrostatic pressure resulting in isotropic shrinkage. Films of liquid in the powder structure therefore aid densification, but simultaneously reduce the structural rigidity of the material. The softened powder particles can also deform under the force of gravity, leading to a net deformation after densification has occurred. The capillary stress formed during densification is generally much larger than the gravitational force, therefore distortion is unlikely in the initial stages of SLPS. After densification has occurred, the part consists of solid grains with liquid films present at the grain boundaries. At this stage, the capillary forces approach zero while the force of gravity remains constant. Eventually, when the semi-solid structure is weak compared to gravity, the part will slump non-uniformly due to the distribution of gravitational stress with height. Evidently, densification and distortion in SLPS are both directly related to the liquid film distribution and thickness in the semi-solid structure.

Although a higher liquid fraction can lead to faster sintering, the rigidity of the semi-solid structure decreases as the liquid fraction increases. Therefore, the SLPS temperature must be strictly controlled in order to prevent too much liquid formation which can cause the material to deform under the force of gravity [11,17,18].

1.5 Grain Growth Mechanics

Polycrystalline materials contain grains which have multiple different crystallographic orientations. The orientation relationship between contacting grains dictates the type of grain boundary formed between them. Low angle, random high angle, incoherent, and coherent boundaries are common types of grain boundaries which are found in polycrystalline metals and the crystal lattice of each respective grain fits together differently depending on the type of boundary [19]. For instance, a low angle grain boundary occurs when the misorientation between two adjacent grains is small, only slightly distorting the bonds between atoms and leaving little free volume. In contrast, in a random high angle grain boundary when the angle of misorientation is much greater, the boundary structure is much more open and the lattices of the grains do not fit well together [19]. Each grain boundary represents a solid-solid interface, which has a grain boundary energy associated with it based on its type and structure. In addition, surface tension forces from the grain boundary angle and curvature are present, making random grain structures, like those found in metal polycrystals, inherently unstable [19].

At elevated temperatures, such as those applied for annealing or sintering, the unbalanced forces exerted on grain boundaries will cause them to migrate toward their center of curvature [19]. Grains with more than 6 contacts will grow while grains with under 6 contacts will shrink and disappear. The result is an overall increase in the average grain size as grain boundaries are eliminated to decrease the net grain boundary energy. This process is referred to as grain growth or grain coarsening and typically occurs in metals above $0.5T_m$ provided that the boundaries are mobile [19].

In metals, grain boundary migration typically occurs via atomic re-arrangement across a grain boundary. Atoms will detach from the high-energy side of a shrinking grain and bond to a growing, adjacent grain at a lower energy site [19]. The boundary itself then migrates a small distance as illustrated in Figure 1-7. This process is thermally activated, and is very similar to diffusion. Though, it is important to clarify that grain boundary diffusion refers to the movement of atoms along grain boundaries, while grain boundary migration refers to the movement of atoms across a boundary.

The diffusion of atoms across a grain boundary faces a host of additional barriers. As is the case in metal alloys, not all solute atoms are equivalent and require different amounts of energy to diffuse [19]. As a result, slow diffusing solute atoms can exert a cumulative drag force on a migrating boundary, reducing its mobility. In addition to this, the segregation of solute atoms to grain boundaries and edges can reduce the ability of other atoms to diffuse across the boundary, further limiting boundary mobility [19].

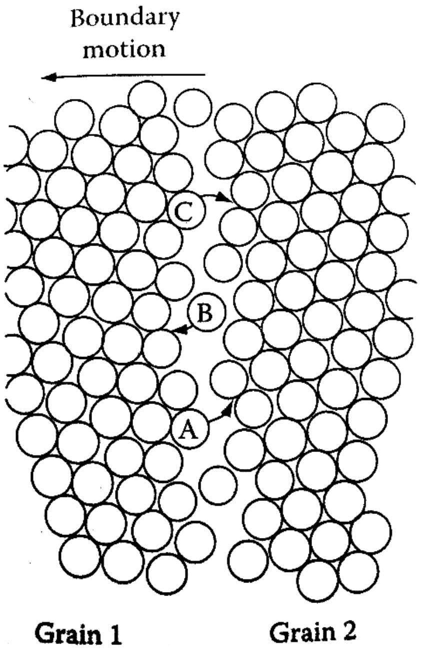

Figure 1-7. Simplified schematic of the atomic movement during boundary migration. If the rate of atomic movement from grain 1 to grain 2 is greater than that from 2 to 1, the boundary migrates toward the left [21].

Republished with permission of Taylor & Francis Group LLC, from Phase Transformations in Metals and Alloys, D.A. Porter, K.E. Easterling, M. Sherif, 3rd edition, 2009. Permission conveyed through Copyright Clearance Center, Inc.

The grain boundary structure itself has a large influence on its mobility. High angle grain boundaries, which have a more open structure, tend to be more mobile due to their large number of vacancies, steps, and ledges which serve as new sites for atoms diffusing across the boundary [19]. Their higher energy, caused by the larger misfit between adjacent lattices, also provides a larger driving force for diffusion across the boundary. However, twin boundaries, whose lattices generally fit together very well, are often considered nearly immobile [19]. Their closed, low misfit, structure restricts the movement of atoms and provides less driving force for boundary migration.

Finally, precipitates and secondary phases greatly influence grain boundary mobility. These phases can exert a pulling force on boundaries as they attempt to migrate past them, restricting the mobility of the boundary. In addition, the presence of these phases within the grain boundary creates additional interfaces with associated energies, raising the net boundary energy. The size, volume fraction, and coherency of secondary phases and precipitates all impact the net grain boundary energy and its mobility [19].

Considering these basic mechanics of grain growth, it could be expected that the grain boundary mobility in complex polycrystalline alloys such as the nickel superalloys would be restricted. In many engineering materials, this restriction of grain growth is viewed as a benefit because of the higher strength fine-grain materials generally exhibit. However, in unique cases where creep resistance is essential and there is a fine starting grain size, the restriction or absence of grain growth can be detrimental. This is the case with the MIM NiSA in this study.

1.6 Analysis Methods

The present research utilises a combination of analysis methods to investigate the sintering response of a metal injection molded Ni-superalloy. A single measure of sintering is largely insufficient to gain a complete understanding of a material's behaviour with time and temperature. Therefore, multiple material parameters are commonly measured both qualitatively and quantitatively to isolate and identify individual events during sintering. These include thermal events, such as melting and solidification which can be used to determine liquid content in the microstructure, shrinkage rates, which can be used to understand the sintering response to various thermal and microstructural events, and microstructural observations, which can be used to characterize microstructural details such as grain size, precipitate morphology, and density. The thermal analysis methods employed in the present work are discussed in the following sections while microscopy methods, including optical microscopy, scanning electron microscopy (SEM), and energy dispersive spectroscopy (EDS), are discussed in the experimental methods section.

1.6.1 Differential Scanning Calorimetry (DSC)

Differential scanning calorimetry (DSC) is a thermal analysis technique that can measure the difference in heat flow between a sample and a reference material during a constant heating or cooling profile. The heat flow versus temperature relationship obtained from DSC can be used to identify and characterize material responses to temperature such as phase transformations, enthalpies of melting and solidification, solvus and precipitation temperatures, and heat capacity, all of which are particularly important in metallurgical work.

Heat flux DSC was employed in the present research. Heat flux DSC instruments consist of a single furnace in which two crucibles are placed on a conductive carrier and connected by a metal strip. A schematic of the DSC instrument set-up is shown in Figure 1-8. Each crucible has its own thermocouple and one crucible contains a reference (i.e. empty or alumina) while the other crucible contains the sample material being tested (i.e. Ni powder). The sample and reference temperatures are determined by the voltage difference between the two thermocouples. As the apparatus is heated at a constant rate, the reference and sample material will heat up and remain at near-identical temperatures over time. This is especially true for heat flux DSC instruments because the metal strip connecting the two crucibles minimizes the temperature difference between the sample and reference. When a thermal event occurs in the sample material, the heat flow in or out of the sample associated with that event will cause the sample temperature to differ from the reference temperature. This temperature difference is measured by the voltage difference between the sample and reference thermocouples and, due to the connecting strip between the crucibles, is directly proportional to the heat flux between the sample and reference materials. The measured difference in temperature is calibrated using well known enthalpy versus temperature relationships for pure materials. For example, the temperature of the DSC can be calibrated by measuring the melting temperatures of well documented pure materials such as aluminum and silver. Similarly, the measured difference signal integrated over time can be related to enthalpy via calibration with the known latent heat of pure materials.

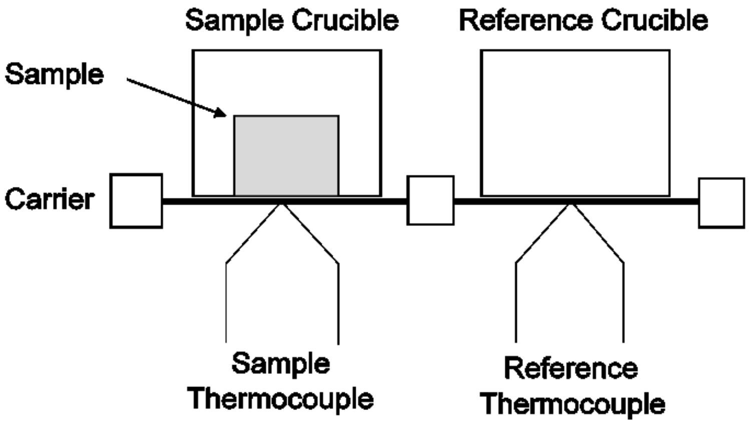

Figure 1-8. Schematic of a common carrier set-up in DSC instruments.

The appropriate interpretation of a DSC trace requires both experience and knowledge of a sample material's response to temperature. As an example, the DSC heating trace for the complete melt of a commercial brazing filler metal powder, BNi-2 (Ni-7Cr-3Fe-4.5Si-3B wt%) [20], is analyzed in Figure 1-9. The first thermal event observed during heating of this powder is an exothermic event, labelled point A in Figure 1-9, which starts at 450°C. This first deviation from the baseline is the start of the recrystallization event for the BNi-2 alloy powder. The full recrystallization event is characterized by three individual exothermic peaks in the DSC trace, labelled points B-D, which occur in the range from 450-700°C. Corbin et al. explain that the rapid solidification of the BNi-2 alloy during powder fabrication leads to the formation of metastable phases which then transform to an equilibrium structure upon heating [20].

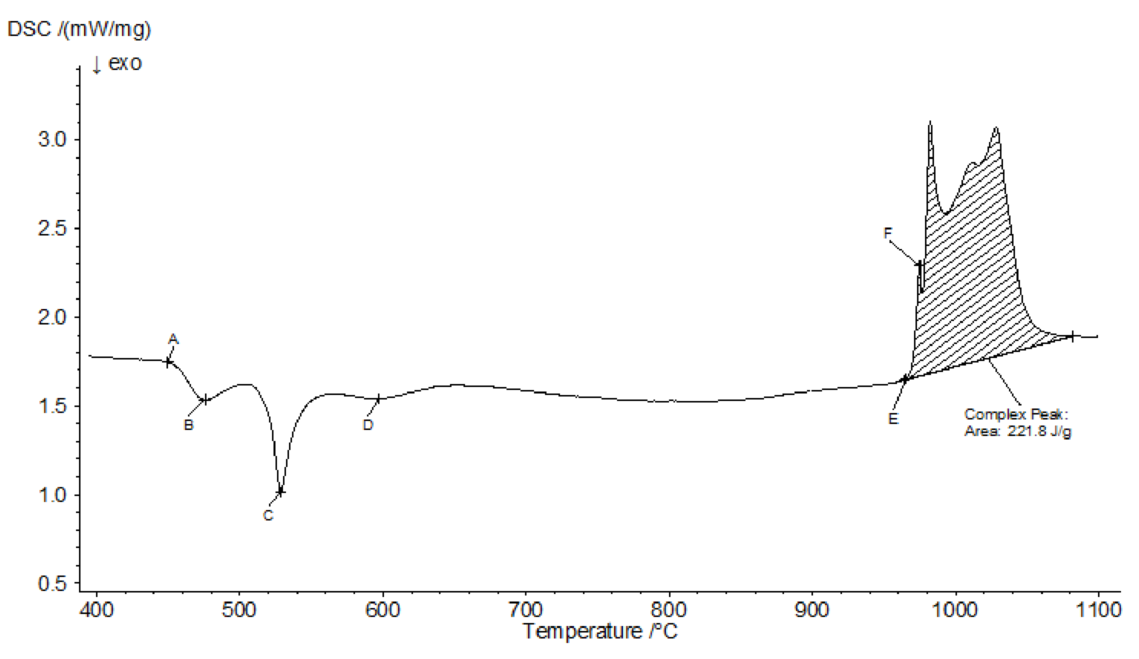

Figure 1-9. DSC trace analysis for BNi-2 powder heated at 20Kpm to 1100°C.

At higher temperatures, a large, multi-peak, endothermic event occurs starting at point E. This is the melting event for the alloy, which has an onset temperature of 968°C. The onset temperature is defined as the temperature at which the tangent lines to the baseline and slope of the peak intersect [21]. However, for more complex alloys such as BNi-2 and the NiSA's, the start of melting is more accurately defined by the first deviation from the baseline [21]. This is because alloys have wider melting ranges than pure metals (which have a single melting temperature) and can exhibit various degrees of incipient melting [21].

The BNi-2 alloy's melting event is a unique example to discuss because of the number of individual peaks detected during the event. These peaks are caused by the multicomponent nature of the BNi-2 alloy, which can form a ternary eutectic, two binary eutectics, and a primary Ni solid solution all which contribute to the melting event [20]. Once melting has finished, the DSC trace returns to a baseline. Constructing a baseline underneath the melting event and taking the integral (area under the curve) results in an enthalpy measurement for the event [21]. This is demonstrated in Figure 1-9, where the area of the melting event is shaded in and the heat of fusion is measured to be 221.8J/g. This result agrees with the enthalpy measurement of 220J/g published by Murray et al. for the BNi-2 powder [22].

Similar to the heating trace, the cooling trace (not presented here) can be used to analyse any thermal events which occur as the DSC returns to room temperature. For the BNi-2 alloy, the exothermic solidification of the alloy occurs while irreversible events, such as the recrystallization, do not reappear [20–22].

One final detail that should be highlighted is the DSC response to heating rate changes during an experiment. During the time directly following a heating rate transition in the temperature profile (i.e. heating at 10°C/min to cooling at 10°C/min) the furnace ramp rate becomes transient for a short time until the new ramp rate is achieved. The DSC response to these transitions can appear as an endothermic or exothermic peak because the sample and reference temperatures lag behind the furnace temperature and the heating rate is not constant. The heating rate and furnace control settings can be used to change the influence of thermal lag on the DSC measurement, but thermal events occurring near ramp rate transitions need to be scrutinized with caution.

The BNi-2 example in Figure 1-9 demonstrates both the difficulty and effectiveness of DSC analysis. Onset temperatures, phase transitions, melting and solidification behaviour, and enthalpy measurements for materials can all be determined from a single experiment. Although, the interpretation of DSC traces can become quite convoluted, especially when little is known about the sample material or when thermal events begin to overlap.

1.6.2 Dilatometry

Dilatometry is a thermal analysis technique that can measure the linear dimensional change of a material *in-situ* in a furnace. This type of measurement can be used to determine a material’s coefficient of thermal expansion and can be used to indicate the dimensional change of a powder compact during sintering. Combined with measurements of density, dilatometry of a material at a constant heating rate can be used to determine rates of densification and activation energies related to sintering. However, the most useful part of dilatometry is commonly the visual representation of the sintering process through dimensional change. The temperature at which densification begins (start of sintering shrinkage) can be clearly identified using a dilatometry curve and the time required to complete the densification process at a given temperature can also be observed. Further, the formation of a liquid phase can often be identified by either swelling (expansion) or rapid densification (rapid shrinkage). Therefore, dilatometry is a useful tool for characterizing the sintering process for many materials.

The instrument set-up of dilatometer includes a sample holder, sample plates, and a push rod. A schematic of the dilatometer set-up is shown in Figure 1-10. The sample is positioned on the sample holder and sample plates are placed against each side of the sample. The plates and faces of the sample must be parallel to allow for accurate measurement of the linear dimensional change. The sample is butted up against the end of the furnace tube wall on one side and the push rod is then put into contact with the sample plate on the opposite side. The push rod is loaded slightly to maintain contact with the sample plate throughout the measurement and transfers any dimensional change in the sample to a variable displacement transformer (VDT), which measures the displacement. Temperature is calibrated by melting pure standard materials (i.e. gold and nickel), which exhibit sudden shrinkage when reach their melting point. The shrinkage measurement is calibrated by measuring a known standard (i.e. alumina or sapphire) at the temperatures, times, and heating rates of interest.

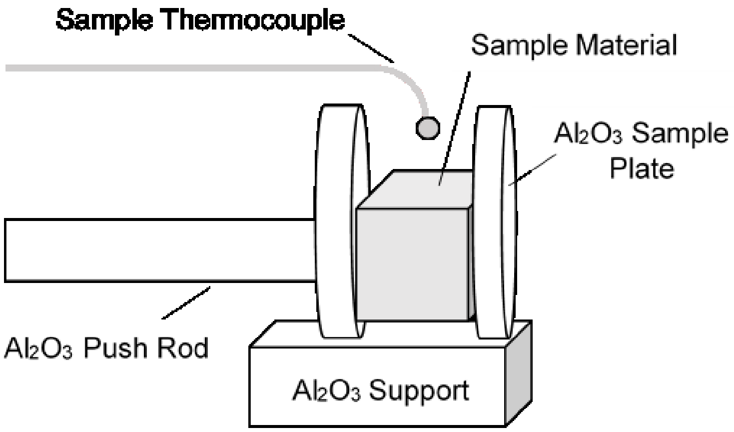

Figure 1-10. Schematic of a common set-up in a dilatometer. The Al_2O_3 push rod transfers dimensional change in the sample to a VDT.

Similar to DSC, the analysis of dilatometry data requires experience with the measurement technique as well as knowledge of the material's behaviour with temperature. An example analysis of a dilatometry curve for a metal injection molded Ni-superalloy is given in Figure 1-11. The DIL curve exhibits steady thermal expansion as the temperature increases at a constant rate. Upon reaching 1100°C, labelled point A, the expansion stops and the curve slowly starts to decrease. Between 1100°C and 1200°C (points A and B), the curve has a steady rate of shrinkage. Upon heating above 1200°C (point B), the rate of shrinkage increases substantially. Between 1200°C and the hold temperature (points B and C), the material changes from a net expansion to a net shrinkage. Although sintering mechanisms are active during heating prior to 1100°C, the DIL curve demonstrates when the material starts to experience sintering shrinkage and densification. The measurement also shows how the rate of shrinkage increases with temperature from points A, B, and C.

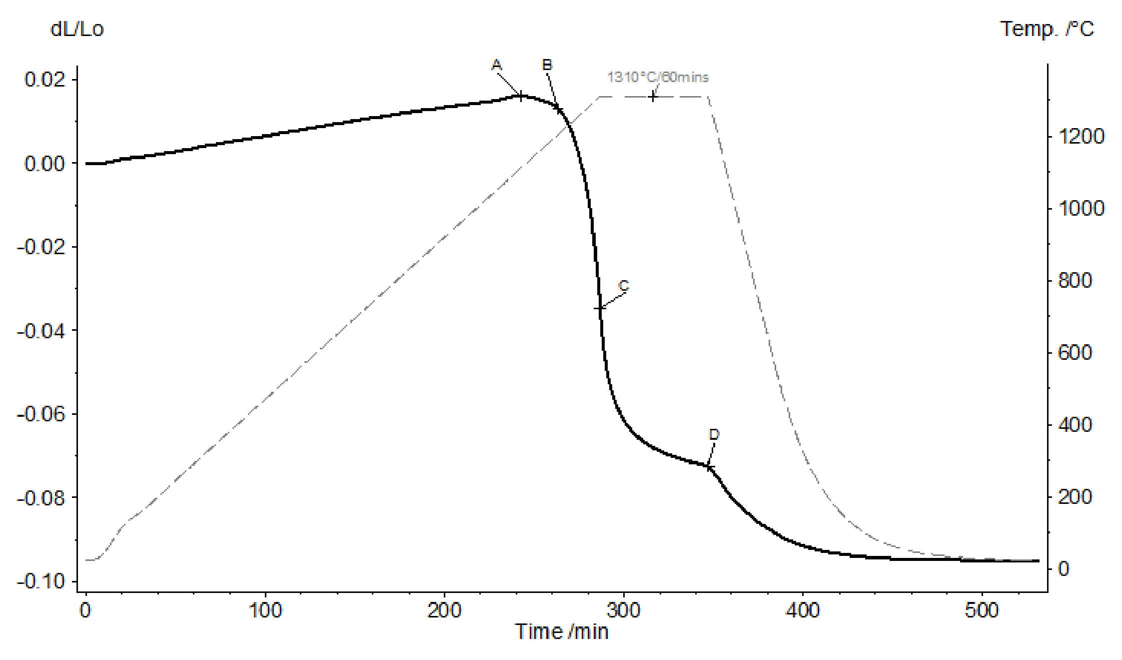

Figure 1-11. **DIL sintering curve for a metal injection molded Ni-superalloy powder heated at 4.5Kpm to 1310°C for 60mins. The temperature profile is shown as the dashed line.**

At point C, the furnace is held at the peak temperature for 60min. During this time, shrinkage continues as the material undergoes sintering densification. The DIL curve shows a decreasing rate of shrinkage, between points C and D, indicating that sintering densification is stagnating. Upon cooling at point D, sintering stops and there is a net material shrinkage due to thermal contraction. A sintering step can be drawn from the peak of the curve at point A to the end of the hold time at point D to determine the change in length associated with sintering. The net dimensional change of the material can then be related to material density with temperature as well as the kinetics of sintering and apparent activation energy [23].

The use of thermal analysis techniques in conjunction with microstructural observation provides a powerful approach to characterizing a material's sintering behaviour. DSC analysis can identify important phase transitions and quantify liquid content, while DIL can demonstrate the dimensional change during the sintering response. Microstructural observations can provide an independent confirmation of the events observed from DSC and DIL. They can also provide a measure of density and grain size while also characterizing shape change, elemental segregation, and liquid phase presence. The net result is an effective set of tools which can provide a clear picture of the sintering process by confirming thermal analysis measurements with microstructural observations.

CHAPTER 2
SCOPE AND OBJECTIVES

Nickel-based superalloys are one specialized group of materials that have been successfully metal injection molded in recent years [4,6,11,14–16,24,25]. Commercial Ni-superalloys such as IN625 and IN718 have been evaluated for non-structural components in aero-engines and exhibit promising high temperature properties [14,16]. However, MIM Ni-superalloys often require specialized sintering conditions in order to obtain the desired density and microstructure [15]. The presence of reactive elements such as aluminium and titanium in these alloys can largely reduce their sinterability by forming numerous oxide and carbide phases. This problem is exacerbated by the carbon pick-up and oxidation behaviour of Ni-superalloy powders during the de-binding stage [4,26]. To combat carbon contamination, low-carbon variants of Ni-superalloy powders have been evaluated for many PM applications [2,3]. Despite this, the solid state sintering of more complex MIM Ni-superalloys containing high amounts of refractory elements, such as W and Ta, have not been fully evaluated in the literature. Low carbon variants of these alloys have been successfully solid state sintered to full density with the presence of very small liquid fractions, but the grain sizes of these MIM alloys are commonly on the scale of 20-30μm [6]. In contrast, cast Ni-superalloys generally have grain sizes on the scale of 1-3mm and exhibit better high temperature creep resistance due to their low grain boundary area [5]. As such, the inhibition of grain growth in PM Ni-superalloys containing high amounts of refractory elements restricts their use in structural, high temperature applications [3,5].

The present work evaluates the effectiveness of multiple sintering approaches to activate grain growth in a MIM NiSA to obtain an increased grain size. The MIM alloy in this study is a NiSA containing Al, Co, Cr, Ta, Ti, W and minor additions of other refractory metals (RM), with the balance Ni. Solid state sintering, liquid phase sintering, and supersolidus liquid phase sintering techniques will be investigated for this MIM NiSA. The sintering behaviour of the NiSA in each of these approaches is primarily characterized using DSC and DIL in conjunction with post-sintered microscopy analysis (optical and SEM). By combining these analysis techniques, a fundamental understanding of the NiSA's sintering response to each approach can be developed.

The objectives of the present research are to identify practical methods which can activate grain growth in the MIM NiSA and to determine the fundamental mechanism(s) behind grain growth in the alloy. DSC analysis will be used to quantify the liquid content during liquid phase sintering approaches (LPS and SLPS) while DIL will be used to qualitatively characterise the densification behaviour of the NiSA during solid state and SLPS approaches. Both DSC and DIL will also be used to characterize the sintering response of the NiSA under different sintering atmospheres. Microstructural details such as grain size, grain boundary structure, and elemental segregation will be determined using post-sintered analyses with optical and SEM-EDS techniques. The combination of these techniques will provide a thorough understanding of each sintering approach and allow important compositional and microstructural differences which influence the grain growth behaviour to be identified.

Although the LPS and SLPS techniques were developed as methods to achieve high densities in difficult to sinter materials, they can also lead to significant grain growth if the time at temperature is long [11]. While it is known that grain growth occurs during LPS and SLPS, grain growth has not yet been targeted as a desired outcome in the literature. In addition, there have been no published studies on the SLPS of MIM Ni-superalloys containing high amounts of refractory elements at the time of writing. The influence of oxygen content in the sintering atmosphere on the SLPS response and grain growth behaviour, currently unavailable in the literature, are further benefits from this research. In addition, the transient nature of liquid content during LPS and SLPS of this NiSA is a theme which has been discovered and discussed extensively in this work.

CHAPTER 3

EXPERIMENTAL METHODS

The reader should note that certain information regarding the nickel superalloy chemistry, powder size, and compositional results are not presented due to commercially sensitive information (CSM) considerations with an industry partner.

3.1 Materials

A pre-alloyed argon gas atomized NiSA powder was used in this investigation. The pre-alloyed NiSA powder contained Al, Co, Cr, Ta, Ti, W and minor additions of other refractory metals (RM), with the balance Ni. A commercially available pre-alloyed BNi-2 brazing powder was also used as a low melting point additive to the NiSA for LPS trials. The BNi-2 powder was inert gas atomized and its composition was Ni-7Cr-4.5Si-3Fe-3B (wt%).

3.2 Powder Characteristics

The BNi-2 and NiSA powders had particle size distributions (PSDs) typical of those used in the PM industry and their particle sizes were fine. The BNi-2 powder was purchased as a -325 mesh (-45µm) particle size powder and the d_{10} and d_{50} of both powders were similar. The BNi-2 powder had a larger particle size throughout the PSD. The d_{90} of the two powders deviated significantly, with the BNi-2 powder containing larger particles than the NiSA.

The NiSA powder size was determined with a Malvern 2600 particle sizing analyzer at the Minerals Engineering Center (Dalhousie University). The NiSA powder morphology was analyzed at Dalhousie University using a Hitachi S-4700 field emission scanning electron microscope. The BNi-2 powder size and morphology was verified by an industrial partner via image analysis of 10 micrographs obtained from a Hitachi S-3400N SEM. Both powders were spherical in morphology which is ideal for the metal injection molding process [4]. An SEM micrograph of the NiSA powder is presented in Figure 3-1. The NiSA powder exhibits a wide range of particle sizes, satellites around larger particles, and some agglomeration.

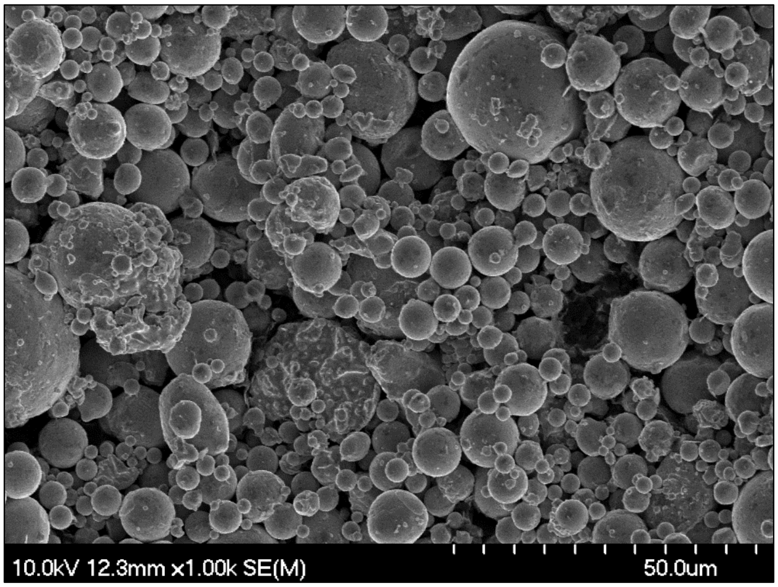

Figure 3-1. SEM micrograph of the pre-alloyed MIM NiSA powder.

3.3 MIM NiSA Samples

MIM NiSA samples were injection molded by an industrial partner and shipped to Dalhousie University in the green state. MIM NiSA LPS materials were also prepared by the industrial partner with BNi-2 powder loadings of 5 and 10wt%. The received green-state MIM samples were in plate form with a thickness of 3.65mm. Samples were sectioned into appropriate sample sizes for DIL and DSC using a thin bladed knife. 3x3mm rectangles with the received plate thickness were sectioned for DSC analysis because the sample size was limited by the 5.8mm diameter crucible and the geometry was simple. The top and bottom surfaces of the samples were not altered in order to maintain a consistent sample height and parallel, injection molded faces, which would maintain good contact with the bottom of the DSC crucible. The sample height was an average of 3.6mm post de-binding. DIL samples were a larger 5x5mm size, but kept the same injection molded faces to maintain parallel faces for the linear dimensional measurement. These DIL samples had the same thickness (or height) as the DSC samples.

The sectioned green-state samples were packed in an inert powder support media within an Al_2O_3 crucible for de-binding. Thermal de-binding was completed in a Sentrotech 1600C tube furnace under flowing high purity Argon gas (99.999% Ar). The thermal profile of the de-binding stage used a 4.5°C/min heating rate and isothermal holds at both 180°C and 850°C [26]. After de-binding, samples were removed from the support media and surfaces cleaned with a fine brush to remove residual powder. Arbitrary samples were massed and dimensioned before and after each de-binding batch to confirm that all binders had been successfully removed. All samples were massed on a Metler-Toledo balance with a resolution of 0.01mg prior to thermal analysis. As well, all samples were dimensioned using Vernier calipers with a resolution of 0.01mm prior to thermal analysis. Sample masses were taken once while dimensions were taken as the average of three individual measurements.

3.4 Mixed Powder Samples

During LPS trials, 5g mixed powder samples of the NiSA with different BNi-2 loadings were created for DSC analysis. The powders were added in the desired proportions by weight measured on a lab balance with a resolution of 0.1mg. Each powder mixture was contained in a glass jar which was then placed on a ball mill for 60mins. The ball mill speed was set to approximately 60rpm such that powder would roll up the side of the jar before falling down on itself, providing adequate mixing. For DSC analysis, a sample of the mixed powder was fully melted in an initial cycle to homogenize the powder into a single alloy. A second DSC test was then performed to measure the thermal events of interest for the BNi-2-NiSA alloy.

3.5 Differential Scanning Calorimetry (DSC)

DSC analysis was performed on de-bound MIM NiSA samples using a Netzsch 404 F1 Pegasus DSC. The instrument's temperature and sensitivity were calibrated by comparing the melting temperatures and enthalpies of 6 pure metals (In, Sn, Zn, Al, Ag, and Au) to their known values. The calibration runs were performed under near-identical conditions to those applied in the sample experiments. The calibration was verified at regular intervals by melting a pure Au standard.

DSC samples were placed as close as possible to the center of an alumina crucible and the crucible was loaded onto the sample side of the DSC carrier. An empty alumina crucible was placed on the reference side of the carrier. The furnace was then closed and evacuated to a minimum vacuum level of 5.4E-5mbar and backfilled with high purity argon gas prior to each test. Samples were heated under 50ml/min flowing 99.999% argon gas in all cases. A zirconium getter ring was used in the majority of tests to remove oxygen from the flowing argon purge gas during the experiments. The absence or presence of the zirconium getter for specific tests will be indicated throughout the results and discussion.

3.6 Dilatometry (DIL)

Dilatometry was performed on de-bound MIM NiSA samples using a Netzsch 402C dilatometer. The instrument's temperature was calibrated by comparing the melting temperatures of 7 pure metals (In, Sn, Bi, Al, Ag, Au, and Ni) to their known values. The DIL measurement was corrected by running an Al_2O_3 standard under identical conditions and thermal profiles to those applied in the sample experiments.

DIL samples were placed on alumina sample holders and were moved as close as possible to the sample thermocouple. Alumina sample plates were then placed on either side of the metal injection molded faces of the sample and the push rod was moved into contact with the sample plates. The furnace was then closed and evacuated to a minimum vacuum level of 5.4E-5mbar and backfilled with high purity argon gas prior to each test. Samples were heated under 50ml/min flowing 99.999% argon gas in cases where a dynamic purge gas was used. In contrast to DSC, a titanium foil getter ring was used in certain DIL tests to remove oxygen from the flowing argon purge gas during the experiments. In certain cases, a high vacuum of greater than 5.4E-5mbar was applied throughout the DIL measurement. The sintering atmosphere used for specific tests will be indicated throughout the results and discussion.

3.7 Microscopy and Energy Dispersive Spectroscopy (EDS)

Stereomicroscopy of MIM NiSA samples was completed with a Zeiss Stereomicroscope and the post-sinter sample heights were measured with calipers to track sample shrinkage and deformation. The MIM NiSA specimens were then mounted in conductive Bakelite (graphite flakes) before being ground and polished. The polished specimens were etched with waterless Kalling's reagent to expose the grain boundaries.

Optical microscopy was performed using a Zeiss Axiotech 100HD microscope capable of 50x-1000x magnifications. The scale of each objective (5x, 10x, 20x, 50x, and 100x) was calibrated using a slide with a laser etched grating. Differential interference contrast (DIC) was commonly used during microscopy to provide better contrast of a specimen's microstructural features.

SEM analysis was performed using a Hitachi S4700 scanning electron microscope equipped with EDS capabilities. When performing EDS, the accelerating voltage and current were set to 15kV and 15μA, respectively, to accurately detect all elements contained in the NiSA.

3.8 Grain Size and Image Analysis

The average grain size of sintered MIM NiSA specimens was measured using the line intercept technique. The measurement method closely followed the ASTM International standard measurement methods outlined in designation E112-13 [27]. The average grain size was determined over 5 fields at 200x magnification using a grid pattern of 10 lines per field. The grid was overlaid on the image using Fiji ImageJ open source software and the number of grain boundary intersections was recorded for each line. There were a total of 50 lines measured per specimen.

Fiji ImageJ software was also used to analyze the average percentage residual porosity for each specimen. The image contrast was adjusted to fill the pores for 5 individual fields at 200x magnification. The percentage area of the regions designated with high-contrast was then determined. Subtracting the percentage area of pores from 100% was used to obtain an approximate density of the specimen, which was then averaged over the 5 fields.

Note that in cases where multiple measurements were made error bars are presented with the associated data set. The error bars represent the standard deviation of the data calculated using standard methods provided in Excel.

CHAPTER 4
RESULTS AND DISCUSSION

4.1 Evaluating the Solid-State Sintering of a Metal Injection Molded Nickel-Based Superalloy under Different Sintering Atmospheres

4.1.1 Results

The DSC heating trace for a 50mg MIM NiSA sample is presented in Figure 4-1 and demonstrates the melting behaviour of the alloy. Incipient melting is observed as the first deviation from the trace's baseline at 1270-1280°C while the onset of melting, determined via an extrapolation method, was 1330°C. A sintering temperature of 1310°C was selected for the dilatometry experiments, however, the DSC trace reveals that a small liquid fraction may form below the extrapolated onset temperature as a result of incipient melting.

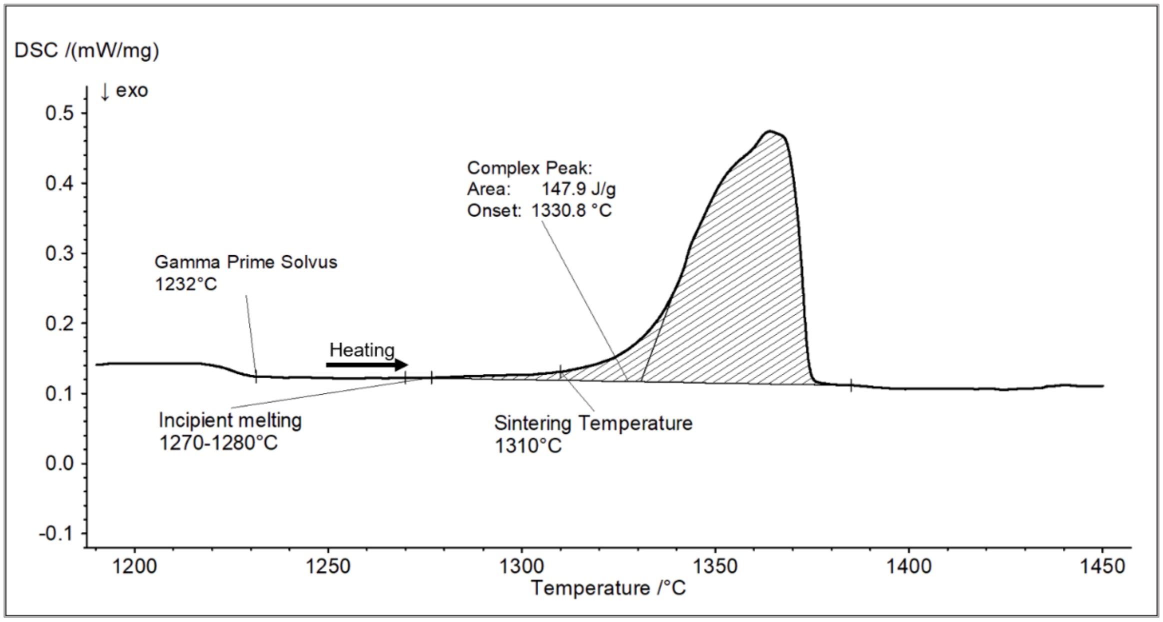

Figure 4-1. DSC trace of the MIM NiSA heated to 1450°C.

Dilatometry curves for MIM NiSA sintered at 1310°C for 1 hour are presented in Figure 4-2 for argon, argon with titanium getter, and high vacuum sintering atmospheres. The dilatometry results demonstrate that the sintering atmosphere has a large influence on the densification of the MIM NiSA alloy. Samples sintered in high purity argon started to densify at 1120°C while samples sintered with a titanium getter had an earlier onset of densification at 1100°C. The samples in argon also exhibited less overall sintering shrinkage than those samples sintered with a Ti getter. The samples sintered in a high vacuum atmosphere had an earlier densification onset at 1070°C and exhibited the highest degree of sintering shrinkage. All samples showed a reduced sintering rate approaching the hold temperature, however the argon samples continued to densify slowly over the hold time while the Ti getter and high vacuum samples showed no, to little further densification after the heating segment.

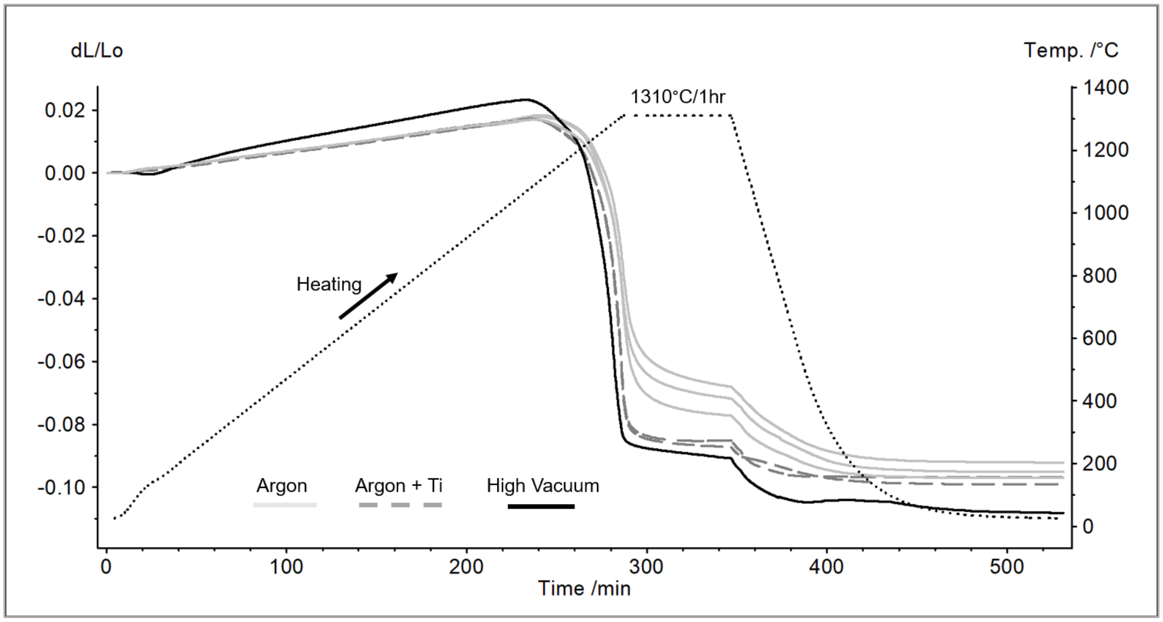

Figure 4-2. Dilatometry results for the NiSA sintered at 1310°C/60mins under argon, argon + Ti getter, and high vacuum atmospheres.

Polished cross sections of the MIM NiSA samples sintered at 1310°C for 1 hour under the three different atmospheres are compared in Figure 4-3. This side-by-side comparison of the microstructures demonstrates that there is a clear progression in the extent of densification achieved as the furnace atmosphere was changed from flowing argon to high vacuum. The apparent density measurements outlined in Table 4-1 support this observation, with a high vacuum atmosphere resulting in the highest sintered density. Additional grain growth was also achieved with progressively cleaner atmospheres, though a high vacuum atmosphere resulted in grains no larger than 20μm. The dilatometry and microstructural results confirm that the cleanliness of the sintering atmosphere can impact the grain size, density, and densification path of the NiSA alloy. However, the grain size has not been substantially increased by changing the sintering atmosphere.

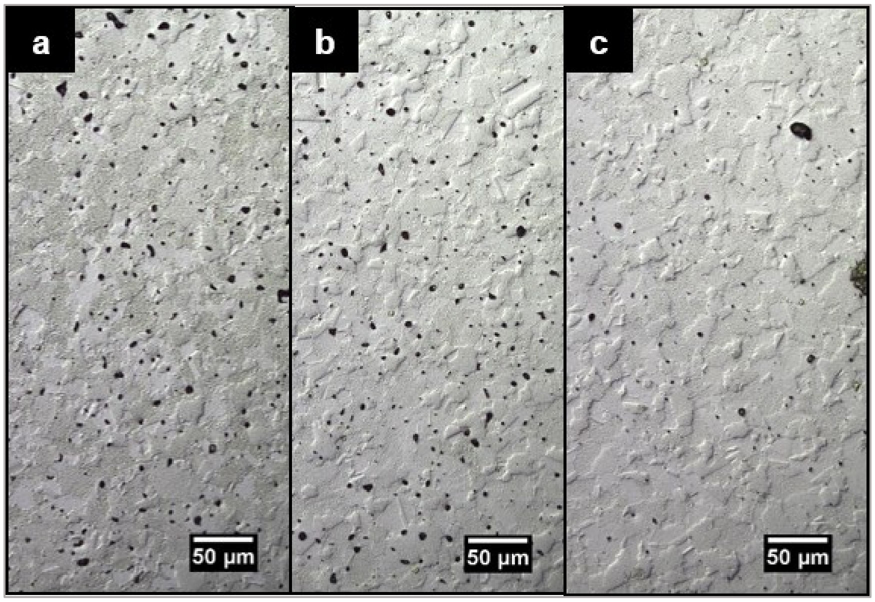

Figure 4-3. Sintered cross section of the NiSA after a) 1310°C/1hr Ar, b) 1310°C/1hr Ar + Ti getter, and c) 1310°C/1hr high vacuum.

Table 4-1. **Grain size and percent density measurements for the NiSA sintered to 1310°C under different rates, hold times, and atmospheres.**

Hold Time (Hrs)	Heating Rate (Kpm)	Atmosphere	Average Grain Size (µm)	Percent Density
1	4.5	Argon	14.3 ± 2.4	95.1 ± 1.6
1	4.5	Argon + Ti	17.4 ± 2.9	96.6 ± 0.5
1	4.5	Vacuum	20.8 ± 2.2	99.3 ± 0.2
1	10	Argon	14.6 ± 1.2	96.3 ± 1.6
2	4.5	Argon	12.6 ± 0.8	94.7 ± 1.3

In additional attempts to modify the grain size, the heating rate and hold time of the sintering cycle were independently varied in the dilatometer study. The heating rate was increased to 10°C/min and the hold time was increased to 2 hours while the peak temperature and atmosphere were maintained as 1310°C and flowing argon, respectively. The resulting grain sizes and densities are outlined in Figure 4-4 and Table 4-1. Increasing the heating rate led to a higher density while additional hold time did not significantly affect the density. Increases in both the heating rate and hold time did not appear to influence the grain size of the MIM alloy, with the average grain size remaining between 12-16µm.

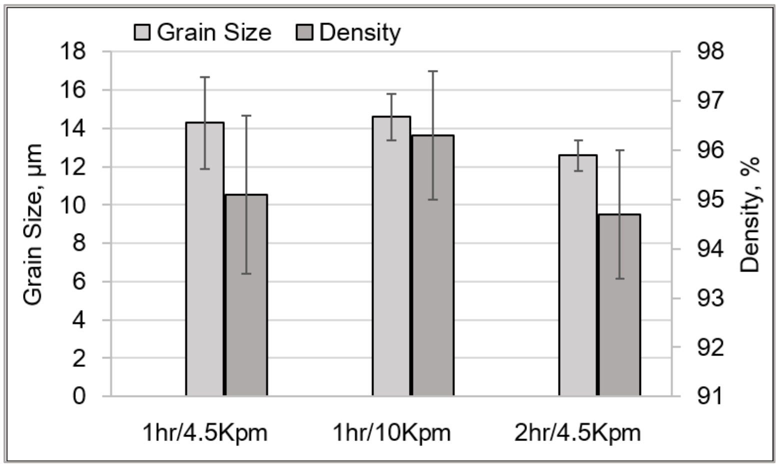

Figure 4-4. **Influence of heating rate and hold time on the grain size and density of the NiSA sintered at 1310°C under a high purity argon atmosphere.**

The results in Table 4-1 demonstrate that the high vacuum atmosphere resulted in a high density and larger grain size in the MIM NiSA alloy. However, the results in Table 4-1 also indicate that grain growth is not active at the sintering temperature regardless of increases in heating rate, hold time, or cleanliness of the furnace atmosphere. The average grain size after sintering at 1310°C is typically sub-20μm.

To try and activate grain growth, the sintering temperature was raised past the solidus temperature to 1350°C. Referring to the melting behaviour of the NiSA alloy in Figure 4-1, sintering the pre-alloyed MIM NiSA powder above the extrapolated solidus temperature of 1330°C will cause a significant liquid phase fraction to form. This technique is termed supersolidus liquid phase sintering (SLPS) which can enact rapid densification and microstructural coarsening in powder compacts [11]. The dilatometry experiments were repeated at 1350°C for the three sintering atmospheres tested previously and the resulting densification curves are presented in Figure 4-5. Comparing Figure 4-2 and Figure 4-5 the dilatometry curve for 1350°C/1hr under flowing argon was very similar to the dilatometry curve at 1310°C/1hr under the same atmosphere. The titanium getter and high vacuum dilatometry tests at 1350°C are almost identical to those tests at 1310°C during the heating stage, but are substantially different upon reaching the solidus temperature. Both tests exhibit a normal sintering curve for NiSA, including a reduction in the sintering rate upon reaching 1310°C. This reduction in measured densification rate could simply be the end of solid state sintering or could be a result of swelling from liquid formation. Upon further heating to 1350°C, both curves exhibit a secondary burst of densification, presumably as a result of the capillary forces exerted by liquid phase formation, which continues through the hold time.

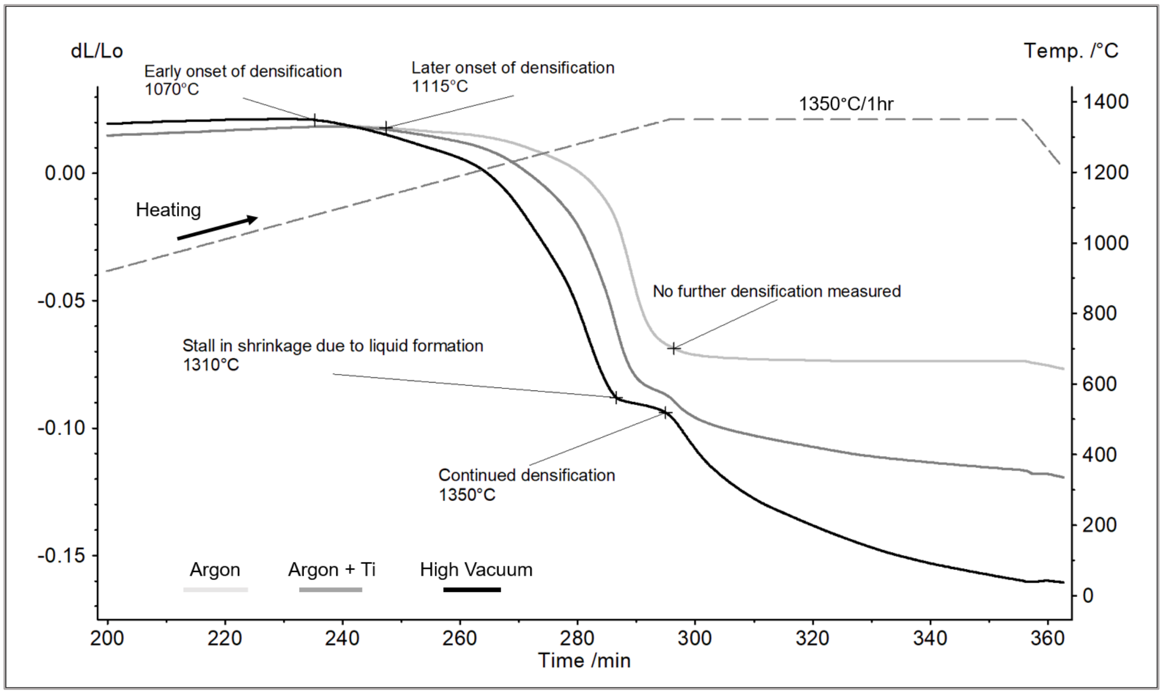

Figure 4-5. DIL curves for the MIM NiSA sintered at 1350°C for 1 hour under argon, argon with Ti getter ring, and high vacuum atmospheres

The SLPS microstructures for the argon gas, argon with titanium getter, and high vacuum atmospheres are compared to the solid-state sintered microstructure under an argon gas atmosphere in Figure 4-6. All microstructure images presented in Figure 4-6 were taken in the center of the sample cross sections. Despite being sintered at sub-solidus (1310°C) and supersolidus (1350°C) temperatures, the samples sintered under the argon gas atmosphere have similar microstructures with little to no grain growth evident. In contrast, significant grain growth has occurred after supersolidus sintering under the Ti getter and vacuum atmospheres, reinforcing that the sintering behaviour of NiSA is influenced by the furnace atmosphere. The results also suggest that grain growth can be achieved during supersolidus sintering, though the furnace atmosphere also appears to play a role in activating grain growth in the alloy.

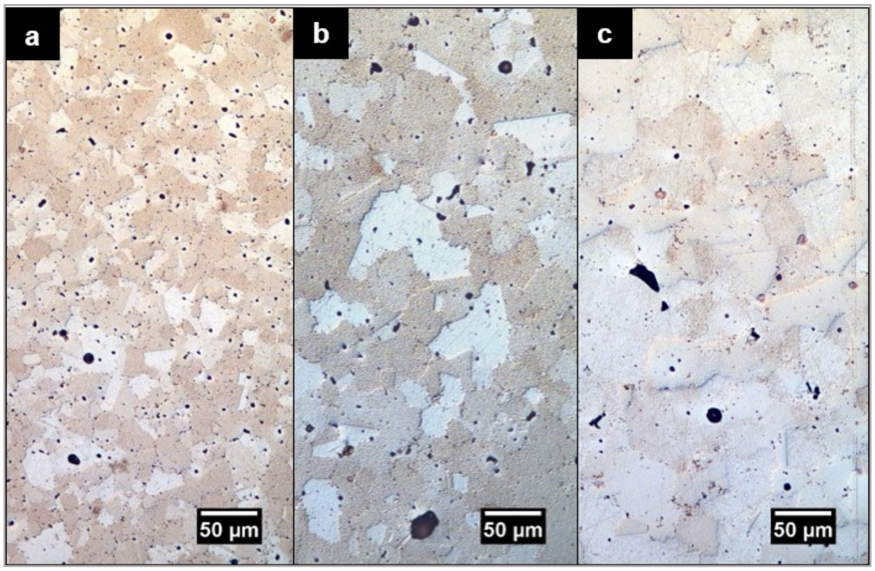

Figure 4-6. Sintered cross section of the NiSA after a) 1350°C/1hr Ar, b) 1350°C/1hr Ar + Ti, c) 1350°C/1hr high vacuum.

Optical microscopy of the MIM NiSA surface layers after supersolidus sintering revealed large microstructural differences between sintering in argon and high vacuum atmospheres. Polished cross sections of the surface layers from both the argon and high vacuum atmospheres are presented Figure 4-7. The sample sintered at 1350°C in argon had an average center grain size of 15.9µm and exhibited a continuous oxide layer on the sample surface. The original particle boundaries and grain boundaries are also dotted by discrete oxide and carbide phase particles which appear to permeate into the bulk of the sample. In contrast, sintering in high vacuum at 1350°C led to an average center grain size of 42.3µm and an oxide-free surface. Few oxide or carbide phase particles are observable within the surface layer of the vacuum sintered sample and a thin, metallic surface layer appears to coat the grain boundaries.

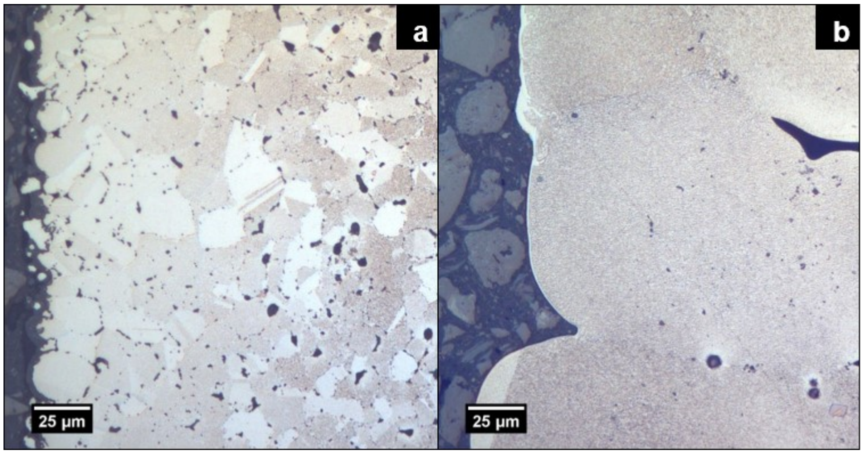

Figure 4-7. Surface layer of the MIM NiSA sintered for 60 minutes at a) 1350°C under high purity argon gas and b) 1350°C under high vacuum.

Density and average grain size measurements for the samples sintered at 1310°C and 1350°C are presented for the three different sintering atmospheres in Figure 4-8 and Figure 4-9, respectively. The density of the sintered MIM NiSA was found to increase as the atmosphere's oxygen content was reduced at both 1310°C and 1350°C. This result supports the dilatometry curves for both temperatures which showed higher sintering rates and larger amounts of densification with cleaner sintering atmospheres. The grain size also increased with cleaner atmospheres, though this effect was less significant for those samples sintered in the solid state. Supersolidus sintering saw a large increase in the grain size for the titanium getter and high vacuum atmospheres while the argon atmosphere led to a similar grain size to those samples sintered in the solid state.

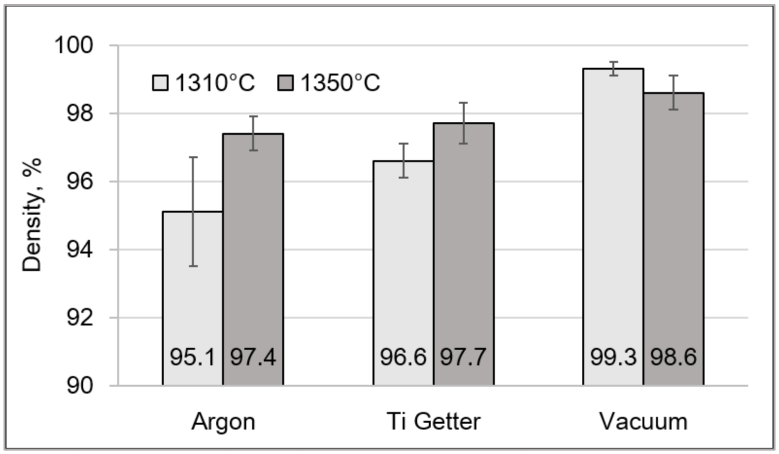

Figure 4-9. **Density of the NiSA sintered for 60 minutes at 1310°C and 1350°C under different atmospheres.**

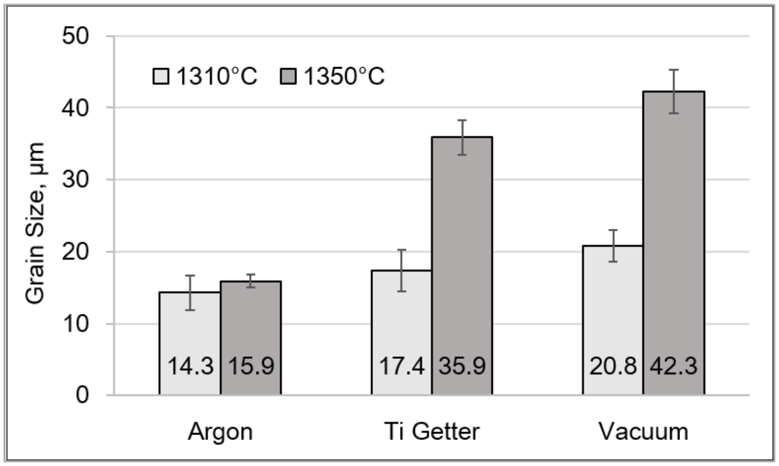

Figure 4-8. **Average grain size of the NiSA sintered for 60 minutes at 1310°C and 1350°C under different atmospheres.**

4.1.2 Discussion

4.1.2.1 Dilatometry Results

Solid state sintering of the MIM NiSA alloy under high purity argon, argon with titanium getter, and high vacuum atmospheres resulted in similar dilatometry profiles, shown in Figure 4-2. Dilatometry of the alloy exhibits a slow onset of densification at approximately 1100°C before the shrinkage rate increases rapidly as heating continues toward 1310°C. The majority of densification occurs during heating between 1200-1310°C. The densification rate of the material then reduces gradually throughout the hold time at 1310°C under all atmospheres. Though this general trend and the overall curve shape is shared between the different atmospheres tested, it is evident that the densification onset temperature and total shrinkage are influenced by the furnace atmosphere. The onset of densification was found to be 1120°C, 1100°C, and 1070°C for the argon, Ti getter, and vacuum atmosphere conditions, respectively. The total shrinkage and sintered density also increased with progressively cleaner atmospheres with the high vacuum atmosphere achieving the earliest onset to sintering, highest density, and largest sintering shrinkage.

One explanation for the observed differences between the dilatometry curves is the sensitivity of the nickel superalloys to oxidation. Superalloys, such as the NiSA in this study, contain a number of reactive elements such as aluminium, titanium, and refractory elements which readily oxidize in the presence of trace amounts of oxygen [26]. The MIM NiSA alloy is also in the form of a fine pre-alloyed powder which are generally more reactive due to their high surface area [3,11]. The oxidation behaviour of similar superalloy powders upon heating has been documented by Whitman et al., where a combined TG-GCMS technique identified CO_2, H_2O, and O_2 as the primary oxidants in the mass change of the alloy powders during heating [26]. In that study, pre-conditions of the furnace atmosphere were shown to have a significant influence on the mass-pick up and oxygen content of the powder after heating to 800°C [26]. The MIM NiSA alloy's dilatometry curves reflect a similar degree of sensitivity to changes in the furnace atmosphere.

The high purity argon atmosphere is 99.999% argon and should contain less than 3ppm O_2. However, air leaks from gas fittings and furnace seals during heating and cooling could provide a source of contamination which would raise the oxygen content in the furnace under the flowing argon gas condition. In order to determine the actual level of oxygen in the furnace, an Alpha Omega 3000 Series trace oxygen analyzer was connected to the furnace outlet while the furnace was ran through a sintering cycle with no sample present. The level of oxygen in the furnace was measured to be approximately 2ppm after long periods of gas purging, but fluctuated between 2-20ppm O_2 during heating, generally drifting upward and exceeding 10ppm O_2. The titanium getter ring was also tested to determine its ability to scrub oxygen from the furnace atmosphere. It was found that the getter was able to successfully eliminate fluctuations of oxygen during heating, maintaining less than 2ppm O_2 at temperatures above 400°C. In contrast, the high vacuum atmosphere, which consistently achieved 5.4E-5 mbar or better in the dilatometry tests, would have an even lower oxygen level on the parts per billion scale.

The flowing argon gas atmosphere had the highest and most variable oxygen content, while the titanium getter with argon maintained a stable O_2 content below 2ppm. The high vacuum atmosphere provided the cleanest atmosphere with an oxygen level on the ppb scale. Combining this knowledge with the dilatometry results in Figure 4-2, it is evident that the oxygen content of the sintering atmosphere impacts the sinterability of the MIM NiSA alloy.

The high vacuum atmosphere provided the highest sintered density and largest grain size, however it is important to realize that a high vacuum condition is generally not practical on an industrial scale. The addition of a titanium getter ring into the furnace led to a similar dilatometry curve, grain size, and density to the high vacuum atmosphere. Therefore, the use of a getter material such as titanium serves as an effective, but more practical, method for cleaning the furnace atmosphere than high vacuum.

The microstructural comparison in Figure 4-3 demonstrates that the density is increased by sintering in a cleaner atmosphere, supporting the dilatometry results. However, the grain size and shape is not significantly modified by sintering in a cleaner atmosphere. Ultimately, the dilatometer results at 1310°C demonstrate the sensitivity of MIM NiSA's sinterability to different oxygen contents and the absence of significant grain growth during solid state sintering.

To activate grain growth in the MIM NiSA alloy, supersolidus liquid phase sintering was carried out at 1350°C in the dilatometer under argon, argon with titanium getter, and high vacuum atmospheres. The dilatometer curves, presented in Figure 4-5, exhibit different features depending on the sintering atmosphere applied. In both the Ti getter and high vacuum tests, the NiSA alloy sintered normally until surpassing the solidus temperature where the densification rate decreased momentarily. This reduction in densification is likely associated with either swelling from liquid formation or the tail-end of solid state sintering. A subsequent burst of densification occurs shortly after reaching the hold temperature, with the high vacuum sample shrinking more than the Ti getter sample. In contrast, the SLPS sample in argon did not show the secondary burst of densification that the samples under a Ti getter and high vacuum atmosphere did. Instead, the dilatometry curve for NiSA sintered at 1350°C under argon was almost identical to the NiSA sintered at 1310°C under argon. Macroscopic inspection of the 1350°C sample after sintering revealed that the material had a deformed hour-glass shape where the outer edges of the sample experienced less shrinkage than the inside bulk of the material. In this condition, the DIL plates used to measure the dimensional change of the sample would have only been in contact with the outer edges of the sample since the inner bulk would have pulled away from the DIL measurement plates. The resulting dilatometry curve is consistent with solid state sintering under argon at 1310°C, suggesting that despite exceeding the solidus temperature, the outer edges of the NiSA alloy did not sinter differently than at 1310°C. The center of the sample likely experienced SLPS-style densification similar to those measured under titanium getter and high vacuum atmospheres, but the oxidation of the outer edges restricted densification, preventing this measurement in dilatometry. The grain size on the outer edge of the sample (shown in Figure 4-7a) was measured to be approximately 10µm which is smaller than the average center grain size of 15.9µm (shown in Figure 4-6a). This difference in grain size indicates that the bulk of the sample experienced more grain growth than the outer edges, as would be the case if sintering was constrained in the surface by oxidation.

4.1.2.2 Oxidation and Restriction of Grain Growth

The dilatometer results demonstrate that the oxygen content of the sintering atmosphere can influence the densification of MIM NiSA. Specifically in the 1350°C tests, the densification of NiSA was shown to be inhibited by the higher oxygen content in the argon atmosphere. The titanium getter and vacuum atmospheres, which contained less oxygen, exhibited a higher degree of densification along with a secondary burst of densification upon reaching the SLPS temperature. Optical microscopy revealed that the outer edges of the sample sintered in argon, shown in Figure 4-7a, had a continuous oxide layer while the sub-surface grain boundaries and previous particle boundaries were dotted with fine oxide and carbide particles. The surface layer of the sample sintered in vacuum, shown in Figure 4-7b, was substantially different, having no surface oxide layer and fewer grain boundary phases. Additional microscopy of the bulk material in both samples is presented in Figure 4-10. The sub-surface microstructure of the sample sintered in argon (Figure 4-7a) is very similar to the bulk material (Figure 4-10a). The grain size and density in the bulk appears slightly higher, but overall there is little difference between the bulk and sub-surface microstructures. Comparing the sub-surface and bulk microstructures for the vacuum sample (Figure 4-7b and Figure 4-10b), the most notable difference is that the surface grains are much larger than in the bulk, though the bulk grain size is larger than the grain size of the sample sintered in argon. Another important feature of the sample sintered in vacuum is that the grain boundaries appear to contain fewer, coarser, oxide and carbide particles than the sample sintered in argon.

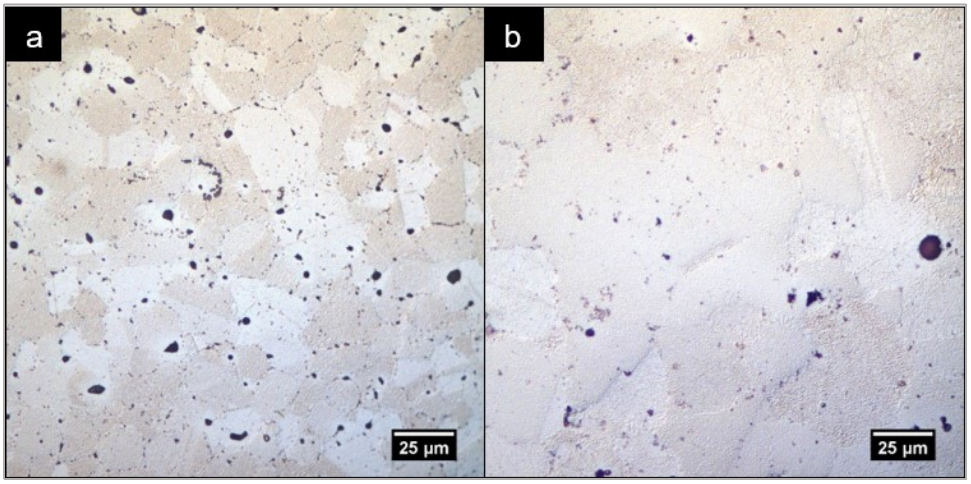

Figure 4-10. Bulk of the MIM NiSA sintered for 60 minutes at a) 1350°C under high purity argon gas and b) 1350°C under high vacuum.

The microstructural differences between samples in Figure 4-7 and Figure 4-10 suggest that the MIM NiSA alloy oxidizes under an argon sintering atmosphere to the extent that densification and grain growth are restricted. When the material was sintered under lower oxygen atmospheres, the grain size and density increased while the oxide layer was absent. The microstructural and dilatometry results demonstrate that reductions of oxygen in the atmosphere correspond to higher densities, faster sintering rates, larger grain sizes, and prevention of a surface oxide layer.

SEM-EDS was performed on the samples sintered in argon and high vacuum atmospheres and micrographs of their surface layers are presented in Figure 4-11. The surface of the sample sintered under argon, shown in Figure 4-11a, had a continuous oxide film along with various other oxide phases. Original NiSA powder particles which had a layered oxide structure were also observed near the sample surface, having failed to sinter into the main structure. EDS analysis revealed that the primary oxide layer (dark) was rich in aluminum while the thin layer surrounding powder particles (bright) was chromium and nickel rich. Refractory metal oxide particles (bright) were also detected in the surface layer.

The sample sintered under high vacuum, shown in Figure 4-11b, had an oxide-free surface. A thin, precipitate-free layer is present at the grain surfaces which is consistent with a liquid film that might be expected to form during SLPS [28]. EDS analysis revealed that this layer was deplete in both tungsten and chromium. The reduced chromium content in the surface layer is likely a result of chromium vaporization under high vacuum sintering conditions [11], while depletion of tungsten is a result of solute segregation during SLPS [29], which will be discussed in more detail in Section 4.2.

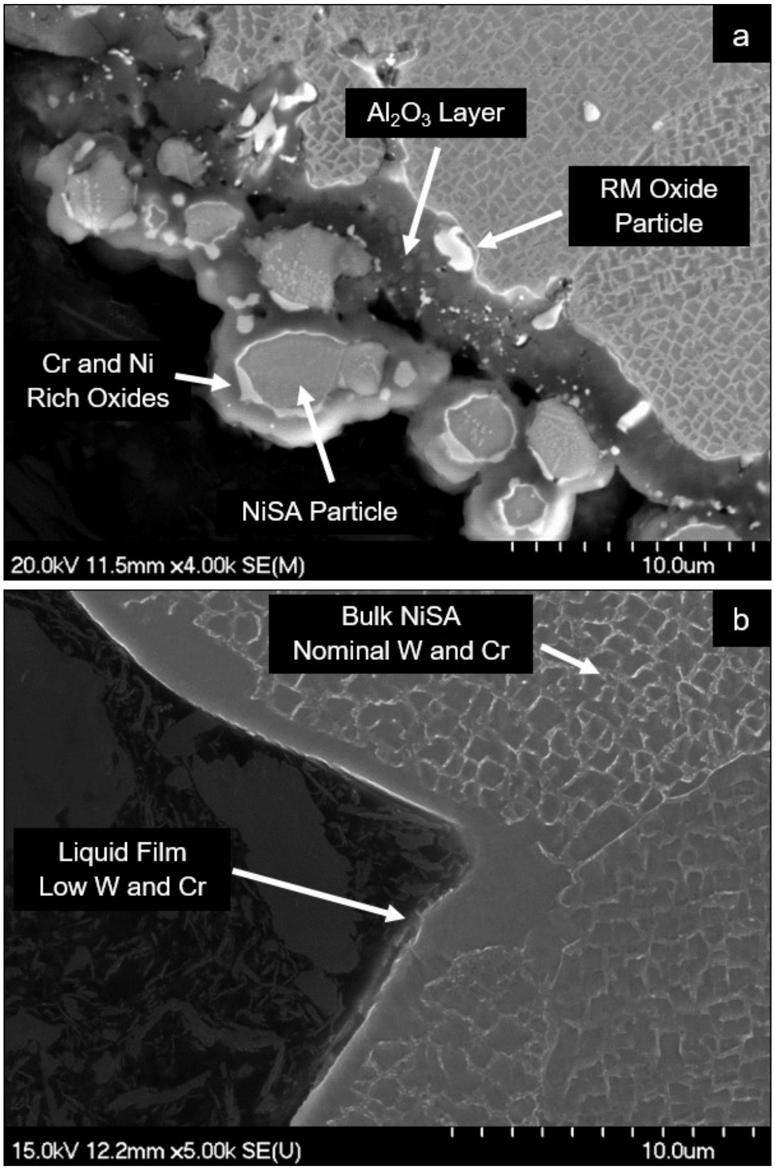

Figure 4-11. SEM micrograph of surface layer of the MIM NiSA sintered for 60 minutes at a) 1350°C under high purity argon gas and b) 1350°C under high vacuum.

The microscopy results provide clear evidence that NiSA oxidizes under the argon sintering atmosphere. The results also demonstrate that a high vacuum atmosphere is effective in preventing the oxidation of NiSA during sintering, which leads to a higher density and grain size at 1350°C. However, the results thus far only document the extent of surface oxidation and do not sufficiently explain the microstructural changes to the bulk of the material. Figure 4-10 offers evidence of a change in grain boundary particle size and distribution with different oxygen contents, but SEM was required to confirm this observation. An SEM micrograph representative of the MIM NiSA bulk after sintering at 1350°C in argon is presented Figure 4-12. The MIM NiSA sintered in argon contained many discrete grain boundary particles which were most commonly refractory metal oxides. The sample sintered in vacuum had fewer, coarser grain boundary particles which were primarily mixed refractory metal carbides which included Ta. Refractory metal oxide particles, or any alternative oxides, were rarely detected in the grain boundaries of the sample sintered in vacuum.

A high magnification SEM micrograph of the grain boundary particles found in the NiSA sintered in the argon atmosphere is presented in Figure 4-13. EDS analysis confirmed that the lighter-coloured areas are rich with a RM and O while the darker regions contain a RM along with higher levels of C and Ta.

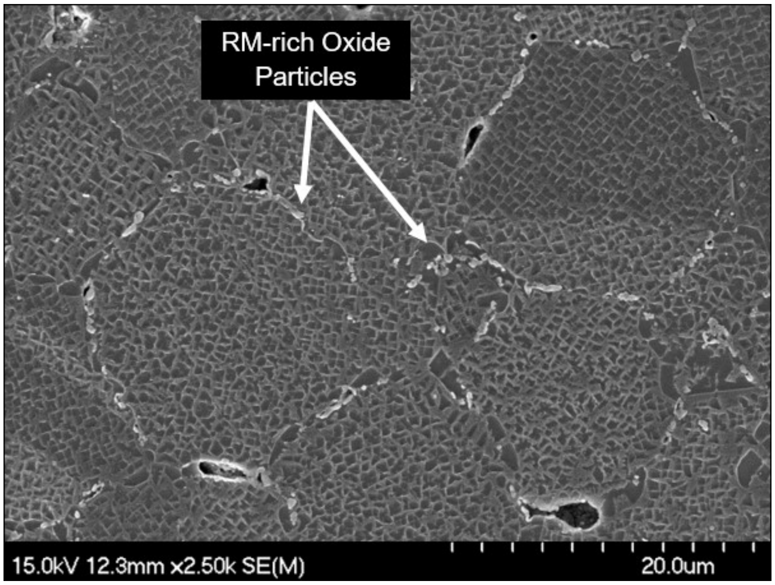

Figure 4-12. SEM micrograph of the MIM NiSA sintered at 1350°C for 1hr under an argon atmosphere.

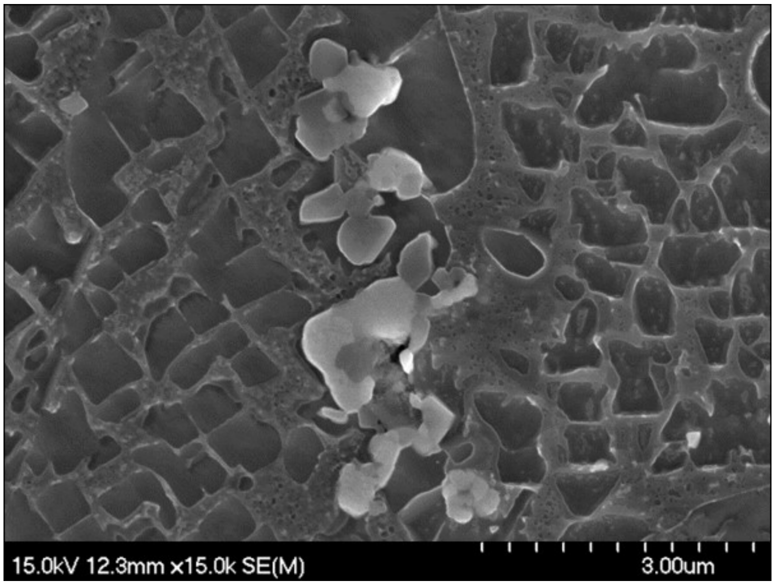

Figure 4-13. Cluster of RM and Ta-rich oxide and carbide particles in the grain boundary of the NiSA after sintering at 1350°C for 1hr under an argon atmosphere. Bright regions are rich in O and RMs while darker regions contain less O and more Ta and C.

The SEM-EDS results from the grain boundaries of the MIM NiSA samples suggest that oxidation occurs throughout the material under the argon gas atmosphere. More specifically, sintering under an argon atmosphere leads to refractory metal oxide particle formation in the grain boundaries of the sample, which appear to restrict densification and grain growth. The reduction of oxygen in the furnace atmosphere via a getter or vacuum decreases the formation of refractory metal oxide particles in the grain boundaries and prevents the growth of an Al_2O_3 surface layer, resulting in better densification and grain growth.

A high magnification SEM micrograph of the grain boundary particles found in the NiSA sintered in the high vacuum atmosphere is presented in Figure 4-14. EDS analysis confirmed that these particles were mixed RM carbide particles with Ta. Note that the grain boundary particles found in Figure 4-12 are different in size, composition, and morphology to those observed in Figure 4-14. The grain boundary itself has also migrated away from the carbide particles in the sample sintered under high vacuum, suggesting that the grain boundaries had become mobile under this condition.

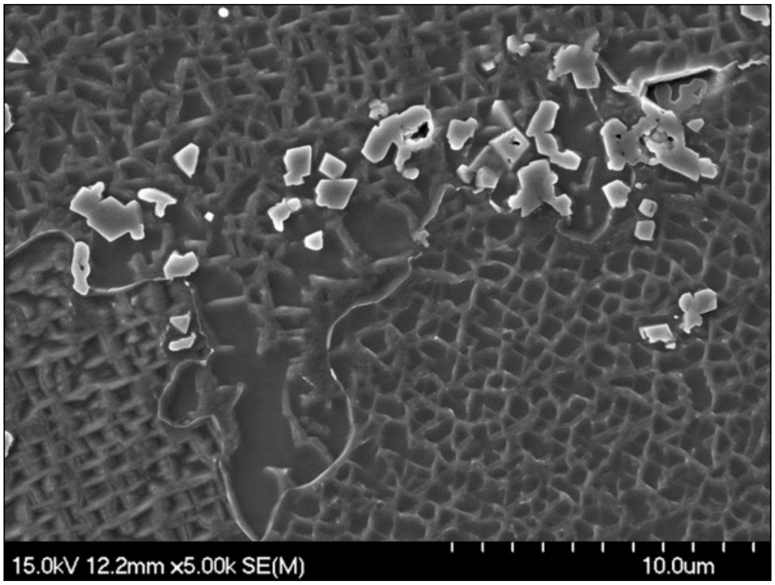

Figure 4-14. RM and Ta-rich carbide particles in the grain boundary of the NiSA after sintering at 1350°C for 1hr under high vacuum.

Particulate composites containing inert phase particles, such as superalloy-Al_2O_3 mixtures, commonly exhibit inhibited or constrained sintering [11]. Generally, as the content of the inert phase particle is increased, the sintering shrinkage is reduced, giving a lower density [11]. This behaviour is not unlike the MIM NiSA because stable RM oxide particles form at the particle boundaries in the presence of trace amounts of oxygen in the argon atmosphere. These particles may act as an inert phase and impart a resistance to the sintering stress on the material, limiting the densification rate [11]. The RM oxide particles may also act as immobile inclusions on the grain boundary, reducing the boundary mobility in a similar way to grain boundary pinning by carbides [19,30]. When the oxidation of the NiSA powder is prevented, fast densification and grain growth is possible with the assistance of a liquid phase from SLPS. In the presence of trace amounts of oxygen, sintering appears to be inhibited in the NiSA alloy, where oxide particles immobilize the grain boundaries and resist sintering stresses, even in the presence of a liquid phase during SLPS.

4.1.2.3 DSC Evaluation of Supersolidus Sintering

Although there is evidence of constrained sintering in the MIM NiSA alloy under the argon atmosphere, the change in oxygen concentration in the furnace atmosphere may also cause changes in the melting behaviour of the alloy. To determine if the oxygen concentration had an effect on the NiSA alloy's melting behaviour, DSC was employed to measure the liquid fraction with sintering temperature under argon and argon with zirconium getter conditions. The liquid fraction was estimated by comparing the partial melt enthalpy to the full melt enthalpy of the alloy under each atmosphere condition [18]. A wider range of peak temperatures from 1300 to 1355°C were included to obtain more comprehensive trends. Figure 4-15 shows the liquid fraction with temperature under each atmosphere in NiSA. The liquid fraction increase with temperature was similar under both atmospheres, but when the zirconium getter was present in the DSC higher melting enthalpies were measured than in the argon gas alone. At 1300°C, the melting enthalpies were very similar, but the enthalpy diverges as the temperature increases. This could be a result of oxygen diffusing into the liquid phase under the argon atmosphere, retarding melting slightly as the temperature increased. At 1340°C, 12% liquid is formed with the Zr getter. Under the argon gas atmosphere, only 8% liquid is formed upon reaching the same temperature.

Although this 4% deviation was relatively small, the trend of lower liquid fractions forming under the argon atmosphere was maintained across the temperature range.

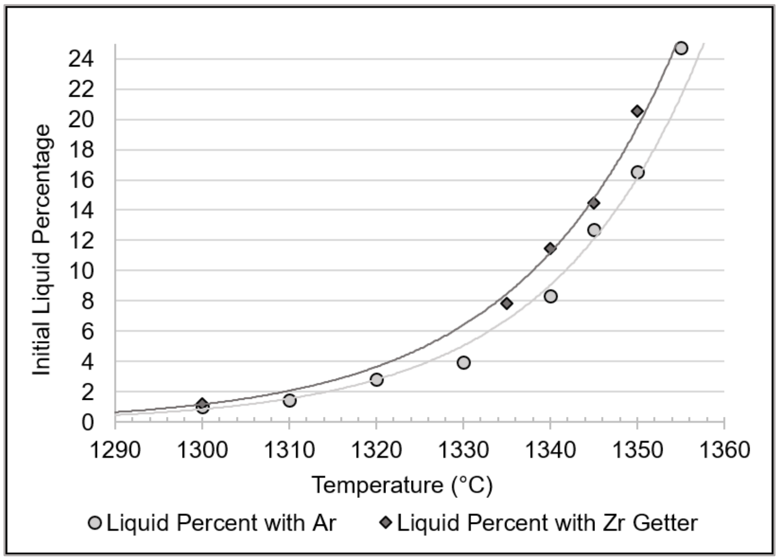

Figure 4-15. Initial liquid percentage formed with temperature in the NiSA under a high purity argon atmosphere with and without a zirconium getter

The observed difference in melting behaviour, though small, could influence the SLPS and grain growth behaviour of the MIM alloy. An increased liquid fraction results in a higher grain boundary film thickness, which can promote mass transport as well as grain sliding and rotation [28]. Additional liquid can also aid in disrupting grain boundary particles, increasing grain boundary mobility. These factors can all contribute to the higher degree of grain coarsening. To gain further insight into this process, grain size measurements of the post-DSC samples heated in the range of 1300 to 1350°C were completed (see Figure 4-16). The grain size of MIM NiSA starts to increase at a lower temperature when the zirconium getter is present than in the argon gas atmosphere. For instance, at 1340°C, the grain size has increased to 30μm under the zirconium getter condition, while the grain size has not surpassed 20μm at 1340°C under the argon gas atmosphere. Grain growth is activated between 1335°C and 1340°C under the zirconium getter condition, while grain growth is only activated after surpassing 1350°C under that argon gas atmosphere. The grain size of MIM NiSA appears to increase at the same rate under both furnace atmospheres, but the activation of that grain growth occurs at a lower temperature when there is less oxygen present in the furnace atmosphere. The constrained sintering effect caused by powder oxidation and the reduced liquid content observed under the argon gas atmosphere both cause a delay in the activation of grain growth in NiSA during SLPS. The removal of oxygen from the furnace atmosphere using a zirconium getter reduces the amount of oxide particle formation in the grain boundary while also increasing the liquid fraction formed at a given temperature, enabling grain growth at a lower temperature.

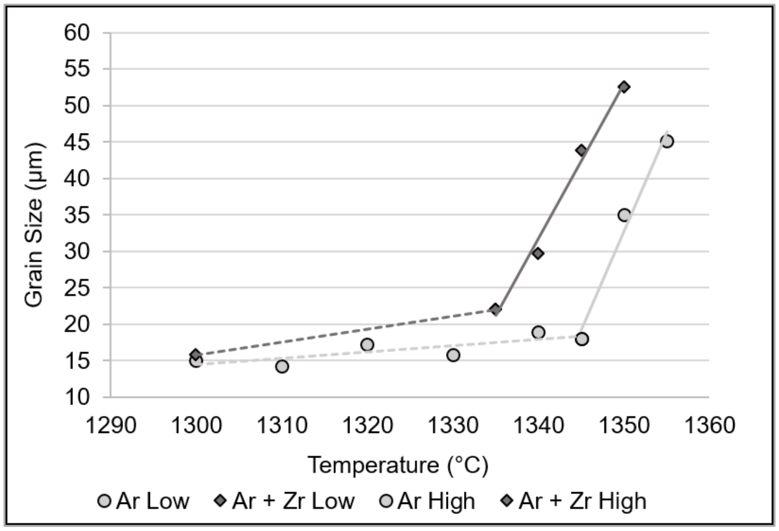

Figure 4-16. Average grain size of the NiSA after sintering for 1 hour at various temperatures under an argon atmosphere with and without a zirconium getter ring.

4.1.2.4 Activation of Grain Growth

The activation of grain growth in the Ni superalloys is a complicated process due to the number of different phases present in the grain boundaries. Precipitate phases, primarily gamma prime, are commonly observed as course phases along the grain boundaries in MIM

NiSA. These phases likely reduce the grain boundary mobility at lower sintering temperatures, though they dissolve completely by the solvus temperature, 1232°C. Despite this, no significant change in grain size is observed between 1200°C and 1300°C sintering temperatures, suggesting that the dissolution of gamma prime does not control grain growth in MIM NiSA.

Above the solvus temperature, carbide phases remain at the grain boundaries. The NiSA alloy was designed to form discrete grain boundary carbide phases which “pin” or immobilize the grain boundaries. Additional carbon imparted to the powder by the MIM process can also result in a high volume fraction of carbide phases in the grain boundaries of the MIM NiSA alloy. Therefore, there is a high degree of grain boundary pinning from carbides in the MIM NiSA material during solid state sintering. However, incipient melting at the interface between the gamma matrix and carbide particles has been reported in the literature [31]. Above 1270°C and into the SLPS temperature range, carbide phases have been observed to dissolve along with the melting of the gamma matrix [31,32]. At some critical point during the melting of the NiSA matrix, it would be reasonable to expect that the carbide phases would lose their ability to pin the grain boundaries, increasing grain boundary mobility and potentially enacting grain coarsening. Referring to Figure 4-15 and Figure 4-16, this critical point depends on the sintering atmosphere. Under argon gas only, grain growth is activated after 1350°C, which corresponds to a liquid fraction of 0.16. With the zirconium getter, grain growth is enabled after 1335°C, which corresponds to a liquid fraction of 0.08, half of the liquid fraction required in the argon atmosphere.

Oxide particles in the grain boundaries arguably pin the grain boundaries in a similar manner to carbide particles. However, oxide particles are typically more stable than carbides and do not dissolve during melting [3]. Therefore, it could be expected that oxide particles would retain their ability to pin the grain boundaries to higher temperatures than the carbides, being only effected by the gamma matrix melting around the particle as opposed to both melting and dissolution of the particle itself (as is the case with the carbide particles). The net result would be that a higher liquid fraction is required to overcome the grain boundary pinning effect from the oxide particles than the carbide particles. This theory is in line with the presented results, which indicate that a higher temperature and liquid fraction is required to activate grain growth under an atmosphere with a higher oxygen content.

Another influence on the activation of grain growth in MIM NiSA may be the total number of grain boundary particles. The NiSA sample under the argon atmosphere was observed to form a higher number of oxide particles in the grain boundaries than the sample tested with the zirconium getter. Both alloys contained similar amounts of carbide particles, therefore the sample sintered in argon had a higher overall number of grain boundary particles than the sample tested with the zirconium getter. It could then be argued that the higher degree of grain boundary pinning in the argon atmosphere sample requires a higher liquid fraction to overcome. From an energy stand point, the presence of grain boundary particles such as carbides and oxides increases the overall grain boundary energy [19]. A higher energy grain boundary then requires a larger amount of energy to become mobile, making grain growth a more difficult process to activate.

4.1.3 Conclusions

Dilatometry (DIL) and differential scanning calorimetry (DSC) were successfully used to sinter metal injection molded (MIM) NiSA superalloy under argon, argon with getter material (Zr or Ti), and high vacuum atmospheres. MIM NiSA samples were found to follow different densification paths during solid state sintering at 1310°C under the different atmospheres, with the high vacuum atmosphere resulting in the earliest onset to densification and highest sintering shrinkage. Analysis of the oxygen content in each atmosphere indicated that the argon atmosphere contained the highest and least consistent level of oxygen, resulting in oxidation of the NiSA alloy. As the oxygen content in the furnace atmosphere was reduced, the amount of densification increased as well as the final density. The grain size was not significantly influenced by changes in the atmosphere's oxygen content and no significant grain growth was observed during solid state sintering of the MIM NiSA material.

Increasing the sintering temperature to 1350°C to enact supersolidus liquid phase sintering (SLPS) revealed that the oxygen content in the furnace atmosphere influences both the densification path and the liquid fraction formed. Samples sintered in the argon atmosphere exhibited a constrained sintering response due to the formation of refractory metal oxide particles in the grain boundaries. The activation of grain growth was delayed under the argon atmosphere when compared to samples sintered under atmospheres with a getter material. A larger liquid fraction was formed at a given temperature under argon than those samples sintered with a zirconium getter in the DSC. Samples sintered under the high vacuum condition exhibited larger grains, fewer grain boundary particles, and a cleaner surface than the samples sintered under argon.

The activation of grain growth in the MIM NiSA alloy was determined to depend on both the liquid fraction and the degree to which the sample was oxidized. Samples sintered in the solid state did not exhibit grain growth regardless of the sintering atmosphere, while SLPS samples experienced rapid grain growth upon reaching a critical liquid fraction which was influenced by the furnace atmosphere. It was concluded that the number of oxide particles formed in the grain boundaries during sintering most likely governs the SLPS liquid fraction required to mobilize the grain boundaries and activate grain growth.

4.2 Supersolidus Liquid Phase Sintering of a MIM Nickel-Based Superalloy using Differential Scanning Calorimetry

4.2.1 Experimental Methods

De-bound MIM NiSA samples were initially heated to 1450°C in the DSC to obtain complete melting and solidification traces for the alloy. A 15mg sample was initially tested to minimize thermal lag effects in the enthalpy measurements. A 46mg sample was then used to confirm that the measured enthalpies did not vary significantly with a larger mass. Partial melting enthalpies at various temperatures within the melting range were used to estimate the theoretical liquid fraction with temperature. Temperatures of 1335, 1340, 1345, and 1350°C were selected as suitable SLPS temperatures to study the SLPS process, corresponding to theoretical liquid percentages of 8, 13, 20, and 31%.

MIM NiSA samples were heated at 4.5Kpm under 50ml/min flowing 99.999% Argon gas to the selected SLPS temperatures of 1335, 1340, 1345, and 1350°C. Samples were held at each SLPS temperature for 0, 15, 30, 60, and 120mins to measure the grain size over SLPS hold time. Samples were subsequently cooled at a rate of 20Kpm to room temperature. The furnace was evacuated to a minimum vacuum level of 5.4E-5mbar and backfilled with high purity argon gas prior to each test. A zirconium getter ring was used to remove any additional oxygen from the furnace during the experiments.

Small samples weighing 46mg ± 1% were tested at hold times of zero minutes to determine the partial melting enthalpy for each SLPS temperature at similar sample masses to the full melt test. Sample weights for the 15, 30, 60, and 120min hold times were maintained at 275mg ± 7% to obtain good consistency between DSC traces. The melting enthalpies from the 46mg and 275mg tests were measured and compared to confirm that the difference in sample mass did not significantly influence the enthalpy values. The percentage error between the partial melting enthalpy for the 46mg samples and the average partial melting enthalpy for the 275mg samples was 1.3, 5.5, 11.6, and 14.2% for the 1335, 1340, 1345, and 1350°C temperatures, respectively. This validation, along with the use of consistent experimental conditions in the DSC tests, allowed a comparative analysis method to be employed without the need to correct each DSC trace.

4.2.2 Results

4.2.2.1 DSC Experiments

The DSC heating trace for a complete melt of the MIM NiSA alloy is presented in Figure 4-17. The first endothermic event corresponds to the dissolution range of the gamma prime precipitates, γ’, beginning at 900°C and continuing until the solvus temperature at 1232°C. There is an exothermic shift in the DSC trace at 1050°C which may correspond to various carbide transformations upon heating [1–3,5,31–33]. Beyond the γ’ solvus temperature the

DSC trace begins to deviate slightly from the baseline at approximately 1270°C. This second endothermic event in the DSC trace corresponds to melting of the NiSA alloy above 1270°C. The onset of melting is estimated to be 1330°C by extrapolation of the baseline and linear portion of the melting peak. The nominal melting range of the alloy is 1330-1380°C when relying on the extrapolation method for the solidus temperature. In the case of this multicomponent/multiphase alloy, the melting event is gradual as seen in Figure 4-17. An alternative measure of the melting range is to note the temperature of deviation from the baseline prior to the melting onset and following melting. The vertical ticks on the linear baseline construction of Figure 4-17 demark these points as 1270°C and 1385°C. This is proposed to be a more realistic melting range for such a complex alloy. The enthalpy of melting over this expanded melting range was measured to be 148J/g using the linear baseline construction.

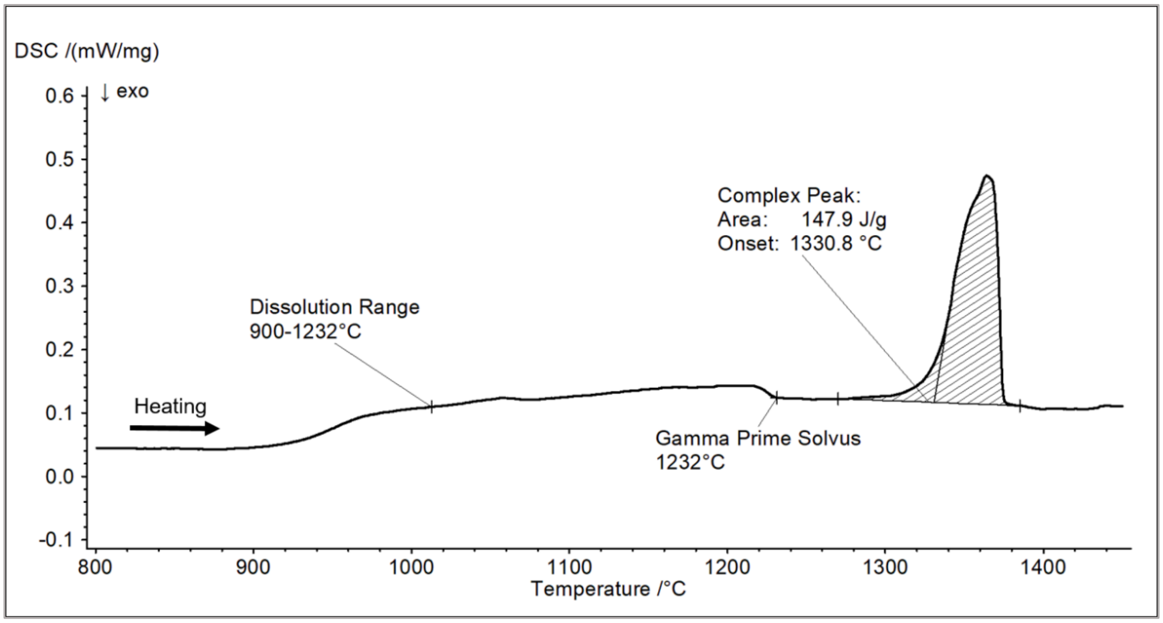

Figure 4-17. DSC trace of the MIM NiSA heated to 1450°C.

Partial area calculations over the melting range were completed to determine the fractional enthalpy at a given temperature. The fractional enthalpy can be used as an indication of the extent of melting within the alloy with temperature and can be used to calculate the percent enthalpy according to Equation (1):

$$\% \, Enthalpy = \frac{H_T}{H_{fusion}} \times 100\% \quad \textbf{(1)}$$

The percent enthalpy at a given temperature is representative of the theoretical percent liquid present [18]. As previously stated, temperatures of 1335, 1340, 1345, and 1350°C were selected as suitable SLPS temperatures, corresponding to theoretical liquid percentages of 8, 13, 20, and 31% based on Equation (1).

The heating and cooling traces for samples tested at the 1345°C SLPS temperature are presented in Figure 4-18 and Figure 4-19, respectively. The heating traces demonstrated good repeatability of the γ' solvus temperature, melting onset temperature, and peak shapes. The average partial melting enthalpy at 1345°C was 20.7 ± 1.3J/g, corresponding to a theoretical liquid fraction of 13.0% when comparing to the full melt enthalpy via Equation (1). Note that this does not agree with the partial integration of the full melting peak, which predicts 20% liquid at 1345°C. This discrepancy is caused by the influence of the different sample masses on the baseline of the DSC traces. Since the lower sample mass for the full melt causes a different baseline slope than the larger mass for the interrupted tests, the liquid fraction predictions diverge with increasing temperature. A higher mass also creates a thermal lag within the measurement, which causes the interrupted test to lag behind the full melt test, decreasing the enthalpy measurement.

Despite their deviation from the partial integration method, the enthalpy measurements in the interrupted tests had a consistent baseline construction and showed excellent agreement. The first deviation from the baseline repeatedly occurred at 1270°C in these tests. The SLPS tests were run in random order to minimize the influence of any instrument drift over the testing period.

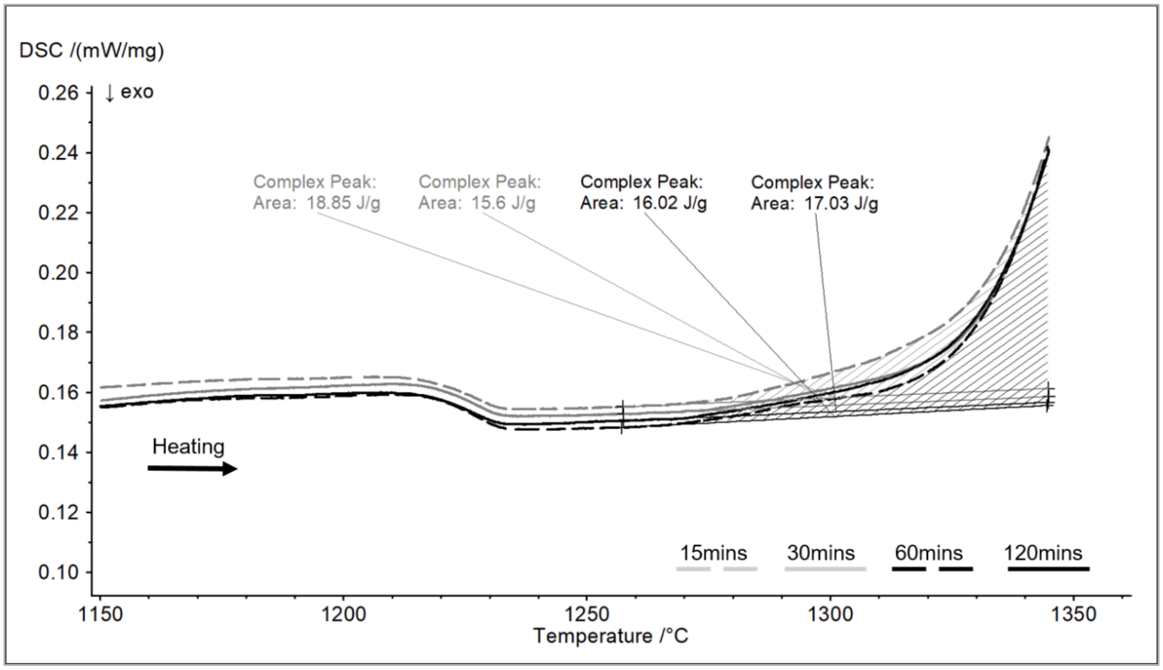

Figure 4-18. **DSC heating traces of individual MIM NiSA samples heated to the SLPS temperature of 1345°C.**

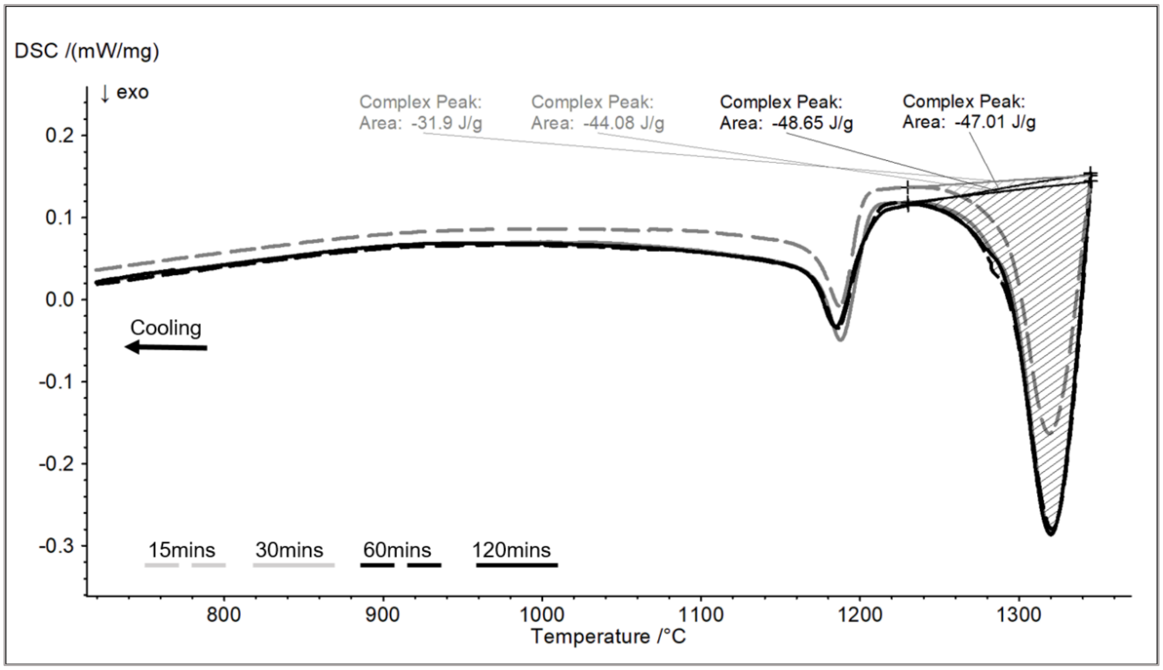

Figure 4-19. **DSC cooling traces of individual MIM NiSA samples heated to the SLPS temperature of 1345°C.**

The cooling traces exhibited two separate exothermic events corresponding to solidification of the alloy and subsequent re-precipitation of γ'. The peak shapes for these thermal events were consistent between samples, however the magnitude of both the solidification and re-precipitation events increased with longer hold times at the peak temperature. The measured solidification enthalpy increased with increased hold time indicating that the liquid fraction present upon cooling was larger than the initial liquid fraction formed upon heating.

The cooling trace from the full melt test of the alloy was analysed to determine the enthalpy upon solidification. The melting and solidification enthalpies are theoretically equivalent, though asymmetry in the thermal response of the DSC can be caused by different scanning rates as well as heating versus cooling. Therefore, it is necessary to compare partial melting enthalpies to complete melting enthalpies during heating at the same rate to determine the fractional enthalpy at a given SLPS temperature. Similarly, partial solidification enthalpies must be compared to the complete solidification enthalpy during cooling at an identical rate. This comparative technique allows the initial and final liquid fractions to be measured from the DSC traces while accounting for any differences in thermal response of the DSC due to heating and cooling at different scanning rates.

The DSC trace for a complete solidification of NiSA is presented in Figure 4-20. The measured solidification enthalpy was 164J/g, which is about 9% larger than the enthalpy measured upon melting (148J/g). The difference between the two measurements can be attributed to differences in the thermal response of the DSC under differing scanning conditions.

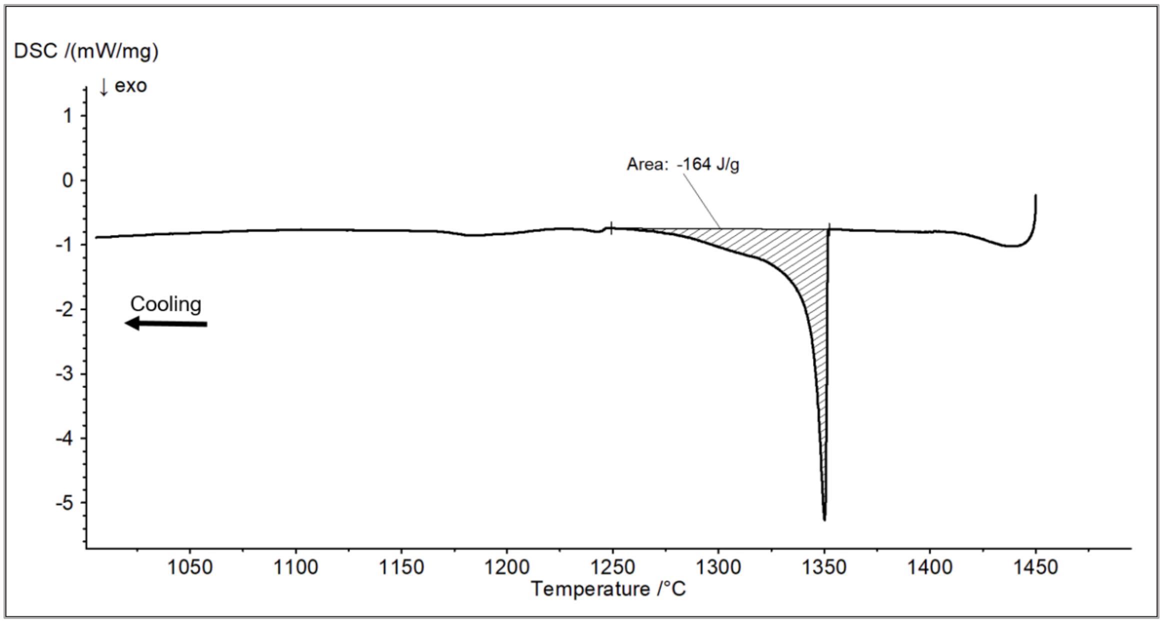

Figure 4-20. DSC of a complete solidification of the NiSA after heating to 1450°C.

The DSC trace in Figure 4-20 does not immediately return to a stable baseline and shows a hook-shaped response upon cooling from 1450°C. This type of response is commonly observed in DSC instruments and is a result of the measurement signal stabilizing under new thermal conditions. In the SLPS experiments, the step change from the isothermal temperature to the cooling rate causes a similar thermal response. However, solidification of the NiSA alloy occurs simultaneously with the instrument response to the rate change, leading to overlapping peaks in the DSC trace. Therefore, the enthalpies measured directly from the solidification events in the SLPS cooling traces contain a contribution from the instrument stabilization and are an overestimation of the true enthalpy. To correct for this, the thermal response upon cooling from an isothermal hold was measured for a NiSA sample in the solid state at 1300°C. The 1300°C temperature prevented any significant liquid formation in the sample, removing the solidification response from the DSC trace while maintaining thermal conditions representative of the higher temperature SLPS tests. The peak generated from the instrument's response to the rate change was evaluated using the same baseline construction technique described above resulting in an apparent area of 1.5J/g. The instrument response was then subtracted from the experimental solidification measurements from the SLPS tests to provide a corrected enthalpy measurement.

The initial liquid fractions and final liquid fractions after each hold time were determined from the DSC experiments and the results are plotted in Figure 4-21. Each SLPS temperature exhibits a power law increase in the liquid fraction present with increasing isothermal hold time. The plotted curves also show an increased rate of liquid formation with increasing SLPS temperatures. In the first 15 minutes of the isothermal hold time the liquid fraction is transient, with the liquid fraction approaching a more steady state at longer hold times. The liquid fraction approximately doubled over 120mins at each SLPS temperature.

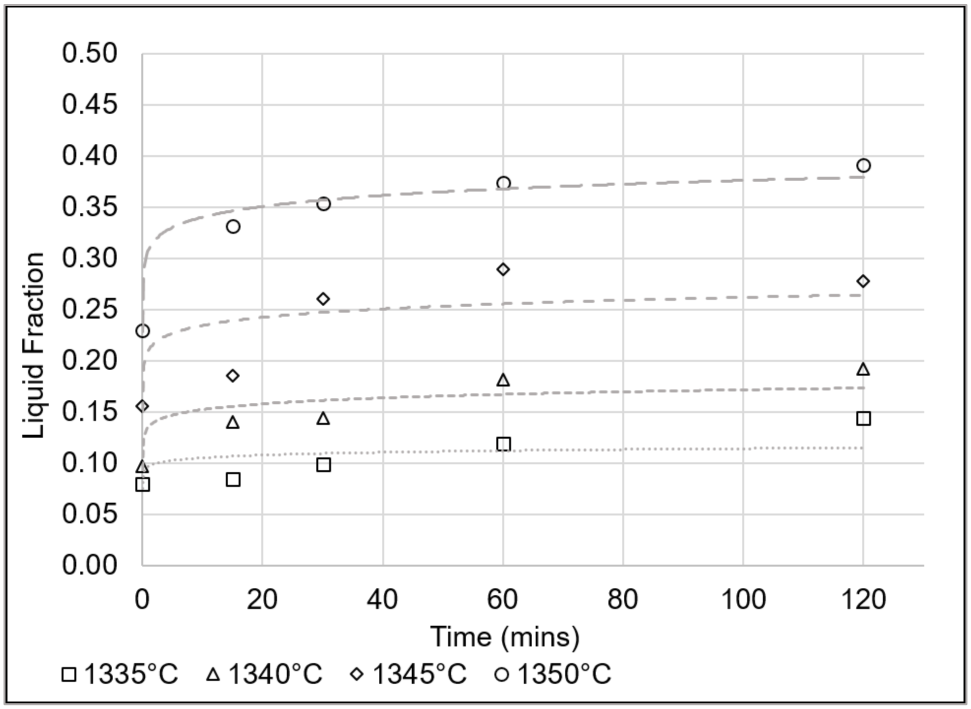

Figure 4-21. Liquid fraction over isothermal hold time at SLPS temperatures of 1335, 1340, 1345, and 1350°C.

The average grain size of each sample is plotted with time and SLPS temperature in Figure 4-22. The initial grain size at the start of SLPS was measured from individual samples held for zero minutes at each SLPS temperature and cooled rapidly to minimize any grain growth during the cooling segment. The average initial grain size among the samples was 15.8 ± 1.5μm which is consistent with the particle sizes in the NiSA powder. The agreement between the powder particle size and the initial grain sizes at each SLPS temperature demonstrates that there is no significant grain growth during heating to the SLPS temperature. The grain size of the alloy increases substantially with increasing isothermal hold time. The grain growth follows a power law at each SLPS temperature, similar to the liquid fraction measurements presented in Figure 4-21. The grain growth rate increases substantially as the SLPS temperature is raised and extended hold times at the 1345°C and 1350°C temperatures lead to additional grain growth at a slower rate. The 1335°C and 1340°C temperatures achieved less grain growth, remaining sub-30μm after 120mins.

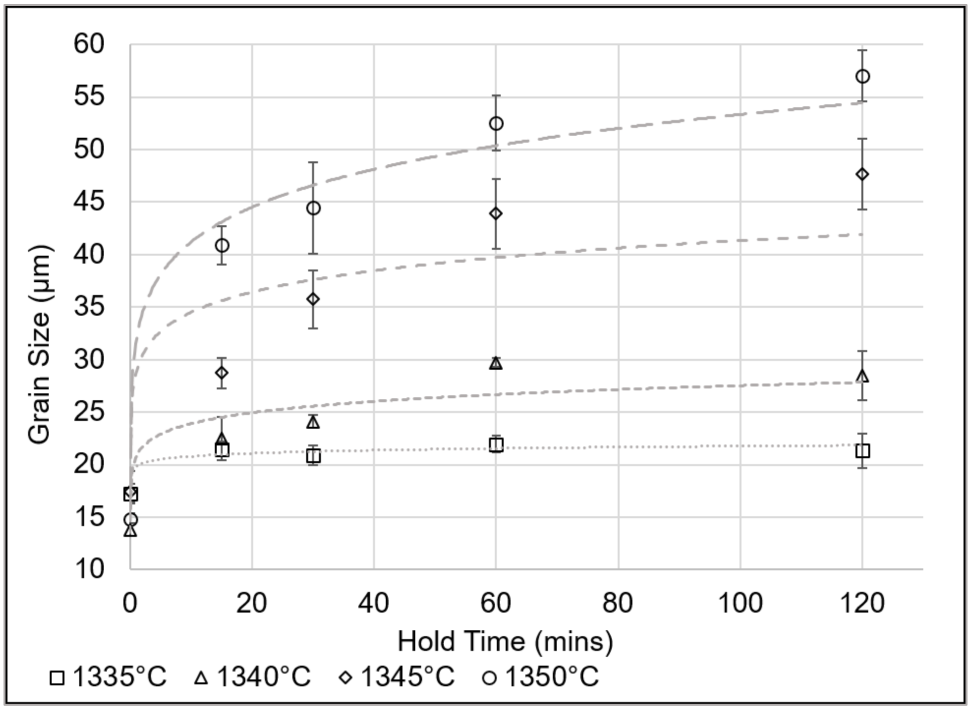

Figure 4-22. Average grain size over isothermal hold time at SLPS temperatures of 1335, 1340, 1345, and 1350°C.

The sintered density of the SLPS NiSA samples over hold time is presented in Figure 4-23 for each peak temperature. All specimens exhibited a sintered density above 98% by the time the peak SLPS temperature was reached. This result is consistent with previous observations of the solid state sinter density in Section 4.1. After holding at the peak temperature for 15mins, the sintered density of the NiSA decreased for all SLPS temperatures. The 1345°C temperature demonstrated the most dramatic drop in density, showing approximately 96% density after the 15min hold time. All specimens exhibited a subsequent increase, or recovery, of the sintered density after 15mins of hold time. After 2 hours at the peak SLPS temperature, all samples exhibited sintered densities of about 98% or higher.

The DSC tests for the 1345°C SLPS temperature were repeated using a new crucible, sample carrier, and instrument calibration in order to verify the trends observed in the SLPS enthalpy measurements. Pure Ni was added to the calibration to ensure the instrument was accurate at high temperatures while Zn was removed from the calibration. The repeat experiments are compared to the original set of tests in Figure 4-24. There is good agreement between the two data sets, confirming the transient nature of the liquid fracturing during SLPS. The 15min hold test from data set A appears to be an outlier to the observed trend while the remaining measurements showed good repeatability. These results validate the developed DSC method for SLPS analysis as well as both instrument calibrations.

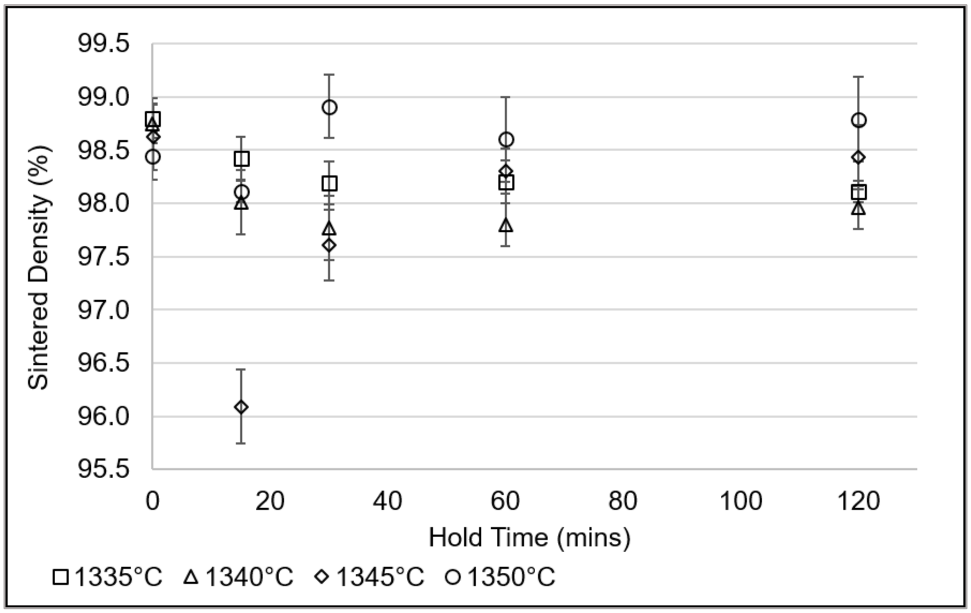

Figure 4-23. Sintered density over isothermal hold time at SLPS temperatures of 1335, 1340, 1345, and 1350°C.

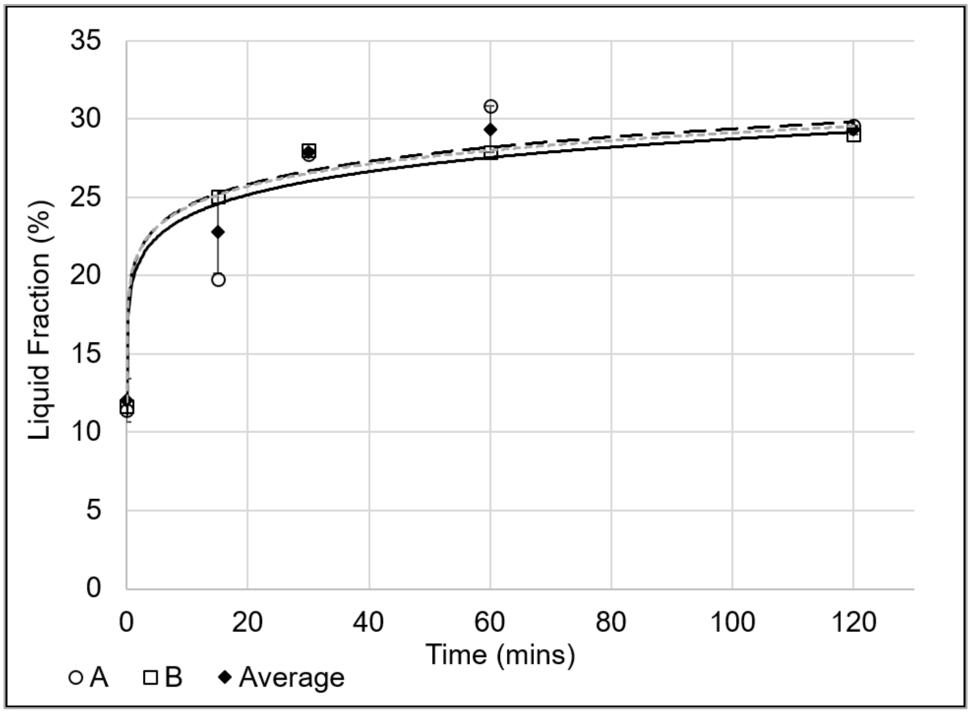

Figure 4-24. Duplicate DSC tests for liquid percentage over time at an SLPS temperature of 1345°C.

4.2.2.2 Macroscopic Shape Retention

Stereomicroscopy of the SLPS samples was completed prior to preparing polished cross sections for optical microscopy to determine the overall shape retention of the samples. The stereomicroscope images for a 15min and 120min hold at temperatures of 1340°C and 1350°C are presented in Figure 4-25 and Figure 4-26**,** respectively. The macro-scale images demonstrate the extent of slumping and deformation with increasing SLPS time and temperature. The 1340°C samples retained their original shape over the 120min hold time and some minor edge rounding was observable in the 120min sample. The sample held for 15mins at 1350°C was deformed to a much larger extent than the sample held for 120mins at 1340°C. The sample held for 120mins at 1350°C the largest amount of slumping and shape loss. The progressive shape loss with increasing hold time at a single temperature demonstrates one consequence of a transient liquid fraction during SLPS. In contrast, the samples held at 1340°C demonstrate the ability of SLPS to achieve good shape retention below a critical liquid fraction.

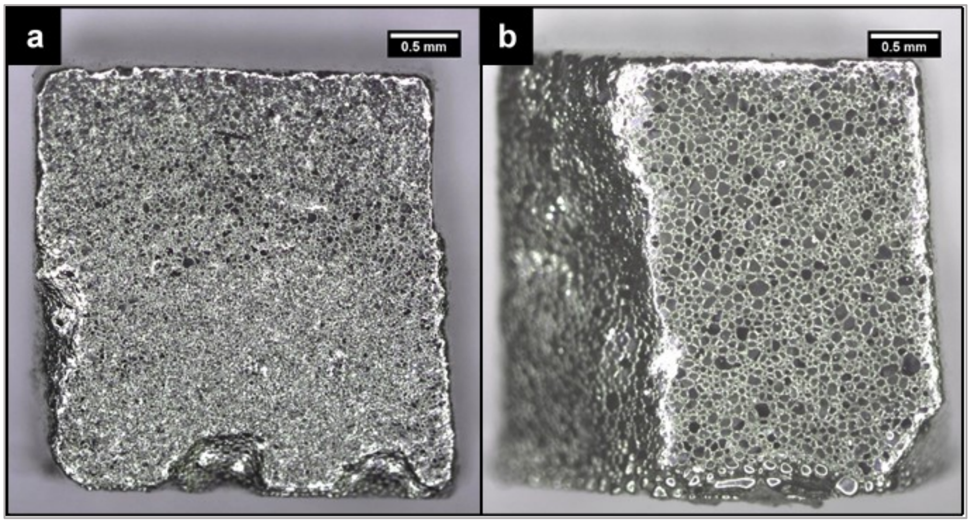

Figure 4-25. Side-view stereomicroscope images of the MIM NiSA after being sintered at 1340°C for a) 15mins and b) 120mins.

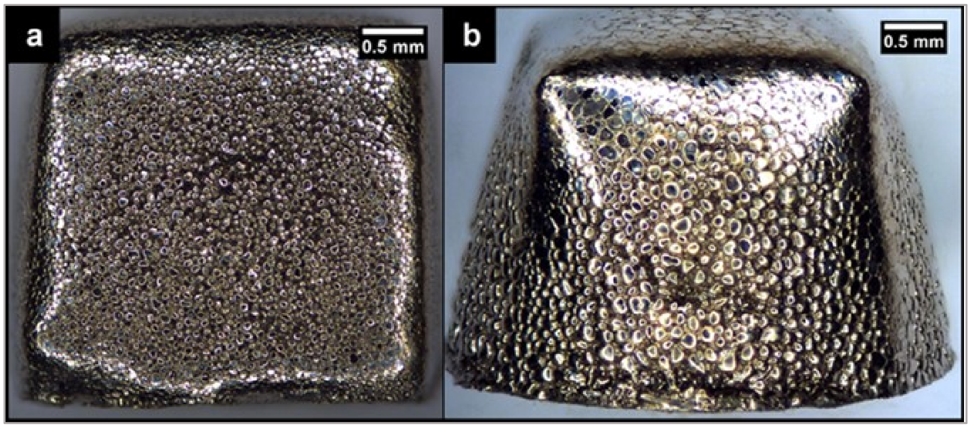

Figure 4-26. Side-view stereomicroscope images of the MIM NiSA after being sintered at 1350°C for a) 15mins and b) 120mins.

As mentioned in Section 3.3, the green height of the samples was very consistent since these were preserved from the as-moulded MIM part. Assuming a consistent sintering shrinkage, the post-sintered sample height can be used as an overall measure of shape retention and slumping.

Three sample height measurements were taken after the SLPS process using calipers. The average sample height is plotted against time for each SLPS temperature in Figure 4-27. The average shrinkage of MIM NiSA samples sintered in a Netzsch 404C Dilatometer at 1310°C for 60mins is also plotted as a baseline of the expected level of solid state sintering shrinkage. Dilatometry at 1350°C (presented in Section 4.1) revealed that the SLPS samples experience the majority of sintering shrinkage prior to the peak temperature. This means that SLPS samples exhibit similar sintering shrinkage amounts at the start of the hold time and that deviations in sample height during the hold time provide an indication of material slumping. The average shrinkage was approximately 10% in all samples sintered at or below 1345°C. In contrast, SLPS at 1350°C caused slumping of the material at all hold times. The standard deviation of the height measurement was much higher for the 1350°C SLPS samples due to the significant amount of edge rounding. Edge rounding was more pronounced with increasing temperature and hold time, however this effect is not completely captured by Figure 4-27. Figure 4-27 captures the ability of the material to support its own weight up to an SLPS temperature of 1345°C and the loss of rigidity at 1350°C.

In addition to the extent of deformation, the macro-scale images of Figure 4-24 and Figure 4-25 reveal the amount of surface grain growth. The surface grain size is visibly increased after holding for 120mins at both 1340°C and 1350°C while the higher SLPS temperatures show a much larger increase in grain size than the lower temperatures.

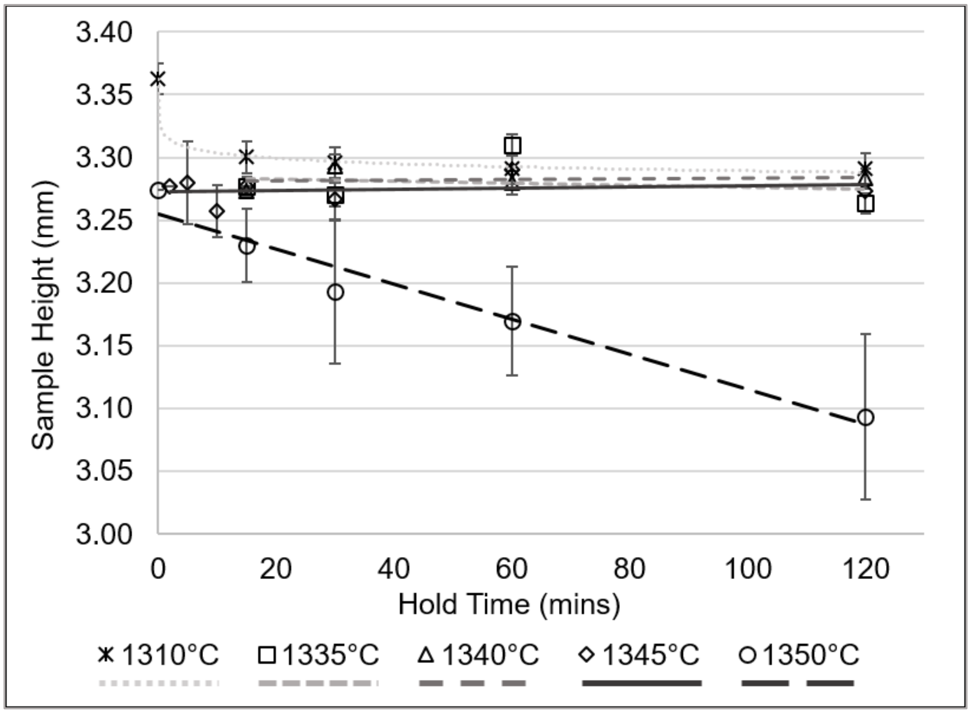

Figure 4-27. Average sample height of the SLPS samples with increasing hold time at each SLPS temperature.

4.2.2.3 Microstructural Analysis

Optical microscopy was performed on all SLPS samples in addition to the completely melted sample. The full melt sample solidified with a dendritic microstructure and had both γ/γ’ eutectic and script-like carbides located in the inter-dendritic regions. Figure 4-28 compares the initial microstructure of the SLPS sample at 1345°C/0mins to a NiSA microstructure solid-state sintered at 1310°C for 1 hour. Both microstructures were etched with waterless Kalling’s reagent to expose the grain boundaries. The average grain size of both microstructures is between 15-20µm, despite the SLPS sample having been heated above the solidus temperature. The solid-state sintered MIM NiSA sample was sintered below solidus with a longer hold time. The lack of grain growth in the solid state sintered microstructure reinforces the inability to increase the grain size during high temperature solid state sintering. The SLPS test at 1345°C for 0mins demonstrates that grain growth does not occur immediately upon heating above the solidus.

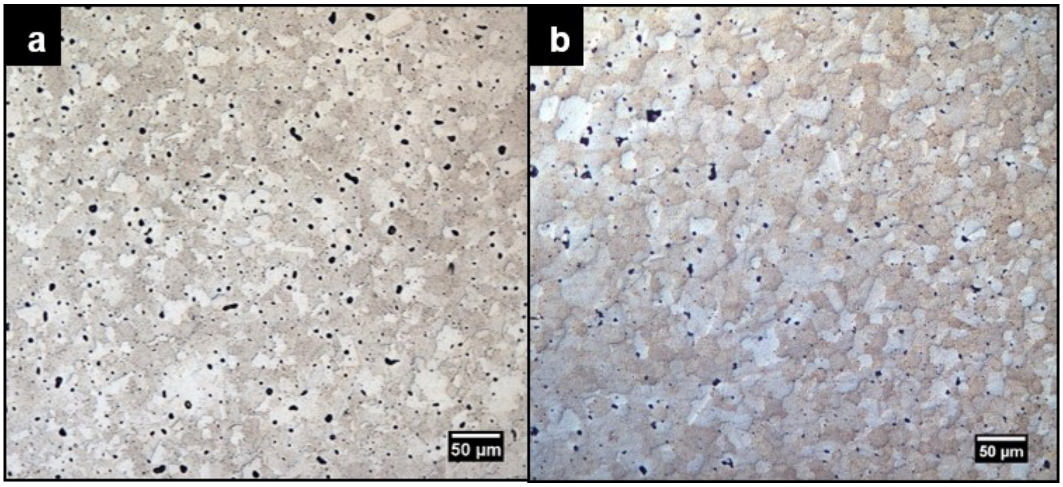

Figure 4-28. Optical microscope images of the MIM NiSA a) sintered in the solid state at 1310°C for 1 hour b) SLPS at 1345°C for 0mins.

The etched microstructures for SLPS samples held at 1345°C for 0, 15, 30, and 120mins are compared in Figure 4-29. The side-by-side comparison of theses samples reveals how the microstructure coarsens over time at an isothermal temperature. The grain structure becomes less angular over time and the grain size increases substantially. The final hour of SLPS sintering did not yield a significant increase in grain size as the majority of the grain growth occurs between 0 and 60mins. Figure 4-22 also demonstrates that the final 90mins of SLPS time in the 1345°C and 1350°C trials results in a 10-15µm increase in grain size, which is consistent with the progression observed in Figure 4-29. This observation is consistent with the DSC results, where the liquid fraction stabilizes after approximately 30mins of SLPS time.

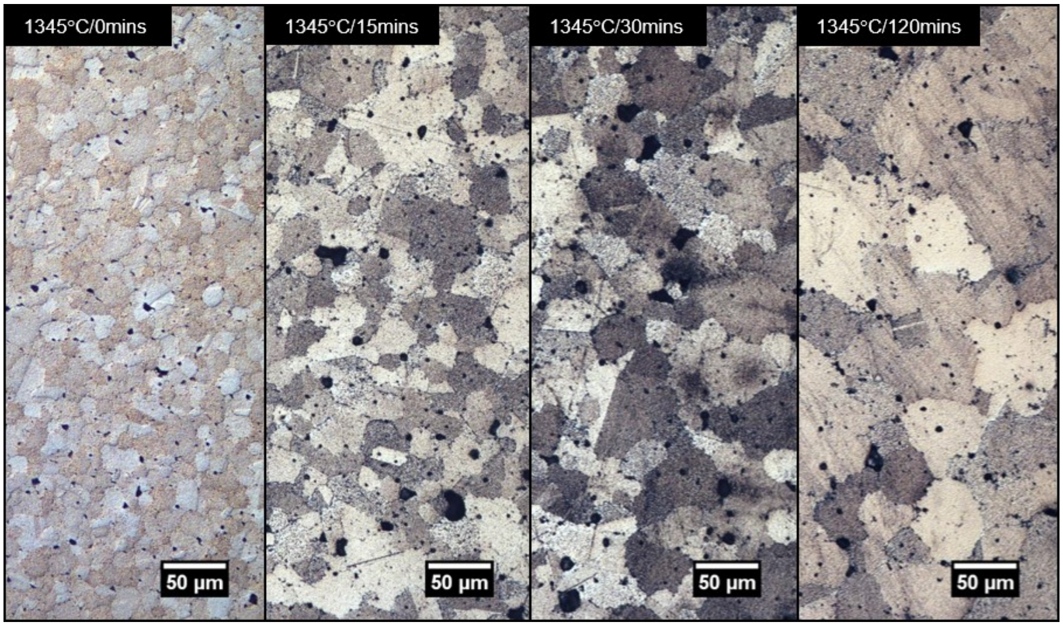

Figure 4-29. Etched microstructures of the MIM NiSA SLPS at 1345°C for 0, 15, 30, and 120mins.

Further optical microscopy revealed that the SLPS process caused a host of additional microstructural changes to the NiSA alloy. With increasing SLPS time and temperature the surface grain structure became more rounded and coarser than the bulk material, open porosity was more prominent at the surface of the material, eutectic pools formed and coarsened, and metal carbide phases became concentrated in the eutectic regions of the alloy. Figure 4-30 compares stitched cross sections of the 15min and 120min holds at 1350°C. Open porosity and coarsening of surface grains is evident at both long and short hold times while the extent of slumping over the SLPS time is also visible. The average grain sizes were 40.9 ± 1.9µm and 57.0 ± 2.4µm for the 15min and 120min holds, respectively.

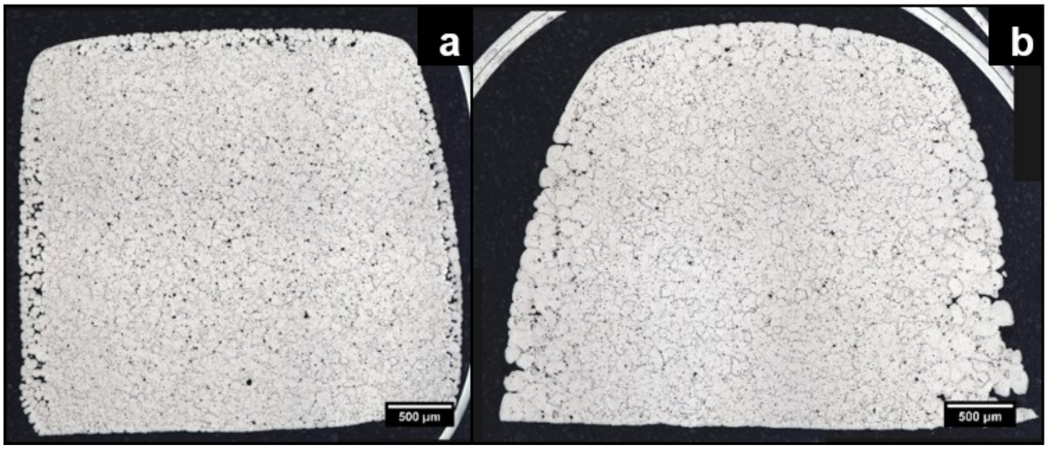

Figure 4-30. **Stitched cross sections of the MIM NiSA superalloy sintered at 1350°C for a) 15mins and b) 120mins.**

20x magnification images of the 1350°C SLPS microstructures are presented in Figure 4-31. The surface and center regions of the cross sections for the 15min and 120min hold times are shown in Figure 4-31a & c and Figure 4-31b & d, respectively. The change in grain size is evident when comparing the microstructures of the two hold times. The surface grain size is notably larger than the bulk of the sample for both hold times and a γ/γ’ eutectic phase is present in the grain boundaries of the surface layer after 120mins. γ/γ’ eutectic is not observable in the surface layer at the lower 15min hold time. The γ/γ’ eutectic regions formed at extended hold times were primarily observed in the surface layer of the SLPS samples and were less prevalent in the bulk of the material.

High magnification images of the γ/γ’ eutectic pools are presented in Figure 4-32. When visible, these eutectic regions were commonly observed at triple point boundaries and demonstrate the extent of liquid penetration in the grain boundaries. Clusters of blocky carbide phases were located inside and surrounding the γ/γ’ eutectic pools. The amount of eutectic pooling observed in the SLPS samples increased with both hold time and temperature which agrees with the increasing liquid fraction observed in the DSC results.

Eutectic pooling was observed at all hold times at 1350°C and after 60mins at 1345°C. γ/γ' eutectic was not observed in the 1335°C and 1340°C SLPS tests.

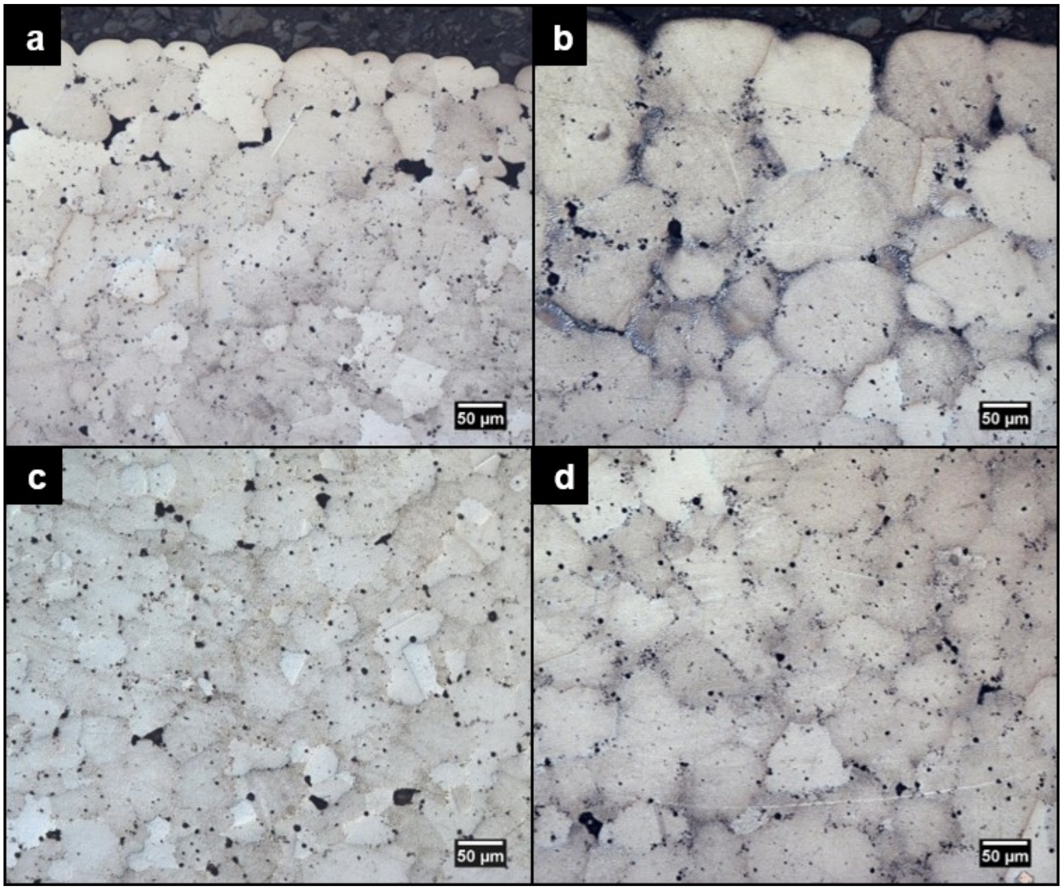

Figure 4-31. Surface and center microstructures of the MIM NiSA sintered at 1350°C for a), c) 15mins and b), d) 120mins.

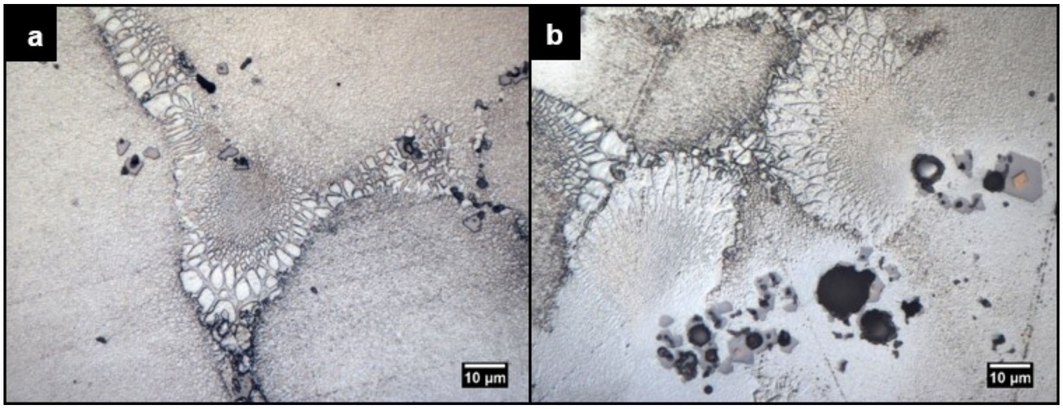

Figure 4-32. High magnification images of γ/γ' eutectic pools in the 1350°C/120min SLPS MIM NiSA material at a) a triple point boundary and b) a cluster of blocky carbides.

A representative area of the surface layer in the 1350°C/120min SLPS sample is presented in Figure 4-33. γ/γ’ eutectic is readily observed within the grain boundaries and triple point regions. A number of grains in the surface layer are surrounded by γ/γ’ eutectic and there has been a considerable amount of grain rounding. Grain diameters more than 100µm are also observable near the surface. The carbide phases observed in the 1350°C/120min microstructure (Figure 4-32 and Figure 4-33) are coarser than those observed in shorter hold times. These coarser carbide phases tend to cluster together near grain boundaries and γ/γ’ eutectic pools in contrast to the fine, evenly distributed carbides found in the solid state sintered and short hold time SLPS microstructures (Figure 4-28 and Figure 4-31a & b).

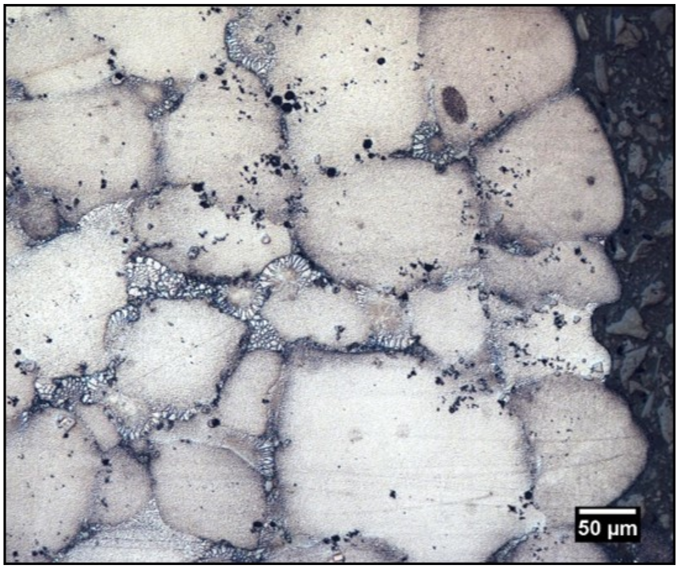

Figure 4-33. Surface layer of the MIM NiSA sintered at 1350°C for 120mins.

4.2.2.4 SEM-EDS Analysis

Further analysis of the SLPS MIM NiSA microstructures was completed using SEM-EDS. The inter-dendritic regions of the completely melted NiSA material were analysed to gain an initial understanding of segregation phenomenon in the alloy. Micrographs of the γ/γ’ eutectic areas at different magnifications are shown in Figure 4-34. The micrographs of the completely melted material demonstrate the large amount of γ/γ' eutectic that is solidified at a 200Kpm cooling rate. γ/γ' eutectic pools were also observed in the microstructures of the 1345°C and 1350°C SLPS samples at extended hold times. A representative micrograph of the γ/γ' eutectic pooling in the 1345°C/120min sample is presented in Figure 4-35. The eutectic pool has a similar size and structure in both the complete melt and 1345°C/120min tests, though carbides are present inside of the eutectic pools in the SLPS test. In the complete melt test, the carbide phases are coarser and are located outside of the γ/γ' eutectic pools only.

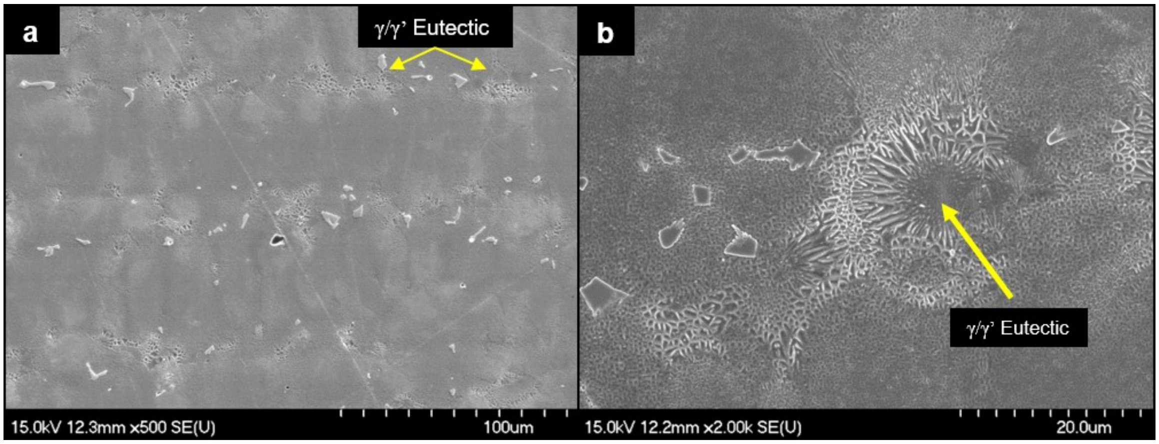

Figure 4-34. Micrographs of the inter-dendritic regions in the completely melted MIM NiSA at a) 500x magnification and b) 2K magnification.

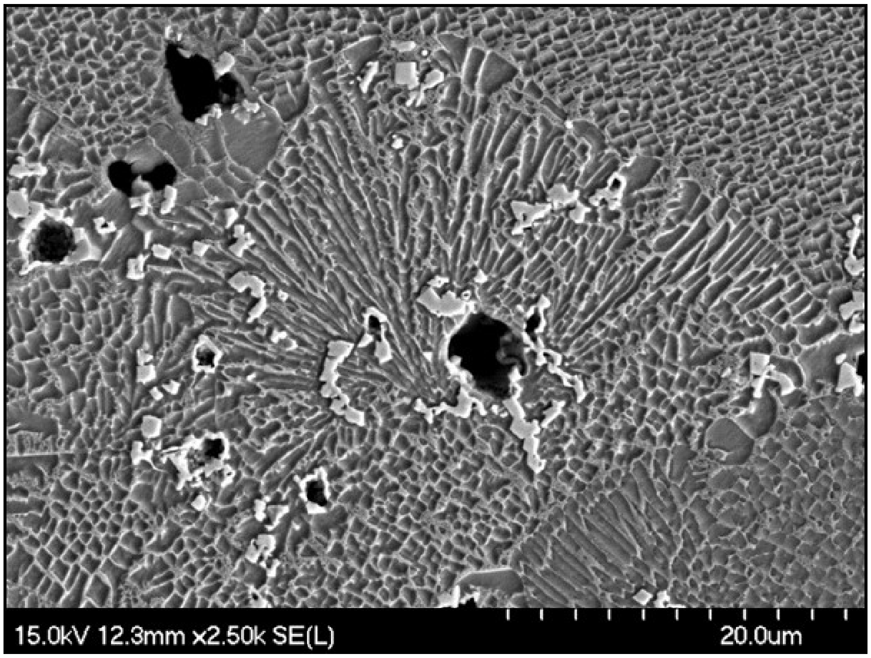

Figure 4-35. Micrograph of γ/γ' eutectic pooling in the 1345°C/120min SLPS sample.

EDS analysis of the eutectic regions was performed to evaluate the liquid composition at a given time and temperature. The composition of the liquid was compared to the composition of the solid regions of the alloy at 1345°C and 1355°C with no hold time. The EDS results are presented in Figure 4-36 and Figure 4-37 as the percentage difference from the solid state sintered MIM NiSA composition with nickel excluded in order to improve the comparison. At 1355°C the alloy has surpassed the solidus temperature and is partially melted. Comparing the solid and liquid compositions from the EDS scans in Figure 4-36 illustrates that some minor segregation of solute elements has occurred. The difference in the tungsten concentration between the solid and liquid is most significant at this temperature. Segregation of the solute elements is more clear in the fully melted, 1450°C sample EDS scans, where tungsten, tantalum, and other RMs all show large differences in concentration between the solid and liquid.

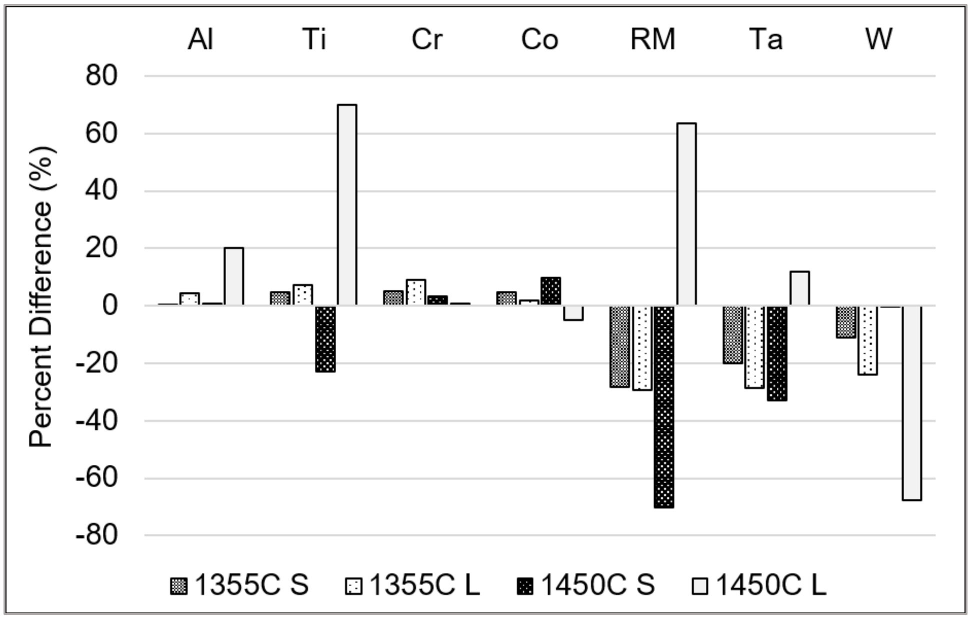

Figure 4-37. Percentage difference of the solid and liquid compositions in the MIM NiSA heated to 1355°C and 1450°C for 0mins relative to the composition of the solid state sintered MIM NiSA. S denotes solid and L denotes liquid.

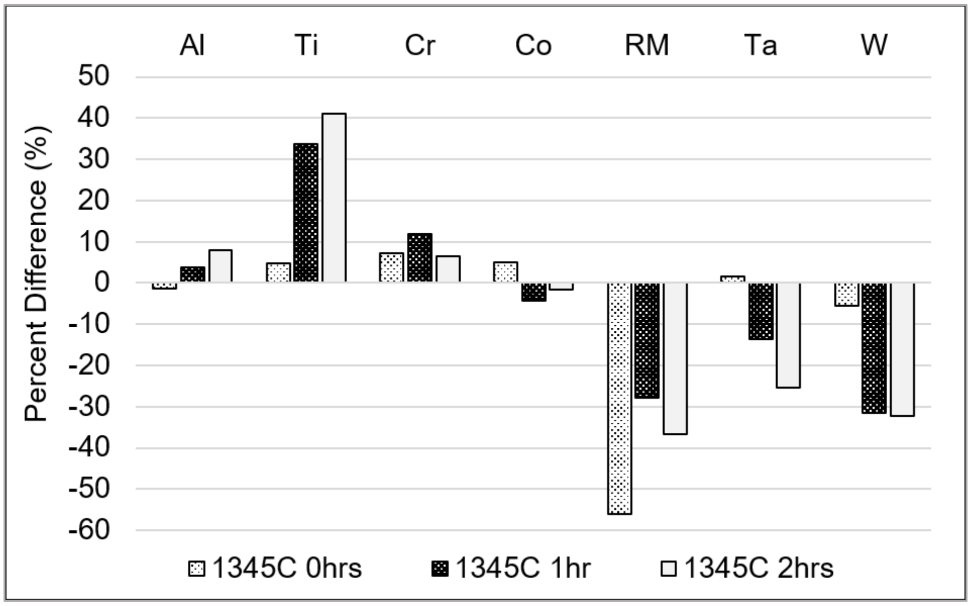

Figure 4-36. Percentage difference of the solid state sintered and the SLPS MIM NiSA composition after different hold times. Note that the 0hr hold time is the composition of the solid and the 1hr and 2hr holds are compositions of the eutectic phase region.

The EDS scans at both 1355°C and 1450°C indicate that tungsten partitions into the solid. The 1450°C scans suggest that the other RMs and tantalum partition into the liquid phase as the γ/γ' eutectic pools are rich in these solutes. The remaining solutes do not show significant segregation with increasing temperature in the melting range, however, Al and Ti appear to partition to the liquid after a complete melt at 1450°C.

The percentage difference of the 1345°C/0mins sample in Figure 4-37 suggests that minimal segregation has occurred over the course of heating from 1300°C to 1345°C. The tungsten and RM concentrations both show a notable decrease upon heating to 1345°C from 1300°C. EDS scans of the eutectic regions after holding at 1345°C for 60 and 120mins show the progressive compositional change of the liquid. The tungsten, tantalum and RM concentrations in the eutectic phase decreased compared to the original 1300°C solid. However, carbide phases located in the eutectic pools, such as those in Figure 4-35, were rich in tantalum and RMs. This result suggests that these RMs are still partitioned into the liquid phase at 1345°C, as suggested by the 1450°C EDS results. The concentration of solute elements remained relatively constant between 60 and 120mins at the 1345°C SLPS temperature. The absence of further solute segregation during this part of the hold indicates that the liquid concentration stabilizes over time at a given SLPS temperature, which supports the liquid fraction results presented in Figure 4-21.

4.2.3 Discussion

4.2.3.1 DSC Analysis

The DSC results presented in Figures 4-17 to 4-20 demonstrate the melting and solidification behaviour of the MIM NiSA alloy under various SLPS conditions. The extrapolated onset of melting for the NiSA was determined to be 1330°C, which agrees with reported solidus temperatures [31,32]. However, the first deviation of the DSC trace from the baseline is observed at 1270°C, which has also been reported as the onset melting temperature for the NiSA [34]. In complex alloys, such as the nickel superalloys, it is generally more accurate to identify the melting temperature using the first deviation of the DSC trace from the baseline due to the likely presence of incipient melting [21]. In the nickel superalloys, incipient melting can occur at the interface between carbides and the gamma matrix phase and has been reported at similarly low temperatures to those observed in the DSC results for the MIM NiSA [31]. Therefore, the shallow endothermic portion at the start of the melting peak is expected to be a result of incipient melting between metal carbides and the gamma matrix.

The melting peak has an inflection point closer to the extrapolated onset temperature of 1330°C which corresponds to continued gamma phase melting [31,32]. The increase in the magnitude of the endothermic event at this temperature indicates that an appreciable amount of melting is occurring in the alloy beyond 1330°C. Partial integration of the DSC trace between 1270°C and 1330°C leads to a theoretical liquid volume of 5% at 1330°C, which is in agreement with the 7.9 ± 0.7% liquid percentage determined for the SLPS test temperature of 1335°C.

The solidification enthalpies increase with longer SLPS hold times in the DSC cooling traces. This result indicates that the liquid fraction is increasing over time at the SLPS temperature. Microstructural evidence of liquid was only observed as γ/γ’ eutectic pools, which developed at longer hold times and higher temperatures. The development of this microstructural feature with time and temperature suggests that there is a liquid fraction increase, which supports the DSC results. The average grain size in Figure 4-22 closely follows the calculated liquid percentage increase exhibited in Figure 4-21, indicating that the significant level of microstructural coarsening with time at temperature is related to the liquid fraction.

Despite heating into the melting range, no significant coarsening occurred in SLPS samples with no hold time. This is particularly evident in Figure 4-22 and Figure 4-28b, where the grain size at zero hold time is the same as the solid state sintered sample, regardless of SLPS temperature.

After heating the NiSA to 1355°C with no hold time, γ/γ’ eutectic was observed in the grain boundaries and the DSC trace indicated that there was a theoretical liquid content of 45%. Similar liquid contents and γ/γ’ eutectic pools were observed in SLPS samples at 1350°C with a 60mins hold time. The formation of the γ/γ’ eutectic at a lower temperature and longer hold time therefore coincides with a higher liquid fraction.

4.2.3.2 Solute Segregation

The completely melted DSC sample exhibited a dendritic microstructure with γ/γ’ eutectic located in the inter-dendritic regions. This microstructure is commonly reported in the cast

NiSA and other Ni-superalloys under various solidification conditions [5,31,32,34]. Solute segregation during solidification causes alloying elements to partition into the liquid or the solid phase according to their relative solubility and the thermal conditions [19]. The magnitude of segregation for a particular alloying element can generally be assessed using the element's partition coefficient, *k*. Assuming that the solid-liquid interface is under equilibrium during solidification, the partition coefficient is defined as the ratio of the solid and liquid concentrations at the solid-liquid interface. If the partition coefficient of a given element is greater than 1, $k > 1$, then the concentration of that element in the solidified material will be greater than the concentration in the liquid. If the partition coefficient is less than 1, $k < 1$, then the concentration in the solidified material will be less than the concentration in the liquid [19,29].

The segregation phenomenon described above is best discussed with the aid of the pseudo binary phase diagram presented in Figure 4-38. Below the solidus temperature (at T_1) the NiSA alloy has a solid composition, X_{NiSA}. Upon heating to the SLPS temperature, T_{SLPS}, the alloy enters the two phase region of the diagram, where the solid and liquid phases coexist with compositions X_S and X_L, respectively. The solute elements partition into the solid or liquid phases over time in order to create a stable equilibrium at T_{SLPS} with compositions X_s and X_L as indicated by the pseudo binary phase diagram. When the partition coefficient is greater than 1, $k > 1$, $X_{NiSA} < X_S$ and $X_{NiSA} > X_L$. When the partition coefficient is less than 1, $k < 1$, $X_{NiSA} > X_S$ and $X_{NiSA} < X_L$, which is the case shown in Figure 4-38. After extended time at T_{SLPS}, the equilibrium compositions of the solid and liquid are established throughout the mixture, leading to an equilibrium volume (or weight) fraction of solid and liquid according to the lever rule. Upon cooling, the liquid phase will undergo non-equilibrium cooling and the production of lower temperature non-equilibrium eutectic phases could occur.

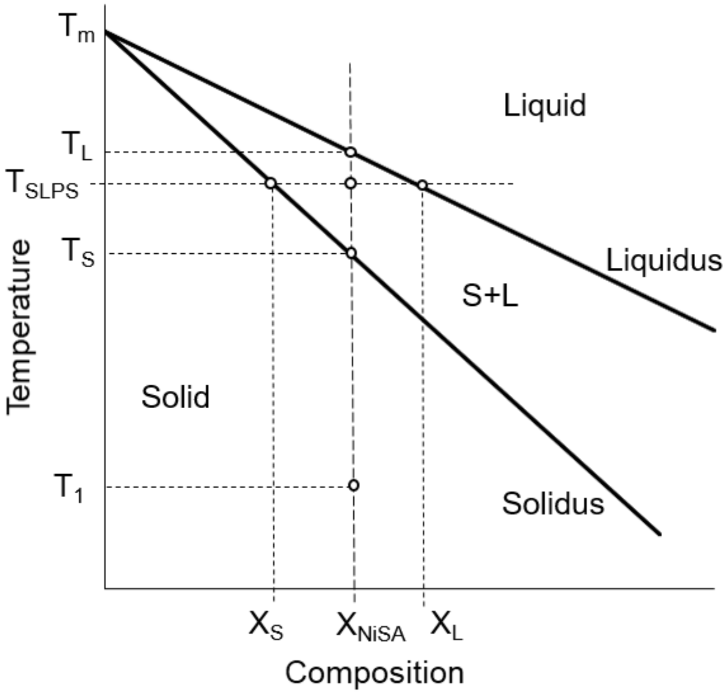

Figure 4-38. Pseudo binary phase diagram illustrating the solid and liquid compositions with SLPS temperature.

Previous work on the micro segregation phenomenon in cast CMSX-4, a similar alloy to the NiSA in this study, identified that Cr and has a partition coefficient close to unity, meaning it exhibits no strong preference to partition into either the solid or liquid phase [29]. Solutes Al, Ti, and Ta are known to have partition coefficients lower than 1, with Ti and Ta displaying a strong tendency to segregate into the liquid phase [29]. In contrast, solutes Co, W, and some RMs have a partition coefficient greater than 1 [29]. Co is typically only slightly more concentrated in the dendritic cores while W and certain RMs strongly partition into the γ solid [29]. This segregation behaviour leaves the residual liquid rich in Ti, Ta, and Al and deplete in W, Co, which is consistent with the presented SEM-

EDS results. The SEM-EDS results in Figure 4-36 and Figure 4-37 demonstrate that the other RMs have a strong segregation preference for the liquid phase, suggesting that they have a segregation coefficient less than one.

The partition coefficients of these solutes have been shown to vary during solidification [29]. As the S/L interface proceeds during non-equilibrium solidification, the relative volume fractions of liquid and solid change while local equilibrium is maintained at the interface. Solute elements demonstrate different segregation characteristics over the solidification path, with W, RMs, Al, Ta, and Ti all showing large changes in their partition coefficient [29]. W exhibited a large increase in partition coefficient, indicating that as solidification progresses the tendency for W to partition into the γ solid increases substantially.

γ/γ' eutectic pools developed in the current MIM NiSA alloy after extended time at temperature. SEM-EDS analysis performed on the γ/γ' eutectic regions showed that the liquid phase was rich in Al, Ti, Ta, and RMs and depleted in W, confirming that W partitions into the solid while Al, Ti, Ta, and RMs partition into the liquid phase. Co, Cr, and another RM all exhibited minimal segregation over the SLPS time. The magnitude of segregation was found to scale with the SLPS temperature as the liquid phase becomes more stable than the solid during continued heating. The increase in liquid fraction at an isothermal temperature is driven by the elemental segregation and lever rule as described in Figure 4-38. Ta and another RM are melting point depressants in Ni whereas W raises the melting point of Ni [1]. The strong segregation of Ta and this RM into the liquid is therefore likely to decrease the melting temperature of the liquid while W segregation into the solid is likely to increase the melting temperature of the solid. This solute segregation enables the relative liquid and solid phase fractions to change based on their shifting compositions and melting temperatures.

Further evidence of the γ/γ’ eutectic phase can be found by revisiting the DSC traces in Figure 4-19. Upon cooling from the 1345°C temperature after 60mins and 120mins the tail of the solidification event contains a small shoulder. This event in the DSC trace occurs just below 1300°C and becomes more evident increasing hold times. It is believed that this shoulder is a γ/γ’ eutectic solidification peak which overlaps the primary gamma solidification event. The magnitude of this secondary solidification event increases with longer hold times and higher temperatures which coincides with the microstructural evolution of the γ/γ’ eutectic pools.

In SLPS, the NiSA alloy is partially melted and then held under isothermal conditions for a given sintering time. During this time, the solid and liquid coexist and must immediately establish an equilibrium at the S/L interface which is governed by the solid and liquid compositions in the pseudo-binary phase diagram. The evolution of a completed, new equilibrium is governed by the composition of the alloy, the SLPS temperature, and the diffusion kinetics of the material. A schematic of the liquid phase distribution around solid grains and the corresponding compositional profile of a solute with $k<1$ are given in Figure 4-39 and Figure 4-40. Figure 4-40 depicts the compositional profiles across the diffusion couple as time progresses. Reaching T_{SLPS} establishes the equilibrium X_L and X_S compositions at the S/L interface. Rapid diffusion in the liquid establishes a uniform equilibrium X_L value within this phase. However, due to limited solid-state diffusion, the core of the solid grain remains at the original solid state homogenized composition of

X_{NiSA}. This establishes the compositional gradient within the solid grain as shown by t_1 in Figure 4-38.

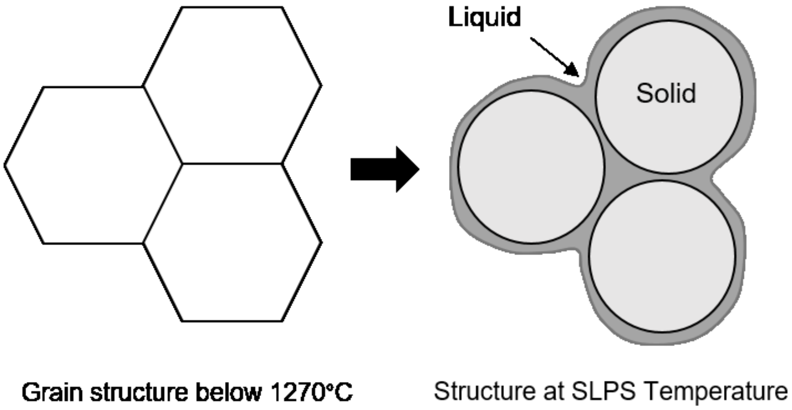

Figure 4-39. Schematic of the solid NiSA microstructure being heated above the solidus temperature and into the semi-solid region.

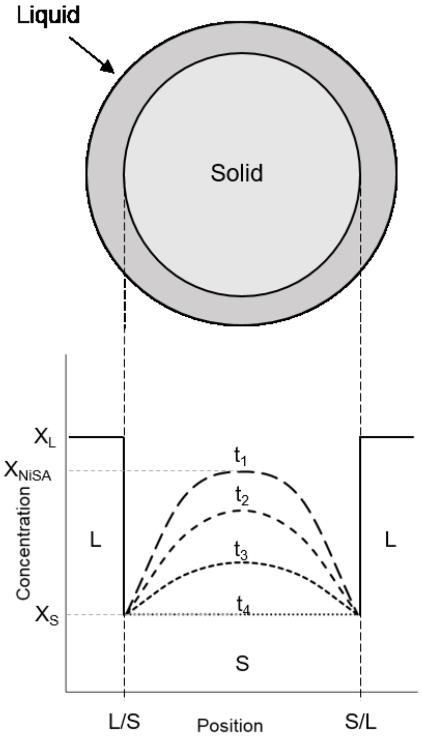

Figure 4-40. Schematic of the liquid phase distributed around a solid particle and the theoretical compositional profile of the solid particle over time.

Over time at T_{SLPS}, the compositional gradient in the solid grain must reduce until it reaches a uniform equilibrium composition of X_S (see Figure 4-40). This involves a solute mass balance of:

$$X_{NiSA} = f_L X_L + f_S X_S^* \qquad \textbf{(2)}$$

where X_{NiSA} and X_L have their previous meaning, f_L and f_S are the liquid and solid fractions respectively and X_S^* is the total solute content contained within the solid grain. Since X_{NiSA} and X_L are constant, as the X_s* value reduces to X_s, the fraction of solid must decrease and the liquid fraction increase.

The SLPS experimental results demonstrate an increasing liquid phase fraction as the alloy reaches equilibrium. An initial liquid fraction is formed at a given SLPS temperature according to the melting behaviour of the MIM NiSA alloy. Based on the results in Figure 4-21, the liquid phase grows rapidly over the first 15mins of holding while the liquid growth rate decreases significantly after the first 15 mins of hold time. Diffusion in the liquid is much faster than in the solid, therefore diffusion of solute elements in the solid likely governs the rate of solute segregation [11,19]. The diffusion rate governs the rate of compositional change in the solid and liquid, which in turn controls the liquid fraction over the hold time. The similarity between the liquid fraction growth and an Arrhenius type relationship offers further indication that the solid-state diffusion rate controls the liquid fraction.

Additionally, as the solid and liquid phases progress toward their equilibrium compositions X_S and X_L, the compositional gradients between them are diminished. Since the compositional gradient provides the driving force for diffusion [19], the rate of elemental segregation will decrease as the compositional gradient is eliminated, slowing the change toward stable equilibrium. The qualitative response of the liquid fraction over SLPS hold time agrees with the diminishing driving force for further compositional change, which explains the slow stabilization of the liquid fraction after 15mins of SLPS time.

4.2.3.3 Short Time SLPS

The liquid fraction and grain growth behaviour presented in Figure 4-21 and Figure 4-22 follow a general power law trend. However, there is insufficient data in those results to conclude that there is an exponential increase in liquid fraction and grain size between 0 and 15mins of hold time. In order to confirm the suspected trend, short time SLPS tests at 2, 5 and 10 minute hold times were completed in the DSC at 1345°C. The resulting data points were added to the previous results and the complete data sets are presented in Figure 4-41 and Figure 4-42. The short time tests determined that the liquid fraction and grain size remain relatively constant for the first 10 minutes of SLPS. No growth in liquid content or grain size was measured during these short time hold experiments. After 15 minutes of hold time, the liquid fraction and grain size have increased substantially. The rapid change in liquid fraction and grain size between 10 and 15 mins indicates that this 5 minute period is very dynamic, which explains the increased scatter in the liquid fraction data for the 15min hold tests (refer to Figure 4-24). After 10mins of hold time, the liquid fraction and grain size follow a similar to the trend to the one originally observed, but offset by the 10min hold time.

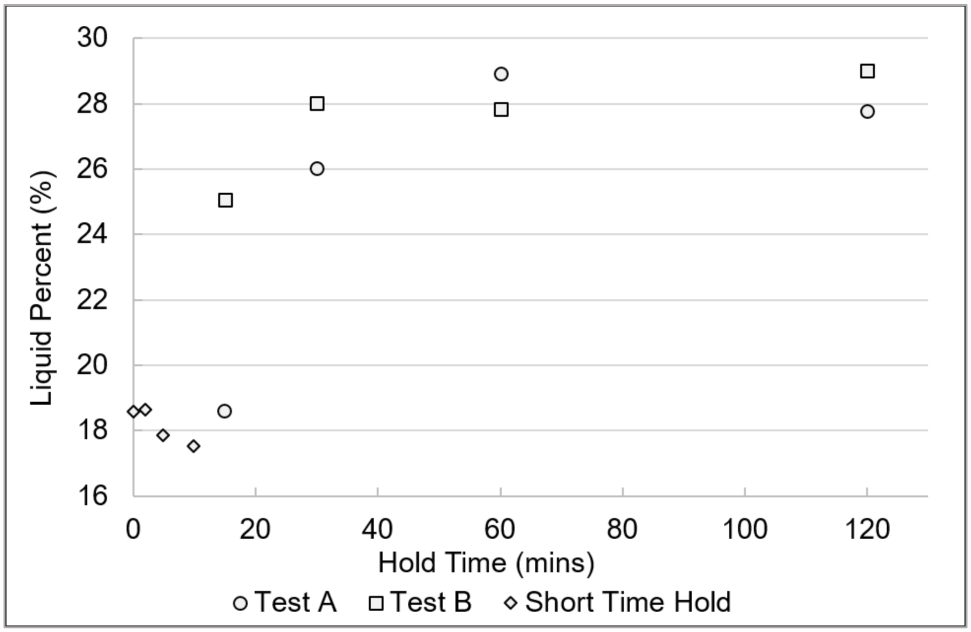

Figure 4-41. **Liquid percentage during hold time at 1345°C including short time SLPS results.**

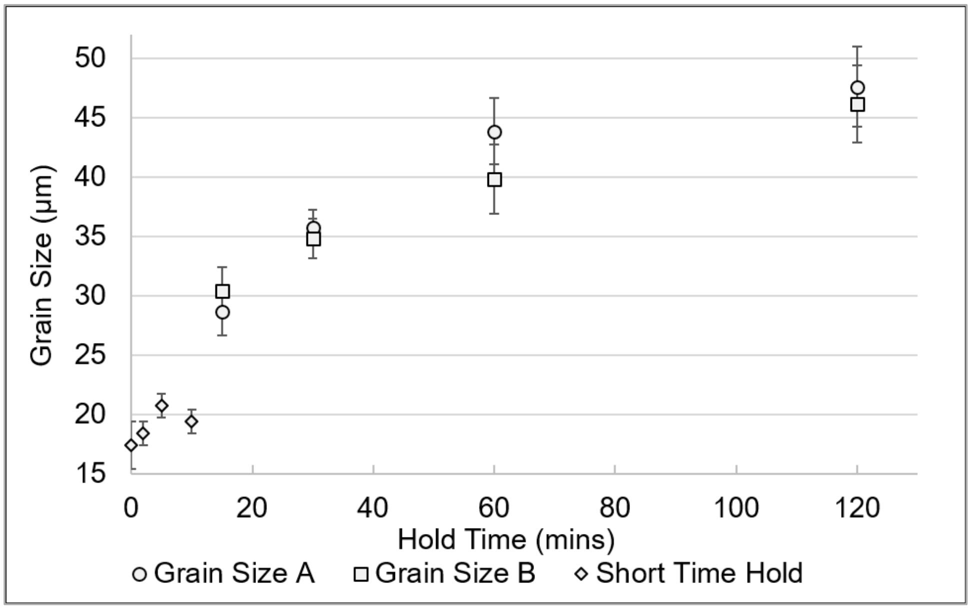

Figure 4-42. **Grain size during hold time at 1345°C including short time SLPS results.**

The sintered density was also measured in both the repeat 1345°C tests and the 2, 5, and 10min hold time tests and the results are plotted in Figure 4-43. The sintered density during the first 10mins of hold time is relatively constant, maintaining about 98.5%. However, the original drop in density after the 15min hold time observed in Figure 4-23 was repeatable, with the sintered density suddenly dropping from 98.5% to 96-97%. The transient behaviour of the sintered density after 10mins at the peak SLPS temperature is consistent with the behaviour observed in the liquid fraction and grain size. Following the density decrease, the material recovers to its original sintered density after 1-2hrs of hold time. The generalized behaviour of the sintered density is presented in Figure 4-44 where the incubation, transitional, and recovery stages of the density are indicated.

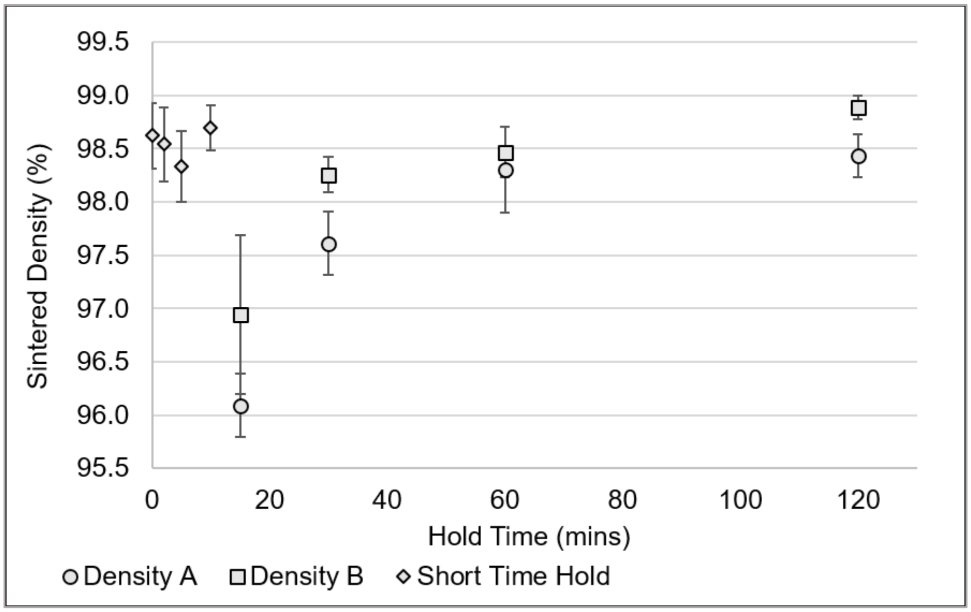

Figure 4-43. Sintered density of SLPS samples sintered at 1345°C for different hold times.

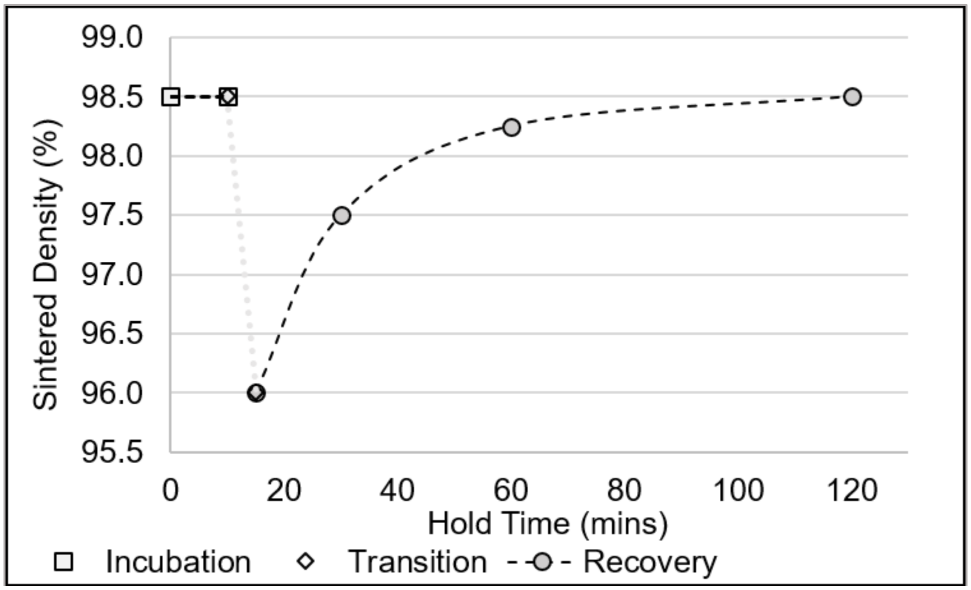

Figure 4-44. Observed sintered density behaviour during SLPS hold time at 1345°C showing the incubation, transition, and recover stages.

The grain growth in the MIM NiSA can be observed by comparing the SLPS sample cross sections with increasing hold time in Figure 4-45. This comparison demonstrates the significant grain size increase after the 10min hold time and the absence of any significant grain growth prior to 10mins.

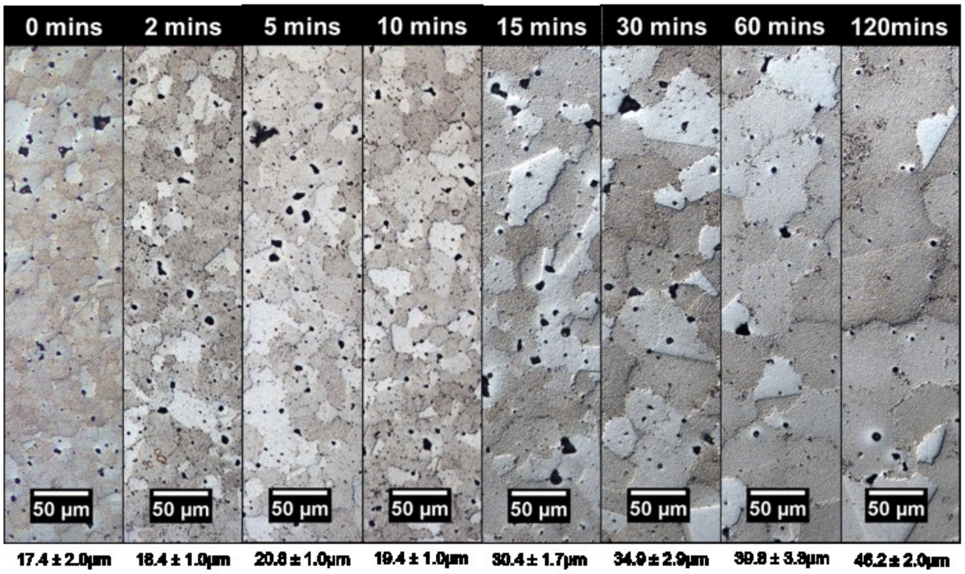

Figure 4-45. Microstructural evaluation of grain growth over time at 1345°C.

The grain sizes below 10mins of holding are the same as those measured after solid state sintering at 1310°C, suggesting that the grain size is still restricted in the initial stages of supersolidus sintering. The initial liquid fraction formed upon reaching 1345°C is also constant during the first 10mins of hold time, indicating that the solid and liquid phases are initially in equilibrium. It is only after an incubation period greater than 10mins and less than 15mins at 1345°C that the liquid fraction and grain size start to increase. Therefore, there must be a microstructural change that occurs in this time period which influences the equilibrium between the solid and liquid phases and enables grain growth.

SEM micrographs of the short hold time SLPS samples are presented in Figure 4-46 where the evolution of the grain boundaries during the SLPS process can be observed. All samples held at 1345°C for less than 10mins contain discrete carbide particles lining the grain boundaries. EDS analysis indicated that the majority of these grain boundary phases were rich in both tungsten and chromium. The morphology and composition of these carbides is consistent with the $M_{23}C_6$ carbide which commonly precipitates in the grain boundaries of the Ni superalloys [2]. Blocky MC carbide particles are also distributed along the grain boundaries and are Ta rich mixed carbides containing another RM.

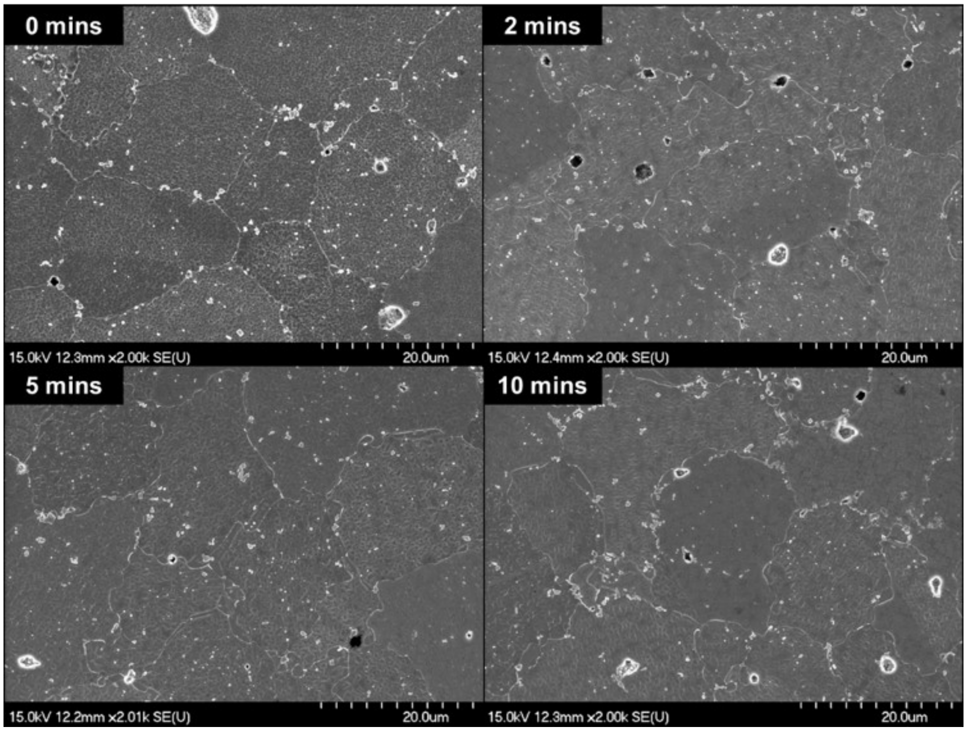

Figure 4-46. SEM micrographs of the short hold SLPS experiments at 1345°C held for 0, 2, 5, and 10mins.

The grain boundaries in Figure 4-46 appear to be lined with a thin, continuous film that appears bright white. The waterless Kalling's reagent preferentially dissolves the γ' precipitates and has been observed to leave a protruding ridge in the γ - γ grain boundaries. These grain boundary ridges have an higher secondary electron emission, making the grain boundaries appear bright [35]. EDS analysis of these thin, bright grain boundary regions consistently returned the base NiSA composition while thicker areas, which appear as discontinuous globules, indicated the W and Cr rich $M_{23}C_6$ composition [2].

Initially, after 0mins of hold time at 1345°C, the grain boundaries appear relatively straight and contain a high number of blocky MC carbides. As hold time increases during the first 10mins of SLPS, the grain boundaries (bright white) become wavy while the grain boundary carbides appear relatively unaffected. This subtle change during the first 10mins of hold time demonstrates that the grain boundary is mobile in areas where there are no MC carbides present, but is restricted or pinned in locations of the grain boundary carbides. Coarse γ' precipitates are also present in the regions adjacent to the curved or mobile sections of the grain boundary, suggesting that there was a higher degree of liquid in these regions [2], aiding grain boundary movement.

The $M_{23}C_6$ carbide is generally only stable to intermediate temperatures in the range of 800-1050°C and likely re-precipitates during cooling [2,31,32,36–42]. The $M_{23}C_6$ carbide would also be dissolved or transformed into more MC carbide during heating prior to reaching SLPS temperatures [2,31,32,36–42]. In addition, the γ' precipitates are completely dissolved by 1232°C [32]. This leaves MC carbide as the only stable precipitate phase remaining in the grain boundary at supersolidus temperatures (aside from any stable oxide and nitride particles present). Therefore, MC carbides are the only prominent phase remaining at SLPS temperatures to impede grain boundary motion and restrict grain growth. Knowing that MC carbides can generally be dissolved above the solidus temperature [2,3,39,43], it is expected that the incubation period observed in the short time SLPS tests is a result of MC carbides restricting grain boundary migration in the initial stages of SLPS. Over time at temperature the MC carbides are dissolved into the liquid phase, enriching the liquid phase with solutes such as C, W, Ta, and RM's while enacting rapid grain growth. The liquid fraction increases due to the dissolution of the MC carbides and subsequent solute segregation caused by the enrichment of the liquid by MC carbide solutes. The grain size increases due to the removal of the MC carbides, which acted as obstacles to grain boundary migration. Once the alloy is constituted of L and γ, grain growth and solute segregation proceed according to the originally observed trends. A complete discussion of the grain boundary evolution in the context of grain growth activation is presented in Section 4.5.

It should be noted that when the $M_{23}C_6$ carbide dissolves, it releases Cr, C, and W into the grain boundary. WC may form readily or other, more thermodynamically stable MC carbides may form in the grain boundary [36,43]. Recall that Ta-RM mixed carbides are commonly observed in the grain boundaries during the 10min incubation period. Once supersolidus temperatures are reached, these higher temperature MC carbides dissolve into the melt, re-releasing Ta, W, and RM solutes into the grain boundary. The presence of W in the grain boundary and MC carbides during the initial stages of SLPS is important because W strongly segregates into the solid phase during SLPS and can act to increase the melting point of NiSAs [1,29]. In contrast, Ta and other RMs strongly segregate to the liquid phase and can depress the melting point [1,29]. Given that solute segregation doesn’t occur until after the 10min incubation period (the solid and liquid appear to be in equilibrium for the first 10mins of hold time), it is expected that the release of solutes into the liquid phase from carbide dissolution drives the liquid fraction increase as the solid and liquid fractions change to maintain equilibrium. While this occurs, the additional liquid content aids microstructural coarsening and grain growth.

The dissolution of MC carbides in the liquid phase would cause the liquid to become rich in C and other solutes such as W, Cr, Ta, and RMs. W segregates into the solid phase during SLPS, decreasing its concentration in the grain boundary. After longer hold times at 1345°C, clusters of blocky Ta-RM mixed MC carbides are observed in grain boundaries and γ/γ' eutectic pools. The Ta and RM which segregate into the liquid phase during SLPS essentially act as sinks for C during cooling, precipitating as numerous MC carbides upon cooling. The decreased concentration of W in the grain boundary region would then limit the extent of $M_{23}C_6$ carbide precipitation, which is consistent with the microstructural observations at extended hold times.

Continuous MC carbide films can also form in the grain boundaries of Ni-superalloys during heating provided that there is a supersaturation of carbon in the grain boundary region [2,3]. Carbon is retained in solution at the grain boundaries if the alloy is rapidly cooled from a high temperature where carbides were dissolved (such as a full melt) [2,3]. The NiSA powder is rapidly cooled during inert gas atomization and subsequent sintering acts as a high temperature soak, therefore satisfying the conditions for MC carbide film formation in the grain boundaries. The relatively high level of W compared to Ti in the NiSA alloy could lead to prevalent WC formation as opposed to TiC.

Time above the solidus temperature during SLPS causes a progressive degradation of the MC carbides, eventually enacting grain growth. The similarity between the grain growth and liquid percentage curves (after the initial incubation period) implies that the grain growth is at least partially dependent on the liquid fraction formed during SLPS. As the SLPS time is increased, the liquid fraction increases until it reaches a new stable equilibrium with the solid. The grain size increases along with the liquid fraction increase, but also stagnates along with the liquid fraction. Increasing the SLPS temperature accelerates the liquid fraction and grain size increase, but the same stabilization is observed in both parameters. Therefore, it is expected that as the material reaches a new equilibrium liquid fraction over the hold time, the grain growth is controlled by the liquid fraction formed. The different SLPS temperatures tested (1335, 1340, 1345, and 1350°C) are also likely to have different incubation periods because the dissolution of MC carbides is both time and temperature dependent. It is expected that higher temperatures, having higher initial liquid fractions, would dissolve MC carbides faster while lower temperatures would require longer times to dissolve the MC carbides. The incipient melting point then represents the minimum temperature required to start MC carbide dissolution, however, the solvus temperature of these carbides is likely much higher.

It is important to highlight the fact that the majority of carbides in the MIM NiSA alloy are located along grain boundaries. This effectively concentrates any incipient melting between the matrix and carbides to the grain boundaries, which may aid in the disruption and dissolution of grain boundary carbides. Incipient melting concentrated in the grain boundaries may also lead to faster growth of the liquid film thickness in the boundaries. A higher liquid film thickness can aid grain sliding, growth, and re-arrangement, but also reduces the rigidity of the sample, causing eventual part slumping if uncontrolled [17].

4.2.3.4 Microstructure

Microstructural analysis of the solid state sintered MIM NiSA reveals a fine grain size in the range of 20-30µm. In contrast, cast nickel superalloys typically have much coarser grain sizes on the scale of millimeters and exhibit superior creep rupture properties to PM superalloys [3]. Previous research has found that additional time at temperature during solid state sintering has no significant influence on the grain size of the MIM NiSA material. Further increasing the sintering temperature to promote grain growth requires partially melting the NiSA alloy in an SLPS process, which can lead to the formation of γ/γ' eutectic phases in the microstructure.

The presence of the γ/γ' eutectic phase in the SLPS MIM NiSA microstructure represents a high degree of solute segregation and inhomogeneity in the material. Segregated regions of γ/γ' eutectic are potential low-melting point regions in the alloy and may reduce high temperature properties despite acting to increase the toughness of the grain boundaries [1,3,32,33]. Coarse γ' plates also form as part of the γ/γ' eutectic phase, locally reducing the volume fraction of precipitates and increasing the inter particle spacing [19,32,33]. Localized reduction in the inter particle spacing facilitates more dislocation bypassing, decreasing strength [7,19,33]. In addition, clusters of coarse carbides, primarily mixed RM-Ta carbides, are observed in the γ/γ' eutectic regions while the grain boundaries of the bulk SLPS material remain relatively carbide-free. Not only do these carbides act as possible crack initiation sites at elevated temperatures, but it is expected that there would be an inherent reduction in the grain boundary pinning effect derived from discrete grain boundary carbide particles, which are critical to the creep strength of alloys such as the NiSA [1,3,33]. Furthermore, limited $M_{23}C_6$ carbide precipitation as a result of W segregation into the solid grains would be detrimental to the creep properties of the alloy because discrete $M_{23}C_6$ carbides in the grain boundaries are critical in resisting grain boundary sliding [2,37,40].

One benefit of certain RMs is that they can segregate into the γ' phase, coarsening grain boundary γ' particles which helps to resist grain boundary sliding and improves the grain boundary ductility [3]. Presence of these RMs in the grain boundary are also thought to aid grain boundary ductility in general [2]. The concentration of RMs in localized γ/γ' eutectics and carbides depletes RMs in grain boundary regions, limiting their ability to promote coarse γ' and grain boundary ductility to provide resistance to grain boundary sliding.

Moreover, the formation of carbides in the γ/γ' eutectic regions locally depletes the concentration of solute elements which would otherwise contribute to solid solution strengthening [1]. The net effect of the γ/γ' eutectic phase is therefore thought to be detrimental to the overall properties of the MIM NiSA material.

Solution and aging heat treatments of cast NiSA alloys are aimed at homogenizing the segregated γ/γ' eutectic regions, precipitating a high volume fraction of fine γ' particles, and refining carbide structures. These heat treatments are commonly applied in industry and have been extensively studied [1,2,31–34], making them practical methods to refine the MIM SLPS microstructure. SLPS could be utilized solely as a method of consolidation and grain growth in MIM materials before applying heat treatment for further microstructural refinement. Though, it should be noted that time at temperature during SLPS segregates the solute elements. A shorter SLPS time will reduce the amount of elemental segregation, reducing the required homogenization time during heat treatment. Therefore there is a trade-off between the grain size achieved by longer SLPS times and the heat treatment time required to re-homogenize and refine the post-SLPS microstructure. Casting experiments on another low carbon (LC) NiSA alloy have demonstrated that the grain size can be controlled using the pour temperature, with lower pour temperatures leading to grain sizes as a fine as 80-90μm [5]. Further investigation of fine grained LC NiSA castings revealed that the creep rupture life was reduced due to the activation of dislocation climb at high temperatures, enacting grain boundary slip. In the same study, coarse grained LC NiSA castings exhibited superior creep strength at high temperatures and stresses due to the lower grain boundary area available for slip [5]. Therefore, if the grain size of the MIM NiSA in this study can be increased to the scale of 1-2mm, the reduction in grain boundary area should reduce the amount of grain boundary sliding, improving creep rupture life [5].

Although the coarse grain LC NiSA exhibits less grain boundary sliding, the fine grained LC NiSA alloy out-performed the coarse grained alloy under lower temperatures and stresses where dislocation climb was not active [5]. The fine grain LC NiSA exhibited better creep rupture properties at lower temperatures derived from a higher volume fraction of γ' and higher number of grain boundaries present to impede dislocation glide [5]. Based on the similarity between the grain size and shape of SLPS MIM NiSA and the fine grain LC NiSA casting studied by Huang et al. [5], one might expect similar creep rupture properties could be achieved by the MIM SLPS material.

4.2.3.5 SLPS Process

SLPS techniques have previously been evaluated for a wide range of materials [11,18,24,25,28,44]. In these investigations, it is generally accepted that the liquid fraction formed during SLPS is constant over the isothermal hold time. This leads to a predictable liquid fraction with temperature and allows for better control over densification, shape retention, and microstructural coarsening. Levasseur and Brochu studied the SLPS process on IN718 alloy and successfully modeled the process limits over time at temperature [18]. Their findings demonstrate that the onset of deformation changes as the microstructure coarsens due to changing rigidity of the material. In SLPS of the MIM NiSA in this study, which has compositional similarities to IN718, the liquid fraction was found to be transient with time at temperature after the initial incubation period. This means that the onset of deformation is a function of both liquid fraction and microstructural coarsening in the NiSA alloy. If the behaviour of the liquid phase under isothermal SLPS conditions is not understood, it is possible that the alloy will be exposed to higher liquid volumes than anticipated, leading γ/γ' eutectic formation and eventual shape loss.

It is possible that other alloy systems, such as IN718, do not exhibit the same transient liquid phase behaviour observed in the MIM NiSA. IN718 does not contain the same refractory metals which are MC carbide formers and strongly segregate in other Ni-superalloys [2,29,31], indicating that these solutes may heavily influence the liquid fraction in SLPS. DSC methods, similar to those applied in this study, could be carried out to evaluate SLPS of other alloys to provide a better understanding of the liquid fraction evolution with time and temperature.

4.2.3.6 Shape Retention

The macro-scale images of the SLPS samples provided a reliable characterization of sample deformation in MIM NiSA. The 1335°C and 1340°C series of experiments did not show significant slumping or edge rounding while the 1350°C series of SLPS tests exhibited significant slumping and edge deformation at all hold times. The 1345°C series samples initially maintained their shape with little slumping, though the edge rounding after 60mins and 120mins was significant. Height measurements were used as a quantitative assessment of sample slumping. Figure 4-27, which plots the average sample height for each SLPS temperature over the hold time, demonstrates the potential to SLPS the MIM NiSA alloy without slumping below 1350°C. At 1350°C, the material slumps under the force of gravity almost instantly. 1350°C appears to be too high of a temperature for the SLPS of NiSA superalloy because the shaping advantages of the MIM process are lost upon reaching this temperature. Though, the critical liquid fraction for deformation can be approximated from the SLPS test results with reference to Figure 4-21 and Figure 4-27. The initial liquid percentage upon reaching 1350°C was 20% on average and 33% after a 15mins hold time. The 1345°C test, which exhibited little slumping, had a liquid percentage of 28% after 120mins of holding. Therefore, the onset of slumping lies between the liquid percentages of 28 and 33%. It is also important to differentiate the measured height and slumping from part deformation in general. Edge rounding and loss of part shape occurs in the 1345°C samples after 60 and 120mins holds, both of which approach the 28-33% liquid fraction over time at SLPS temperature. At 1340°C/120mins, edge rounding is also observed, despite the liquid percentage only approaching 20%. Therefore, localized part deformation begins earlier than the total loss of rigidity, which causes slumping and net sample height change.

Additionally, there is an overlap in liquid fraction formation between different SLPS temperatures and hold times. For instance, performing SLPS at 1340°C for 60mins achieves a similar liquid fraction to SLPS at 1345°C for 15mins and a higher liquid fraction than 1345°C for 0mins. This complicates SLPS process design since the liquid fraction at low temperatures with long hold times can exceed the liquid fraction at high temperatures with short hold times. Microstructural coarsening also influences the rigidity of the sample and should be considered along with the liquid fraction. Due to the transient nature of the liquid fraction in this MIM NiSA, complete shape retention cannot be expected unless both the influence of SLPS temperature and hold time are properly considered.

4.2.4 Conclusions

The behaviour of MIM NiSA superalloy during supersolidus liquid phase sintering (SLPS) has been evaluated. The grain size was successfully increased from the 20-30μm to 50-60μm range using SLPS and the grain growth behaviour with time and temperature was determined. The liquid fraction during SLPS was found to be transient with time at an isothermal temperature and its growth profile with time and temperature was identified. The initial time at SLPS temperature causes no grain growth or increase in liquid fraction. At 1345°C, a 10min incubation period was required to dissolve grain boundary MC carbides and enact liquid fraction growth and grain growth. The transient nature of the liquid fraction was primarily caused by the segregation of refractory elements including Ta and W. W was observed to partition into the solid phase while Ta and other RMs were rejected into the liquid during the SLPS process. Extended times at a given SLPS temperature leads to the formation of the γ/γ' eutectic phase, which may have deleterious effects on the final properties. Clusters of course carbide particles also formed near the γ/γ' eutectic regions leaving the grain boundaries with few discrete carbide particles.

The dissolution of the grain boundary carbides coincided with the liquid fraction growth, which was found to be strongly related to the grain growth behaviour during SLPS. It is apparent that the observed grain growth was activated in the NiSA by dissolution of the grain boundary carbides, while time at temperature is still required for grain growth to progress.

Longer SLPS hold times also gave rise to significant microstructural coarsening and poor shape retention. Slumping of the material was monitored throughout the experiments and was only found to occur at an SLPS temperature of 1350°C or at liquid fractions above 28-

30%. Reasonable shape retention was achieved without slumping at lower SLPS liquid fractions and hold times.

A comparative DSC method has been successfully developed and applied to evaluate SLPS. The behaviour of the liquid fraction with time and temperature was determined using this DSC technique and validated using subsequent microstructural analysis. The results demonstrate the importance of time and temperature to the microstructural evolution and shape retention in SLPS processes. DSC has been proven as an effective tool for predicting the SLPS behaviour based on liquid fraction and can provide critical information for SLPS process design.

4.3 Liquid Phase Sintering of a Metal Injection Molded Nickel-Based Superalloy with additions of BNi-2 alloy powder using Differential Scanning Calorimetry

4.3.1 Introduction

Precipitation hardened nickel-based superalloys are commonly used in high temperature areas of aero engines [2,5]. These alloys derive the majority of their high temperature strength from a combination of finely dispersed gamma prime precipitates, γ', and discrete grain boundary carbide particles. The presence of the discrete grain boundary carbides reduces grain sliding by pinning the grain boundaries, increasing the creep resistance. However, grain boundary pinning is known to inhibit grain growth in Ni superalloys, especially in those Ni superalloys containing high amounts of refractory elements such as W and Ta [3,11,30].

Liquid phase sintering (LPS) can achieve rapid densification of powder metallurgy (PM) components [11]. In LPS, a lower melting point alloy powder is added to the primary alloy powder to form a liquid phase during sintering. LPS is then performed at a temperature above the melting point of the additive, but below the solidus of the primary alloy. The liquid phase migrates through the porous structure under capillary forces and acts as a rapid diffusion and mass transport pathway. The presence of a liquid phase also enables grain re-arrangement and the net effect is rapid densification of the powder structure. The volume fraction of the low melting point additive must be properly selected to form a liquid fraction which will sinter the material to full density without shape loss [11,17,18].

LPS is typically applied as a method to achieve high densities in difficult to sinter materials, but it can also lead to grain growth with prolonged time at temperature [11]. While it is known that grain growth occurs during LPS, grain growth is generally not considered as desired outcome in the literature. In addition, at the time of writing there have been no published studies on the LPS of MIM nickel-base superalloys (NiSA) containing high amounts of refractory elements. The objective of this research was to study the LPS of these MIM NiSA materials as a method of increasing grain size and improving their high temperature properties.

4.3.1.1 Transient Liquid Phase Bonding Alloys for LPS

Transient liquid phase bonding or brazing (TLPB) is a common joining and repair technique applied to nickel-base superalloys in the aerospace industry [20,45–47]. In TLPB, a braze alloy material containing melting point depressants (MPDs) is positioned on or between the base material(s) being joined or repaired. The assembly is then heated to a brazing temperature where the braze alloy melts completely, ideally wetting and spreading throughout the joint. During heating and time at the brazing temperature, the MPDs diffuse into the base metal, causing the braze liquid to undergo diffusional solidification (DS) [46]. Boron and silicon are both potent MPDs commonly used in brazing materials to provide DS by rapidly diffusing into the base metal over time at temperature. The loss of MPDs into the base metal at a constant temperature causes isothermal solidification (IS), a more specific subset of diffusional solidification [20].

Complete IS of the braze material is desirable because a solid solution γ-Ni microstructure free from deleterious binary and ternary eutectic phases can be obtained [46,47]. Consequently, a TLPB joint which has experienced complete IS can exhibit mechanical properties equivalent to that of the base metal [47,48]. If IS is not completed during the brazing process, then athermal solidification of the remaining braze liquid can cause the formation of undesirable binary and ternary eutectic phases in what are termed athermally solidified zones (ASZs), negatively impacting the overall joint properties [20,22,48].

An alternative approach to liquid phase sintering a NiSA is to use an LPS additive with a composition similar to the NiSA itself, but containing MPDs. Comprehensive research has been completed on TLPB of Ni-superalloys with filler metals such as BNi-2 [20,22,45–47,49], making it a suitable alloy to study in an LPS application. The BNi-2 alloy (Ni-7Cr-4.5Si-3Fe-3B) has a significantly lower melting temperature than the NiSAs due to the presence of MPD elements Si and B. These MPDs are also fast diffusing elements which may impact the grain growth behaviour of MIM NiSAs.

The purpose of this research is to explore the LPS behaviour of a MIM NiSA using the BNi-2 alloy as a low melting point powder additive. The NiSA in this study was a NiSA containing Al, Co, Cr, Ta, Ti, W and minor additions of other refractory metals (RM), with the balance Ni. The influence of liquid fraction, time at temperature, and the LPS additive on the grain growth behaviour is evaluated and compared to both solid state and supersolidus sintering of the base MIM NiSA.

4.3.2 Experimental Methods

MIM NiSA LPS materials were created with BNi-2 powder loadings of 5 and 10wt%. These LPS samples were prepared via MIM by an industrial partner and sent to Dalhousie University for thermal analysis. Both powders were gas atomized and the BNi-2 alloy was purchased as a -325 mesh (-45μm) powder. The BNi-2 and NiSA powders had particle size distributions (PSDs) typical of those used in the PM industry. The d_{10} and d_{50} of both powders were similar, with BNi-2 having the larger particle size throughout the PSD. However the d_{90}s of the two powders deviated significantly, with the NiSA having a d_{90} of 22μm and the BNi-2 powder containing larger particles than the NiSA.

Differential scanning calorimetry (DSC) was used to characterize the sintering behavior of the BNi-2 modified samples. De-bound MIM NiSA LPS samples were heated in the DSC at 4.5°C/min to a peak temperature of 1290°C under an Ar + Zr getter atmosphere and were held for times of 0, 15, 30, 60, and 120mins before cooling to room temperature. Additional samples of the 5wt% and 10wt% BNi-2 loadings were heat treated at 1050°C for 30mins in the DSC post de-binding. This interrupted test was used to assess the extent of wetting and spreading of the BNi-2 liquid after the first heat above the solidus temperature of BNi-2 (968°C) [20].

4.3.3 Results

4.3.3.1 DSC of BNi-2 Modified NiSA in the Range of 900-1050°C

DSC heating traces for 5wt% BNi-2, 10wt% BNi-2, and 100% NiSA samples heated to 1050°C, after previously being de-bound at 850°C for 1 hour, are presented in Figure 4-47. The MIM NiSA heating trace has a shift in the baseline from 940-960°C which is associated with the start of γ' dissolution [32]. Both the 5wt% and 10wt% BNi-2 loadings exhibit the same shift in the baseline due to their high NiSA content. Having been thermally de-bound at a peak temperature less than 900°C, the heating traces shown in Figure 4-47 are the first heat above the solidus temperature of the BNi-2 alloy (968°C [20]) for these materials. No melting events are observed in DSC traces of the 5wt% and 10wt% BNi-2 samples in this temperature range despite heating through the melting range of the BNi-2 alloy. The absence of melting can be explained by two factors: The influence of heating rate on the DSC trace or diffusion of MPDs into the NiSA powder particles.

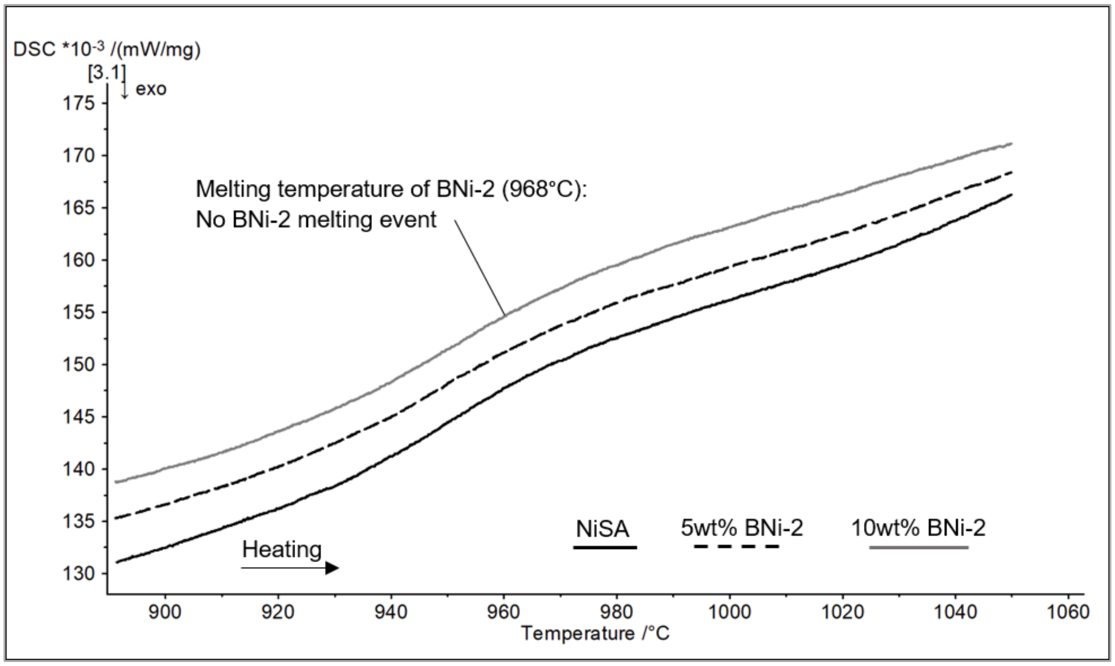

Figure 4-47. Heating traces of 5 and 10wt% BNi-2 modified NiSA and 100% NiSA through the melting range of the BNi-2 braze alloy.

The heating rate in the DSC tests presented in Figure 4-47 was 4.5Kpm. However, the apparent size of a thermal event peak on a DSC trace can be influenced by the heating rate (or scanning rate) used [21].

In general, faster heating rates lead to a larger response in the DSC trace because the energy evolved (or absorbed) occurs over a shorter period of time. In the case of a small thermal event, it may be possible that the peak may not be visually detected at slower heating rates.

To verify if the heating rate influenced the DSC trace for the BNi-2 modified NiSA materials, ad-mixed BNi-2 and NiSA powder samples with the 10wt% BNi-2 loading were heated in the DSC at 20Kpm and 4.5Kpm. The ad-mixed powder samples were not exposed to the de-bind cycle and therefore had no previous time at temperature for solid state diffusion to occur. DSC traces for the two different heating rates are presented in Figure 4-48. By comparing the 20 and 4.5Kpm heating rates it can be observed that a small melting peak is detected in the DSC trace at the heating rate of 20Kpm. Therefore, there is a melting event of the BNi-2 alloy upon first heating of the BNi-2 loaded materials above 968°C. However, the slower heating rate also had additional time at sufficient temperatures for solid state diffusion to occur. Loss of MPD elements into the NiSA powder due to solid state diffusion during heating could have reduced or prevented BNi-2 melting in this temperature range at the slower heating rate.

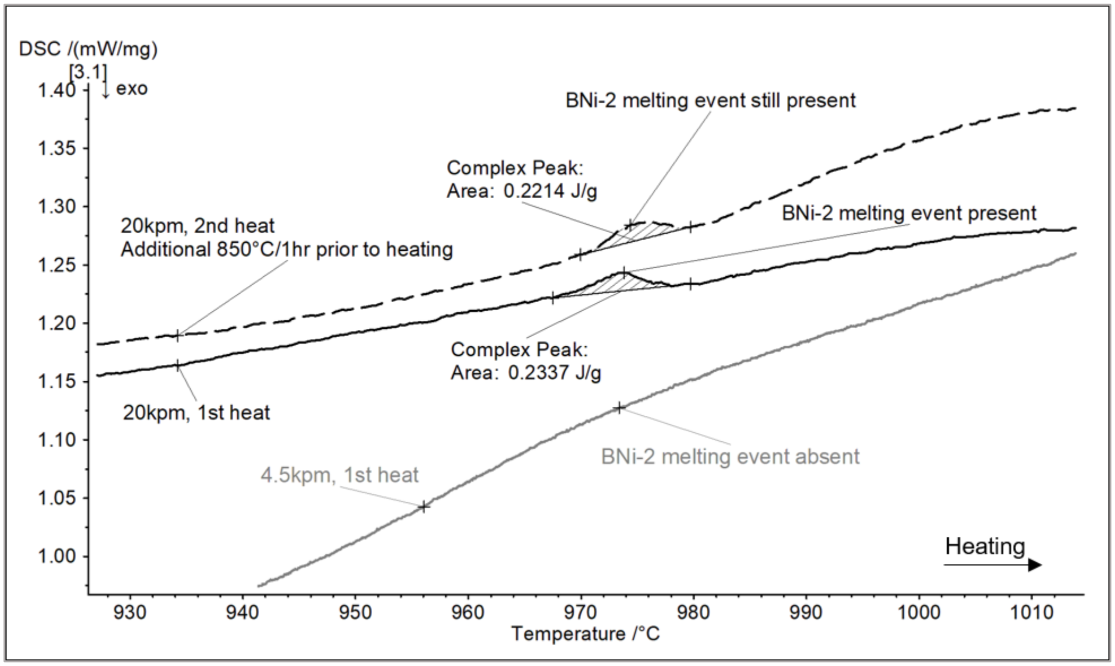

Figure 4-48. DSC heating traces of the 10wt% BNi-2 ad-mixed powder at a heating rate of 4.5Kpm (grey line), 20Kpm (solid black line), and 20Kpm with additional 850°C/1hr heat treatment (dashed black line).

A DSC test of the 10wt% BNi-2 powder mixture was also performed at a heating rate of 20Kpm with an additional heat treatment prior to heating past 968°C. This additional heat treatment was designed to simulate the thermal de-binding process and help determine if extra time for solid state diffusion impacts the BNi-2 melting peak. The DSC trace for this experiment is presented in Figure 4-48 (dashed line) where it can be directly compared to the 4.5Kpm and 20Kpm tests which had no thermal exposure prior to heating past 968°C. The melting event detected at a heating rate of 20Kpm is very similar to the test with additional time at temperature for solid state diffusion. The comparison in Figure 4-48 indicates that the absence of the BNi-2 melting event at the 4.5Kpm heating rate is an effect of heating rate alone. When the heating rate is increase to 20Kpm, the melting event for BNi-2 is detected upon first heating at 968°C. When additional time at temperature is provided for solid state diffusion of MPDs to occur, the BNi-2 melting peak is detected at the same temperature and has the same magnitude. Therefore, additional time at temperature below the solidus temperature of the BNi-2 alloy has no measureable impact on the extent of melting that occurs at 968°C up to the maximum tested rate of 20Kpm.

Diffusion of MPDs B and Si from the BNi-2 particles into the base metal would effectively increase the melting temperature of the braze particles by homogenizing them with the NiSA, which has a much higher solidus temperature of 1330°C. The absence of any melting event in the temperature range of 900-1050°C at a heating rate of 4.5Kpm provides strong evidence of this homogenization during heating. Furthermore, the enthalpy of the BNi-2 melting event that was detected at a faster rate of 20Kpm (0.2 to 0.3J/g) is far smaller than the heat of fusion for the BNi-2 alloy (214J/g) [22]. This large enthalpy difference is an indication that only a small fraction of the potential liquid forms upon heating the MIM material above 968°C. In a previous study, Murray et al. [20] observed that there is a large degree of inter-diffusion between mixed BNi-2 and Ni powder particles upon heating past 968°C. In their work, Murray et al. [20] found that the rapid solute uptake of B and Si into the Ni particles results in rapid diffusional solidification of the liquid phase, greatly reducing the liquid fraction formed for brazing. The rapid solute uptake described by

Murray et al is consistent with the phenomena observed in the BNi-2 modified NiSA where the liquid fraction formed is greatly reduced due to the simultaneous diffusional solidification of the BNi-2 melt.

4.3.3.2 DSC of BNi-2 Modified NiSA above 1200°C

A DSC scan to a higher temperature of 1335°C was performed with the 5wt% BNi-2 MIM material. The heating trace of this sample is compared to the same test for a 100% NiSA MIM sample in Figure 4-49. Both DSC traces are similar with the exception of a melting event between 1240°C-1290°C in the 5wt% BNi-2 loading, which is not associated with either of the pure BNi-2 or NiSA alloys. This discovery supports the theory that diffusion of MPDs into the base NiSA raises the melting temperature of the braze powder additive and that there is a re-melt event of the BNi-2 particles in this temperature range. DSC heating traces to 1290°C for both BNi-2 loadings are compared to the pure NiSA in Figure 4-50. Melting was observed in the 5wt% BNi-2 loading between 1240-1290°C. This event occurs between the solvus temperature (~1230°C) and onset of melting (~1290°C) of the NiSA. In contrast, the 10wt% BNi-2 loading exhibits melting at approximately 1200°C. This melting peak is interrupted by the exothermic event of crossing the NiSA's solvus temperature. The net result of these overlapping events is an initial endothermic peak at 1200°C followed by a plateau caused by the simultaneous exothermic event. Once the solvus temperature has been surpassed, melting continues with a peak at about 1260°C and an end at 1270°C.

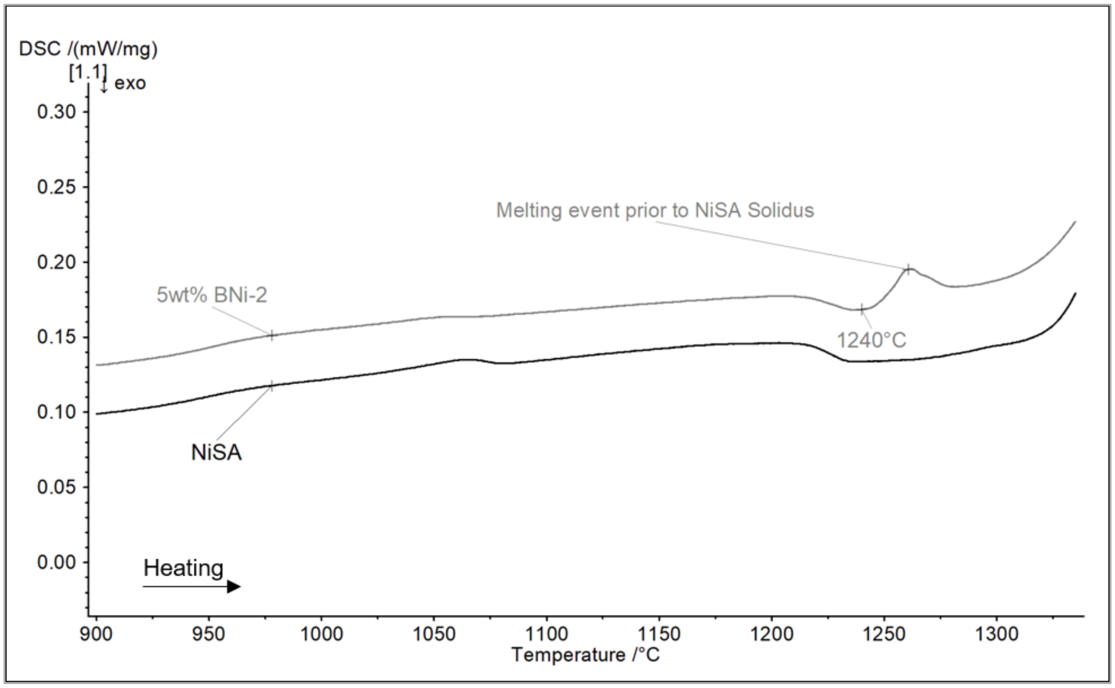

Figure 4-49. DSC heating traces of the 5wt% BNi-2 and 100% NiSA materials.

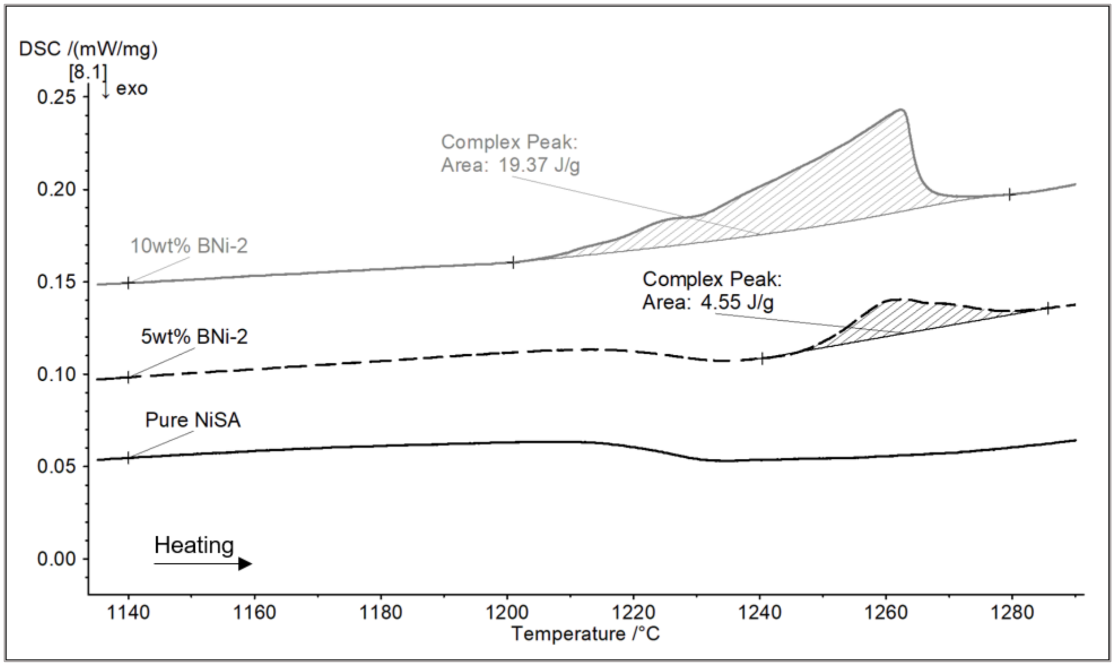

Figure 4-50. DSC traces of the BNi-2 modified NiSA's during heating.

Heating and cooling DSC traces of the 5wt% BNi-2 alloy are compared to the NiSA in Figure 4-51. The melting and solidification events in the 5wt% BNi-2 material are a clear result of the BNi-2 addition to the NiSA, though the detected events are not a result of either pure alloy by itself. Note that the solidification event in the 5wt% BNi-2 alloy occurs after the DSC baseline has stabilized, but before the re-precipitation of gamma prime in the NiSA.

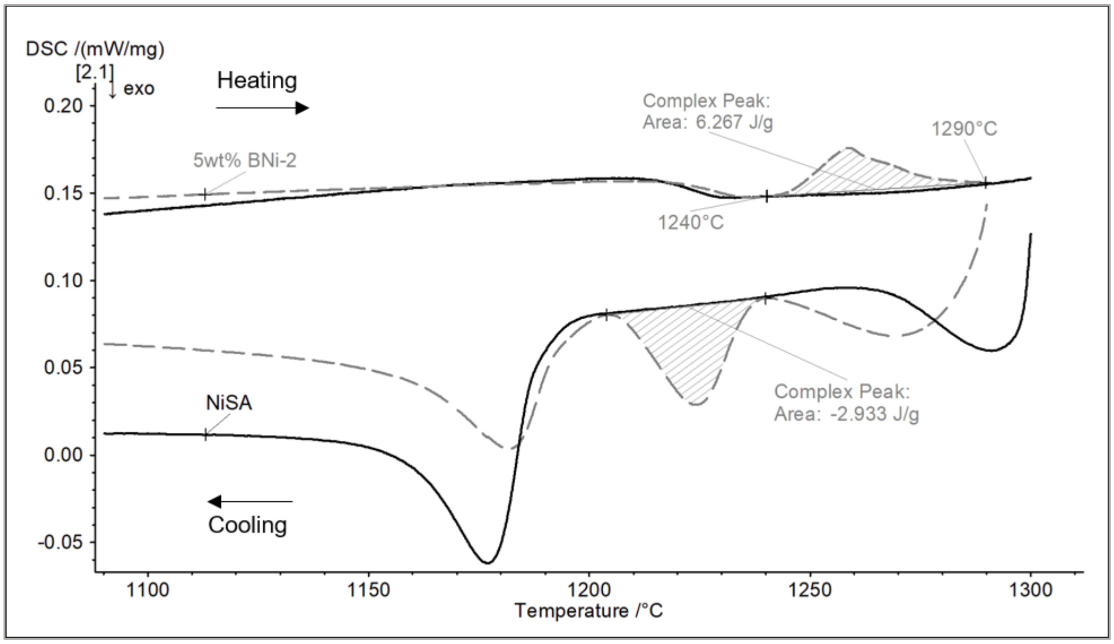

Figure 4-51. Heating and cooling traces of 5wt% BNi-2 NiSA overlaid with the 100% NiSA.

10wt% BNi-2 MIM samples were sintered in the DSC at 1290°C for hold times of 0, 15, 30, 60, and 120mins to evaluate the grain growth behaviour of the material with time at temperature. The heating and cooling DSC traces for these sintering tests are presented in Figure 4-52 and Figure 4-53, respectively. The melting event from 1200°C-1280°C was repeatable in enthalpy, temperature, and peak shape for all samples. The solidification events after different hold times were progressively different in shape and enthalpy, but occurred at the same temperature. The solidification peaks all have an initial exothermic peak starting at 1230°C. This exothermic response is interrupted by a second exothermic peak at 1200°C which is likely a result of gamma prime re-precipitation, since this is the temperature range that this precipitation event occurs in the 100% NiSA.

Finally, a third exothermic shoulder evolves in the solidification event as the hold time is increased. The enthalpy of solidification increases slightly over the isothermal hold time, however the measured solidification enthalpy values cannot be directly compared to the initial melt enthalpies upon heating because of the unknown influence of the overlapping gamma prime re-precipitation thermal event. Note that the solidification of the 10wt% BNi-2 loading is very different than the solidification of the 5wt% BNi-2 loading.

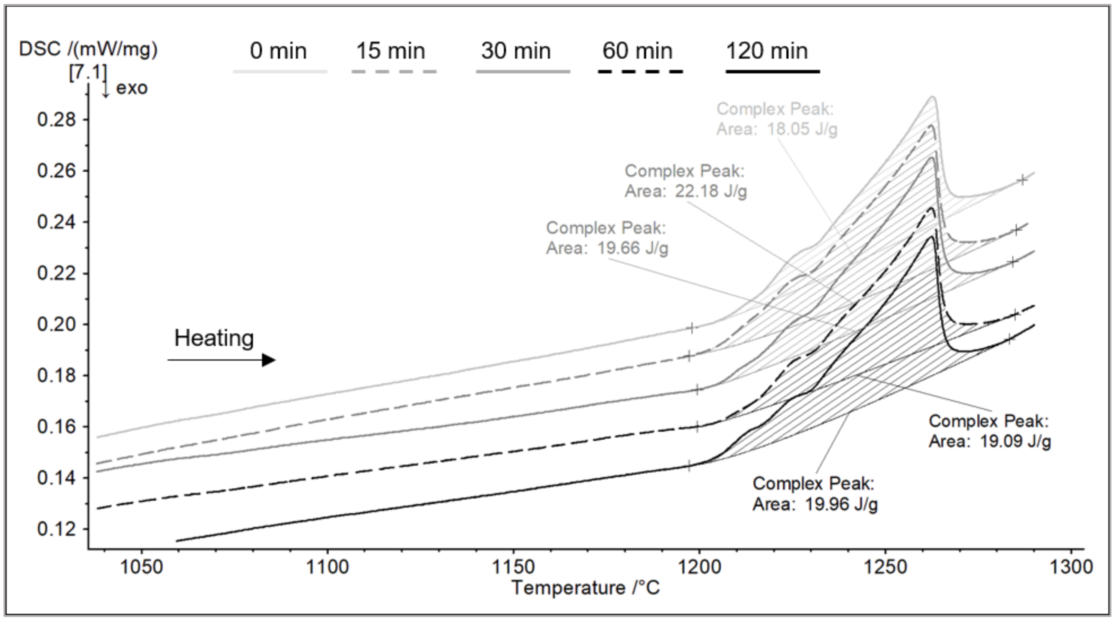

Figure 4-52. Heating traces of individual 10wt% BNi-2 MIM samples showing the melting event between 1200°C-1280°C.

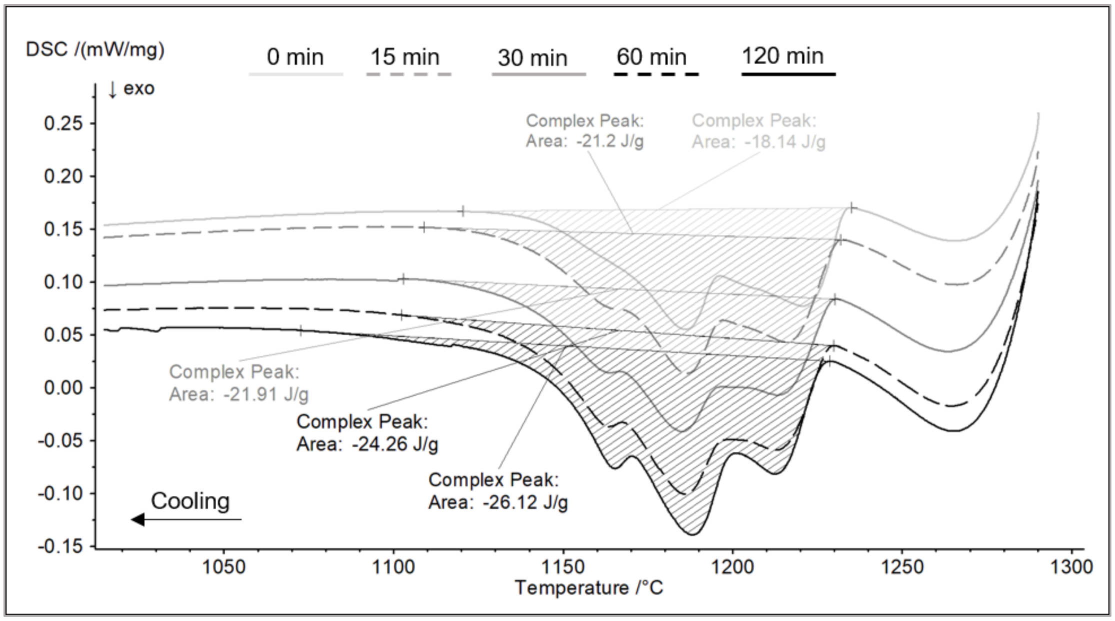

Figure 4-53. Cooling traces of individual 10wt% BNi-2 MIM samples held at 1290°C for 0, 15, 30, 60, and 120mins.

4.3.3.3 DSC of Ad-Mixed BNi-2 and NiSA Powders

The enthalpy of melting of the liquid phase formed in Figure 4-50 through Figure 4-53 must be an in-situ alloyed phase between BNi-2 and NiSA powder. Both the BNi-2 and NiSA powders were fully melted in the DSC to determine their melting enthalpies. The enthalpy of melting for the BNi-2 alloy and NiSA were found to be 214J/g and 150J/g, respectively. Given that there is a large difference between these enthalpies and that an in-situ alloy's enthalpy of fusion does not necessarily follow a rule of mixtures, ad-mixed BNi-2 and NiSA powders in BNi-2 loadings of 10, 20, 50, 80, 90, and 95wt% were created to determine the enthalpy of melting for these BNi-2 modified NiSAs. Each ad-mixed powder sample was fully melted and re-solidified to homogenize the alloy prior to measuring the melt enthalpy. By determining the enthalpy of melting for the 10wt% BNi-2 loading, the melt enthalpies measured during sintering at 1290°C can be compared to the full melt enthalpy of the alloy to obtain a liquid fraction. Heating traces from loose powder samples of each BNi-2 loading are presented along with the pure BNi-2 alloy in Figure 4-54.

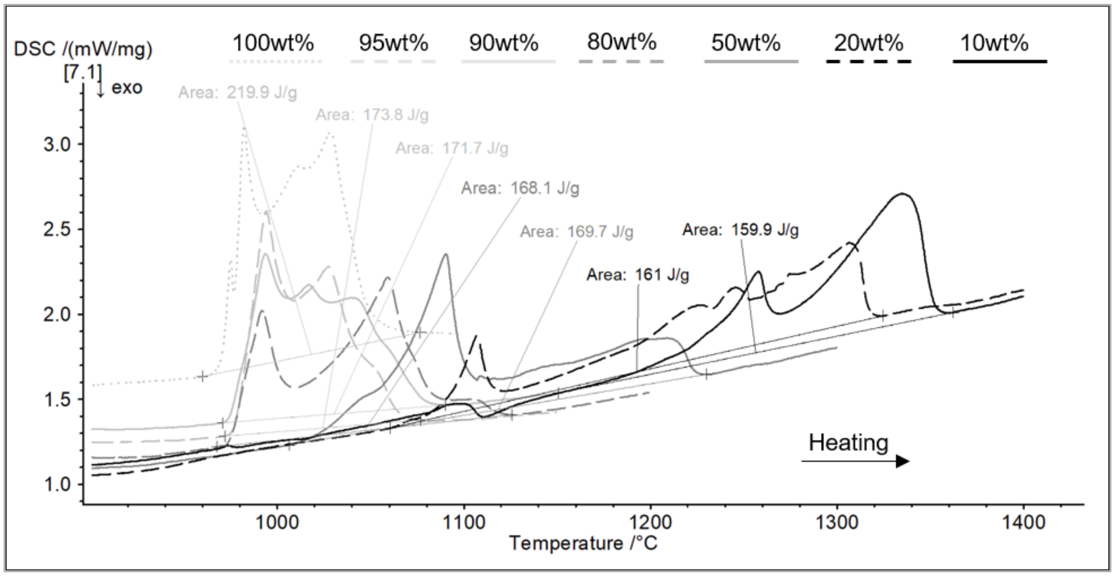

Figure 4-54. Heating traces of ad-mixed NiSA powder samples containing decreasing BNi-2 loadings from 100-10wt% BNi-2.

The results in Figure 4-54 demonstrate how the addition of the NiSA influences the melting behaviour of the BNi-2 alloy. The pure BNi-2 alloy melts in the range of 968°C-1050°C and displays a number of peaks because of its multi-component nature [20]. As the NiSA content of the alloy is increased, the melting event widens and changes shape. The melting onset remains at approximately 968°C up to 20wt% NiSA. The onset of melting is pushed above 1000°C in the 50-50 mixture of BNi-2 and NiSA powder and the melting peak widens significantly further. At the 10wt% BNi-2 loading, two distinct melting peaks emerge with the first peak being consistent with those presented in Figure 4-52. Due to the fact that the ad-mixed powders were fully homogenized prior to the re-melt events shown in Figure 4-54, the melting ranges differ from the in-situ melting behaviour determined in

Figure 4-50 through Figure 4-53. This is likely caused by the homogenization of B with the NiSA, leaving the NiSA in the ad-mixed alloys with a higher average B content. In contrast, the in-situ NiSA would have a lower B content because the BNi-2 and NiSA have not fully homogenized, causing the ad-mixed and in-situ alloys to exhibit slightly different melting ranges.

The measured enthalpy of melting for the ad-mixed powders are plotted with composition in Figure 4-55. The melting enthalpy of the pure BNi-2 alloy was measured as 220J/g. Alloy loadings between 5 and 50wt% BNi-2 had a consistent enthalpy of fusion of 170J/g. The 20 and 10wt% BNi-2 loadings both had a melting enthalpy of 160J/g while the NiSA was measured to have a melting enthalpy of 150J/g. Figure 4-55 demonstrates that the enthalpy of fusion for the BNi-2 modified NiSA does not follow a rule of mixtures and that the 10wt% BNi-2 mixture has a larger full-melt enthalpy than the pure NiSA. Therefore, when determining liquid fractions based on a comparative enthalpy technique (dividing the partial melt enthalpy by the full melt enthalpy as outlined in Section 4.2) 160J/g will be used as the full melt enthalpy of the alloy. Similarly, when calculating the liquid fraction remaining upon solidification after time at temperature, the enthalpy measured during a full solidification event will be used (110J/g in this case).

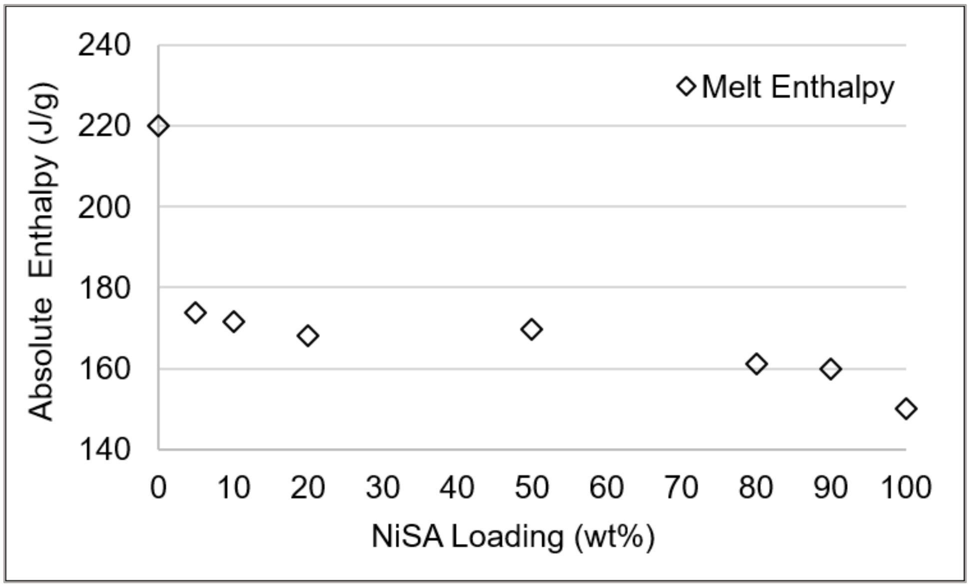

Figure 4-55. Measured melt enthalpies for different wt% NiSA loadings in the BNi-2/NiSA ad-mixed powder DSC tests.

4.3.3.4 Liquid Fraction, Grain Growth, and Density

The liquid fraction formed during sintering of the 10wt% BNi-2 NiSA can be determined by comparing the enthalpy of melting or solidification during a sintering experiment to the full melt or solidification enthalpies reported in Section 4.3.3.2. However, the solidification event of the 10wt% BNi-2 NiSA alloy overlaps with the re-precipitation event for the gamma prime phase. To account for this, liquid fraction calculations based upon solidification measurements must have the enthalpy of re-precipitation subtracted out. To do this, the enthalpy of gamma prime re-precipitation was measured from the cooling traces of pure NiSA sintering tests at 1300°C for 1hr. The re-precipitation event in these tests were found to have an average enthalpy of 6.0 ± 0.4J/g. Therefore, this enthalpy is subtracted from the solidification measurements obtained from the 10wt% BNi-2 cooling traces to obtain the corrected enthalpy of solidification after each hold time.

The liquid percentage as a function of hold time at the sintering temperature is presented in Figure 4-56. The liquid percentage during SLPS of the pure NiSA is also plotted in Figure 4-56 for comparison. The initial liquid contents for the pure NiSA and 10wt% BNi-2 loading are different because of the higher sintering temperature for the pure NiSA. The 10wt% BNi-2 loaded material increases in liquid content at a slower, more linear rate than the pure NiSA during the first hour of hold time. The liquid content during SLPS of the NiSA plateaus after approximately 1 hour of hold time while the 10wt% BNi-2 liquid content appears to continue its linear growth. Despite having similar initial liquid percentages, the final liquid content for the pure NiSA is approximately 10% higher than the 10wt% BNi-2 after 2 hours of hold time. In contrast, the 5wt% BNi-2 alloy does not display an increase in liquid content over hold time. The 5wt% BNi-2 loading achieves about 3% liquid at the peak sintering temperature and maintains this liquid phase over the first hour.

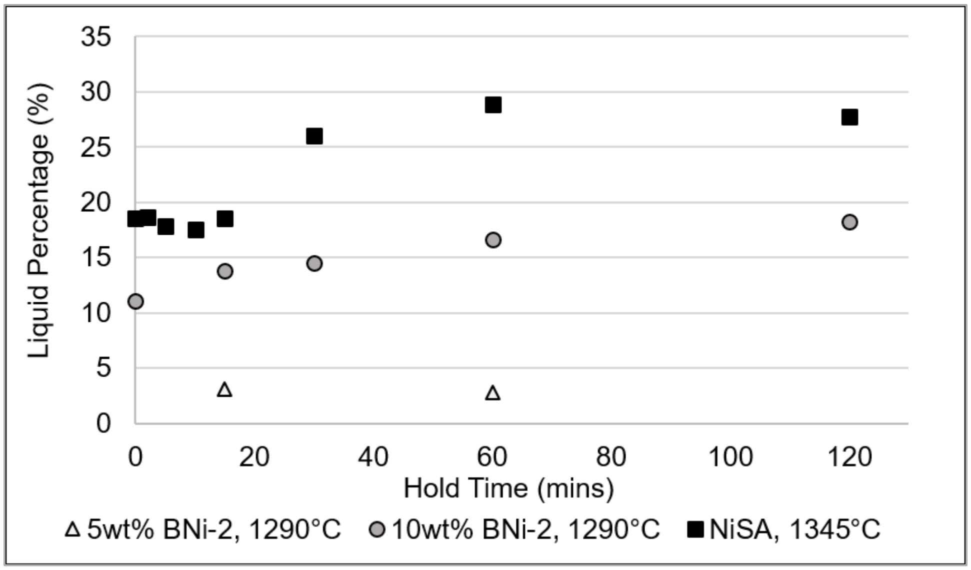

Figure 4-56. Final liquid percent with increasing hold time at the peak sintering temperature for the 5wt% BNi-2, 10wt% BNi-2, and pure NiSA

The average grain sizes of the 10wt% BNi-2 samples were measured after sintering at 1290°C for each hold time. The resulting grain sizes are plotted against hold time in Figure 4-57 along with the grain sizes achieved during SLPS of the pure NiSA and during sintering of the 5wt% BNi-2 material. The 5wt% BNi-2 material exhibited no grain growth after 15mins and 60mins hold times at 1290°C, maintaining the initial sub-20μm grain size. In contrast, the 10wt% BNi-2 alloy exhibits grain growth behaviour similar to SLPS of the pure NiSA at 1345°C. The grain sizes measured in the first 30mins of hold time are consistent between the 10wt% BNi-2 and SLPS sintering trials. Beyond 30mins, the SLPS grain size continues to increase, exceeding the 10wt% BNi-2 grain size by about 10μm after 1 hour before grain growth rate slows for both alloys. A maximum grain size of 39μm was achieved in the BNi-2 alloy after 2 hours while SLPS of the pure NiSA achieved 48μm after 2 hours.

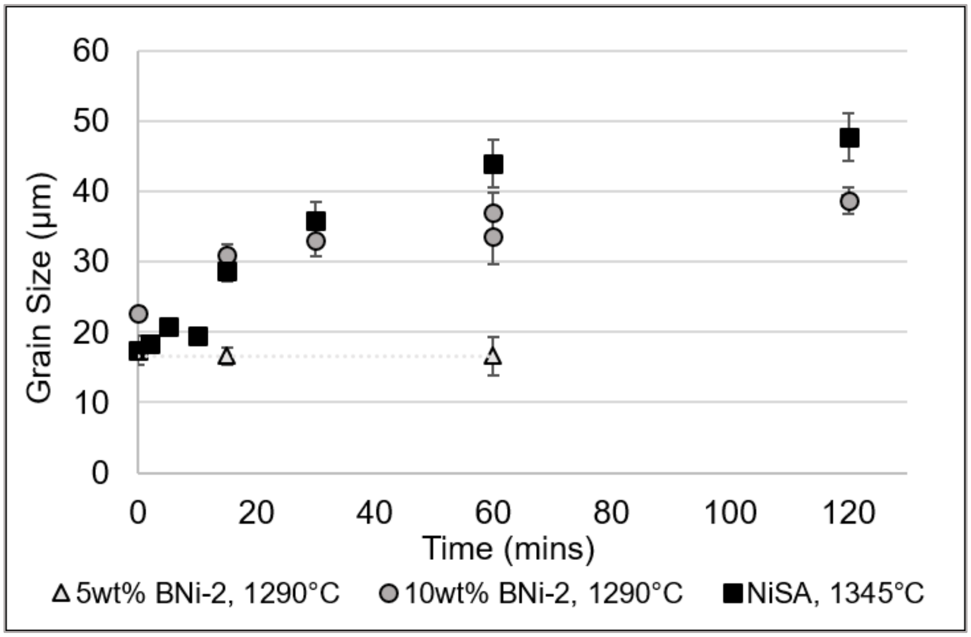

Figure 4-57. Average grain size as a function of hold time for the 5 and 10wt% BNi-2 alloys at 1290°C, and for the pure NiSA at 1345°C.

The sintered density of the 10wt% BNi-2 and NiSA SLPS samples is plotted against hold time in Figure 4-58. Upon reaching the peak SLPS temperature, the NiSA SLPS density is above 98%. In contrast, the 10wt% BNi-2 has a lower density of about 96% upon reaching its peak temperature of 1290°C. The lower peak sintering temperature as well as the absence of internal powder particle densification from SLPS likely result in the lower density measurement for the 10wt% BNi-2 alloy at zero hold time. Both materials exhibit a sharp 1-2% drop in density by 15mins of hold time and then subsequently recover to their initial density after 60-120mins. Holding at the peak temperature for 15mins is detrimental to the sintered density in both cases, though both materials exhibit a similar recovery path to a higher sintered density.

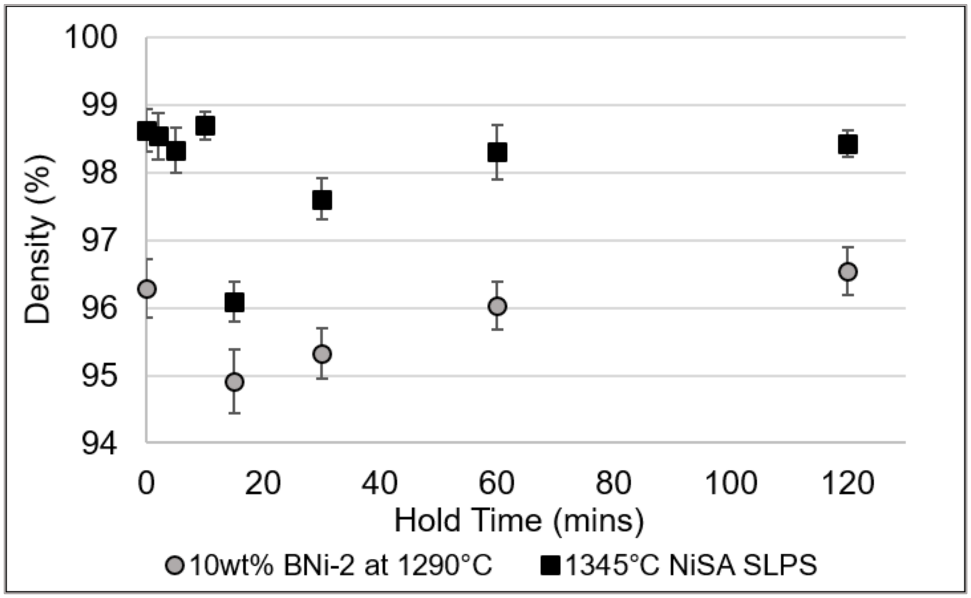

Figure 4-58. Sintered density of the 10wt% BNi-2 LPS and NiSA SLPS samples over hold time.

4.3.3.5 Microstructures and SEM-EDS

Polished cross sections of the pure MIM NiSA and the BNi-2 loaded MIM NiSAs are presented in Figure 4-59. The pure NiSA was solid state sintered at 1310°C for 1 hour and had a fine-grain microstructure with an average grain size of 17.4 ± 2.9µm. The 5wt% and 10wt% BNi-2 loadings were sintered at 1290°C for 1hr and had grain sizes of 16.6 ± 2.7µm and 37.0 ± 2.8µm, respectively. Figure 4-59 demonstrates that despite having a persistent liquid phase in the 5wt% BNi-2 material, no grain growth occurs relative to the solid state sintered NiSA. At a BNi-2 loading of 10wt%, significant grain growth is observed under the same sintering conditions as the 5wt% BNi-2 loading.

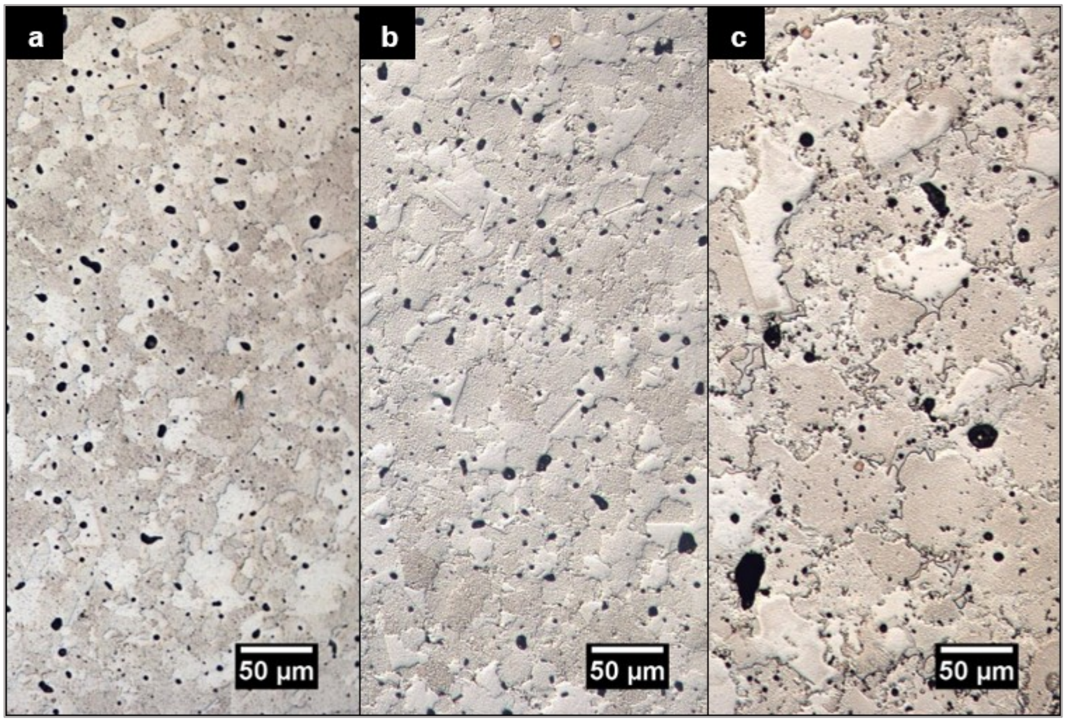

Figure 4-59. Microstructures of a) the pure MIM NiSA sintered at 1310°C/1hr, b) 5wt% BNi-2 loading sintered at 1290°C/1hr, and c) 10wt% BNi-2 loading sintered at 1290°C/1hr.

Higher magnification images of the BNi-2 modified NiSA bulk microstructures are shown in Figure 4-60. Script-like boride phases are observed in both the 5wt% and 10wt% BNi-2 alloys. These boride phases are sub-10µm in the 5wt% BNi-2 alloy and are much coarser in the 10wt% BNi-2 alloy. The boride phases are also evenly distributed throughout the 5wt% BNi-2 microstructure while the sub-surface microstructure of 10wt% BNi-2 alloy differs significantly from its bulk microstructure. The sub-surface microstructure of the 10wt% BNi-2 alloy is presented in Figure 4-61 where multiple phases can be observed in the grain boundaries. These regions presumably contain eutectic boride and silicide phases which have precipitated from the remaining liquid during solidification. Circular and rounded regions (very bright) as well as dendritic areas (darker) are only observed in the 10wt% BNi-2 loading. In addition, areas of γ/γ' eutectic appear in the areas surrounding the boride and silicide phases, supporting the theory that these phases precipitate from the liquid phase during cooling.

Back scatter electron (BSE) SEM micrographs of bulk microstructure in the 5wt% and 10wt% BNi-2 loadings sintered for 15 and 60mins at 1290°C are presented in Figure 4-62. The script phases evidently coarsen with increasing hold time in the 10wt% BNi-2 material while there is no readily observable coarsening of these phases over hold time in the 5wt% BNi-2. As previously observed in Figure 4-60, the higher BNi-2 content leads to the formation of much coarser script-like phases and a larger grain size. EDS of the script-like phases in Figure 4-62 revealed that they were primarily rich in both W and Cr. The matrix adjacent to these script-like phases was found to be the approximate NiSA composition, but depleted in both W and Cr.

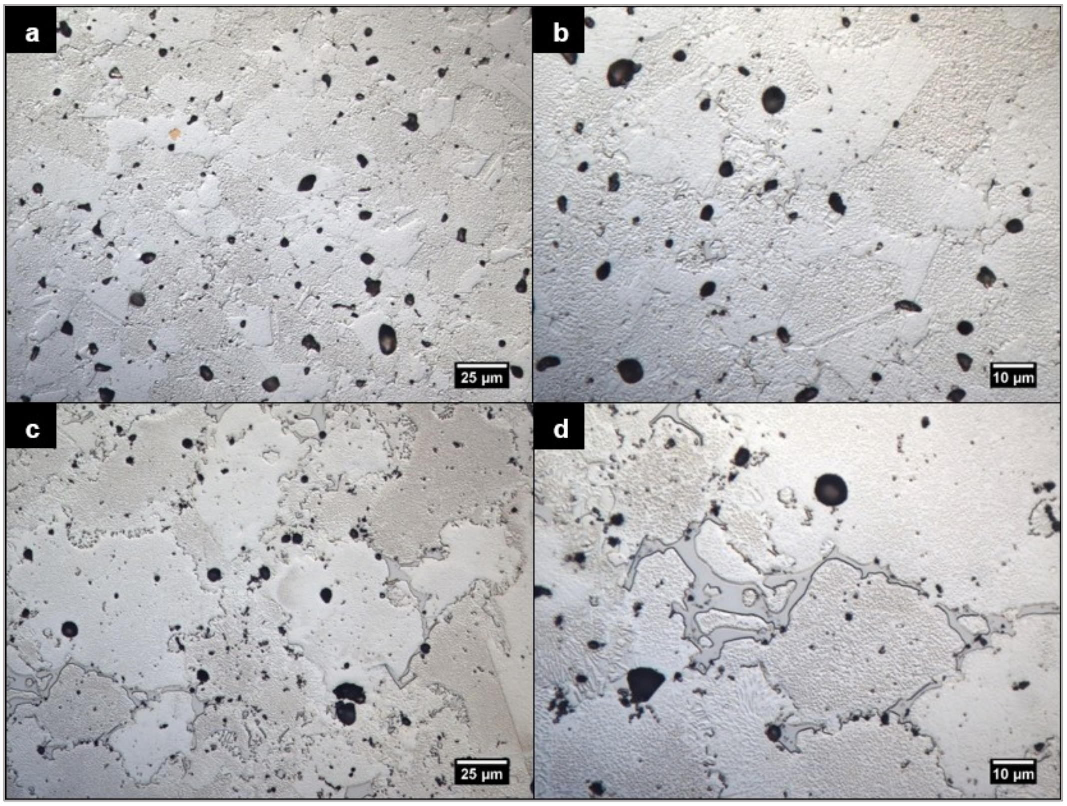

Figure 4-60. **High magnification microstructures of the 5wt% BNi-2 NiSA (a, b) and the 10wt% BNi-2 NiSA (c, d) sintered at 1290°C for 1 hour.**

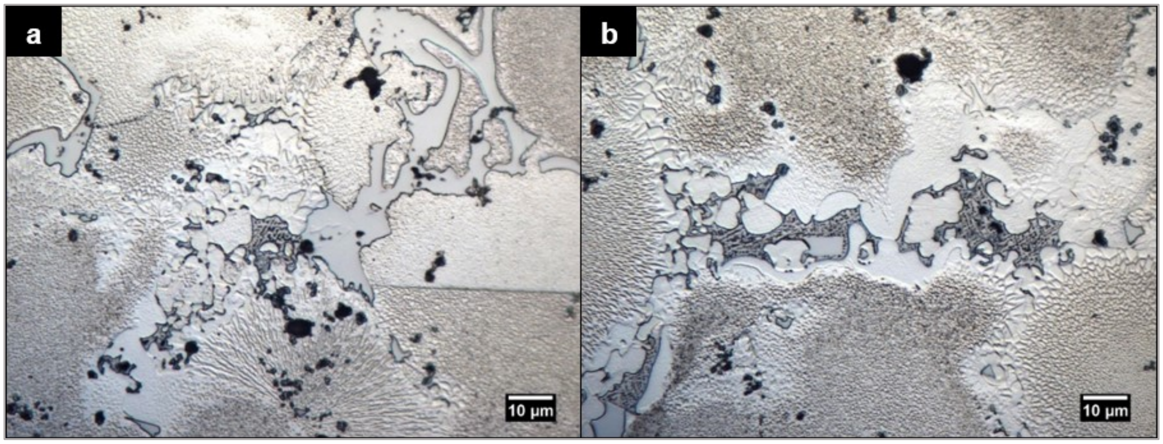

Figure 4-61. **High magnification images of the grain boundary phases observed in the 10wt% BNi-2 loading sintered at 1290°C for 1 hour. Images a) and b) refer to separate regions of the sub-surface microstructure.**

EDS of the sub-surface grain boundary phases observed in Figure 4-61b was also completed. The various phases which were scanned are labelled in Figure 4-63 while the EDS results are tabulated in Table 4-2. Region A appears as part of a solid NiSA grain and has the NiSA composition with some solute depletion, including W. Region B appears as a circular raft which appears only when the eutectic like phase (region C) is present. The circular rafts contain Ni-Ta-Al-Co in order of decreasing composition along with minute amounts of other solutes from the NiSA. In contrast, the eutectic like phase, scanned as region C, contains primarily Ni and other RM’s. The remaining regions, D-F, are similar to the γ/γ’ eutectic phase composition and are either rich in Co and Cr or rich in Al and Ta. The SEM/EDS results from the sub-surface grain boundaries in the 10wt% BNi-2 material demonstrate that the liquid phase undergoes a multi-component solidification process. This is consistent with the DSC trace which exhibits at least two distinct solidification peaks. In addition, the eutectic like phase in Figure 4-61b and Figure 4-63 has precipitated in the center of the grain boundary and appears to be the last region to solidify. The morphology and location of this phase is consistent with many centerline eutectics which form as an ASZ in nickel superalloy brazing [45–50]. It should be noted that B was excluded from EDS analysis due to difficulties in detecting this light element. It is expected the eutectic like C region will contain elevated B content.

Table 4-2. EDS results for sub-surface grain boundary phases in 10wt% BNi-2 loaded NiSA.

Phase	Al	Ti	Cr	Fe	Co	Ni	Ta	W	RM	Identity
A	Base NiSA Composition									NiSA (Low Al, Ti, Ta, W)
B	5.7	2.4	2.6	0.2	5.4	69.4	7.7	2.7	3.8	Ni-Ta-Al-Co
C	0.5	0.6	3.1	0.2	9.0	61.0	4.9	0.9	19.8	Ni-RM-Co-Ta
D	2.3	0.8	9.4	0.7	13.3	68.1	0.8	2.2	2.5	γ/γ' Eutectic (Co, Cr rich)
E	2.5	0.8	9.2	0.5	12.9	68.0	0.7	3.0	2.4	γ/γ' Eutectic (Co, Cr rich)
F	6.1	1.3	4.9	0.4	6.5	70.2	4.4	5.4	0.8	γ/γ' Eutectic (Al, Ta rich)

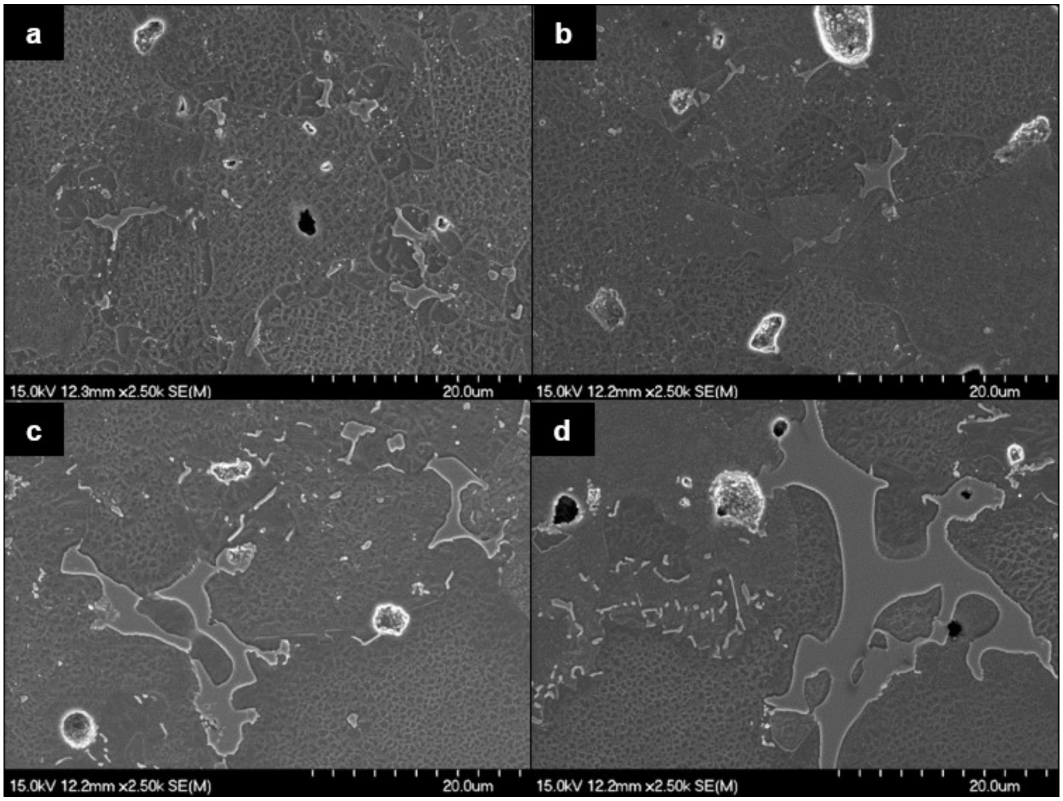

Figure 4-62. SEM micrographs of the 5wt% BNi-2 (a, b) and 10wt% BNi-2 (c, d) loadings sintered at 1290°C for a) 15mins, b) 60mins, c) 15mins, and d) 60mins.

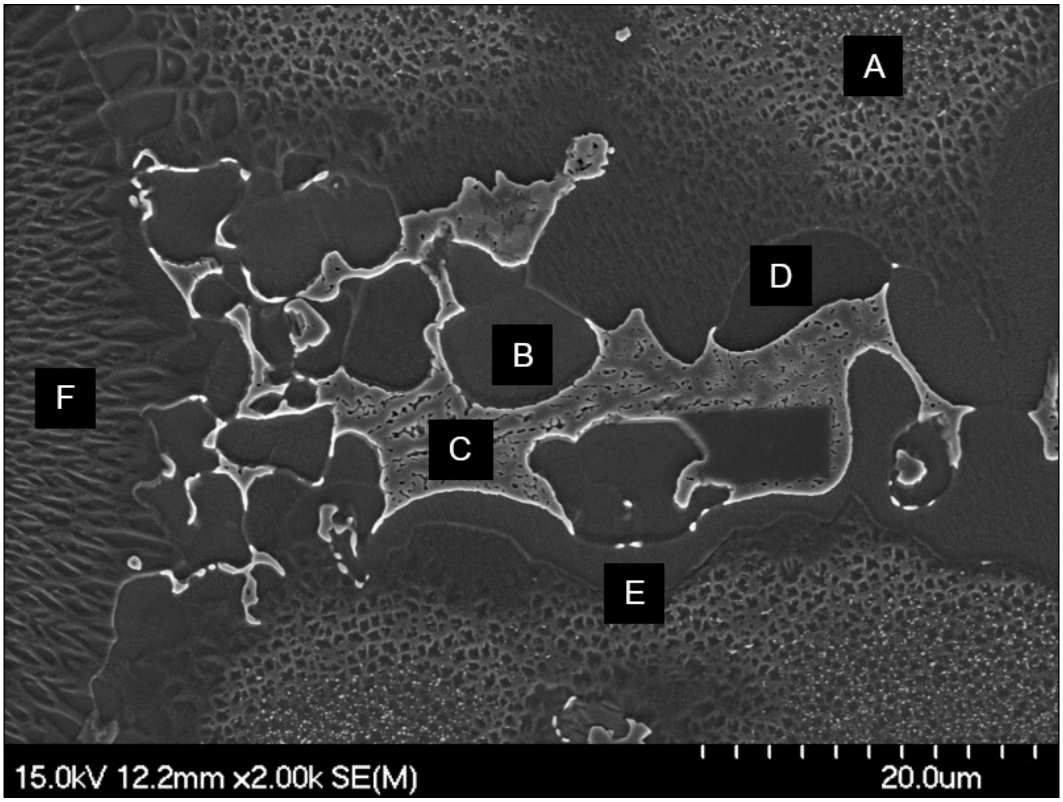

Figure 4-63. Sub-surface grain boundary microstructure in the 10wt% BNi-2 material sintered at 1290°C for 60mins with EDS sample areas labelled A-F.

4.3.4 Discussion

4.3.4.1 Alloy Behaviour from 968°C-1050°C

The DSC investigation presented in Section 4.3.3.1 supports the theory that a liquid phase forms within the BNi-2 modified NiSA at the BNi-2 solidus temperature (968°C). The DSC results also indicate that the liquid fraction formed at 968°C is small because the enthalpy of the melt event is much less than the enthalpy of fusion for the pure BNi-2 alloy (0.3J/g compared to 214J/g). Even accounting for the 10wt% BNi-2 content of the mixture, full melting of this additive would be on the order of 21J/g. Therefore it can be estimated that only 10% of the BNi-2 melts at 968 °C. These large differences in enthalpies are expected due to the significant solute uptake of B and Si which has been shown to cause rapid diffusional solidification upon melting of BNi-2 [20]. The BNi-2 alloy contains the fast diffusing MPD elements B and Si to suppress the solidus temperature for brazing and enable the diffusional solidification process. In addition, the high surface area associated with fine metal powders used in these MIM materials increases the contact area available for rapid solute uptake to occur. Since the BNi-2 loadings are low, there is also more NiSA volume available to uptake B and Si. Taking all of these factors into account, it is reasonable to expect the BNi-2 liquid to undergo rapid diffusional solidification upon contacting and wetting the adjacent NiSA particles.

A sample of the 10wt%BNi-2 material was sectioned and polished after being heated to 1050°C for 30mins to confirm the presence of a liquid phase and observe any wetting and spreading of the liquid in the powder structure. An optical microscope image of the polished cross section is presented in Figure 4-64a while an SEM micrograph of the same particle is shown in Figure 4-64b. EDS was performed to confirm the particle's identity and to determine the local compositional changes in the NiSA and BNi-2 particles. The etchant, waterless Kallings reagent, does not appear to etch the BNi-2 particles and the resulting contrast in Figure 4-64a makes it straight forward to visually identify the BNi-2 particle. The BNi-2 particle appears to have melted partially, with the liquid phase wetting the adjacent NiSA particles to form rounded necks. The NiSA particles further away from the BNi-2 particle do not display the same degree of necking, providing further evidence of a liquid phase in the localized vicinity of the BNi-2 particles. However, the limited extent of liquid spreading and powder consolidation suggests that the liquid phase was only present for a short time. These microstructural observations are consistent with the DSC results and the suspected rapid diffusional solidification of the liquid upon melting.

In Figure 4-64b, the BNi-2 particles appear as a solid solution phase while the NiSA particles contain many small, secondary phase particles (which appear bright). EDS confirmed that the bulk of the particle in Figure 4-64 was the BNi-2 composition. Multiple points were scanned along a 16μm line across the neck between the BNi-2 and NiSA particles indicated in Figure 4-64b. The results of these scans are plotted in Figure 4-65 where the neck's centerline is at the 8μm distance while the BNi-2 and the NiSA particles are at the 0μm (left of Figure 4-65) and 16μm (right of Figure 4-65) distances, respectively. Each element's concentration in the EDS results has been normalized relative to that element's concentration in the average NiSA. Since the relative concentration of Si and Fe is high in BNi-2 compared to the NiSA, the Si and Fe concentrations (black lines) are plotted on a secondary axis to improve the comparison. The neck region was found to contain a compositional gradient of solutes Co, Al, Si, Fe and other refractory metals. Co and Al, neither of which originate in the BNi-2 alloy, are detected within the original BNi-2 particle along with lower quantities of other refractory elements which originated in the NiSA. Si and Fe are detected in the NiSA particle at low quantities as well, indicating that there has also been solute diffusion from the BNi-2 particle into the NiSA. Notably, W has a steep concentration gradient across the neck region indicating that it was either a slowly diffusing element at this temperature or segregated into the liquid and did not diffuse into the BNi-2.

EDS box scans of contacting NiSA and BNi-2 particles as well as neck regions were completed to determine their bulk compositions. Separate NiSA particles not in contact with the BNi-2 particles were also scanned as a reference for the NiSA and the results are plotted in Figure 4-66. These EDS results are also presented as relative concentrations to the NiSA and a secondary bar graph has been used to separate the higher Si and Fe relative concentrations to improve the comparison.

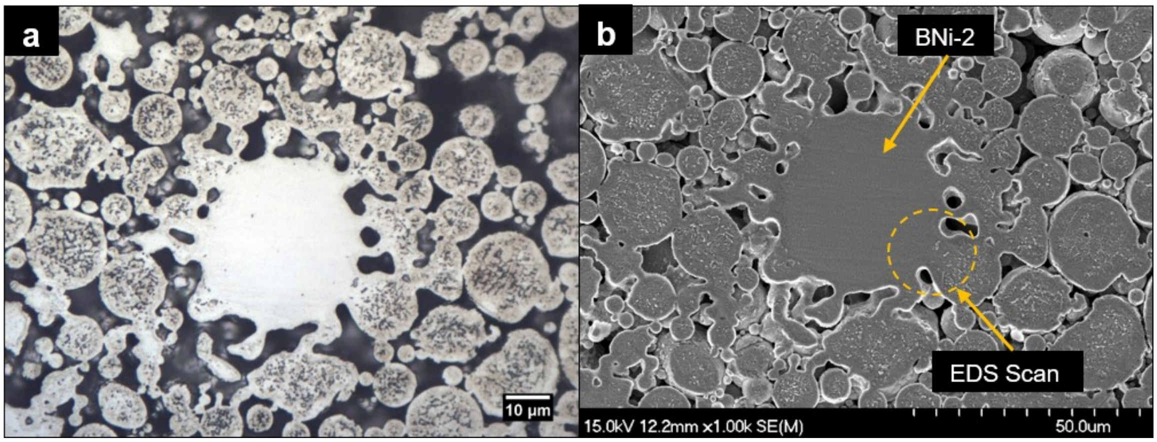

Figure 4-64. Optical microscope (a) and SEM (b) images of a partially melted BNi-2 particle in the 10wt%BNi-2 NiSA heated to 1050°C for 0.5hrs.

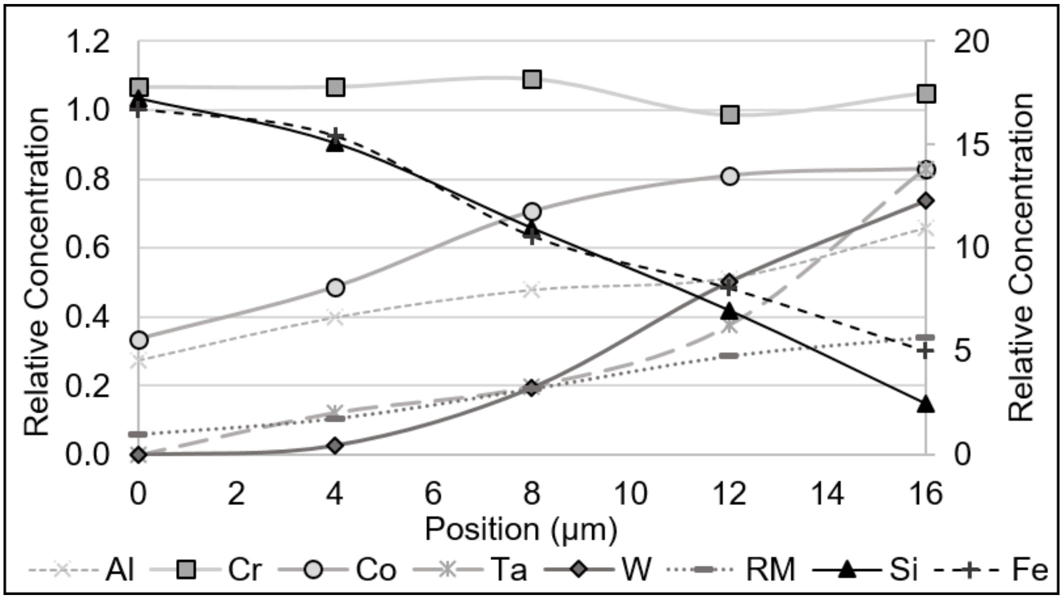

Figure 4-65. Relative element concentrations along a 16µm line in the neck between the BNi-2 and NiSA particles highlighted in Figure 4-64b. The 8µm position is at the center of the neck while the 0µm and 16µm positions are in the BNi-2 and NiSA particles, respectively. Si and Fe (black lines) are plotted on the secondary axis.

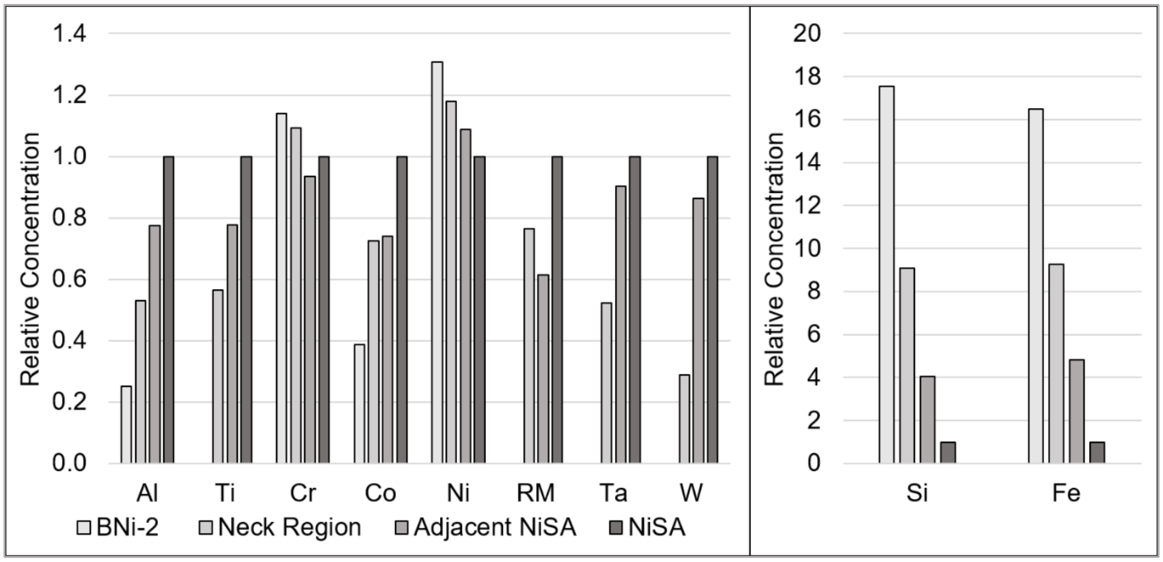

Figure 4-66. Relative element concentrations from average EDS results for different areas of the 10wt% BNi-2 loaded material heated to 1050°C for 0.5hrs.

The EDS results demonstrate that the original BNi-2 particles no longer have the standard BNi-2 composition. Instead, the particles now contain Co and Al with less Si. The neck regions, which were presumably part of the liquid phase that wet and spread across the adjacent NiSA particles, contain Co, Al, Si, and W along with other refractory elements. B, although detected, was excluded from the EDS results due to the inability of the INCA-EDS software to accurately quantify light elements along with heavier refractory elements such as W. Therefore, the presented EDS results can only serve as a semi-quantitative evaluation of the solute distribution in the 10wt% BNi-2 material after 1050°C for 0.5hrs. However, based on the behaviour of B in other TLPB studies [20,45–47,49,50], it is expected that B has rapidly diffused into the NiSA particles at this stage. It is reasonable to expect that the loss of MPDs B and Si into the NiSA via rapid solute uptake and subsequent diffusion causes the liquid phase formed at 968°C to diffusionally solidify shortly after forming. The segregation of refractory elements such as W into the liquid from the NiSA could also exacerbate this process by quickly raising the solidus temperature of the liquid.

4.3.4.2 Sintering at 1290°C

As the BNi-2 modified NiSA is heated above 1200°C to the sintering temperature of 1290°C, the diffusionally solidified alloy from the 968-1050°C BNi-2 melt event begins to re-melt. The DSC traces in Figure 4-50 demonstrate that the re-melt event begins at 1240°C when the alloy contains 5wt% BNi-2 and at 1200°C when the alloy contains 10wt% BNi-2. The re-melted alloy, which is a mixture of the BNi-2 and NiSA at this stage, acts as a liquid phase sintering aid for the NiSA. It is important to note that the BNi-2 modified NiSA deviates from the traditional LPS approach in the sense that the liquid phase composition which aids the sintering process at 1290°C is not the same composition as the lower melting point powder additive (BNi-2) which was originally added to create a liquid phase. Briefly, the BNi-2 additive creates a brazing product with the NiSA that ultimately forms a liquid phase which can aid sintering once the re-melt temperature is surpassed.

Looking at Figure 4-50 it is evident that without the BNi-2 additive no liquid would form in the pure NiSA at 1290°C. The addition of BNi-2 to the NiSA then successfully allows for liquid phase sintering to occur below the solidus temperature of the NiSA, despite the liquid phase not being the original BNi-2 composition. Though the liquid phase is persistent, the percentage of liquid increases over isothermal hold time at 1290°C. The initial liquid percentage formed with the 10wt% BNi-2 loading was determined to be 11% while the liquid percentage after 2 hours was 18.3%. This increase in liquid content is likely a result of NiSA dissolution and solute segregation as the NiSA and liquid homogenize.

Figure 4-56 compares the liquid percentages for supersolidus sintering of the NiSA at 1345°C and for liquid phase sintering of the 10wt% BNi-2 alloy at 1290°C. The SLPS approach results in rapid liquid fraction growth during the first 30mins of sintering at 1345°C before the liquid fraction begins to plateau. Although the liquid fraction in the 10wt% BNi-2 alloy also increases, its growth is slower and more linear than in SLPS at 1345°C. Figure 4-56 demonstrates that despite both sintering approaches starting with similar liquid fractions, SLPS of the pure NiSA and LPS with the BNi-2 additive cause the liquid phase to behave differently. If in both cases the liquid fraction growth is driven by solute segregation, the liquid fraction behaviour would then be governed by the differing compositions of the solid and liquid phases in each alloy. In addition, the higher temperatures used in the SLPS method would increase the diffusion rate of solutes, leading to faster segregation of elements and a higher rate of liquid growth.

The grain growth behaviour over time at temperature is compared for LPS of the 10wt% BNi-2 alloy and SLPS of the pure NiSA in Figure 4-57. Both alloys exhibit a similar initial increase in grain size with the SLPS approach achieving larger grain sizes at longer hold times. The similarity of the grain growth behaviour between these alloys suggests that the liquid content does not govern grain growth in the MIM NiSA. Both alloys obtain above 10% liquid upon reaching their sintering temperature, but the liquid content grows faster and is higher in SLPS of the NiSA. Despite this, grain growth is very similar for both sintering temperatures and alloys. This could indicate that the additional liquid formed during the SLPS process is not a substantial benefit to grain growth and that the same grain growth mechanism is activate in both alloys.

The 5wt% BNi-2 alloy, also included in Figure 4-56 and Figure 4-57, contains about 3% liquid upon reaching the sintering temperature of 1290°C and exhibits no liquid fraction or grain growth over time at temperature. The absence of grain growth in the 5wt% BNi-2 loading indicates that there is a critical liquid fraction required to enact grain growth in the BNi-2 modified NiSA between 3% and 10% liquid.

Upon cooling, the liquid in the BNi-2 modified alloys undergoes a solidification sequence which produces a number of non-equilibrium phases. The 5wt% BNi-2 loading, presented in Figure 4-60 and Figure 4-62, precipitates a number of script-like W/Cr rich borides. The 10wt% BNi-2 alloy, shown in Figure 4-63, has a more complex solidification path which produces coarse script-like W/Cr rich borides along with a number of other non-equilibrium solidification products. EDS of the 10wt% BNi-2 alloy, outlined in Figure 4-63 and Table 4-2, indicated that there are at least 5 individual phases that solidify from sub-surface liquid pools in addition to borides and silicides. These highly segregated regions of the microstructure are on the scale of 50-100μm and typically contain the γ/γ' eutectic phase commonly formed in NiSAs. The bulk microstructure of the 10wt% BNi-2 alloy typically contains only the coarse script-like W/Cr rich borides, suggesting that liquid tends to pool in the sub-surface microstructure. The sub-surface liquid pools are likely the last liquid remaining during solidification due to their size. As solidification proceeds, solutes would be rejected into the liquid from the newly formed solid, enriching the composition of the liquid toward eutectic compositions. Upon reaching these compositions, the remaining liquid would solidify as a non-equilibrium eutectic phases, such as region C in Figure 4-63. Given the complex nature of the alloy and the fact that the BNi-2 alloy can form a combination of binary and ternary eutectics [22], it is likely that the liquid phase forms a primary phase, binary eutectics, and ternary eutectics along the solidification path.

The formation of coarse non-equilibrium solidification products in the 10wt% BNi-2 alloy microstructure is detrimental to the material's properties. The coarse, script-like, borides are brittle phases which would act as sites for crack propagation and reduce the strength of the material [2,48]. In addition, these non-equilibrium phases would limit the grain boundary ductility, reducing the alloy's creep resistance [2]. The nickel superalloys also generally depend on discrete grain boundary particles, such as carbides and borides, to pin the grain boundaries and reduce grain boundary sliding during creep [2]. The continuous morphology of the boride phases in the BNi-2 modified NiSA would cause embrittlement of the grain boundaries, reducing the high temperature strength of the alloy [2].

The 5wt% BNi-2 alloy only exhibited fine, script-like, borides. The smaller scale and more homogeneous distribution of these borides is thought to be less detrimental to the overall properties of the alloy than the microstructures observed at the 10wt% BNi-2 loading. Unfortunately, at the BNi-2 loading of 5wt% and less, grain growth was not observed. Therefore, despite having a more homogenous microstructure which may have similar properties to the base NiSA, the 5wt% BNi-2 content does not activate grain growth as desired.

At 10wt% BNi-2, substantial grain growth is observed, but the final microstructure contains deleterious non-equilibrium solidification products. These phases are expected to limit the useful temperature of the alloy due to the number of eutectic phases formed. In typical brazing operations [20,46–48], isothermal solidification of the brazing filler metal leaves a solid solution phase with a melting temperature similar to that of the base metal.

When brazing is performed at higher temperatures, solute enrichment of the brazing liquid can reduce or prevent isothermal solidification, leaving the solute rich liquid to undergo athermal solidification [45]. LPS of the BNi-2 modified NiSA is a more extreme version of this case, where the liquid phase does not solidify as a solid solution over time at temperature, but instead, solidifies athermally, forming a number of deleterious eutectic phases during cooling.

4.3.4.3 Grain Growth Behaviour

Based on the results of the previous section, the minimum liquid fraction required to activate grain growth lies between 3% and 10% liquid. In terms of BNi-2 loading, the minimum BNi-2 loading required to activate grain growth would be between 5 and 10wt%.

While the liquid fraction growth between SLPS at 1345°C and LPS of the 10wt% BNi-2 at 1290°C are different, the grain growth behaviour was found to be very similar between both methods, including the incubation period which was discussed in Section 4.2. In Figure 4-56 through Figure 4-58, these microstructural parameters exhibit a plateau in the first 10mins of hold time for the SLPS tests. The solution of grain boundary MC carbides causes the liquid fraction to increase and enables the grain boundary motion necessary for grain growth. In addition, the 1-2% drop in density observed in Figure 4-58 for both the NiSA and 10wt% BNi-2 alloys corresponds with these microstructural changes. The sintered density decreases in both materials after the initial incubation period and the final densities are very similar after 60-120mins of holding despite different densities at time zero. The similarities in the sintered density behaviour suggests that the same coarsening phenomenon is active in both sintering approaches. Therefore, although no short time hold tests were completed for the BNi-2 modified LPS alloys, it is expected that the grain size, liquid fraction, and sintered density all remain relatively constant until the solution of grain boundary MC carbides occurs. This is followed by grain and pore coarsening along with an increasing liquid fraction.

The similarities between the two alloys' grain growth suggests that the same grain growth mechanism is active in both the SLPS and LPS sintering approaches regardless of the liquid fraction behaviour. Therefore, although there is a minimum liquid fraction required to activate grain growth, the liquid fraction does not appear to govern the grain growth process. This is further supported by comparing these results to liquid fraction and grain size of the 1340°C SLPS of the NiSA in Figure 4-67 and Figure 4-68. These comparisons demonstrate that the liquid fractions in the 1340°C SLPS and 10wt% BNi-2 LPS methods are nearly identical over time at temperature. Despite this, the grain size increases faster in the BNi-2 modified NiSA, suggesting that the addition of BNi-2 to the NiSA also enhances grain growth. However, the 1345°C SLPS grain growth curve outpaces the BNi-2 LPS alloy. Since the 1345°C SLPS process has a much higher liquid fraction than the BNi-2 LPS, it is expected that the higher liquid content does assist in the grain growth process, but does not govern the grain growth rate.

Given the similarity of grain growth activation between the BNi-2 modified NiSA and SLPS of the NiSA, further discussion on the specific grain growth activation mechanism is presented in Section 4.5.

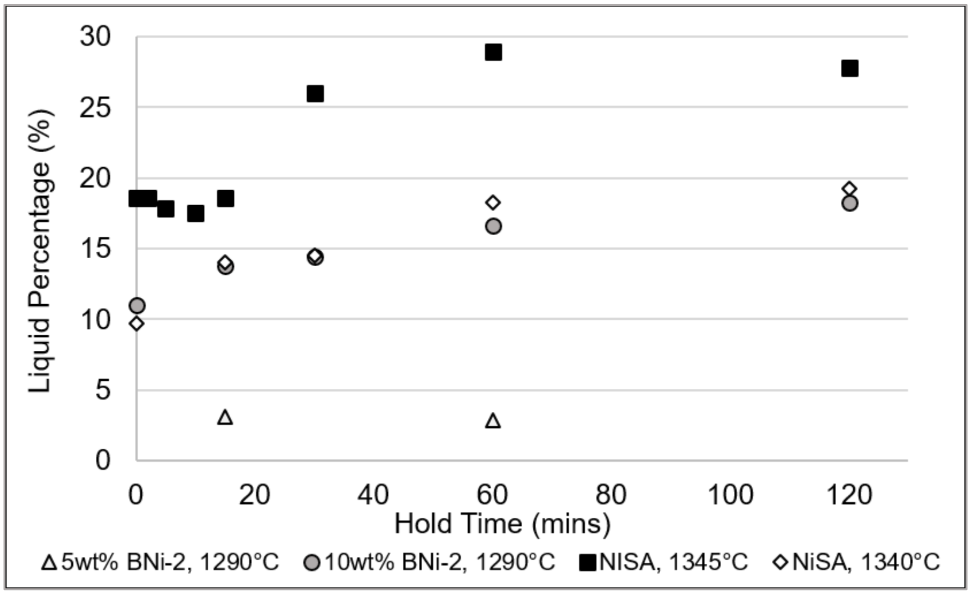

Figure 4-67. Comparison of the liquid percentages over time at temperature in the SLPS and BNi-2 LPS approaches to sintering the NiSA.

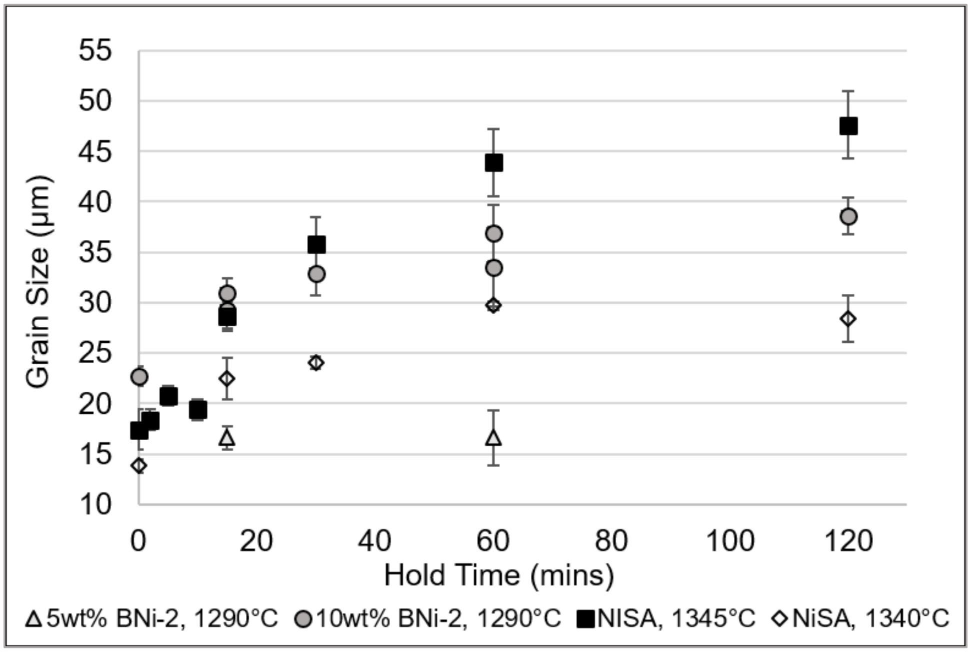

Figure 4-68. Comparison of the grain size over time at temperature in the SLPS and BNi-2 LPS approaches to sintering the NiSA.

4.3.4.4 Benefits and Drawbacks of the BNi-2 Modified NiSA

The BNi-2 modified NiSA can be liquid phase sintered at 1290°C to achieve grain growth. The same grain growth behaviour is observed in LPS of the BNi-2 modified alloy and in SLPS of the pure NiSA at 1345°C. Therefore, the BNi-2 modified NiSA can achieve similar grain sizes to SLPS at a lower sintering temperature. Unfortunately, a BNi-2 loading of 5wt% is insufficient to enact grain growth at 1290°C due to its lower liquid content. A BNi-2 loading above 5wt% is required to increase the grain size using this LPS approach. However, at higher BNi-2 contents, undesirable non-equilibrium solidification products form in the microstructure. These deleterious phases may impact the material properties due to their coarse and heterogeneous distribution throughout the alloy. More specifically, the presence of coarse non-equilibrium eutectic phases in the 10wt% BNi-2 loading likely reduces grain boundary ductility, offsetting the benefit of obtaining the larger grain size to combat grain boundary sliding. In addition, the 10wt% BNi-2 alloy becomes highly segregated with time at temperature, reducing the material's compositional homogeneity which is one of the primary benefits of the MIM process.

Although the 5wt% BNi-2 alloy did not exhibit grain growth, it did contain a more homogenous microstructure which contained fine, script-like borides. Although these brittle borides likely reduce the ductility and strength of the alloy relative to the base NiSA, their impact on the overall material properties is likely less detrimental than the coarse borides observed with the 10wt% BNi-2 loading.

One of the main challenges associated with SLPS of the NiSA is that the growth of the liquid phase can lead to distortion and slumping of the part. Figure 4-69 compares the slumping behaviour of 10wt% BNi-2 alloy at 1290°C with sintering of the MIM NiSA at multiple temperatures.

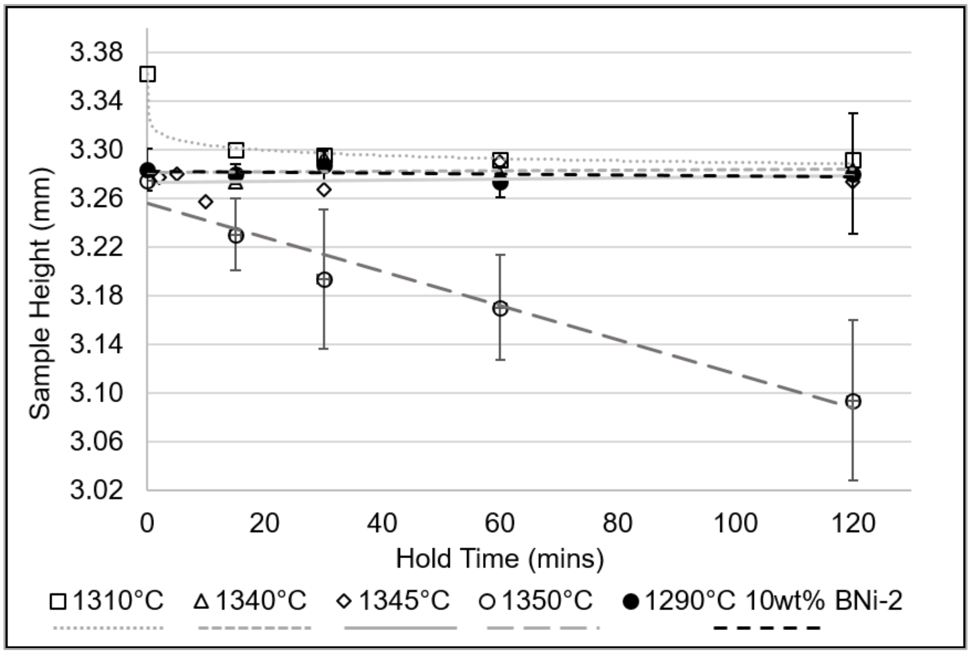

Figure 4-69. Final sample height versus hold time for the pure NISA sintered at 1310°C, 1345°C, and 1350°C as well as the 10wt% BNi-2 alloy at 1290°C.

During solid state sintering at 1310°C, the sample shrinkage over the hold time was determined from dilatometry data. Post-sintered sample heights for the SLPS tests were measured with calipers, although, dilatometry at 1350°C revealed that SLPS samples experience the majority of sintering shrinkage prior to the peak temperature. This means that SLPS samples exhibit similar sintering shrinkage amounts at the start of the hold time and that deviations in sample height during the hold time provide an indication of material slumping. Figure 4-69 demonstrates that the SLPS temperature is limited by the slumping phenomenon observed at 1350°C. However, at 1290°C with the BNi-2 additive, the sample height is stable, much like in the 1345°C and 1340°C SLPS cases. The large standard deviation in height measurement for the 120min 10wt% BNi-2 sample was caused by deformation at the sample edges, which indicates that the sample was starting to lose rigidity at this longer hold time. Surprisingly, the 10wt% BNi-2 modified material can be sintered to larger grain sizes than the 1340°C SLPS'd NiSA with a lower, more consistent liquid fraction. It also has a lower liquid fraction than the 1345°C SLPS case, but a similar final grain size. The apparent ability to obtain large grain sizes with lower liquid contents suggests that the 10wt% BNi-2 NiSA presents a lower risk of sample slumping than SLPS of the 100% NiSA.

4.3.5 Conclusions

A metal injection molded nickel superalloy was modified by adding 5 and 10wt% BNi-2 as a liquid phase sintering additive. DSC investigations of the BNi-2 modified NiSAs determined that the BNi-2 additive undergoes rapid diffusional solidification upon heating to its solidus temperature of 968°C, limiting the liquid fraction formed and the time available for liquid wetting and spreading. The diffusionally solidified product was discovered to re-melt at 1240°C in the 5wt% BNi-2 loading and at 1200°C in the 10wt% BNi-2 loading. MIM samples of the BNi-2 modified alloys were sintered at 1290°C and the liquid percentage and grain size were determined for various hold times. The 5wt% BNi-2 alloy exhibited a constant liquid content over time at temperature and no grain growth. The 10wt% BNi-2 alloy exhibited a liquid percent increase over time at temperature that was smaller and more linear than SLPS of the pure NiSA at 1345°C. Despite the difference in liquid fraction behaviour between the LPS and SLPS methods, the grain growth behaviour was similar in both cases. Therefore, it was concluded that a minimum liquid fraction is required to enact grain growth in the BNi-2 modified NiSA, though the liquid fraction itself does not govern the grain growth rate.

Deleterious non-equilibrium solidification products were found in the BNi-2 modified NiSA microstructures. The 5wt% BNi-2 loading exhibited fine, script-like boride phases which were rich in W and Cr and were homogeneously distributed throughout the microstructure. The 10wt% BNi-2 loading contained very coarse, script-like borides which were also rich in W and Cr. Liquid was observed to pool in the sub-surface microstructure of the 10wt% BNi-2 alloy, causing additional binary and ternary eutectic phases to form during cooling. These regions were similar to centerline eutectics commonly observed in NiSA brazing tests where isothermal solidification was incomplete.

DSC analysis of ad-mixed BNi-2 and NiSA powders exposed the evolution of melting behaviour as a function of NiSA loading in the BNi-2 alloy. The enthalpy of fusion for the 10wt% BNi-2 alloy was determined to be 160J/g.

A comparative DSC method has been successfully applied to evaluate LPS of the BNi-2 modified NiSAs. The liquid content with time and temperature was determined using this DSC technique and subsequent microstructural analysis validated the results. The research demonstrates the importance of time and temperature to the microstructural evolution of the BNi-2 modified NiSA. DSC has been established as an effective tool for predicting sintering behaviour based on liquid content and can provide fundamental information for LPS alloy design.

4.4 Modeling the Supersolidus Liquid Phase Sintering Behaviour of a Metal Injection Molded NiSA Superalloy

4.4.1 Introduction

SLPS has been successfully applied to difficult to sinter Ni-alloys such as IN718 to achieve high densities in short sintering cycles [18,24,51]. However, sintering above the solidus temperature reduces a material's strength and rigidity, which can lead to part distortion and slumping [11,17,28]. If an SLPS process is designed improperly the material may lose its rigidity to the extent that it deforms under the force of gravity, sacrificing the net-shaping advantages of MIM. The liquid film formed at the grain boundary during SLPS can act as both a lubricant for grain sliding and a source of grain cohesion via viscous resistance to deformation [17,28]. Therefore, an understanding of the liquid behaviour with time and temperature is an essential part of applying SLPS to achieve high density and shape retention. In addition, more complex alloys such as the MIM NiSA in this study have not yet been evaluated for SLPS.

SLPS can cause significant microstructural coarsening in addition to high densities [11]. It may be possible to leverage the microstructural coarsening of SLPS to activate grain growth in the MIM NiSA superalloy. Though, as the grain size increases during SLPS, the grain boundary liquid film thickness increases, reducing the compact's resistance to distortion [28]. Therefore, a more complete understanding of the NiSA's SLPS behaviour is required in order to control the grain growth process while achieving complete densification and shape retention.

Numerous studies have been focused on modeling SLPS from first principles in order to predict the material response to time and temperature [17,18,28,52–56]. The SLPS model employed in this study, based on the work of Campbell and Liu et al. [17,56] serves as a qualitative model for SLPS behaviour. Though more realistic models are available in the literature [52,53], the model from Campbell and Liu et al. serves as a more accessible approach to modeling general SLPS behaviour [17,56]. Liu et al. comment on this, noting that the qualitative characteristics of the model agree with the expected response of real systems [17]. The successful application of this model to IN718 by Levasseur et al. [18] further affirms this conclusion.

The model presented by Liu et al. predicts the onset of densification and distortion based on the sintering temperature, liquid fraction, and physical properties of the alloy. The model also incorporates the influence of microstructural coarsening on the SLPS behaviour. The aim of the current work was to utilize differential scanning calorimetry in conjunction with the existing theory to model the SLPS behaviour of this MIM NiSA alloy with both time and temperature.

4.4.1.1 SLPS Theory

SLPS causes liquid to form at particle contacts and in the grain boundaries within the powder particles [11]. The liquid formed within the powder particles causes them to soften, enabling densification in response to the capillary forces which develop at the particle contacts [17]. The average capillary force throughout the material acts as a net hydrostatic pressure resulting in isotropic shrinkage. Films of liquid in the powder structure therefore aid densification, but simultaneously reduce the structural rigidity of the material. The softened powder particles can also deform under the force of gravity, leading to a net deformation after densification has occurred. The capillary stress formed during densification is generally much larger than the gravitational force, therefore distortion is unlikely in the initial stages of SLPS. After densification has occurred, the part consists of solid grains with liquid films present at the grain boundaries. At this stage, the capillary forces approach zero while the force of gravity remains constant. Eventually, when the semi-solid structure is weak compared to gravity, the part will slump non-uniformly due to the distribution of gravitational stress with height. Evidently, densification and shape retention in SLPS are both directly related to the liquid film distribution and thickness in the semi-solid structure. The microstructures during the initial and latter stages of the SLPS process are depicted in Figure 4-70.

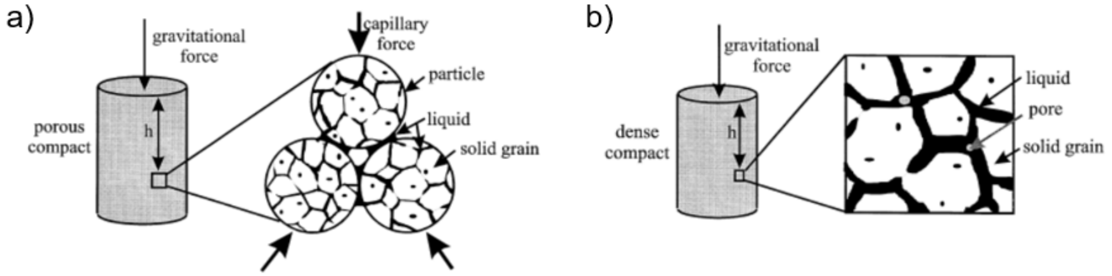

Figure 4-70. Schematics of the microstructures present during SLPS a) in the initial stages when the compact is porous, liquid is present within the powder particles and at grain boundaries, and capillary force is high and b) in the latter stages after the majority of densification has occurred, the microstructure has coarsened, liquid is primarily present at the grain boundaries, and capillary force is near-zero [17].

Reprinted from Acta Materialia, 47, J. Liu, A. Lal, R.M. German, Densification and shape retention in supersolidus liquid phase sintering, 4615-26, 1999, with permission from Elsevier.

The strength of part during SLPS is provided by both the solid bonds present between particles and the viscous resistance of the liquid providing cohesion between particles. Knowledge of the liquid volume and its distribution in the grain boundaries is critical to assessing the rigidity of the material during SLPS. Liu et al. evaluated the rigidity of semi-solid structures during SLPS based on the liquid content and the extent of microstructural coarsening in the material [17]. The fractional grain coverage by liquid, F_c, can be expressed as [17,18,56]:

$$F_c = 2.64\left(\frac{V_L}{a}\right)^{1/2} \tag{3}$$

Where V_L is the liquid fraction present in the semi-solid structure and the parameter a is dependent on the dihedral angle, φ, [17]:

$$a = \sqrt{3} + \frac{3}{\tan\left[30 - \left(\varphi/2\right)\right]} - \left[\frac{30 - \left(\varphi/2\right)}{60}\right] \cdot \left[\frac{\pi}{\sin^2\left[30 - \left(\varphi/2\right)\right]}\right] \tag{4}$$

The distribution of liquid throughout the grain boundaries is therefore dependent on the dihedral angle. An idealized geometry for the intersection of three grains is shown in Figure 4-71 to demonstrate the influence of the dihedral angle on the grain structure. In SLPS, the liquid volume fraction and dihedral angle are typically low and the idealized geometry presented in Figure 4-71 exists for dihedral angles below 60°. This angle determines the stable neck size which forms between adjacent powder particles and is determined by the ratio of the solid-solid and solid-liquid interfacial energies, γ_{SS} and γ_{SL}, respectively.

The extent of solid bonds present in the structure can be defined in terms of contiguity, C_{SS}, which is dependent on the fractional grain coverage by liquid [17]:

$$C_{SS} = 1 - F_C \tag{5}$$

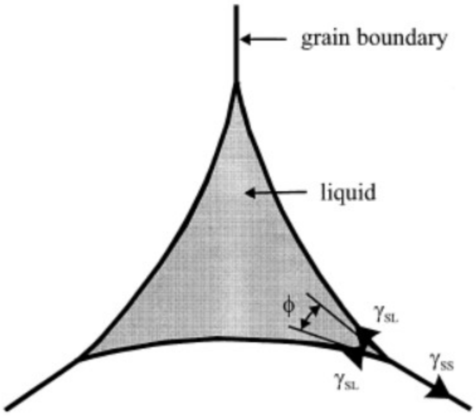

Figure 4-71. Schematic of the ideal geometry formed at the intersection of three adjacent grains. The dihedral angle, φ, dictates the stable neck size formed between particles, the liquid distribution in the grain boundaries, and is a function of the solid-solid and solid-liquid interfacial energy ratio. SLPS systems typically exhibit low dihedral angles associated with the depicted geometry [17].

Reprinted from Acta Materialia, 47, J. Liu, A. Lal, R.M. German, Densification and shape retention in supersolidus liquid phase sintering, 4615-26, 1999, with permission from Elsevier.

Contiguity can be used to determine the grain boundary film thickness, δ, of the liquid phase using the average grain size, *G,* and the liquid and solid volume fractions V_L and V_S [17]:

$$\delta(1 - C_{SS}) = \frac{G}{3} \cdot \frac{V_L}{V_S} \tag{6}$$

Equation (6) states that the liquid film thickness increases as the grain size and liquid volume fraction increase. If the liquid film thickness increases, the resistance to movement between two grains, *R*, is decreased [17]:

$$R = \frac{\eta_L v A^2}{\delta^3} \tag{7}$$

Where η_L is the liquid viscosity, v is the relative velocity of two adjacent grains, and A is the grain face surface area. Therefore, the fractional grain coverage by liquid and liquid film thickness are dependent on the dihedral angle, average grain size, and liquid volume fraction. The dihedral angle is a physical constant for a given material, while the grain size and liquid fractions are variable with the processing conditions. The fractional grain coverage by liquid and the liquid film thickness both influence the structural rigidity of the material, and therefore play a role in controlling both densification and distortion.

Liu et al. derived a softening parameter, ζ, which combines multiple microstructural parameters to model the rigidity of the semi-solid structure during SLPS. An upper and lower bound on the SLPS process were defined as the onset of densification and onset of distortion [17]:

$$\zeta_{dens} = \left(\frac{\alpha\eta_L}{\sigma_{SS}}\right)^{1/3} \cdot \frac{(1 - C_{SS})^{1/5}}{(A - C_{SS})^{1/3}}; \quad A = \frac{2.6\gamma_{LV}\cos\theta}{D\left(1 - \left(\rho_g/\rho\right)^{1/3}\right)} \cdot \frac{1}{\sigma_{SS}} \tag{8}$$

$$\zeta_{dist} = \left(\frac{\alpha\eta_L}{\sigma_{SS}}\right)^{1/3} \cdot \frac{(1 - C_{SS})^{5/3}}{(B - C_{SS})^{1/3}}; \quad B = \frac{\rho g h}{2} \cdot \frac{1}{\sigma_{SS}} \tag{9}$$

$$\zeta = \frac{G^{1/3}}{3} \cdot \frac{V_L}{V_S} \tag{10}$$

where α is a velocity constant, σ_{ss} is the strength of the solid-solid bonds, ρ_g is the green density, ρ is the instantaneous sintered density, D is the average particle size, and γ_{LV} is the liquid-vapour surface energy. The onset of densification criterion in Equation (8) is dependent on the shear force between two grains overcoming the resistance to grain sliding. Based on this criterion, there is a critical liquid film thickness, δ, at a given contiguity and grain size which will cause densification. The onset of distortion in Equation (9) occurs when the force of gravity is greater than the resistance of the structure to deformation. This criterion is also satisfied at a critical liquid film thickness with a given contiguity and grain size. The generalized softening parameter, ζ, in Equation (10) is dependent on the grain size and liquid fraction formed. The contiguity, which is dependent on the fractional grain coverage by liquid, is also encompassed in the model to reflect the microstructural characteristics during SLPS. Liu et al. also highlight that the upper and lower bounds of the densification and distortion are dependent on η_L, σ_{ss}, and C_{SS}, all of which are temperature dependent and none of which have a time dependence [17].

4.4.2 Experimental Methods

MIM NiSA samples were prepared and de-bound according to methods previously described in Chapter 3. The de-bound samples were supersolidus liquid phase sintered using DSC in order to measure the enthalpy during melting and solidification for each temperature. The experimentally determined enthalpies for melting and solidification were used to calculate the liquid fraction formed according to Equation (1). The liquid fraction and average grain sizes were then used to determine their relationship with SLPS hold time and temperature. These relationships were then used as inputs to the outlined SLPS model from Liu et al. [17].

4.4.3 Results and Discussion

In Section 4.2 it was discovered that the liquid fraction and grain size are initially constant upon reaching the SLPS temperature of 1345°C. After an initial 10min hold, both the liquid fraction and grain size were found to increase substantially. This dynamic response is important to model because the grain size and liquid fraction both influence the microstructure's liquid film thickness and resistance to distortion. In order to apply the model to the SLPS data, time zero was defined as the time at which grain growth starts. In the 1345°C tests, grain growth started after 10mins of isothermal hold time. Therefore, 10mins was defined as time zero for the SLPS model. A power law relationship was then fitted to the 1345°C data sets for both grain size and liquid fraction and the time zero data point was adjusted to maximize the R-squared values. The resulting data sets are presented in Figure 4-72 and Figure 4-73 along with their fitted equations. The time-zero data points were adjusted to *t=0.5mins* (30sec) after the initial 10min hold to obtain the best fit.

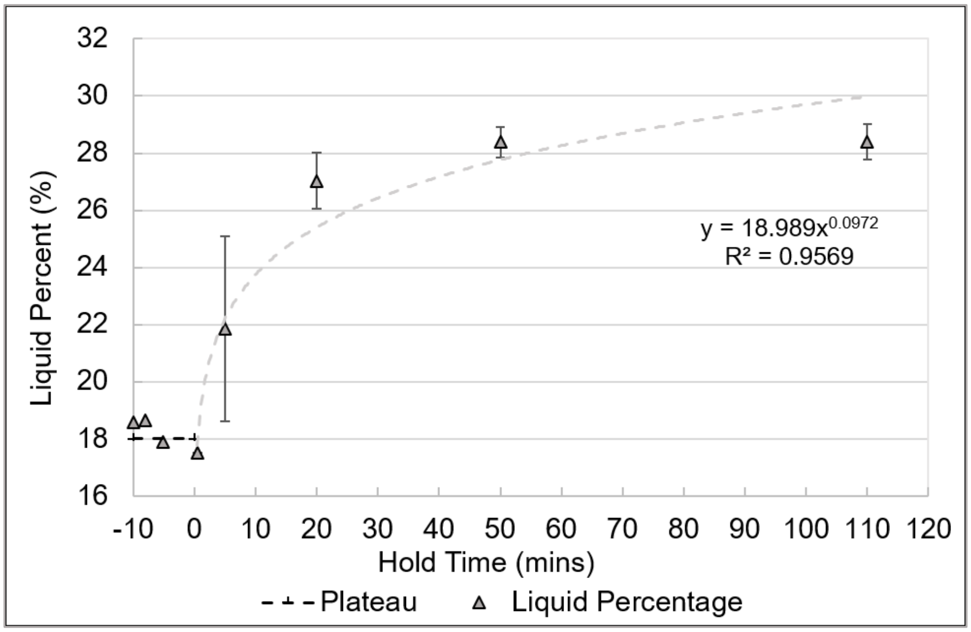

Figure 4-72. Liquid percentage in the MIM NiSA during isothermal hold time at 1345°C with fitted power-law equation after initial 10min plateau.

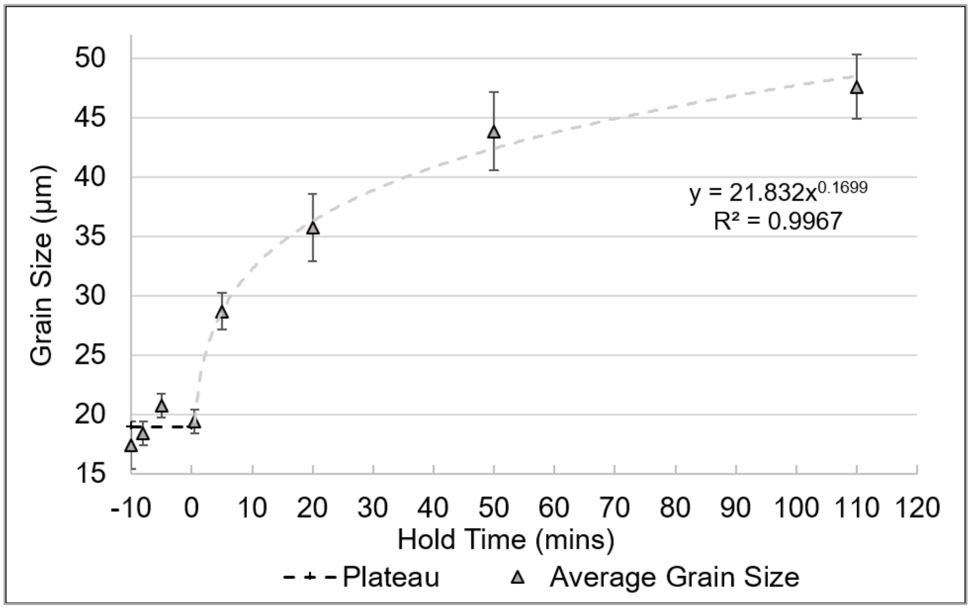

Figure 4-73. Average grain size in the MIM NiSA during isothermal hold time at 1345°C with fitted power-law equation after initial 10min plateau.

Figure 4-72 demonstrates that there is a significant increase in the liquid content over isothermal hold time once the initial 10min threshold has been exceeded. The dynamic nature of the liquid fraction beyond this threshold is caused by the solution of MC carbides and the subsequent time required for the NiSA to re-establish a stable equilibrium between the solid and liquid phases (see discussion in Section 4.2). Previously developed SLPS models have not incorporated the time dependence of the liquid fraction due to relatively short times to reach equilibrium [17,18]. However, the NiSA in this study exhibits a sluggish segregation response to the solution of the MC carbides, taking over 50 minutes from the time of their dissolution to approach a new equilibrium liquid fraction. Therefore, the time dependency of the liquid fraction must also be incorporated into the SLPS model for this NiSA.

The SLPS grain size, presented in Figure 4-73, appears to be closely related to the liquid fraction given its similar power-law relationship. Based on this observation, the grain coarsening of the MIM NiSA also exhibits a time dependency. Both the liquid fraction and grain size are dependent on temperature as well as time in the case of this NiSA, a feature that has not been reported in the literature for other SLPS PM superalloys.

To incorporate the time dependency of the liquid fraction and grain size into the existing SLPS model, the slope and exponent values for each function of time were plotted against temperature to determine the relationship between temperature and the power-law constants. These relationships were solved for the 1340, 1345, and 1350°C SLPS temperatures to determine the power-law constants for the liquid fraction and grain size. These relationships represent the liquid fraction and grain size as a function of both time and temperature. The 1335°C temperature exhibited different liquid fraction and grain growth behaviour than the higher SLPS temperatures suggesting that the SLPS mechanisms being modeled were not yet active. Therefore, the 1335°C temperature was excluded from the model.

The generalized softening parameter was then calculated from Equation (10) as a function of time and temperature using the experimentally determined grain size and liquid fraction relationships. The onset of densification and distortion were also calculated as function of time and temperature using Equations (8) & (9). These equations were solved for σ_{ss} using the experimental value for ζ_{dens}, a viscosity of 7.2mPas for liquid IN718 at 1336°C [57], a dihedral angle of 35° [28], and a velocity constant of 3.3E5m/s [18]. The physical parameters used in the model are outlined in Table 4-3. The strength of the solid bonds was found to be 73.7MPa which falls within the wide range of yield strengths reported for semi-solid systems [18,28,58].

Table 4-3. Parameters used to calculate the onset softening parameters for densification and distortion.

Viscosity η_L (mPa·s)	Dihedral Angle φ (deg)	Wetting Angle θ (deg)	Surface Energy γ_{LV} (J)	Green Density ρ_g	Sintering Onset Density ρ_{onset}	Distortion Onset Density ρ_{dist}	Sample Height *h* (mm)
7.2 [57]	35 [28]	0 [28]	1.5 [28]	0.6	0.61	1	3.65

The modeled results for the softening parameter over time at the various SLPS temperatures are presented in Figures 4-74 to 4-76. The curve derived from experimental results is shown as a solid line. The evolving onset of distortion and densification predictions are also plotted against SLPS hold time as dashed lines and represent the upper and lower bounds of the SLPS process.

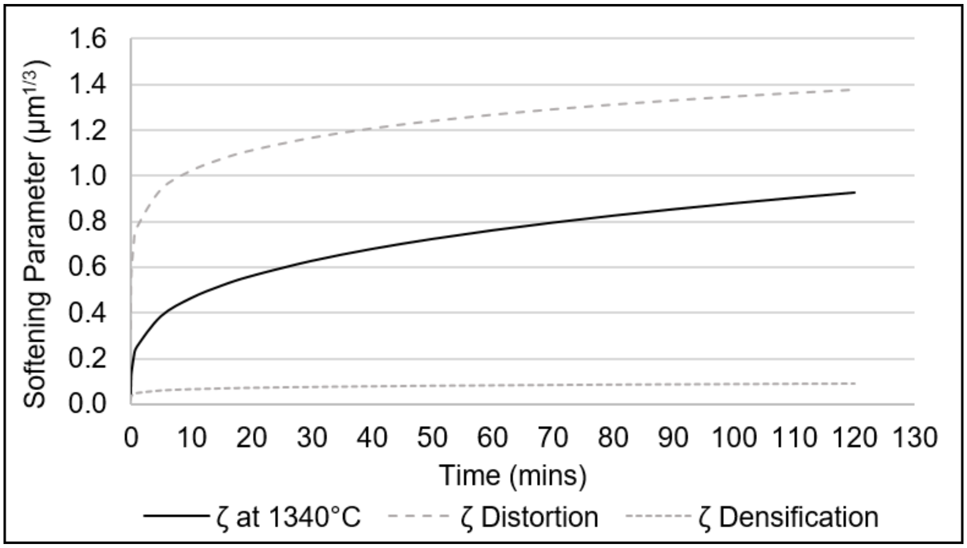

Figure 4-74. Modeled softening parameter as a function of hold time at 1340°C with the onsets of densification and distortion.

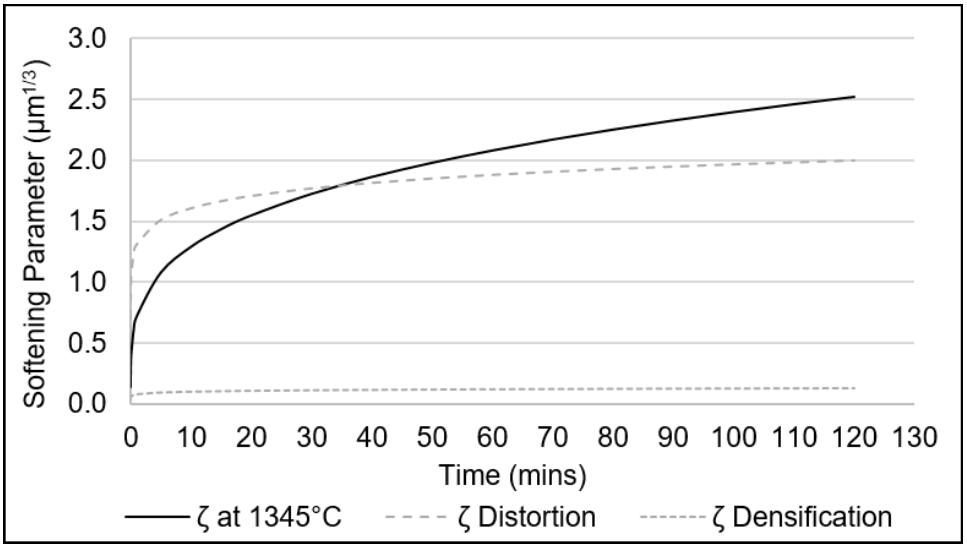

Figure 4-75. Modeled softening parameter as a function of hold time at 1345°C with the onsets of densification and distortion.

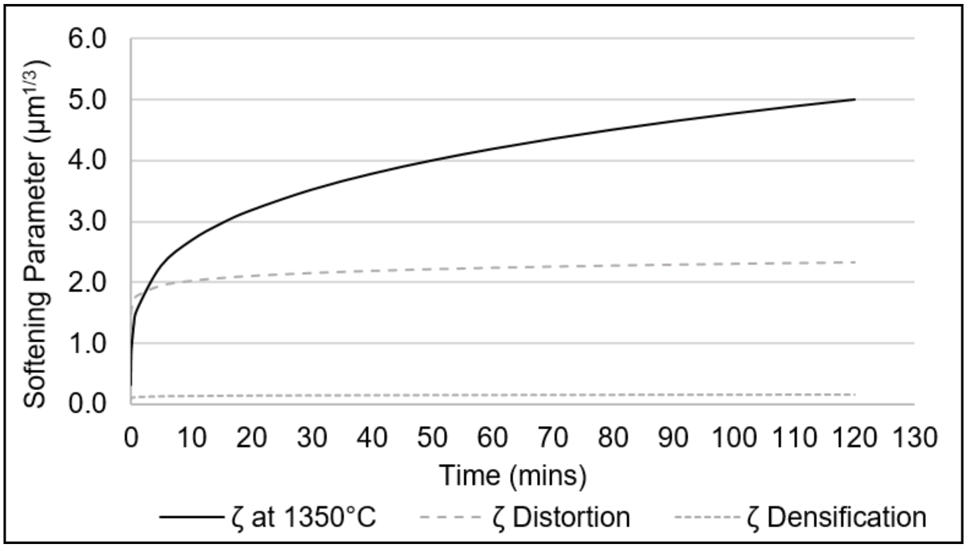

Figure 4-76. Modeled softening parameter as a function of hold time at 1350°C with the onsets of densification and distortion.

The predictions for the onset of densification is relatively constant over time and is lower than the predicted onset of distortion at all SLPS temperatures. The onset of distortion shows an initially rapid increase with SLPS time before reaching more steady values after 10 and 30 minutes. The upper and lower dashed onset lines represent the operating range of the SLPS process where densification will occur without distortion. This predicted operating range widens with increasing SLPS temperature.

The experimental softening parameter increases rapidly at the beginning of the SLPS process due to the increasing liquid fraction and grain size. It is important to remember that time zero in Figures 4-74 to 4-76 represents the time at which grain growth begins. The start of grain growth is associated with the solution of grain boundary MC carbides and occurs after approximately 10mins of hold time at the SLPS temperature of 1345°C. Time zero was assumed to be at the same 10min threshold for all modeled temperatures.

Once grain boundary MC carbides go into solution and the liquid fraction has increased, the alloy starts to approach a new equilibrium composition. As this occurs, the softening parameters trend toward a more steady state value. The 1340°C SLPS model in Figure 4-74 predicts that the NiSA will sinter within the operating range defined by the onset lines. The SLPS specimens at this temperature exhibited densification without distortion, supporting the modeled results (refer to Section 4.2). At 1345°C, the softening parameter of the material rises faster than the onset of distortion, crossing above the upper bound after approximately 30mins (40mins of actual SLPS hold time and 30mins beyond the MC solution threshold). Based on this model, the material will retain its shape at SLPS hold times less than 40mins and lose its shape at times equal to or greater than 40mins at 1345°C. The DSC specimens agree with the model, exhibiting no slumping or significant edge rounding in the 15 and 30min hold tests and notable shape loss in the 60 and 120min hold tests. The 1350°C model predicts that the material will soften beyond the onset of distortion almost immediately upon exceeding the 10min MC solution threshold. This was observed to be the case in the DSC specimens where none of the samples completely retained their shape. Interestingly, the softening parameter in the 1350°C model continues to increase over the hold time, surpassing the distortion bound of the model by a factor of two by 120mins. The experimental results also confirmed this trend as the 1350°C samples were the only samples to slump, decreasing in height under the weight of gravity after all hold times.

During the initial stages of SLPS for this MIM NiSA, grain boundary MC carbides are dissolved. After a critical threshold, dissolution of the MC carbides causes the liquid fraction to increase as the material progresses toward a new stable equilibrium liquid fraction. The microstructure also coarsens during this process, causing the grain size to increase along with the increasing liquid fraction. These trends are clear in Figure 4-72 and Figure 4-73, where the liquid fraction and grain size increase according to a power-law relationship over the hold time. Assuming the original powder particles densify quickly in the initial stages of SLPS, the following liquid fraction increase causes the grain boundary liquid film thickness to increase. The formation of additional liquid in the grain boundaries increases the fractional grain coverage by liquid according to Equation (3), decreasing the contiguity and resistance to deformation as stated by Equations (5) and (7). Therefore, the liquid fraction increase observed during SLPS causes the material's overall rigidity to decrease. In addition, the increasing liquid fraction and its distribution throughout the grain boundaries aids microstructural coarsening and grain growth. As grains grow at an isothermal SLPS temperature, the total grain boundary area is reduced leading to further increases in the grain boundary liquid film thickness, causing additional softening of the material.

The presented model is supported by the macroscopic results which exhibit deformation at times and temperatures above the predicted onset of distortion. Samples sintered at lower SLPS temperatures did not exhibit enough softening over the hold time to distort. Softening likely continued well past the onset of distortion in higher temperature tests due to the substantial microstructural coarsening. In addition, each SLPS temperature would result in a separate equilibrium liquid fraction according to the phase equilibrium at the given peak temperature. This means that higher SLPS temperatures will result in larger softening parameters, a trend which is correctly captured by the model.

The liquid fraction and grain size relationships used in the presented model are plotted with the actual experimental data in Figure 4-77 and Figure 4-78, respectively. The modeled liquid fraction behaviour exhibits good agreement with the measured liquid fractions for all three SLPS temperatures. The highest percent error between the modeled and experimental liquid fraction was 26% for 1345°C/5mins while the lowest percent error was 0.8% for 1340°C/50mins. The modeled grain size also agrees with the measured grain sizes for all three SLPS temperatures. The highest percent error between the modeled and experimental grain size was 13% for 1350°C/20mins while the lowest percent error was 0.5% for 1340°C/50mins. The highest percent error for both parameters occurs during the first 20mins beyond the MC solution threshold, which is the most transient time period for the microstructure. However, the model and measured data sets show reasonable agreement overall, with the majority of the modeled behaviour exhibiting less than 10% error with the measured data for both liquid fraction and grain size.

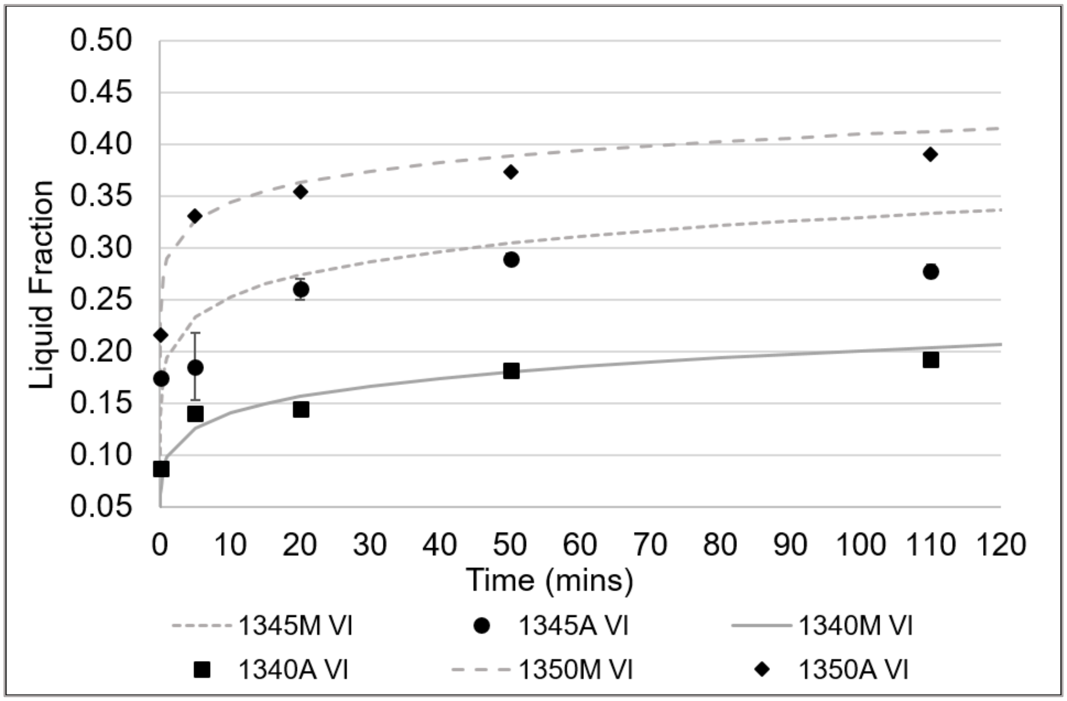

Figure 4-77. **Comparison of the modeled ("M", lines) and actual ("A", black markers) liquid fraction (Vl) over time for each SLPS temperature.**

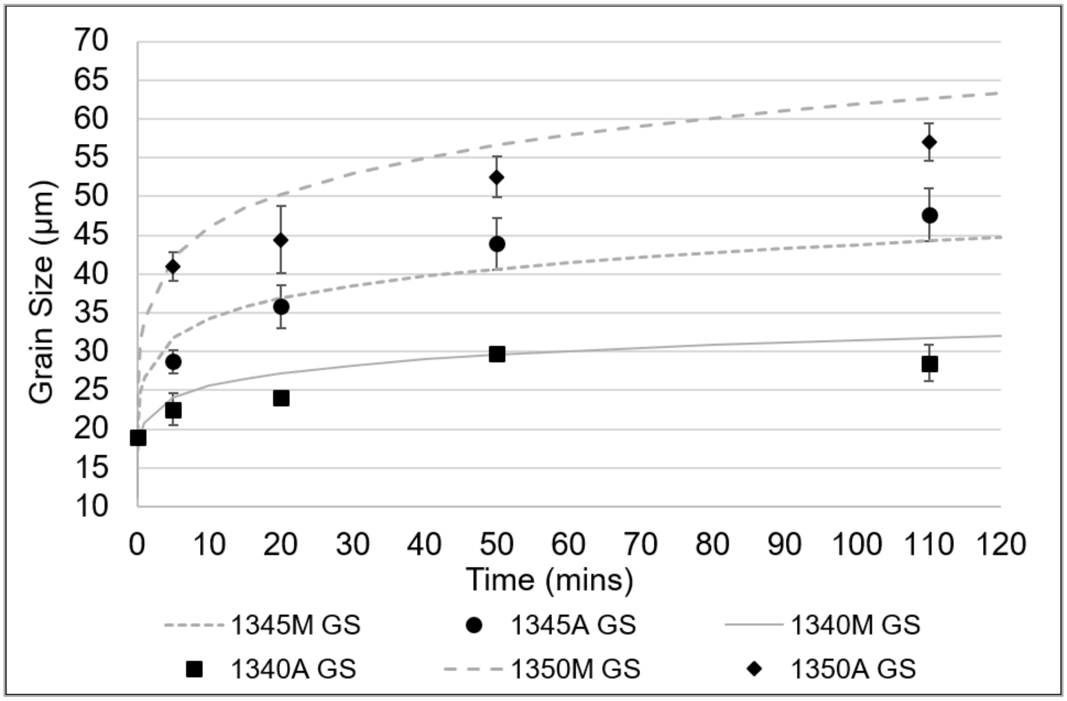

Figure 4-78. **Comparison of the modeled ("M", lines) and actual ("A", black markers) grain size (GS) over time for each SLPS temperature.**

The sluggish segregation response of the NiSA alloy to the solution of MC carbides complicates the SLPS process. For instance, sintering the NiSA alloy at 1340°C for 60mins leads to a similar final liquid fraction to sintering at 1345°C for 15mins with the same resulting grain size. However, sintering at 1345°C for 60mins forms less liquid than 1350°C for 30mins, but the resulting grain sizes are almost identical. The dynamic behaviour of the liquid fraction in NiSA makes predicting these SLPS results challenging as both time and temperature influence the process to different extents via different mechanisms. The temperature determines the initial and final volume fractions of the solid and liquid phases as well as their equilibrium compositions. The temperature also controls the diffusion rates in the solid and liquid, the kinetics of MC carbide dissolution, and the liquid viscosity. The hold time controls the instantaneous liquid fraction and grain size, both of which determine the fractional grain coverage by liquid and the material's overall rigidity.

Therefore, process designers require a comprehensive understanding of the material's behaviour above the solidus temperature to practically apply SLPS to complex alloys such as this MIM NiSA. The SLPS model presented in this work captures the time-temperature dependency of the liquid fraction and grain size on the rigidity of the material, enabling a reasonable prediction of SLPS behaviour for a given time and temperature.

4.4.4 Conclusions

The solution of grain boundary MC carbides during the initial stage of SLPS causes the liquid fraction to increase over an isothermal hold time. Simultaneous grain growth is aided by the transient liquid fraction, making grain size a function of time as well. Both the liquid fraction and grain size influence the material's overall rigidity during SLPS, causing the softening of the material to be transient with time. Therefore, a modified SLPS model which incorporates the time dependency of these parameters above the solidus temperature was developed for the MIM NiSA. The behaviour of both the grain size and liquid fraction over time and temperature were incorporated into the accepted SLPS model to determine the instantaneous softening parameter of the material and onsets of both densification and distortion. The modeled results predict that no deformation will occur at 1340°C for hold times under 120mins. The model also predicts that distortion will begin to occur after 40mins at 1345°C and immediately upon MC carbide dissolution at 1350°C. Macroscopic observations of shape retention from previous work in Section 4.2 support the modeled results, indicating that the modifications made to the model for this NiSA are appropriate. The results also illustrate the necessity for metallurgists to have thorough knowledge of an alloy's behaviour above the solidus temperature when attempting to apply SLPS as a consolidation technique for geometry critical processes such as MIM.

4.5 Grain Boundary Evolution during Supersolidus Liquid Phase Sintering of a MIM Nickel-Based Superalloy

4.5.1 Introduction

The supersolidus liquid phase sintering (SLPS) of a metal injection molded (MIM) Nickel-base superalloy (NiSA) has been evaluated in Section 4.2. During SLPS of this MIM NiSA, the liquid fraction formed at the SLPS temperature increases substantially over isothermal hold time due to the segregation of solute elements. Significant grain growth also occurs during the SLPS process, resulting in grain sizes in the 40-60μm range. Short hold time

SLPS tests led to the discovery of an initial incubation period during the first 10mins of sintering at 1345°C. During this period, neither the liquid fraction nor grain size increase, indicating that the solid and liquid phases exist in equilibrium and that grain growth is not yet active. Beyond the initial 10min hold, the liquid phase and grain size both exhibit a dynamic response, rapidly increasing. By 15mins of hold time at 1345°C the liquid percentage has increased by approximately 5% and the grain size has increased by about 10μm. Longer SLPS hold times result in additional liquid phase and grain size increases, but the growth rate gradually reduces with continued hold time.

For powder metallurgy Ni-superalloys, the small starting particle size results in a fine grain size which cannot be easily modified [3]. This fine grain size is detrimental to high temperature creep properties because of the higher grain boundary area available for grain sliding to occur [5,7]. The inability to increase the grain size in some Ni-superalloys has been previously observed in literature [3,30] and in Section 4.1 of this work. The Ni-superalloys commonly rely on discrete carbide particles to pin the grain boundaries and resist grain boundary sliding during high temperature creep [1–3,5,37,40]. These carbides are generally critical to the alloy's high temperature properties [2]. However, the carbides also restrict grain boundary mobility and can impede grain growth [2,3,30]. Similarly, oxide particles which form in the grain boundaries due to poor sintering atmosphere conditions can also prevent grain growth [3] (also refer to Section 4.1). Determining the evolution of the grain boundary structure during the first 15mins of SLPS will identify the mechanism(s) of grain growth activation in the MIM NiSA. In addition, the composition of grain boundary phases over time at temperature may help explain the rapid liquid fraction growth upon surpassing 10mins at 1345°C.

In order to understand the initial plateau in the liquid fraction and grain size, the grain boundary structure was analyzed as the SLPS hold time was increased. Interrupted SLPS tests at 1345°C for 0, 2, 5, 10, and 15min hold times were evaluated using SEM-EDS to study the evolution of the NiSA's grain boundaries. Emphasis was placed on the precipitate phases present and changes in the local grain boundary chemistry with time and temperature.

4.5.2 Results and Discussion

4.5.2.1 SLPS Results

The average liquid fraction and grain size after SLPS at 1345°C for different hold times are presented in Figure 4-79 and Figure 4-80, respectively. A horizontal line has been added to the initial plateau in each data set to help demonstrate the observed response of the microstructure. The initial liquid content remains constant at approximately 18% liquid for the first 10mins of hold time and there is a substantial increase in liquid fraction by 15mins of hold time. The average grain size remained sub-20µm for the first 10mins of hold time, but was notably larger after 15mins of hold time. Figure 4-79 and Figure 4-80 suggest that there is a sudden transition in the material between 10 and 15mins of hold time at 1345°C which causes rapid growth of the liquid fraction and grain size. The fact that both responses appear to start simultaneously also indicates that the liquid fraction growth does not govern the grain growth directly.

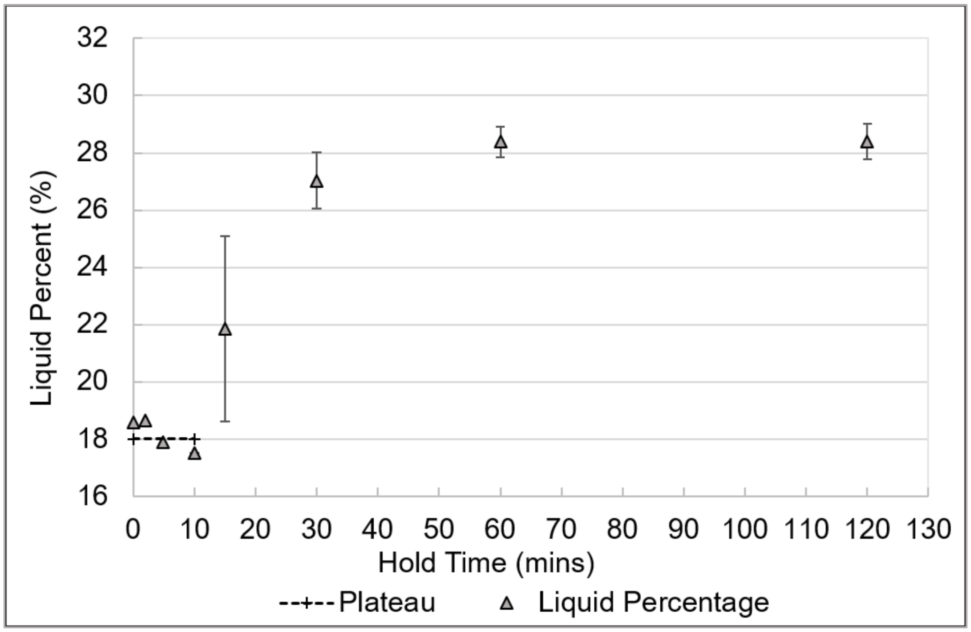

Figure 4-79. **Liquid percentage in the MIM NiSA during isothermal hold time at 1345°C.**

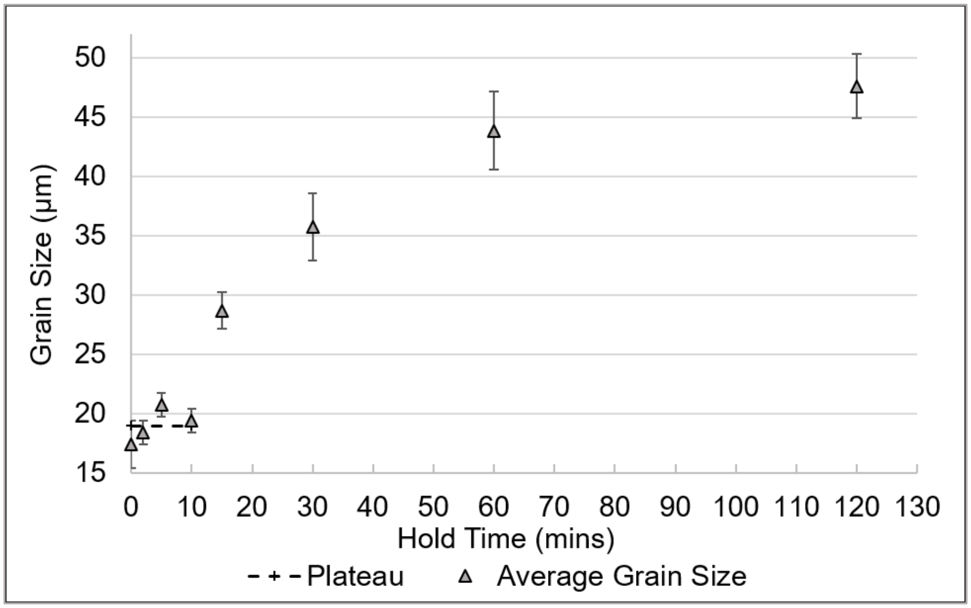

Figure 4-80. **Average grain size in the MIM NiSA during isothermal hold time at 1345°C.**

4.5.2.2 SEM-EDS Analysis

Low and high magnification SEM micrographs of the MIM NiSA grain boundaries for 0, 2, 5, and 10min hold times are presented in Figure 4-81 and Figure 4-82, respectively. The lower magnification images demonstrate that the grain size remains constant over the first 10mins of hold time. The grain boundaries, which appear bright white, also contain numerous discrete carbide phases. The high magnification images reveal more detail about the carbide morphology and grain boundary structure. The cross sections in Figure 4-81 and Figure 4-82 also demonstrate that although the NiSA grain size does not change significantly during the first 10mins at 1345°C, the grain boundary structure is altered.

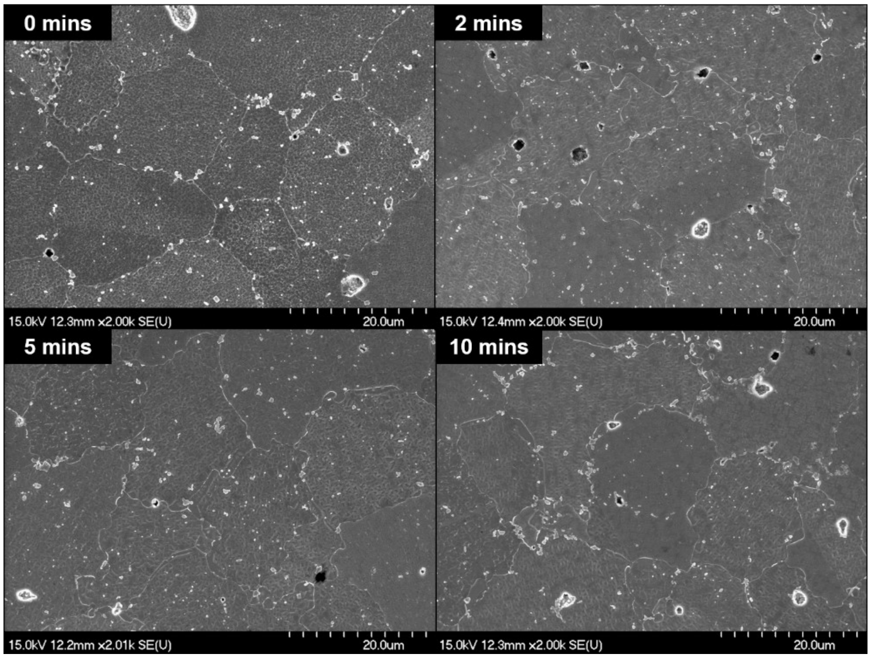

Figure 4-81. SEM micrographs of SLPS samples held at 1345°C for 0, 2, 5, and 10mins.

The waterless Kalling's reagent used to etch the sample cross sections preferentially dissolves the γ' phase, leaving protruding ridges of γ phase in the grain boundaries which have a higher degree of secondary electron, SE, emission [35]. This etching effect causes the γ-γ grain boundaries in many Ni-superalloys to appear bright white. EDS analysis of these grain boundary regions confirmed that they were the base NiSA composition.

Both globular and blocky carbide phases can be observed in the grain boundaries in Figure 4-81 and Figure 4-82. EDS analysis of these precipitate phases confirmed that the grain boundary globules were rich in W and Cr while the blockier phases were rich in Ta and another RM. $M_{23}C_6$ carbides are generally Cr rich, can contain W, and have a globular morphology which is consistent with those carbides found in the MIM NiSA grain boundaries [2]. Mixed MC carbides containing Ti, Ta, RM, and W are also common in high refractory element containing Ni-superalloys, supporting the formation of blocky RM-Ta mixed MC carbides in the grain boundaries [2,43]. In addition, the grain boundaries in Figure 4-81 appear to become wavier with increasing hold time and coarse γ' precipitates can be observed adjacent to the grain boundaries in Figure 4-82.

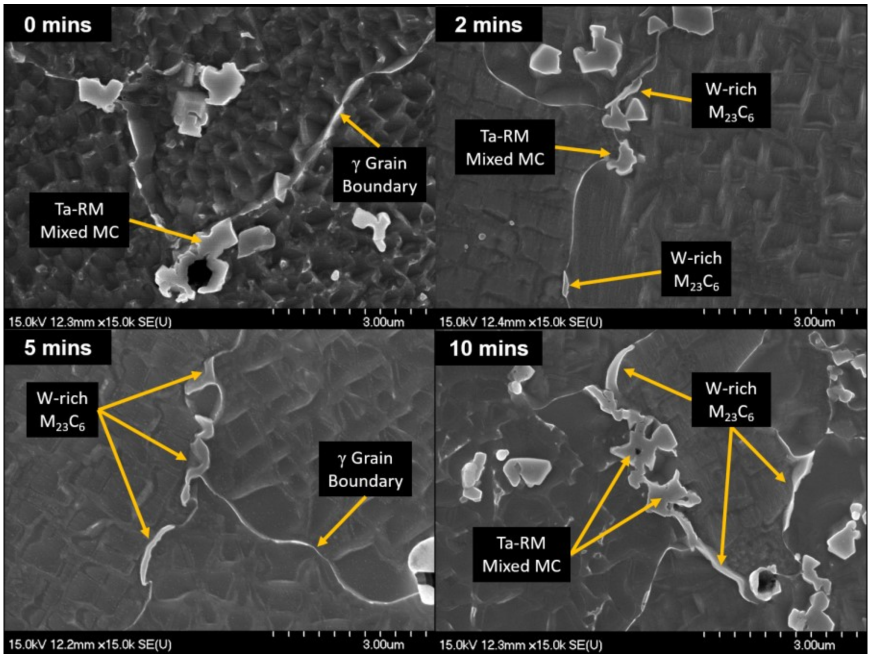

Figure 4-82. **SEM micrographs of the SLPS NiSA grain boundaries held at 1345°C for 0, 2, 5, and 10mins.**

A high magnification micrograph of a γ-γ grain boundary in the 0min SLPS sample is presented in Figure 4-83. These γ-γ grain boundary ridges are present throughout the sample, are sub-500nm in width, and appear bright white due to the high contrast from increased SE emission. The γ-γ grain boundaries also have the morphology of a γ matrix film with the cuboidal γ' precipitates dissolved on each side. Comparing Figure 4-81 and Figure 4-82 it is evident that the wider, globular, phases in the grain boundary are carbides while EDS analysis of the thin, bright sections of the grain boundaries consistently detected the base NiSA composition.

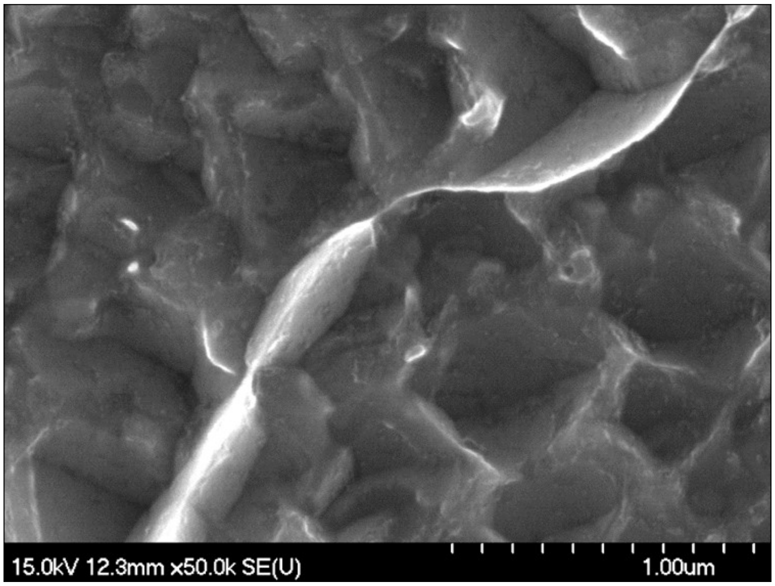

Figure 4-83. High magnification micrograph of a γ-γ grain boundary ridge in the MIM NiSA sintered at 1345°C for 0mins. The ridges appear bright white due to their higher secondary electron emission.

SEM micrographs taken at different magnifications are presented side-by-side in Figure 4-84 and Figure 4-85 to compare the 0 and 10min microstructures and the 10 and 15min microstructures, respectively. Figure 4-84 demonstrates once more that the grain size does not change significantly over the first 10mins of hold time at 1345°C, however the grain boundaries become wavier after the 10min hold. The primary grain boundary carbides also appear to be coarser along with the γ' precipitates after 10min hold time. Figure 4-85 shows that there is a substantial change in grain size and grain boundary structure after 15mins of hold time at 1345°C. The majority of primary MC carbides have been removed and the γ' precipitates coarsen considerably. The bright contrast from the γ-γ grain boundaries is no longer observed throughout the grain boundaries, suggesting that the grain boundary etches differently after 15mins of hold time. One explanation for this change is that the increased volume fraction of liquid and subsequent precipitation of coarse γ' in the grain boundaries removes the γ-γ grain boundary structure which is resistant to the etchant.

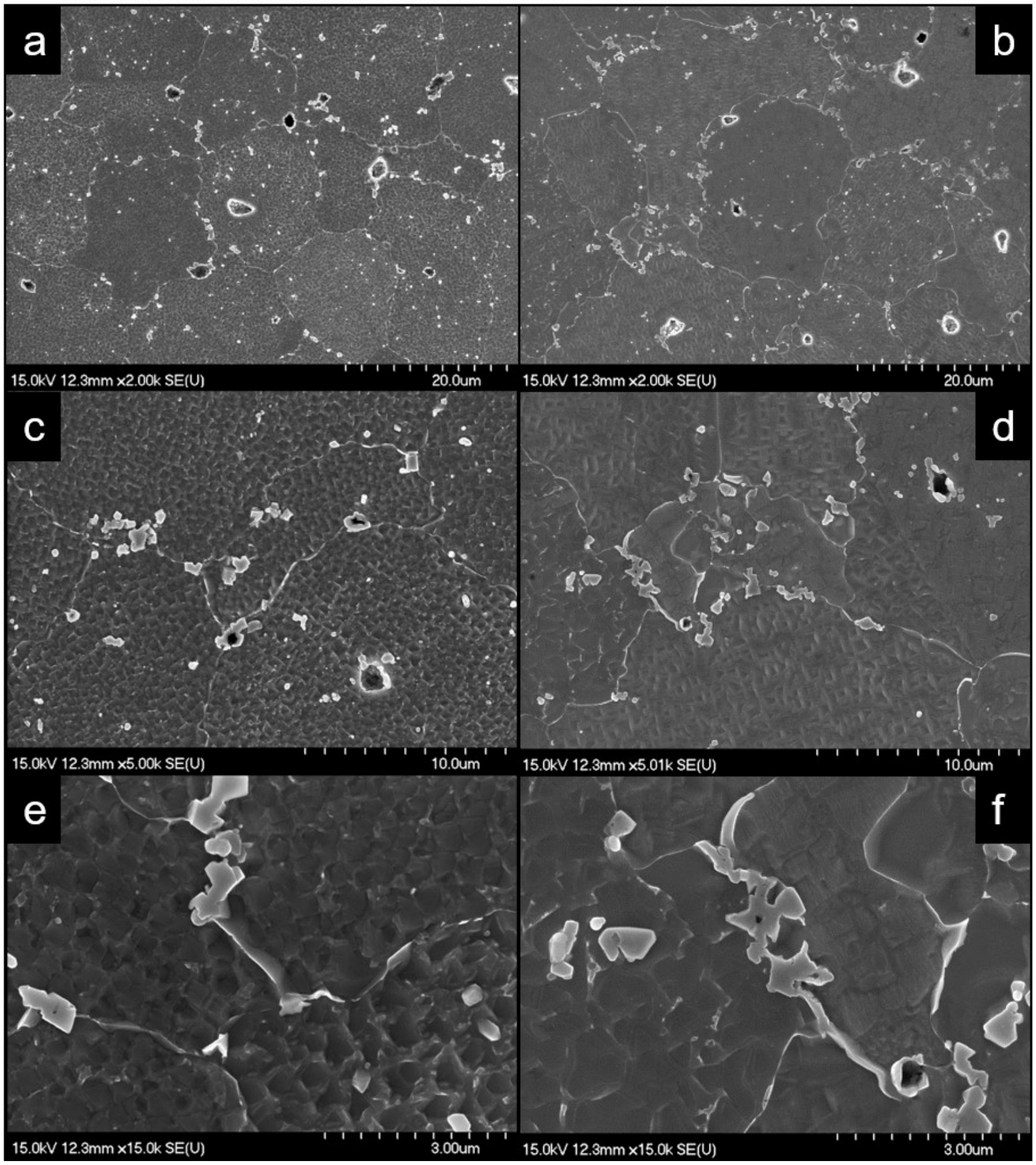

Figure 4-84. Different magnification SEM micrographs of the grain boundaries in the MIM NiSA sintered at 1345°C for 0mins (a, c, e) and 10mins (b, d, f).

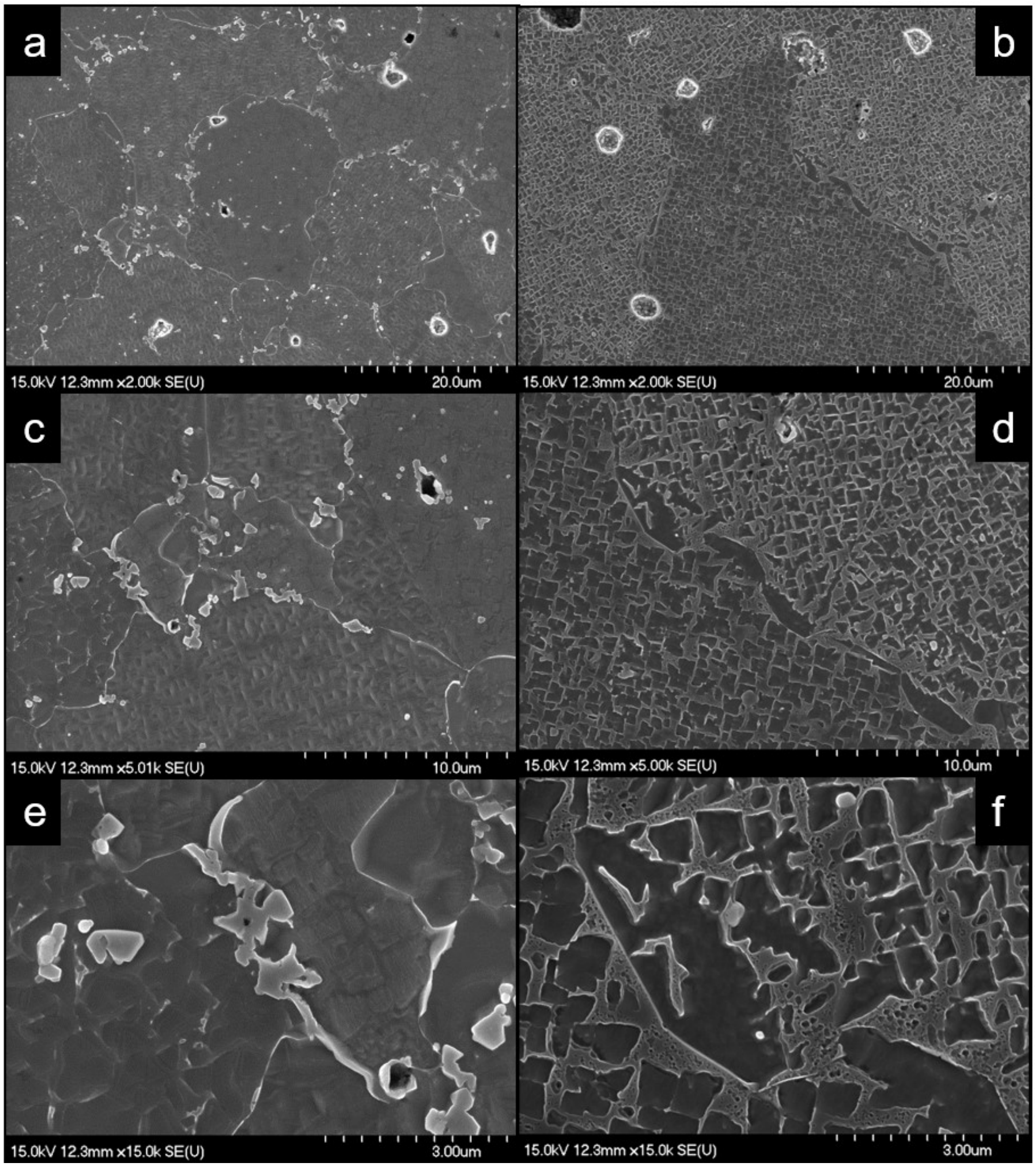

Figure 4-85. Different magnification SEM micrographs of the grain boundaries in the MIM NiSA sintered at 1345°C for 10mins (a, c, e) and 15mins (b, d, f).

SEM-EDS analysis was also performed on MIM NiSA samples sintered in the solid state at 1100, 1200, and 1300°C for 1 hour to determine the primary MC carbide composition on the prior particle boundaries (PPBs) and in the grain boundaries below the solidus temperature. Different magnification SEM micrographs of the 1100°C/1hr and 1200°C/1hr

MIM NiSA samples are presented in Figure 4-86. SEM micrographs of the sample sintered at 1300°C/1hr are shown in Figure 4-87.

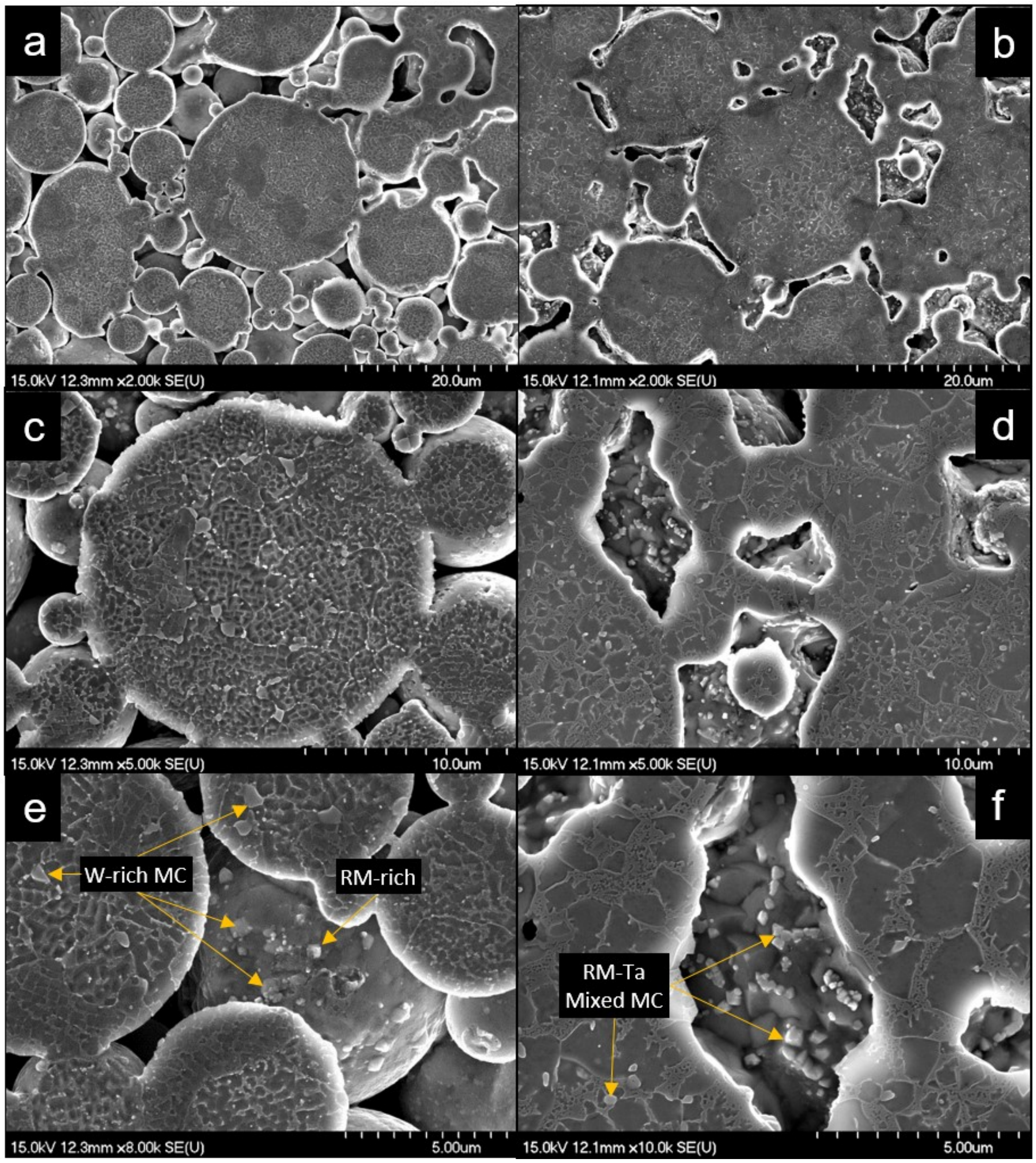

Figure 4-86. Different magnification SEM micrographs of the MIM NiSA sintered at 1100°C for 1hr (a, c, e) and 1200°C for 1hr (b, d, f).

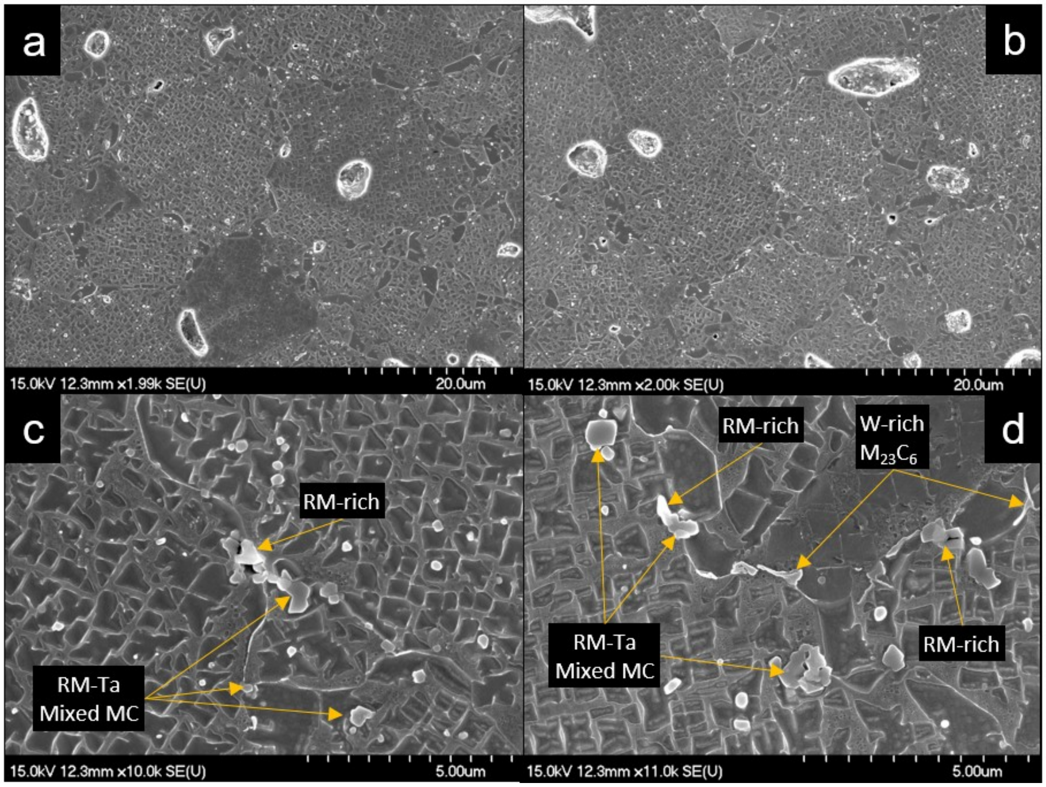

Figure 4-87. Different magnification SEM micrographs of the MIM NiSA sintered at 1300°C for 1hr showing overall microstructure (a, b) and grain boundary structure (c, d).

After 1hr at 1100°C (Figure 4-86a) the MIM NiSA exhibits a microstructure consistent with the initial stage of solid state sintering [11]. At this stage, the powder particles have bonded together to form necks and minor consolidation of the powder structure has occurred. The microstructure of the individual powder particles can be observed to be polycrystalline, containing individual ultra-fine grains and grain boundaries. In Figure 4-86c and Figure 4-86e the powder particles can be observed to contain W-rich MC carbide particles as well as many fine, RM-rich carbide particles. The free surfaces of the particles, shown in Figure 4-86e, also have a high number of W-rich MC particles.

The MIM NiSA has reached the intermediate stage of sintering after 1hr at 1200°C (Figure 4-86b). The powder particles exhibit a large degree of coalescence and densification of the powder structure has occurred. Figure 4-86d and Figure 4-86f show that there is a substantial change in the powder's internal microstructure from sintering at 1100°C to sintering at 1200°C. The individual particles appear to have undergone significant microstructural coarsening where the grain size and γ' size have both increased. Comparison of Figure 4-86c and Figure 4-86d indicate that the ultra-fine internal grains within the powder particles at 1100°C have been completely removed at 1200 °C. As reported in an earlier chapter, the γ' solvus of this alloy was measured to be 1232 °C. Therefore, undissolved γ' precipitates substantially coarsen during this one-hour exposure just below the solvus temperature. The larger, blocky, W-rich MC carbides are also absent from the power particles and their surfaces, suggesting that the W-rich MC carbide is not stable in the alloy at 1200°C. The surfaces of the particles (Figure 4-86d and Figure 4-86f) are instead decorated with many small blocky RM-Ta rich mixed MC carbides, suggesting that the RM-Ta mixed MC carbide forms at the expense of the W-rich MC carbide at the 1200°C sintering temperature.

The sample sintered at 1300°C for 1hr (Figure 4-87) displays the final stage of sintering. The powder structure has been largely consolidated and there is residual porosity that remains to be closed. The grain size remains sub-20μm and the grain boundaries are decorated with RM-Ta mixed MC carbides. Some W-rich $M_{23}C_6$ carbide has formed in the grain boundaries as well, likely precipitating upon cooling. RM-rich carbides and oxide particles are observed throughout the grain boundaries at this stage of sintering, however the most prominent carbide is RM-Ta mixed MC at this stage. The γ' precipitates within the grains are finer than those observed in the 1200 °C sample. Dissolution of the coarsened precipitates would have largely occurred by 1300 °C, with finer γ' precipitates reforming during cooling. The γ-γ grain boundaries appear bright white and the γ' precipitates adjacent to the grains appear coarse. It is important to note that the γ' precipitates after 1300°C/1hr are coarser than the γ' precipitates observed in those samples sintered at 1345°C for 0-10 mins. The γ-γ grain boundaries are also not as bright white. Therefore, the longer time at 1300 °C has caused some grain boundary modification such that its structure seems intermediate between the 0-10 mins and 15 mins, 1345 °C samples.

4.5.2.3 Grain Boundary Evolution

The precipitate phases observed in the MIM NiSA grain boundaries after solid state sintering and after SLPS for 0-10mins are γ', $M_{23}C_6$ carbides, and MC carbides. The size, morphology, and composition of these phases are largely dependent on the thermal history of the alloy and play a major role in determining its high temperature properties [1,2,37,39,41]. Therefore, in order to fully understand the grain boundary structure observed in the SLPS MIM NiSA, the alloy's complete thermal history must be discussed.

The MIM samples were produced using a pre-alloyed NiSA powder which was manufactured via inert gas atomization. The gas atomization process can produce fine powders, such as the NiSA investigated in this study, by rapidly solidifying the atomized alloy melt [2,3]. Prior to atomization, the NiSA melt would have MC carbides in solution. The rapid cooling rate of the alloy during the atomization process leaves very little time for elemental diffusion to occur and limits the amount of MC carbide precipitated in the powder [59]. The retention of MC carbide in solution from the initial melt can cause a supersaturation of free carbon in the pre-alloyed powder particles [2,59]. A similar problem can arise during forging of Ni superalloys where a high temperature soak can cause solution of the MC carbides in the alloy [2]. Rapid cooling after forging then leaves a supersaturation of carbon at the grain boundaries as the MC carbides are retained in solution [2]. Upon subsequent heat treatment, the carbon potential in the alloy favours the formation of MC carbides as continuous films in the grain boundaries [2]. Similarly, it is reasonable to expect that the supersaturation of carbon in the pre-alloyed NiSA particles from gas atomization would favour the precipitation of MC carbide during the subsequent MIM process cycles of de-binding and sintering. Blocky W-rich MC carbides were observed along with fine RM-Ta mixed MC carbides both at the powder free surfaces and in the particle bulk after solid state sintering.

The MIM process itself can also increase the carbon content of the alloy through carbon contamination from the organic binders used during injection molding of the material [4]. The thermal de-binding and pre-sintering processes used in MIM have sufficient time and temperature for solid state diffusion to occur. As de-binding progresses, the decomposition of the organic binders can leave residual carbon on the powder surface, which can then diffuse into the metal particles, increasing the overall carbon content of the alloy [4]. Generally, the only way to avoid excess carbon from being added to the alloy in the de-binding stage is to ensure all organic compounds are completely removed from the powder before pre-sintering and final consolidation [4].

To confirm whether or not the de-binding stage was causing carbon contamination of the MIM NiSA, carbon analysis was completed on the as-received NiSA, de-bound MIM, and sintered MIM materials. The carbon content was determined using an Eltra CS2000 analyzer. The sintered MIM part which was analyzed was sintered in the solid state at

1300°C for 1hr. The carbon content of the NiSA after the various stages of the MIM process are compared in Figure 4-88. The NiSA remains within the alloy chemistry specification for carbon throughout the MIM process and no carbon pick-up was observed. This result indicates that the de-binding and sintering steps employed in this MIM process do not impart excess carbon to the alloy. Therefore, the only source of carbon is the alloy's original chemistry and the powder atomization technique used to manufacture the powder then pre-disposes the alloy to carbide formation in the MIM process.

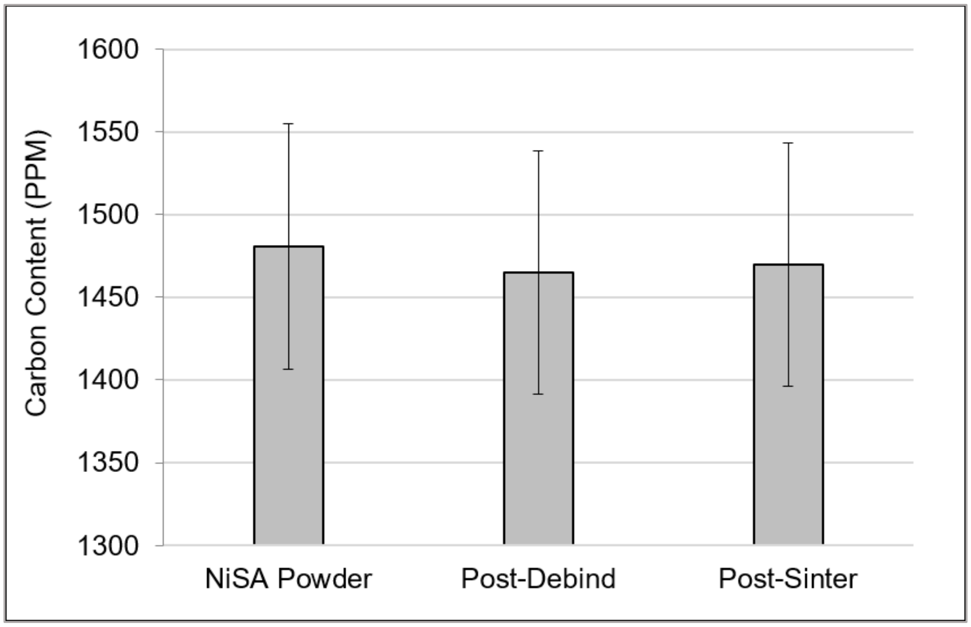

Figure 4-88. Carbon content of the MIM NiSA after each stage of the MIM process determined with 5% relative uncertainty.

The high free carbon content from powder atomization with time at elevated temperatures lends itself to the formation of MC carbides at the powder surfaces. The formation of MC carbides, along with any oxides in the steps prior to powder consolidation, creates a layer of stable compounds at the particle surfaces. This is observed in Figure 4-86e and Figure 4-86f on the powder free surfaces and in Figure 4-87 as RM-Ta mixed MC and RM-rich particles dotting the grain boundaries. These layers of carbides and oxides has been observed to delineate the prior particle boundaries, PPBs, in sintered Ni-superalloys [59]. These PPBs can inhibit grain growth and are highly sensitive to the carbon concentration, concentration of RM elements, and thermal history of the alloy [59]. It is important to highlight that some RM alloying elements act as strong carbide and oxide formers and will promote the formation of these problematic PPB layers [59]. Therefore, despite the benefits of forming certain RM carbides to combat grain boundary sliding, the presence of those same RM elements in the alloy can make sintering MIM NiSAs more challenging. In contrast, the presence this specific RM promotes the formation of stable, discrete MC carbide particles throughout the particle bulk and prevents the formation of more detrimental carbide films at the PPBs [59].

Previous work has concluded that the powder manufacturing route has a major influence on the grain coarsening behaviour of alloy IN-100 [60,61]. In argon atomized IN-100 powder, it was found that grain growth is inhibited by the presence of MC carbides concentrated on the PPBs. Producing the IN-100 powder instead by a rotating electrode process, REP, the grain growth behaviour is similar to that of the cast and wrought versions of the alloy, which exhibit considerable grain growth above 1175°C [60,61]. It was determined that the formation of large carbide particles in the interior of the REP powder particles decreases the concentration of MC carbides at the PPBs, enabling grain growth. Evidently, changes in carbide distribution and the removal of carbides from PPBs can impact the ability to coarsen the grain size of PM superalloys. As such, the concentration of MC carbides at PPBs as a result of the powder atomization process is a likely culprit of grain growth inhibition in the MIM NiSA used in this work.

$M_{23}C_6$ carbide is a stable compound at intermediate temperatures and is known to form from the decomposition of MC carbides during intermediate heating in the following reaction [1,36,37,40]:

$$MC + \gamma \leftrightarrow M_{23}C_6 + \gamma' \tag{11}$$

As a consequence, MC carbides present after powder atomization, may undergo the above reaction in the intermediate stages of sintering with $M_{23}C_6$ formation occurring in parallel with γ' precipitation. This reaction has been observed to take place over a wide range of intermediate temperatures from 650-1050°C [1–3,31,32,36–40]. Since the de-binding and pre-sintering stages in MIM processes generally utilize temperatures in this range [4,14], it is possible for $M_{23}C_6$ carbides to form on the particle surfaces in addition to any MC carbide and oxides which have formed from previous thermal exposure. As well, given the fast solidification of the alloy powder during atomization, it is likely that the powder surface contains a high amount of γ supersaturated solid solution since there was little time to precipitate γ' during freezing. The higher Cr content of the γ phase favours the precipitation of the $M_{23}C_6$ carbide, which is typically Cr-rich [1–3,37,40]. The high amount of γ solid solution in the powder combined with the supersaturation of C from powder atomization would also favour $M_{23}C_6$ carbide formation during de-binding and pre-sintering.

Although some MC carbides may transform to $M_{23}C_6$ at intermediate temperatures, further heating above 1050°C would cause these $M_{23}C_6$ carbides to dissolve back into solution, once again promoting the formation of the more stable MC carbides. Indeed, numerous MC, but no $M_{23}C_6$ carbides, were observed after sintering the MIM NiSA at 1100°C and

1200°C for 1hr. It is reasonable to expect that some $M_{23}C_6$ carbide might re-precipitate during cooling from these temperatures, but it is also possible that the 20°C/min cooling rate used in these experiments was fast enough to prevent the formation of $M_{23}C_6$. However, $M_{23}C_6$ carbides are observed after sintering at 1300°C for 1hr, suggesting that their formation is more related to the peak temperature and/or the exceedance the γ' solvus temperature. As well, any M_6C carbide, which is also only stable at intermediate temperatures, would go into solution by these temperatures in the sintering cycle [2]. RM-Ta mixed MC carbides were observed to form at the expense of W-rich MC carbides at 1200°C. This transformation likely occurs due to the greater high temperature stability of RM-Ta carbides than W carbides. Further heating beyond 1232°C would see the complete dissolution of the γ' precipitates, leaving γ and RM-Ta mixed MC carbides as the constituent phases of the alloy (aside from any stable RM oxides which may have been formed [2]).

MC carbides, and more specifically RM MC carbides, are very stable compounds [2,3]. These carbides are typically referred to as high temperature carbides because they are the first to solidify from the melt of Ni superalloys and may not dissolve completely above the solidus or liquidus temperatures [2,3]. In addition, oxide particles can be even more stable than MC carbides, making them more difficult to dissolve in the melt [2,3]. In solid state sintering, MC carbides and oxide particles remain stable and do not degrade or dissolve. In the MIM NiSA in this study, RM-Ta mixed MC carbides are situated at previous particle boundaries, PPBs, and throughout the grain boundaries due to grain boundary segregation of RM solutes during solid state diffusion and supersaturation of carbon from powder production. MC carbides and inert oxide particles act to immobilize the grain boundaries, restricting grain growth and sintering of the alloy (see Section 4.1).

Upon reaching the SLPS temperature, γ solid solution, liquid, and RM-Ta mixed MC carbides are the only stable phases present (aside from any residual nitrides and oxides). Provided that the PPBs contain few oxides and nitride particles and primarily contain MC carbides, the primary RM-Ta mixed MC carbides are the only remaining obstacles to grain boundary motion. These primary MC carbides slowly dissolve into the liquid phase as SLPS time increases, releasing solute elements RM and Ta into the liquid phase. After a certain incubation time, the MC carbides dissolve to the extent that the solid phase must dissolve further to maintain an equilibrium concentration with the liquid phase. This causes the liquid fraction to increase substantially once the incubation time has been exceeded and the primary MC carbides have gone into solution. At the same time, the solution of primary MC carbides into the liquid phase causes a sudden reduction in grain boundary pinning, enabling grain boundary migration. This explains the simultaneous increase in both the grain size and liquid fraction upon surpassing 10mins of hold time at 1345°C. Both the liquid fraction increase and the grain coarsening behaviour during SLPS are a result of the solution of primary MC carbides in the grain boundary.

It is agreed in the literature that grain coarsening in some Ni superalloys is controlled by the dissolution of certain grain boundary phases [39,61]. For instance, the grain size in some Ni superalloys alloys can be coarsened by exceeding the grain coarsening temperature, GCT [39,61]. The GCT is a transition temperature above which grain growth occurs rapidly and is often related to the dissolution of the γ' precipitates or MC carbides [39,61]. In alloys such as Astroloy, two distinct grain coarsening regimes have been observed; one after the γ’ solvus temperature and another after the MC carbide solvus temperature due to the large temperature interval between the two transitions [61]. However, other alloys such as Nimonic 80 exhibit a more sluggish response to exceeding the GCT while René 95 only experiences grain coarsening above the solidus temperature because of its high volume fraction of γ’ and similar γ’ and MC solvus temperatures. [61].

In the MIM NiSA in this study, the grain coarsening response is similar to that of René 95 where the transition occurs rapidly and above the solidus temperature. Since both the MIM NiSA and René 95 have close γ’ and MC solvus temperatures and high volume fractions of γ’, it is not surprising that the behaviour of these alloys are similar. However, the MIM NiSA also exhibits a time dependency above the solidus temperature that has not previously been noted in the literature. The liquid content and grain size results for SLPS of the MIM NiSA at 1345°C demonstrate that time is required to dissolve the primary MC carbides to a critical point where these parameters increase substantially. At lower SLPS temperatures, the extent of grain coarsening and liquid increase is greatly diminished, likely as a result of requiring a longer incubation time for solution of MC carbides or sintering below the solvus temperature of the MC carbides. Above 1345°C, it is reasonable to expect that the MC carbides would dissolve to a critical extent in less time, leading to an earlier increase in liquid fraction and grain size.

Short time at temperature (under 10mins) at 1345°C is insufficient for the MC carbides to go into solution or fully dissolve. Therefore, the grain boundaries are still immobile due to the GB pinning effect of MC carbides. The grain boundaries become increasingly wavy with increased hold time because local areas of the boundary can migrate while other regions remain pinned. In areas where the boundary has been observed to migrate, coarse γ’ has precipitated, likely as a result of liquid phase presence (which tends to precipitate coarse γ’ in γ/γ’ eutectic regions). The presence of specific RMs in these areas has also been noted to cause the γ’ precipitates to grow with cellular or dendritic morphologies [62]. Segregated phases such as γ/γ’ eutectic pools provide further evidence of this effect as they contain high levels of RM elements along with coarse γ’ plates and dendrites.

However, coarse γ’ precipitates are a more general indication of RM segregation to the grain boundary [3]. The grain boundaries observed after sintering a 1300°C for 1hr (Figure 4-87) are similar to those observed after 10mins at 1345°C (Figure 4-85a, c, e), demonstrating that coarse γ’ precipitation can occur in the solid state when little to no liquid may be present in the grain boundary. Therefore, coarse γ’ precipitation is an indication of RM segregation to the grain boundary and not necessarily an indication of liquid presence in the grain boundary. In the case of this NiSA, the liquid phase is rich in RM, which also promotes the precipitation of coarse γ’.

The short time SLPS grain boundaries also contain $M_{23}C_6$ globules which are notably coarser than the γ-γ grain boundary ridges. Since these carbides are unstable above 1050°C they are thought to precipitate during cooling in the current samples. However, their presence would be beneficial to the grain boundary pinning effect required to combat grain boundary sliding during post processing high temperature creep service. The RM-Ta mixed MC carbides are also still present in the grain boundaries after short times at the SLPS temperature.

After 15mins at 1345°C, the grain boundaries contain far less MC carbide, the grain size has increased substantially, the liquid fraction increased, and coarse γ’ is precipitated in the grain boundaries. The grain boundaries are also far less wavy, indicating that the grain boundary pinning effect has been overcome. The grain boundaries contain much less $M_{23}C_6$ as a result of W segregating into the solid gamma grains, decreasing the W concentration in the liquid phase and the grain boundary region. The edges of course γ' precipitated in the grain boundaries still appear bright white, though the composition and morphology of the coarse γ' impacts how the microstructure is etched. This explains the absence of the bright white γ-γ ridges originally observed in the low-time SLPS samples.

4.5.2.4 Grain Growth during SLPS

Ultimately, the grain boundaries observed after holding for 10mins or less at 1345°C contain RM-Ta mixed MC carbides, W-rich $M_{23}C_6$ carbides, and γ-γ grain boundary ridges. It is expected that the W-rich $M_{23}C_6$ carbides form during cooling as they are not observed prior to SLPS and are not stable at SLPS temperatures. During SLPS, liquid is present in the grain boundary along with RM-Ta mixed MC carbides. These MC carbides, which have formed both on PPBs and grain boundaries, pin the grain boundaries and inhibit grain growth during the initial hold time. Exceeding 10mins at 1345°C provides enough time at temperature for the MC carbides to dissolve into the liquid phase, enabling grain boundary motion and enacting grain growth. The release of solute elements RM and Ta from the solution of MC carbides causes the equilibrium between the solid and liquid phase to shift such that the γ solid fraction must decrease and the liquid fraction must increase to maintain equilibrium. The additional liquid formed by this process increases the grain boundary film thickness, widening the pathway for fast diffusion and mass transport while aiding grain re-arrangement. Both of these aspects further promote grain growth, which occurs rapidly until the liquid fraction stabilizes at the new equilibrium composition.

After holding at 1345°C for 15mins or longer, solute segregation causes the liquid phase to become enriched in Ta and another RM and deplete in W. As discussed in Section 4.2, W preferentially partitions into the solid γ-grains over time during SLPS, depleting the grain boundaries of W. As the concentration of W in the solid phase increases, its melting temperature is also likely to increase [1]. In contrast, the RM and Ta which segregate into the liquid phase likely depress the liquid's melting point further [1]. Upon solidification, mixed RM-Ta MC carbides form preferentially from the liquid phase which is concentrated in the grain boundaries. These mixed RM-Ta MC carbides primarily form as clusters inside or at the periphery of γ/γ' eutectic pools, indicating that they precipitate from the melt and that the liquid is enriched in both that specific RM and Ta. This feature can be clearly observed in Figure 4-32 Figure 4-35 from Section 4.2. Coarse γ' also precipitates in the grain boundaries while few $M_{23}C_6$ carbides are observed. The re-distribution of discrete MC carbide phases from the PBBs to clusters of MC carbides in the liquid phase regions provides further evidence that the original MC carbides in the NiSA powder go into solution during SLPS.

4.5.2.5 Other Variables

The previous solid state sintering work, presented in Section 4.1, demonstrated that the PPBs of the MIM NiSA were decorated with RM-oxide particles if the level of oxygen in sintering atmosphere was not properly controlled. As a result of this PPB oxidation, grain growth was inhibited during SLPS of the NiSA at 1350°C. Further, it was found that the removal of oxygen from the sintering atmosphere improved the sintering response and enabled grain growth in the alloy. Therefore, the presence of RM-oxide particles on the

PPBs inhibits grain boundary motion during SLPS similar to how MC carbides inhibit grain growth. However, the RM-oxides are more stable than the MC carbides and do not dissolve at the SLPS temperatures explored, making them the most critical PPB contaminant to avoid forming in the NiSA. As evidenced by the results, RM-Ta mixed MC carbides are also detrimental to the grain growth behaviour during SLPS. Limiting the amount of oxygen and carbon in the NiSA powder is therefore critical to activating grain growth in this alloy. The MIM NiSA grain size can be coarsened under a controlled atmosphere and with a long enough time above the solidus temperature to dissolve the primary RM-Ta mixed MC carbides. It is necessary to minimize the presence of inert particles on the PPBs in order to achieve grain growth in this MIM NiSA.

The liquid fraction behaviour in the BNi-2 modified MIM NiSA was different than in SLPS of the pure NiSA. However, the grain size was increased in the 10wt% BNi-2 alloy and the grain growth behaviour was similar to what was observed during SLPS. In order to interpret these results, it is important to consider the role of W in the alloy and the fact that the liquid phase is a different composition than both BNi-2 and the NiSA.

The sintering temperature of the BNi-2 modified NiSA was 1290°C, which is lower than both the SLPS and solid state sintering temperatures for the NiSA. Therefore, the RM-Ta mixed MC carbides do not dissolve in the BNi-2 modified alloy. However, the W-rich MC carbides observed in the NiSA powder at 1100°C transform at 1200°C to RM-Ta mixed MCs. It is expected that this transformation leaves the grain boundaries rich in W, which explains why the most prominent boride formed in the BNi-2 modified NiSA is W-rich. In addition, since the W-boride morphology is script-like post-sintering at 1290°C, it is expected that this is the last liquid in the microstructure upon cooling, suggesting that W and B remain in the liquid phase during the LPS process. The apparent retention of W in the liquid phase combined with the absence of RM and Ta enrichment from solution of MC carbides helps to reduce the elemental segregation of the alloy. The net result of these differences is that the liquid fraction remains much more stable over the hold time in comparison to the SLPS process.

In SLPS of the MIM NiSA, grain growth requires the solution of the RM-Ta mixed MC carbides. However, that is not the case in the BNi-2 modified NiSA. Grain growth is only activated in the 10wt% BNi-2 alloy, suggesting that there is a critical liquid fraction required for grain growth to occur. In addition, the lower temperature of the SLPS process likely prevents substantial coarsening and further formation of RM-Ta mixed MC carbides, something that can be observed over the first 10mins of SLPS (see Figure 4-81 and Figure 4-84). The fewer, smaller, primary MC carbides present in the grain boundaries at 1290°C impose a smaller energy barrier for grain boundary motion. Therefore, with a high enough liquid content at 1290°C, such as in the case of the 10wt% BNi-2 alloy, the grain boundary pinning effect can be overcome prior to the solution of primary MC carbides. It should be noted that this can only be accomplished with a liquid phase additive approach.

4.5.2.6 SLPS as a Practical Approach

It is known that the MIM NiSA evaluated in this work can be sintered to full density below the solidus temperature. However, the fine grain size associated with the solid state sintered version of this NiSA limits its creep life and prevents its use in high temperature, structural components for aero engines. The research presented demonstrates that SLPS can activate grain growth in this MIM NiSA. By coarsening the MIM NiSA grain size via an SLPS process, creep resistance can be increased by reducing the grain boundary area available for grain sliding to occur.

To achieve grain coarsening in this MIM NiSA, time at an isothermal SLPS temperature is required to dissolve primary MC carbides situated at the grain boundaries. These carbides are very stable and act as obstacles to grain boundary motion, inhibiting grain growth. At 1345°C, solution of the MC carbides requires a minimum of 10mins. After this initial hold period, the solution of the MC carbides causes the initial liquid phase composition to change. In order to maintain equilibrium, the liquid phase fraction increases, aiding grain sliding, diffusion, and mass transport. Simultaneously, the solution of the MC carbides eliminates them as obstacles to grain boundary motion, allowing grain coarsening to occur. Additional time at the SLPS temperature allows for further grain coarsening and stabilization of the liquid phase fraction. Figure 4-79 and Figure 4-80 show that at 1345°C it takes approximately 60mins to reach a stable liquid content of 28% and a grain size of 45μm. In contrast, at 1345°C the liquid content and grain size in the 10mins prior to MC carbide dissolution are approximately 18% and 20μm, respectively.

For SLPS of the MIM NiSA to successfully activate grain growth, the sintering atmosphere must be scrubbed of oxygen. The research in Section 4.1 demonstrates that RM oxides readily form on the PPBs of the NiSA during heating. These RM oxide particles act as obstacles to grain boundary motion much like the MC carbides do, but do not dissolve at practical SLPS temperatures. Therefore, to achieve grain coarsening it is critical that the SLPS atmosphere be designed to prevent oxidation of the NiSA's PPBs. In this work, the use of high purity argon gas in combination with a Zr or Ti getter material successfully prevented oxidation of the PPBs that was previously sufficient to inhibit grain growth.

Due to the transient nature of the liquid phase after the MC carbides go into solution, it is necessary that process designers consider the time-temperature dependency of the grain size and liquid fraction for the MIM NiSA. It should be stressed that although longer times at temperature can achieve additional grain growth, the increased liquid fraction can cause eventual deformation and shape loss, defeating the MIM process entirely. In addition, longer times above the solidus temperature increase the degree of solute segregation, decreasing alloy homogeneity and coarsening undesirable grain boundary phases such as the γ/γ' eutectic pools. Therefore, a practical SLPS hold time must consider the trade-offs between alloy homogeneity, shape retention, and grain size. Using Figure 4-79 and Figure 4-80 as a guide, it appears reasonable to select a 60min hold time at 1345°C to obtain a considerable grain size increase while avoiding shape loss. Additional hold time at this temperature would yield diminishing returns as the grain growth rate is slow and coarsening of undesirable phases will continue.

Alternative options to increasing the grain size of PM Ni superalloys have previously been identified [61]. One such option is to start with a low carbon pre-alloyed powder instead of the nominal composition of the cast alloy. By reducing the carbon content, the concentration of grain boundary carbides can be reduced such that grain coarsening can take place at lower temperatures. A post-grain coarsening treatment would then be required to carburize the alloy and immobilize the grain boundaries to provide resistance against grain boundary sliding.

Another approach to obtaining a coarse grain size in this MIM NiSA is to reconsider the powder manufacturing route. As previously discussed in Section 4.5.2.3, other powder manufacturing methods such as REP have been found to form MC carbides within the powder particles as opposed to on the PPBs. Knowing that grain growth inhibition from primary MC carbides on PPBs is one of the main challenges associated with solid state sintering of this specific MIM NiSA, producing this powder via REP may overcome this issue.

4.5.3 Conclusions

The grain boundary evolution of a MIM NiSA during SLPS has been explored using DSC and SEM-EDS analysis. The activation of grain growth in the alloy has been discussed considering the NiSA powders complete thermal history through powder manufacturing and the MIM process. Inert gas atomization of the powder in conjunction with the potential for carbon contamination from the MIM process leaves the NiSA powder vulnerable to detrimental MC carbide formation at the particle surfaces and grain boundaries. The most prominent MC carbide was found to be RM-Ta mixed carbide. The formation of additional RM-Ta mixed MC carbides at the expense of W-rich MC carbides above 1100°C leads to the grain boundaries and previous particle boundaries, PPBs, becoming decorated with numerous primary MC carbides which are stable at supersolidus temperatures. These RM-Ta mixed carbides inhibit grain growth in the alloy and do not readily dissolve at SLPS temperatures. At 1345°C, an incubation time of 10mins or greater is required to dissolve the RM-Ta mixed MC carbides to an extent where rapid grain growth occurs. This solution of the primary MC carbide dumps solutes RM and Ta into the liquid phase, causing the liquid fraction to shift in order to maintain equilibrium with the solid phase at 1345°C. The resulting liquid fraction increase aids grain growth, but decreases the alloy's rigidity and homogeneity. The results highlight the importance of considering the thermal history of Ni-superalloys when interpreting their microstructure and demonstrate how a fundamental understanding of sintering behaviour can help guide process design.

CHAPTER 5

RECOMMENDATIONS

The objective of the presented work was to identify and understand the fundamental mechanisms of grain growth in this MIM NiSA. It was determined that the formation of stable MC carbides on the powder particle surfaces and in the grain boundary structure inhibited grain growth during sintering of the alloy. In addition, oxygen contained in the furnace atmosphere during sintering caused the formation of refractory metal oxides on the particles surfaces and in the grain boundaries, inhibiting both densification and grain growth. For these reasons, the carbon content of the NiSA and the oxygen content of the sintering atmosphere must be strictly controlled in order to activate grain growth. It was found that the carbon content of the NiSA was not increased during the MIM process stages, suggesting that control of the carbon content can be achieved by appropriate alloy selection. Adequate control of the oxygen level in the sintering atmosphere was achieved using both oxygen gettering materials and high vacuum atmosphere.

The disruption of grain boundary MC carbides by dissolution and by a liquid phase was required for the activation of grain growth in this MIM NiSA. Although SLPS can successfully provide these conditions and enact grain growth, the practicality of meeting the strict dimensional tolerances of MIM parts in the aerospace industry remains a challenge. Further development of an SLPS approach to grain growth in this MIM NiSA therefore includes a more detailed evaluation of SLPS process limits with respect to shape retention. In addition, the time-temperature profile required to achieve an optimal density, grain size, homogeneity, and dimensional tolerance must be developed. Beyond this, the material properties, specifically creep properties, of the SLPS MIM NiSA need to be tested to understand if the grain size increase achieved by SLPS yields any substantial advantage in terms of creep life. In addition, heat treatment of the SLPS NiSA has not been considered in this research, but could be a useful area of development for the MIM NiSAs.

It is equally important to encourage future research toward alternative methods of creating the appropriate conditions for grain growth activation. As evidenced by the BNi-2 modified NiSA, grain growth can be achieved at sub-solidus temperatures during liquid phase sintering. Considering the microstructural pitfalls of the BNi-2 modified NiSA, a B and Si free liquid phase additive would be a logical next step in this research. Furthermore, future work on liquid phase additions to this NiSA should focus on alloys with similar chemistry to the base alloy chemistry in order limit deviation from industry alloy specifications and to avoid the introduction of detrimental phases.

Ultimately, the root-cause of grain growth inhibition in this NiSA is the carbon available for MC formation. Lower carbon variants of the NiSA need to be considered as potential avenues to grain growth in this alloy. Fortunately, low carbon (LC) variants of a number of NiSAs have already been created specifically for alternate manufacturing routes to traditional casting. This is often the case with NiSA chemistries designed and optimized for castings – the PM manufacturing route, like directional solidification, requires chemistry modification in order to achieve optimal properties. MIM should be treated no different in this regard and a reduction in carbon content should be considered as an avenue to accessing grain growth in these alloys.

It is recommended that alternate routes to enact grain growth be explored. The disruption of MC grain boundary carbides may be achievable by other, more practical means than LPS or SLPS. It is highly recommended that these alternate routes be searched for and evaluated as they may lead to substantial property and process improvements for the MIM NiSAs.

CHAPTER 6
CONCLUSIONS

A fundamental understanding of the sintering behaviour of a MIM NiSA was developed in the present work. DSC, DIL, optical microscopy, and SEM-EDS analyses were effectively combined to evaluate the influences of sintering atmosphere, temperature, time, liquid fraction, and grain boundary evolution on sintering of the NiSA. The present work also identifies and describes the specific microstructural barriers to grain growth in this MIM NiSA and successfully achieves grain coarsening using two separate avenues which can overcome these barriers.

Dilatometry (DIL) and differential scanning calorimetry (DSC) were used to sinter the MIM NiSA under an Ar, Ar with either Ti or Zr getter, and high vacuum atmosphere. DIL revealed that the solid state sintering response of the NiSA at 1310°C was sensitive to the oxygen level in the furnace atmosphere. As the O_2 parts per million (ppm) in the furnace was lowered by the getter material and high vacuum conditions, the sintering shrinkage occurred earlier, more rapidly, and to a greater extent. Lower O_2 ppm levels also resulted in higher sintered densities.

Despite the improvement in sintering response, grain growth was not observed under any of the sintering atmospheres at 1310°C, confirming the inability to access grain growth during solid state sintering of the MIM NiSA. The sintering temperature was increased to 1350°C to study the effect of sintering atmosphere on the SLPS response of the NiSA. DSC analysis concluded that the level of O_2 in the atmosphere influenced the liquid content formed during SLPS. DIL experiments demonstrated that the O_2 ppm in the atmosphere also has a major impact on the densification response of the NiSA. At higher levels of O_2, the NiSA experiences a constrained sintering effect where the oxidation of near-surface grain boundaries restricts densification. Less liquid is also formed at higher levels of O_2, meaning there is less liquid available for rapid densification through the grain re-arrangement process. At lower O_2 levels, the NiSA experiences rapid densification associated with SLPS and the grain size increases considerably. Further investigation using SEM-EDS analysis revealed that higher O_2 levels in the sintering atmosphere cause the formation of refractory metal oxide particles at the PPBs of the NiSA. The oxidation of the NiSA's PPBs inhibits densification and grain growth in a high purity Ar atmosphere. This work identified that an Ar with getter ring or high vacuum sintering atmosphere can effectively prevent detrimental levels of PPB oxidation in this MIM NiSA. Prevention of PPB oxidation prior to consolidation is also critical to the activation of grain growth in this MIM NiSA.

DSC was used in conjunction with optical microscopy and SEM to evaluate SLPS of the MIM NiSA at 1335, 1340, 1345, and 1350°C for hold times between 0-120mins. A maximum average grain size of 60μm was achieved in the 1350°C/120min SLPS sample while lower SLPS temperatures resulted in lower grain sizes. DSC analysis revealed that an initial plateau in liquid content exists between 0-10mins of hold time at 1345°C. Following the initial plateau, the liquid content becomes transient, increasing over time at temperature until a new equilibrium liquid fraction is reached. Similarly, it was discovered that grain growth was not active during the first 10mins of hold time at the SLPS temperature of 1345°C. It was concluded that RM-Ta mixed MC carbides present throughout the grain boundaries restrict grain boundary mobility and prevent grain growth during the initial 10mins of holding at the 1345°C SLPS temperature. After 10mins of hold time at this peak temperature, the MC carbides go into solution, reducing the energy barrier to grain boundary motion and enacting grain growth. The solution of the MC carbides releases solute elements into the pre-existing liquid phase, causing the equilibrium liquid fraction to increase, creating a transient response in the liquid content beyond the 10min hold time. The investigative work presented gives a detailed outline of the grain growth and liquid content behaviour with time and temperature for SLPS of this MIM NiSA.

Over time at SLPS temperature, it was identified that W partitions into the solid phase while RM and Ta partition into the liquid phase. The solution of MC carbides into the liquid also increases the concentration of these solutes in the liquid phase. At extended times at temperature, liquid pools of γ/γ' eutectic formed in the microstructure. These pools often contained clusters of RM-Ta mixed MC carbides which are thought to precipitate during cooling. Thus, although the MC carbides dissolve during SLPS, they likely re-precipitate during cooling in clusters within the solidifying liquid, explaining the observed re-distribution of the RM-Ta mixed MC carbides in the MIM NiSA microstructure.

The ability of the NiSA material to retain its shape during SLPS was characterized using sample height measurements. It was found that material slumping and overall distortion under the force of gravity only occurred at the 1350°C SLPS temperature. At 1350°C, it was found that material slumping and general distortion began immediately upon reaching the peak temperature. At lower SLPS temperatures, loss of material rigidity was not observed. However, qualitatively, the edges of SLPS samples became more rounded as the process temperature, time and liquid content increased. A more thorough, quantitative, evaluation of the edge shape retention is recommended to distinguish the exact process limits for the MIM NiSA shape retention during SLPS.

Previous researchers have modelled material rigidity and softening with grain coarsening during the SLPS process. These models were validated through empirical data, where temperature was the primary controlling parameter, i.e time at temperature was not considered. The present research identifies that certain alloys' rigidity and softening, like the MIM NiSA in this study, display a time dependency. The accepted SLPS model has been modified to incorporate the time dependency of the NiSA's rigidity and softening parameters. The onsets of densification and distortion as well as the instantaneous softening parameters were determined for the NiSA at different SLPS temperatures. The modified SLPS model predicted no deformation at 1340°C, distortion after 40mins at 1345°C, and immediate shape loss at 1350°C. The modeled softening behaviour was aligned with the experimental SLPS results, where significant distortion was not observed until 60mins at 1345°C. Slumping of the material also occurred immediately upon reaching 1350°C as predicted by the model.

A commercial brazing filler metal, BNi-2, was added to the MIM NiSA in 5wt% and 10wt% quantities to create a lower melting point liquid phase for sintering. The BNi-2 modified MIM NiSAs were evaluated using DSC in conjunction with optical microscopy and SEM. Initial trials revealed that rapid diffusional solidification of the braze alloy occurred upon first melting at 968°C, limiting the amount of liquid wetting and spreading in the microstructure. LPS tests at higher temperatures led to the discovery of re-melt events occurring at 1240°C and 1200°C in the 5wt% and 10wt% BNi-2 modified alloys, respectively. These re-melt events were not associated with either of the BNi-2 or NiSA pure alloys, indicating that the diffusional solidified alloy from the first melt at 968°C acts as the liquid phase sintering aid.

LPS was carried out at 1290°C for hold time between 0-120mins and the liquid content and average grain size was measured. The liquid content and grain size was constant in the 5wt% BNi-2 material over time at temperature. Relatively fine, script-like W-rich boride phases were present throughout the microstructure in the 5wt% BNi-2 alloy. In contrast, both the liquid fraction and the grain size increased over time at temperature in the 10wt% BNi-2 alloy. Coarse, script-like, W-rich borides were present throughout the microstructure and multiple non-equilibrium solidification products formed in regions of high liquid content. These non-equilibrium solidification products exhibited dendritic like growth and rejected RM solute elements into a eutectic-like phase which appeared to be the last liquid to solidify. Although the mechanical properties of the BNi-2 modified NiSAs were not evaluated in this work, the script borides and eutectic-like regions are expected to act as crack initiation sites in the microstructure to the overall detriment of the alloys' strength. The present work also determined that the enthalpy of fusion for the 10wt% BNi-2 NiSA is 160J/g.

The evolution of the NiSA's grain boundary structure was studied using SEM-EDS and an evaluation of the alloy's thermal history. The NiSA powder itself has an inherent risk to oxygen and carbon contamination due to the presence of reactive elements, such as Ti and other RMs, as well as its fine particle size and high surface area. The gas atomization technique, used to manufacture the NiSA powder, was identified as a possible contributor to the carbide forming conditions at powder free surfaces. The MIM process was also identified as a potential source of carbon contamination in the powder. The cumulative result of these factors is the decoration of PPB's with MC's and/or oxide particles.

Interrupted sintering tests at 1100°C, 1200°C, and 1300°C were performed to determine the nature of the PPBs during powder consolidation. Blocky WC particles, which were observed after sintering at 1100°C for 1hr, were determined to dissolve or transform after sintering at 1200°C for 1hr. In the 1200°C/1hr condition, the powder particle surfaces were found to be decorated with fine RM-Ta mixed MC type carbides. These carbides persisted on the PPBs during final consolidation, appearing as discrete grain boundary carbides in the post-sintered microstructures. The presence of RM-Ta mixed MC carbides on the powder surfaces and throughout the grain boundaries inhibits grain growth during sintering. Similarly, as concluded in the solid state sintering work in Section 4.1, the oxidation of the PPB's with discrete RM rich oxide particles can also inhibit grain growth and sintering.

The present research has identified that time above the solidus temperature of the NiSA is required to dissolve the RM-Ta mixed MC carbides situated in the grain boundaries. At 1345°C a minimum of 10mins is required for this process to occur to a sufficient extent for grain growth to be activated. Upon solution of the MC carbide, solute elements are dumped into the liquid phase, increasing the equilibrium liquid fraction and causing the liquid content to increase. Simultaneously, grain growth occurs and is aided by the increasing liquid fraction. Consequently, the increasing liquid fraction causes the rigidity of the semi-solid structure to decrease and the elemental segregation to increase. Therefore, although the solution of MC carbides enables grain growth and the subsequent increase in liquid content aids that process, there is a simultaneous loss of part rigidity and alloy homogeneity.

The present research has evaluated the sintering behaviour of a MIM NiSA under a wide range of sintering conditions. Oxygen and carbon contamination of the alloy powder was found to cause the formation of RM rich oxides and RM-Ta mixed MC carbides, respectively, on the PPB’s prior to final powder consolidation. The formation of these stable compounds on the powder free surfaces prior to consolidation situates them in the grain boundaries during sintering, inhibiting sintering (in the case of oxides) and grain growth (in the case of either compound). It was concluded that grain growth can be achieved in this MIM NiSA by heating above the solidus temperature to dissolve the grain boundary carbides. In an SLPS process, grain growth activation requires a minimum of 10mins at 1345°C. In an LPS approach with BNi-2 as the additive, grain growth is achieved after 15mins of sintering at 1290°C with a minimum of 10wt% BNi-2. It is suspected that a similar time at temperature is required to dissolve grain boundary MC carbides prior to grain growth activation in the BNi-2 modified NiSA.

REFERENCES

[1] Reed RC. The Superalloys: Fundamentals and Applications. Combridge University Press; 2008.

[2] Donachie MJ, Donachie SJ. Superalloys: A Technical Guide. 2nd ed. ASM International; 2002.

[3] Gessinger GH. Powder Metallurgy of Superalloys. Cambridge: Butterworth & Co.; 1984.

[4] German RM, Bose A. Injection Molding of Metals and Ceramics. Metal Powder Industries Federation; 1997.

[5] Huang H-E, Koo C-H. Characteristics and Mechanical Properties of Polycrystalline CM 247 LC Superalloy Casting. Mater Trans 2004;45:562–8. doi:10.2320/matertrans.45.562.

[6] Meyer A, Daenicke E, Horke K, Moor M, Müller S, Langer I, et al. Metal injection moulding of nickel-based superalloy CM247LC*. Powder Metall 2016;59:51–6. doi:10.1080/00325899.2016.1142058.

[7] Ashby MF, Jones DRH. Engineering Materials An Introduction to their Properties and Applications. 1980.

[8] Smith WF. Structure and Properties of Engineering Alloys. 2nd ed. McGraw-Hill; 1993.

[9] Callister WD, Rethwisch DG. Materials Science and Engineering An Introduction. 8th ed. John Wiley & Sons; 2010.

[10] German RM. Powder Metallurgy and Particulate Materials Processing. MPIF; 2005.

[11] German RM. Sintering Theory and Practice. New York: John Wiley & Sons; 1996.

[12] Rao GA, Srinivas M, Sarma DS. Influence of modified processing on structure and properties of hot isostatically pressed superalloy Inconel 718. Mater Sci Eng A 2006;418:282–91. doi:10.1016/j.msea.2005.11.031.

[13] Glatzel UWE, Albert B, Vo R. High-Temperature Oxidation Behavior of Two Nickel-Based Superalloys Produced by Metal Injection Molding for Aero Engine Applications 2014;45:4561–72. doi:10.1007/s11661-014-2391-1.

[14] Özgün Ö, Gülsoy HÖ, Yılmaz R, Fındık F. Microstructural and mechanical characterization of injection molded 718 superalloy powders 2013;576:140–53. doi:10.1016/j.jallcom.2013.04.042.

[15] Hens K, Grohowski J, German R, Valencia J, McCabe T. Processing of Superalloys via Powder Injection Molding. Adv Powder Metall Part Mater 1994;4:137–49.

[16] Özgün Ö, Gülsoy HÖ, Yilmaz R, Findik F. Injection molding of nickel based 625 superalloy : Sintering , heat treatment , microstructure and mechanical properties. J Alloys Compd 2013;546:192–207. doi:10.1016/j.jallcom.2012.08.069.

[17] Liu J, Lal A, German RM. Densification and shape retention in supersolidus liquid phase sintering. Acta Mater 1999;47:4615–26. doi:10.1016/S1359-6454(99)00320-1.

[18] Levasseur D, Brochu M. Supersolidus Liquid Phase Sintering Modeling of Inconel 718 Superalloy. Metall Mater Trans A Phys Metall Mater Sci 2016;47:869–76. doi:10.1007/s11661-015-3244-2.

[19] Porter D, Easterling K, Sherif M. Phase Transformations in Metals and Alloys. Third. CRC Press Taylor & Francis Group; 2009.

[20] Corbin SF, Murray DC, Bouthillier A. Analysis of Diffusional Solidification in a Wide-Gap Brazing Powder Mixture Using Differential Scanning Calorimetry. Metall Mater Trans A 2016;47:6339–52. doi:10.1007/s11661-016-3799-6.

[21] Boettinger WJ, Kattner UR, Moon WK, Perepezko JH. DTA and Heat-Flux DSC Measurements of Alloy Melting and Freezing. National Institute of Standards and Technology; 2006.

[22] Murray DC, Corbin SF. Determining the kinetics of transient liquid phase bonding (TLPB) of inconel 625/BNi-2 couples using differential scanning calorimetry. J Mater Process Technol 2017;248:92–102. doi:10.1016/j.jmatprotec.2017.05.013.

[23] Rayner AJ, Clemmer RMC, Corbin SF. Determination of the activation energy and master sintering curve for NiO/YSZ composite solid oxide fuel cell anodes. J Am Ceram Soc 2015;98. doi:10.1111/jace.13405.

[24] Chan JL, Alcock JR, Stephenson DJ. Supersolidus liquid phase sintering of moulded metal components. J Mater Sci 1998;33:5131–6.

[25] Tang CF, Pan F, Qu XH, Duan BH, He XB. Nickel base superalloy GH4049 prepared by powder metallurgy. J Alloys Compd 2009;474:201–5. doi:10.1016/j.jallcom.2008.06.038.

[26] Whitman CA, O'Flynn JT, Rayner AJ, Corbin SF. Determining the oxidation behavior of metal powders during heating through thermogravimetric and evolved gas analysis using a coupled thermogravimetry-gas chromatography-mass spectrometry technique. Thermochim Acta 2016;638:124–37. doi:10.1016/j.tca.2016.06.019.

[27] ASTM International. E112-13: Standard Test Methods for Determining Average Grain Size 2015:1–28. doi:10.1520/E0112-13.1.4.

[28] German RM. Supersolidus Liquid-Phase Sintering of Prealloyed Powders. Metall Mater Trans A 1997;28A:1553–67.

[29] Wang F, Ma D, Bührig-Polaczek A. Microsegregation behavior of alloying elements in single-crystal nickel-based superalloys with emphasis on dendritic structure. Mater Charact 2017;127:311–6. doi:10.1016/j.matchar.2017.02.030.

[30] Song K, Aindow M. Grain growth and particle pinning in a model Ni-based superalloy. Mater Sci Eng A 2008;479:365–72. doi:10.1016/j.msea.2007.09.055.

[31] Azevedo e Silva PRS, Baldan R, Nunes CA, Coelho GC, Costa AMDS. Solution heat-treatment of Nb-modified MAR-M247 superalloy. Mater Charact 2013;75:214–9. doi:10.1016/j.matchar.2012.11.006.

[32] Baldan R, Rocha RLP, Tomasiello RB, Nunes CA, Silva Costa AM, Barboza MJR, et al. Solutioning and Aging of MAR-M247 Nickel-Based Superalloy. J Mater Eng Perform 2013;22:2574–9. doi:10.1007/s11665-013-0565-4.

[33] Huang H-E, Koo C-H. Effect of Solution-Treatment on Microstructure and Mechanical Properties of Cast Fine-Grain CM 247 LC Superalloy. Mater Trans 2004;45:1360–6.

[34] Przeliorz R, Piatkowski J. Application of DSC Method in Studies on Phase Transitions of Ni Superalloys. Arch Foundry Eng 2017;17:133–6. doi:10.1515/afe-2017-0144.

[35] Wusatowska-Sarnek AM, Blackburn MJ, Aindow M. Techniques for microstructural characterization of powder-processed nickel-based superalloys. Mater Sci Eng A 2003;360:390–5. doi:10.1016/S0921-5093(03)00498-2.

[36] Dong R, Li J, Zhang T, Hu R, Kou H. Materials Characterization Elements segregation and phase precipitation behavior at grain boundary in a Ni-Cr-W based superalloy. Mater Charact 2016;122:189–96. doi:10.1016/j.matchar.2016.11.002.

[37] Garosshen TJ, Mccarthy GR. Low Temperature Carbide Precipitation in a Nickel Base Superalloy 1985;16:1213–23.

[38] Bai G, Li J, Hu R, Zhang T, Kou H, Fu H. Effect of thermal exposure on the stability of carbides in Ni – Cr – W based superalloy. Mater Sci Eng A 2011;528:2339–44. doi:10.1016/j.msea.2010.11.088.

[39] Xu S, Dickson JI, Koul AK. Grain Growth and Carbide Precipitation in Superalloy , 1998;29:2687–95.

[40] Koul AK, Castillo R. Assessment of Service Induced Microstructural Damage and Its Rejuvenation in Turbine Blades 1988;19.

[41] Dong X, Zhang X, Du K, Zhou Y, Jin T, Ye H. Microstructure of Carbides at Grain Boundaries in Nickel Based Superalloys. J Mater Sci Technol 2012;28:1031–8. doi:10.1016/S1005-0302(12)60169-8.

[42] Hu R, Bai G, Li J, Zhang J, Zhang T, Fu H. Precipitation behavior of grain boundary M 23 C 6 and its effect on tensile properties of Ni – Cr – W based superalloy. Mater Sci Eng A 2012;548:83–8. doi:10.1016/j.msea.2012.03.092.

[43] Chen J, Lee JH, Jo CY, Choe SJ, Lee YT. MC carbide formation in directionally solidified MAR-M247 LC superalloy 1998;247:113–25.

[44] Liu ZY, Loh NH, Khor KA, Tor SB. Microstructure evolution during sintering of injection molded M2 high speed steel. Mater Sci Eng A 2000;293:46–55. doi:10.1016/S0921-5093(00)01244-2.

[45] Idowu OA, Richards NL, Chaturvedi MC. Effect of bonding temperature on isothermal solidification rate during transient liquid phase bonding of Inconel 738LC superalloy 2005;397:98–112. doi:10.1016/j.msea.2005.01.055.

[46] Egbewande AT, Chukwukaeme C, Ojo OA. Joining of superalloy Inconel 600 by diffusion induced isothermal solidification of a liquated insert metal 2007;9:3–10. doi:10.1016/j.matchar.2007.08.023.

[47] Duvall DS, Owczarski WA, Paulonis DF. TLP Bonding: A new method for joining heat resistant alloys. Weld J 1974;53:203–14.

[48] Miglietti W. Correlation between microstructure and mechnical properties of diffusion brazed MAR-M247. ASME 1993.

[49] Wikstrom NP, Ojo OA, Chaturvedi MC. Influence of process parameters on microstructure of transient liquid phase bonded Inconel 738LC superalloy with Amdry DF-3 interlayer 2006;417:299–306. doi:10.1016/j.msea.2005.10.056.

[50] Wu X, Chandel RS, Li H. Evaluation of transient liquid phase bonding between nickel-based superalloys 2001;6:1539–46.

[51] Ozgun O, Gulsoy HO, Yilmaz R, Findik F. Microstructural and mechanical characterization of injection molded 718 superalloy powders. J Alloys Compd 2013;576:140–53. doi:10.1016/j.jallcom.2013.04.042.

[52] Tucker SP, Hochgraf FG. The equilibrium morphology of grain boundary phases. Metallography 1973;6:457–64. doi:https://doi.org/10.1016/0026-0800(73)90043-8.

[53] Thorpe MF. Continuous deformations in random networks. J Non Cryst Solids 1983;53:355–70. doi:https://doi.org/10.1016/0022-3093(83)90424-6.

[54] Liu Y, Tandon R, German RM. Modeling of Supersolidus Liquid Phase Sintering " I . Capillary Force 1995;26:2415–22.

[55] Liu Y, Tandon R, German RM. Modeling of Supersolidus Liquid Phase Sintering: I1. Densification 1995;26.

[56] Campbell J. Dihedral angle and the equilibrium morphology of grain boundary phases. Metallography 1971;4:269–78. doi:10.1016/0026-0800(71)90018-8.

[57] Valencia JJ, Quested P.N. Thermophysical properties. ASM Handb Cast 2008;15:468–81. doi:10.1361/asmhba0005240.

[58] Flemings MC. Behavior of Metal Alloys in the Semisolid State. Metall Trans A 1991;22A.

[59] Gessinger GH. Physical Metallurgy of Pre-alloyed Powders. Powder Metall. Superalloys, Cambridge: Butterworth & Co.; 1984, p. 35–42.

[60] Larson JM. Modern Development in Powder Metallurgy. vol. 8. New York: Plenum Press; 1974.

[61] Gessinger GH. TMP for Coarse Grain Sizes. Powder Metall. Superalloys, Cambridge: Butterworth & Co.; 1984, p. 123–8.

[62] Gessinger GH. Structure of Nickel-base Superalloys. Powder Metall. Superalloys, Cambridge: Butterworth & Co.; 1984, p. 4–6.

APPENDIX A
PRELIMINARY INVESTIGATIONS OF LIQUID PHASE SINTERING A METAL INJECTION MOLDED NICKEL-BASE SUPERALLOY WITH ADDITIONS OF IN625 POWDER USING DIFFERENTIAL SCANNING CALORIMETRY

A.1. Introduction

One of the main objectives of this research was to increase the grain size of the metal injection molded (MIM) nickel superalloy (NiSA) in order to obtain better creep properties. The present work demonstrates that grain growth in the MIM NiSA is restricted by the formation of stable grain boundary carbides during sintering. Supersolidus liquid phase sintering (SLPS) and liquid phase sintering (LPS) processes have both been identified as effective methods for enacting grain growth in this NiSA and have been thoroughly evaluated. However, preliminary work was also completed using an alternate LPS material which employed Inconel 625 (IN625) as the low melting point additive. As in the case with the addition of BNi-2 to the MIM NiSA in Section 4.3, the objective of this research was to study the LPS of a MIM IN625-NiSA material as a method of increasing grain size and improving the alloy's high temperature properties.

A.1.1. Addition of Inconel 625 to NiSA

An alternate approach to liquid phase sintering the MIM NiSA is to add a second, lower melting temperature nickel superalloy powder to the primary MIM NiSA feedstock. By adding another nickel superalloy powder, the bulk alloy chemistry can be maintained closer to the industry chemistry specification for the base NiSA. IN625 is a chromium-rich, solid solution strengthened nickel superalloy which is widely used in the aerospace industry. IN625 has a melting range of 1290°C-1350°C and will begin melting below the NiSA's solidus temperature, which lies in the range of 1330-1340°C (refer to Section 4.2 for more detail). Pre-alloyed IN625 powder was added to the MIM NiSA to provide a small liquid fraction at solid state sintering temperatures for the NiSA (i.e. 1300°C). The weight fraction of IN625 added to the MIM NiSA was kept low to maintain the IN625-NiSA LPS mixture within the NiSA's chemistry specification. Note that this approach differs from the LPS approach presented in Section 4.3, where the chemistry specification for the NiSA was not considered and the melting point depressants (MPDs) Si and B were introduced to the alloy via the addition of BNi-2, a commercial brazing filler metal.

A.2. Experimental Methods

A.2.1. Inconel 625 Modified NiSA

2wt% IN625 pre-alloyed powder was added to the MIM NiSA feedstock to create an IN625 LPS MIM material. The IN625 addition was made such that the solids loading of the MIM feedstock was not changed from the original NiSA mixture. The average particle size of both powders were similar and both powders had a spherical morphology with a range of particle sizes typical of that used in MIM. IN625-NiSA LPS samples were injection molded by an industry partner and sent to Dalhousie University for thermal analysis. The as-received green-state MIM LPS samples were sectioned into small pieces weighing approximately 150mg for DSC analysis. MIM LPS samples used for dilatometry were prepared by cutting a cylindrical LPS MIM specimen into 3mm thick disks. The faces of these disks were sanded flat with SiC paper to obtain stable, parallel, contact surfaces with the alumina plates used for dilatometry. Pure MIM NiSA samples were also prepared for DSC and DIL using the same techniques, however the as-received pure NiSA DIL samples were rectangular. The sample size for DSC was limited by the 5.8mm diameter crucible size used in the instrument.

The green-state samples were packed in an inert powder bed for de-binding. Thermal de-binding was completed in a Sentrotech 1600C tube furnace under flowing high purity argon gas (99.999% Ar). Samples were removed from the inert powder bed and surfaces cleaned with a fine brush to remove residual de-binding support media. Samples were weighed before and after the de-binding step to track check the amount of binder removal.

The IN625 and NiSA powders were each heated to 1450°C in a Netzsch 404 F1 DSC to obtain complete melting and solidification traces for both alloys. The instrument's temperature and sensitivity were calibrated using 6 pure metals (In, Sn, Zn, Al, Ag, and Au) under near-identical conditions to those applied in the sample experiments.

Both MIM NiSA and IN625 LPS samples were heated at 4.5Kpm under 50ml/min flowing 99.999% Argon gas in the DSC to peak sintering temperatures ranging from 1300-1350°C. Samples were held at the peak sintering temperature for 60mins. Samples were subsequently cooled at a rate of 20Kpm to room temperature. The furnace was evacuated to a minimum vacuum level of 5.0E-5mbar and backfilled with high purity argon gas prior to each test.

The larger rectangular and disk MIM specimens were sintered in a Netzsch 402C dilatometer at 1310°C with a 60min hold time and heating rate of 4.5Kpm. Sintering experiments were carried out with flowing high purity argon gas (99.999% Ar) at 50ml/min. The furnace was evacuated to a vacuum level of 5.4E-5mbar or lower and subsequently back filled with Ar twice before each dilatometry test.

Samples were mounted and polished before being etched with waterless Kalling's reagent to expose the grain boundaries. Image analysis was performed using Fiji ImageJ to determine the percentage density. Optical microscopy was performed using a Zeiss Axiotech 100HD microscope. The average grain size of each sample was measured via the line intercept technique with 25 lines per sample.

A.3. Results

A.3.1. DSC and DIL Experiments

The DSC traces for the full melting tests of the NiSA and IN625 powders are presented together in Figure A-1. As expected, the pre-alloyed IN625 powder displays an earlier melting onset than the NiSA. However, as previously discussed in Section 4.2, the NiSA displays a degree of incipient melting which causes melting prior to the traditionally accepted solidus temperatures in the range of 1330-1340°C. This causes the first liquid to appear at similar temperatures in both alloys. The melting events also overlap to a significant degree which means that the IN625 additive cannot be fully melted without also melting the base NiSA.

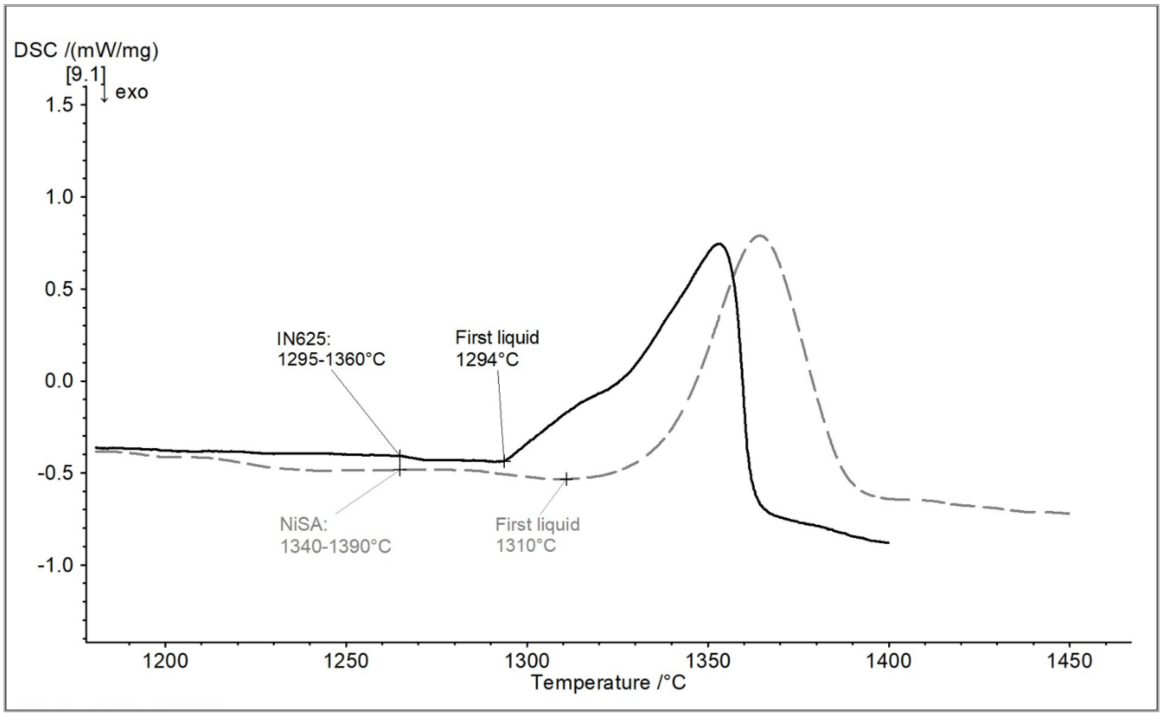

Figure A-1. DSC traces of the pre-alloyed NiSA (dashed line) and IN625 (solid line) powders during heating.

Further analysis of the melting and overall sintering behaviour was performed by sintering both the pure NiSA and LPS IN625 material at increasing temperatures for 60mins in the DSC. The initial liquid fraction and average grain size for both the MIM NiSA and IN625 LPS materials are plotted in Figure A-2 and Figure A-3. The initial liquid fractions formed upon heating the MIM LPS material to temperatures in the range of 1300-1350°C were very similar to those measured for the pure MIM NiSA. The LPS material only begins to form a higher liquid fraction upon heating above 1340°C, demonstrating that the 2wt% IN625 addition does not provide a significant change in the bulk alloy's melting behaviour. Similarly, the average grain size was nearly identical between the IN625 LPS and pure NiSA MIM materials in the 1300-1340°C temperature range. Once a sintering temperature above 1340°C is reached, the grain size in the IN625 LPS material becomes larger than the pure NiSA.

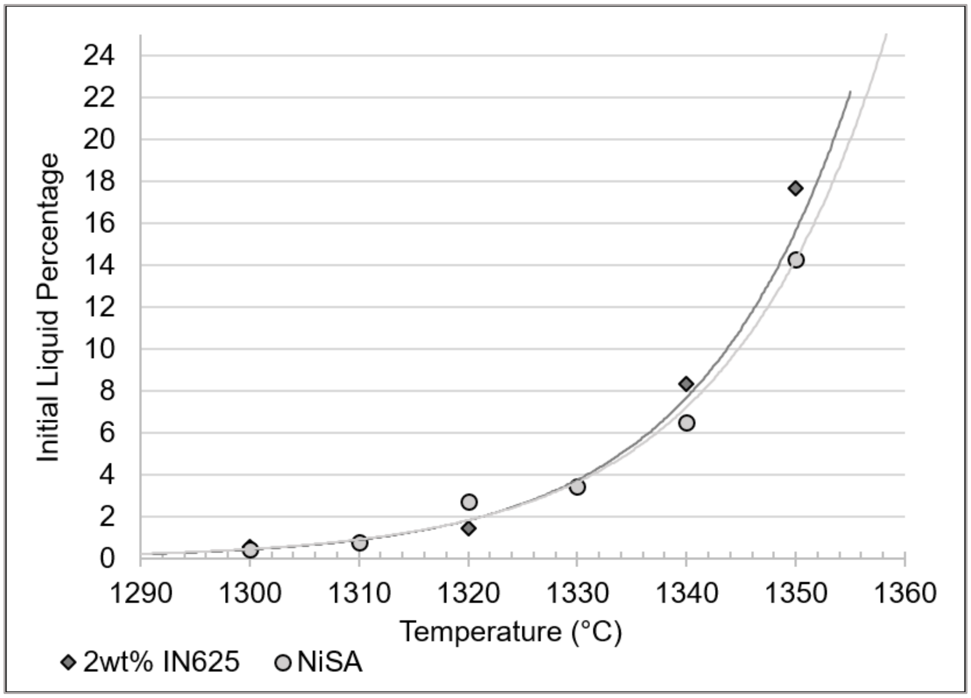

Figure A-2. **Initial liquid percentage with temperature determined for the 2wt% IN625 LPS material and the pure NiSA.**

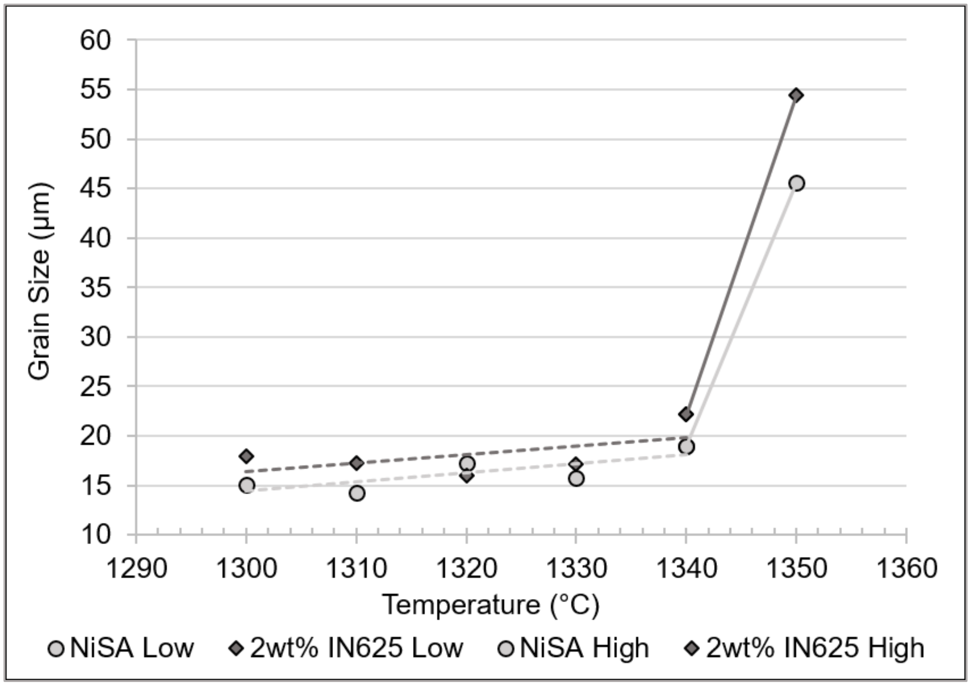

Figure A-3. **Average grain size of the LPS and pure NiSA materials with temperature. The lower and higher temperature grain size trends are indicated by the dashed and solid linear approximations, respectively.**

The response of the DSC measurement upon cooling from the hold temperature was too inconsistent to accurately determine the final liquid fractions for each peak temperature. Therefore, only the initial liquid fractions are presented here. From an alloy design perspective, the initial melting behaviour of the LPS alloy is important to evaluate because the selected LPS addition must provide a sufficient liquid fraction to benefit the sintering process. Although not assessed in this work, it is expected that the liquid fractions formed in this LPS mixture also increase over isothermal time at SLPS temperatures, as was discovered in Section 4.2 for the pure NiSA.

The MIM IN625 LPS and NiSA materials were also sintered in the dilatometer at 1310°C for 60mins. The resulting DIL curves for two of each sample are presented together in Figure A-4. The overall sintering shrinkage measured for the LPS samples was greater than the NiSAs, indicating that the LPS material achieved a higher degree of densification. The onset temperature of densification was also slightly lower for the LPS material, exhibiting sintering shrinkage at 1100°C compared to 1120°C for the NiSA. A decrease in the rate of densification can also be observed at approximately 1200°C for both materials. Upon reaching the peak temperature of 1310°C the NiSA has only experience about 50% of its total shrinkage. In contrast, the LPS material has nearly completed 100% of its total sintering shrinkage upon reaching the hold temperature.

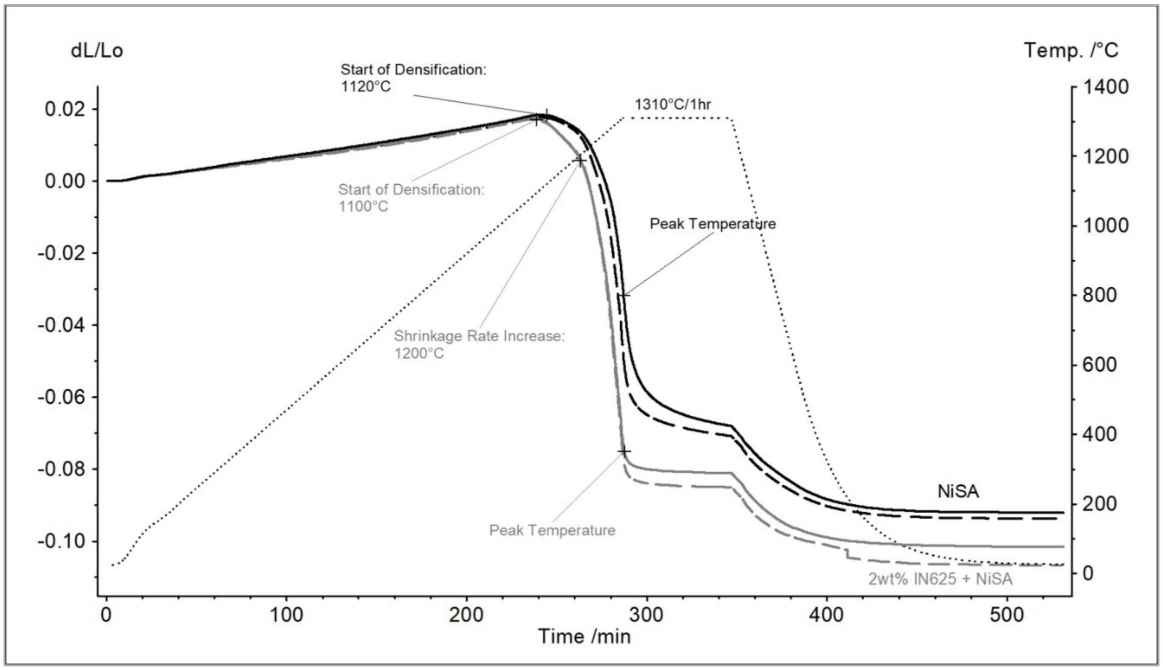

Figure A-4. Dilatometry curves for the pure NiSA and LPS material sintered at 1310°C for 1hr.

A.3.2. Microstructural Analysis

The DSC samples were mounted and polished to examine their grain size and general microstructure using optical microscopy. Microstructures from the center of the LPS and NiSA materials are compared side-by-side in Figure A-5 for the 1340°C and 1350°C sintering temperatures. The transition in grain size from sintering at 1340°C to 1350°C is clearly observable in Figure A-5 for both materials. From Figure A-3, the average grain size remains relatively unchanged and sub-20µm as the peak sintering temperature is increased from 1310°C to 1340°C. After sintering at 1350°C for 60mins, the grain size has increased substantially. It is important to note that from this preliminary work, the LPS material appears to behave similarly to the SLPS of the pure NiSA. The effect of adding 2wt% IN625 to the MIM NiSA is not readily observable by microstructural analysis.

One final note is that the carbide distribution in the LPS material appears to be different from the pure NiSA. In Figure A-5, the pure NiSA sintered at 1350°C contains many carbide phases within the individual grains while the LPS grains appear relatively free of these carbides. Though this may, to some degree, be an etching effect, it is worth comment due to the previously identified importance of carbides to grain growth in this MIM NiSA.

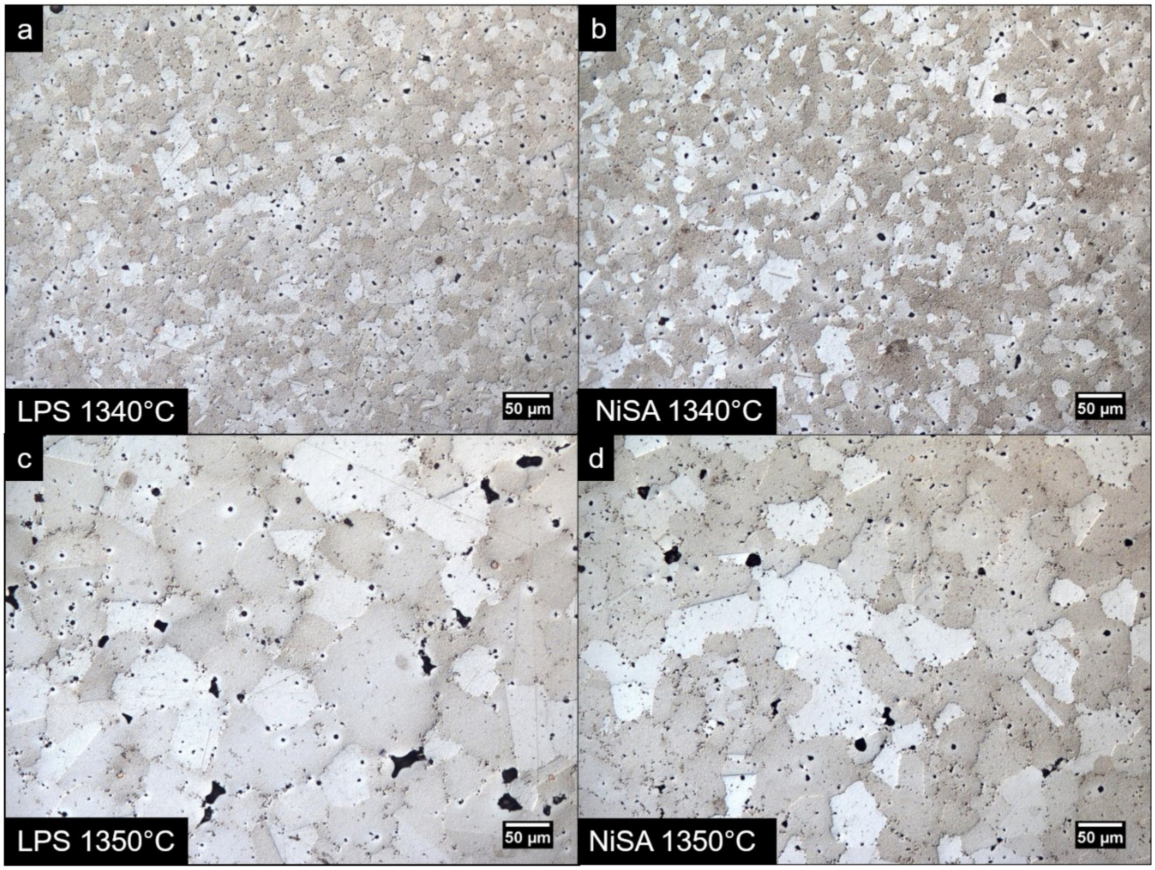

Figure A-5. Optical microscopy images of the center microstructure in the a) LPS 1340°C, b) NiSA 1340°C, c) LPS 1350°C, and d) NiSA 1350°C materials each sintered for 1hr.

A.4. Discussion

The 2wt% addition of IN625 to the MIM NiSA provided no substantial benefit to the sintering response of the pure NiSA. The dilatometry curves for the LPS material exhibit both an earlier onset to densification and a higher densification rate, though these improvements are relatively minor. The DSC tests revealed that despite having a lower melting range, the IN625 additive did not change the melting response significantly between 1300°C and 1340°C. Higher liquid fractions were measured in the LPS material at temperatures exceeding 1340°C, which also coincided with higher average grain sizes at these temperatures. In addition, the grain growth response of the LPS material below 1340°C was nearly identical to the pure NiSA. These results demonstrate that only a marginal benefit is achieved by adding 2wt% IN625 to the MIM NiSA.

The grain size of the LPS material also does not increase until the sintering temperature has been raised well within the NiSA melting range. Although liquid fractions in the LPS material are increased at higher temperatures compared to the pure NiSA, it is evident that SLPS is still required to increase the grain size of the NiSA. Interpreting these results in the context of Section 4.5, the absence of any substantial grain growth at temperatures under 1340°C in the LPS material is consistent with the absence of enough liquid and temperature to dissolve MC carbides during SLPS of the pure NiSA.

Recall that the 2wt% addition was selected in order to comply with the NiSA chemistry specification. Based on these preliminary results, it appears necessary to increase the weight percent addition of IN625 to extract more substantial changes to the sintering response, melting behaviour, and grain growth characteristics of the NiSA. Overall, this makes sense because 2wt% is a relatively small addition which does not change the bulk alloy composition significantly. Of course, increasing the weight percent addition of IN625 beyond 2wt% will violate the chemistry specification of the NiSA, but it is important to highlight that this may be the only possible path toward accessing grain growth below the solidus temperature of the base NiSA.

Another important aspect of this preliminary work is that the presented sintering trials were performed in a high purity argon atmosphere. In Section 4.1, it was found that sintering under argon with a getter material or under a high vacuum atmosphere was required to prevent detrimental levels of oxidation during sintering. Based on those results, it is expected that higher liquid fractions and degrees of grain growth would be obtainable in the LPS material by decreasing the ppm O_2 in the sintering atmosphere. To verify this expectation, the liquid fraction and grain size data for the NiSA sintered under the Ar with Zr getter atmosphere in the DSC from Section 4.1 was plotted alongside the LPS material data presented in Figure A-2 and Figure A-3. These comparisons are shown in Figure A-6 and Figure A-7. The NiSA samples sintered under an argon with Zr getter atmosphere exhibited a higher degree of melting and an earlier onset of grain growth than both the LPS and pure NiSA sintered under argon. This result explains why the pure NiSA from Section 4.1 exhibited a larger grain size than the LPS material after sintering at 1340°C/60mins. This comparison also demonstrates the NiSA's sensitivity to oxygen during sintering and indicates that the melting and grain growth behaviour of the alloy is more sensitive to the ppm of oxygen in the sintering atmosphere than a 2wt% addition of IN625.

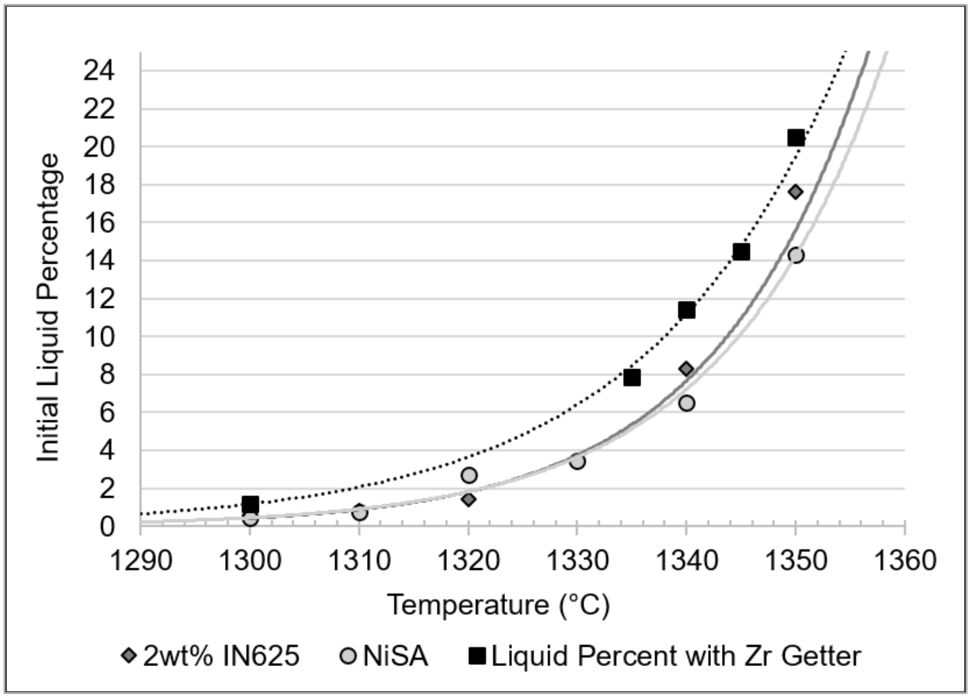

Figure A-6. **Initial liquid percentages with temperature for the 2wt% IN625 LPS material and the NiSA sintered under both an argon and argon with Zr getter atmosphere.**

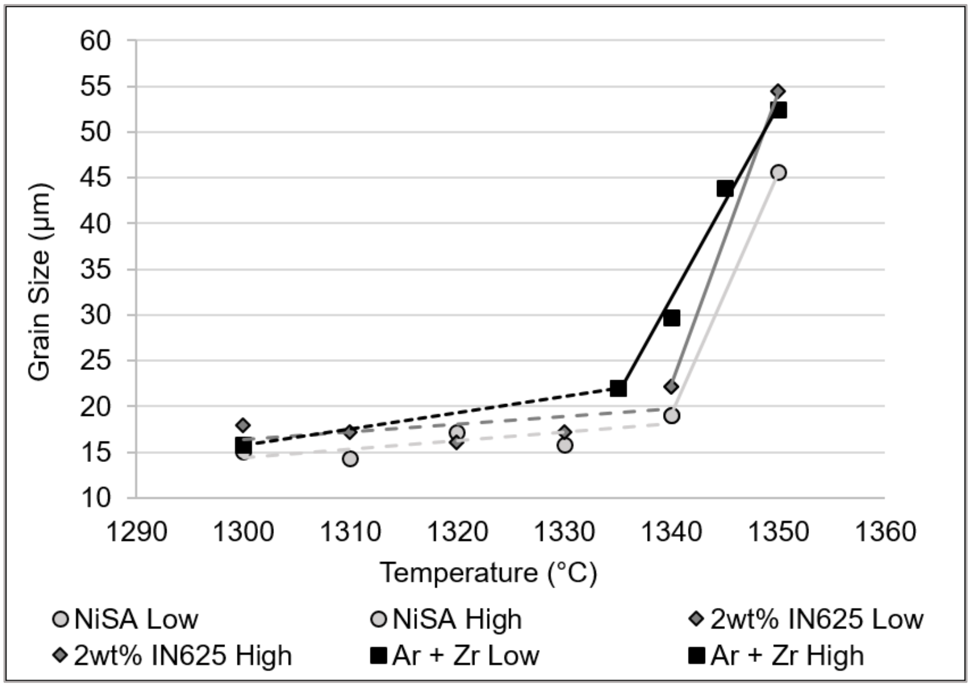

Figure A-7. **Average grain size with temperature for the 2wt% IN625 LPS material and the NiSA sintered under both an argon and argon with Zr getter atmosphere.**

A.5. Conclusions

A 2wt% IN625 pre-alloyed powder addition was made to the MIM NiSA to create a liquid phase during sintering. DSC and DIL analysis of the IN625-modified MIM NiSA material revealed that the sintering response, liquid fraction formed, and grain growth behaviour were marginally improved by the addition of 2wt% IN625. It was determined that despite having the lower melting point addition of IN625, the absence of a Zr getter in the furnace to reduce the oxygen level in the sintering atmosphere played a larger role in the sintering behaviour. It was also evident that SLPS was still required to enact grain growth in the NiSA. It was concluded that larger additions of the IN625 alloy would have to be made in order to provide a sufficient liquid phase to significantly alter the sintering behaviour at solid state sintering temperatures. This preliminary work reinforces the critical role that oxidation plays in inhibiting grain growth and highlights the challenges associated with increasing the grain size in this MIM NiSA.

APPENDIX B
A VISUAL GUIDE TO SUPERSOLIDUS LIQUID PHASE SINTERING OF A METAL INJECTION MOLDED NICKEL-BASE SUPERALLOY

B.1. Introduction

In the present research, the SLPS behaviour of the MIM NiSA is discussed in detail. The liquid fraction, grain size, and change in height of the NiSA during SLPS have all been evaluated experimentally. However, it is also beneficial to study the SLPS process visually. Polished cross sections of all SLPS NiSA samples were analyzed using optical microscopy and their images stitched together to create a detailed image of the entire sample. By comparing these cross sections with time and SLPS temperature, the shape retention and grain growth response of the MIM NiSA can be quickly and clearly observed. From a practical standpoint, this collection of sample cross sections serves as a quick reference guide for the response of the NiSA to select process parameters. Note that all samples presented in this section were sintered under Ar with a Zr getter.

B.2. Image Preparation

Sintered MIM NiSA specimens were mounted and polished before being etched with waterless Kalling's reagent to expose the grain boundaries. Optical microscopy was performed using a Zeiss Axiotech 100HD microscope. Image stitching and editing was performed using Fiji ImageJ software. All cross sections are oriented in side view, with the bottom facing down.

B.3. Visual Guide to SLPS

Stitched cross sections of the MIM NiSA are compared for the 1335-1350°C SLPS temperatures in Figures B-1 to B-5. Further commentary is provided in Section B.4.

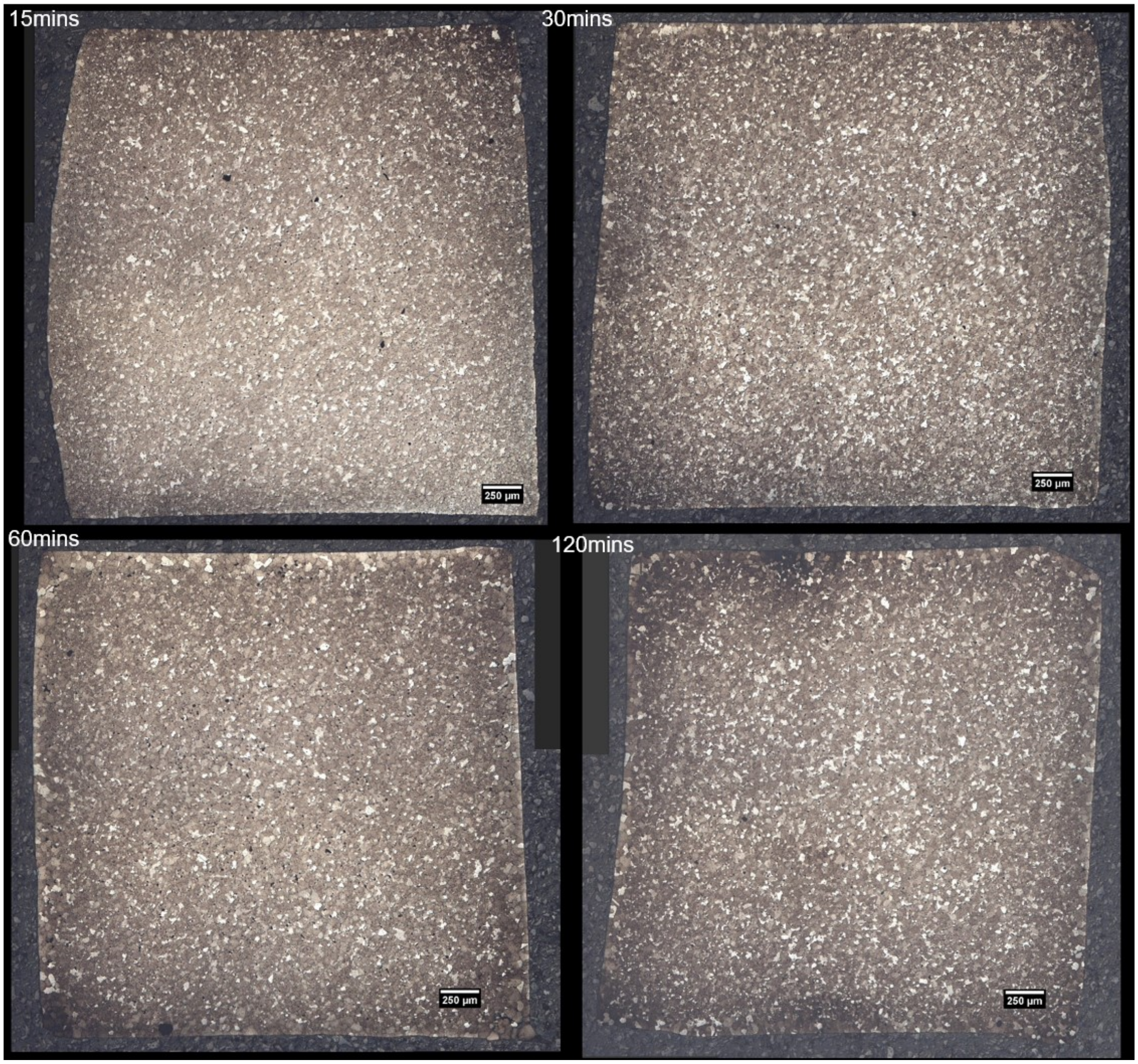

Figure B-1. Etched cross sections of the MIM NiSA SLPS samples sintered at 1335°C for 15-120mins.

In the 1335°C series of SLPS tests, shown in Figure B-1, there is no apparent grain growth of the bulk material over the 15-120min range. Some minor grain growth can be observed at the sample surfaces after 60mins of hold time and the part's shape is retained throughout

120mins. Overall, sintering at 1335°C does not enact grain growth in the MIM NiSA and is too low of a process temperature if grain growth is desired.

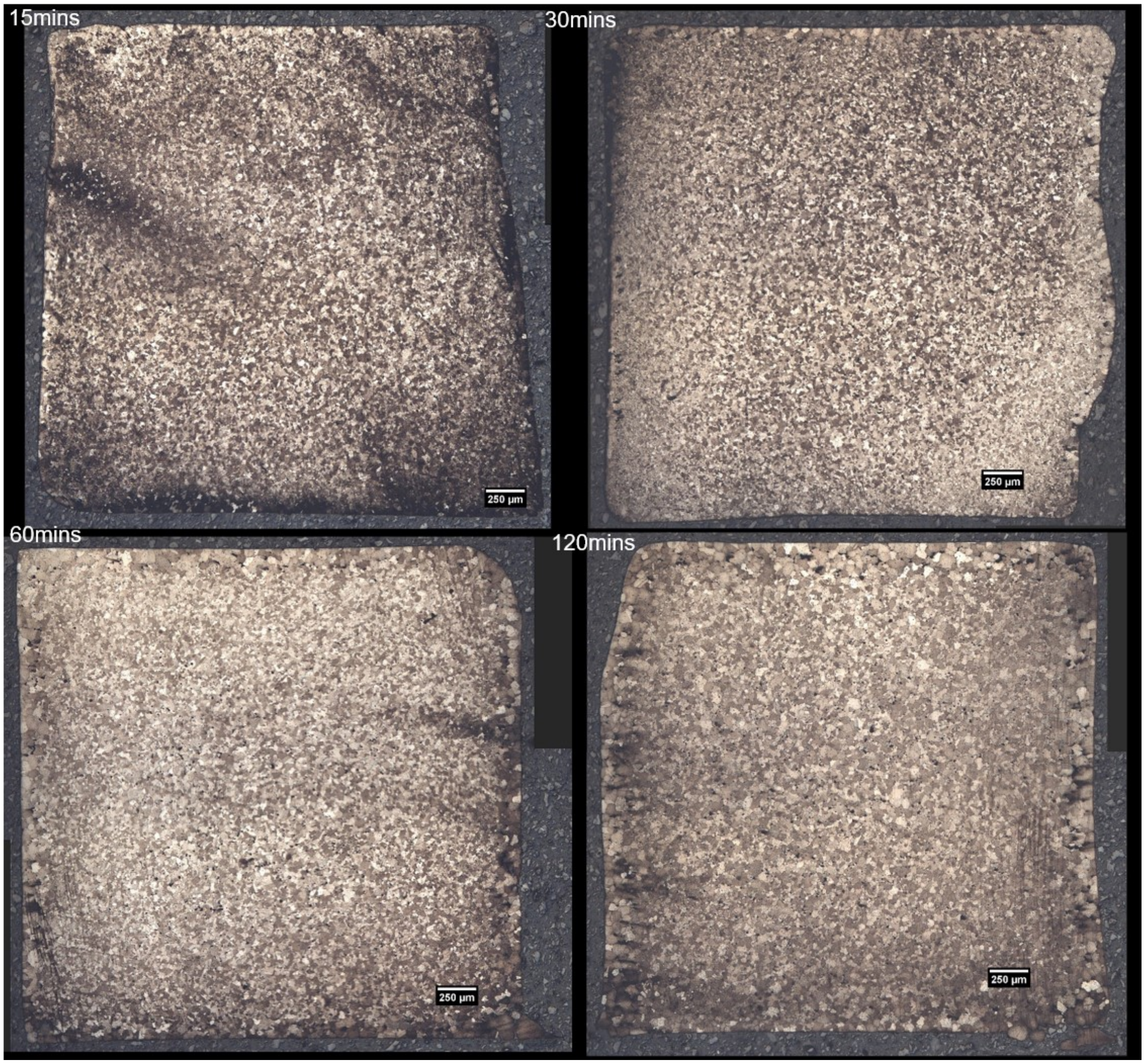

Figure B-2. **Etched cross sections of the MIM NiSA SLPS samples sintered at 1340°C for 15-120mins.**

In the 1340°C series of SLPS tests, shown in Figure B-2, grain growth is apparent in the bulk material after 60 and 120mins. Grain growth can also be observed starting at the sample surfaces after 30mins of hold time and the surface grain size remains larger than the bulk grain size through 120mins. The part's shape is retained over 120mins, however edge rounding is evident after 30mins. After 60mins, the bottom of the sample has started to wet the alumina crucible. Overall, grain growth and shape retention are achievable at the 1340°C process temperature.

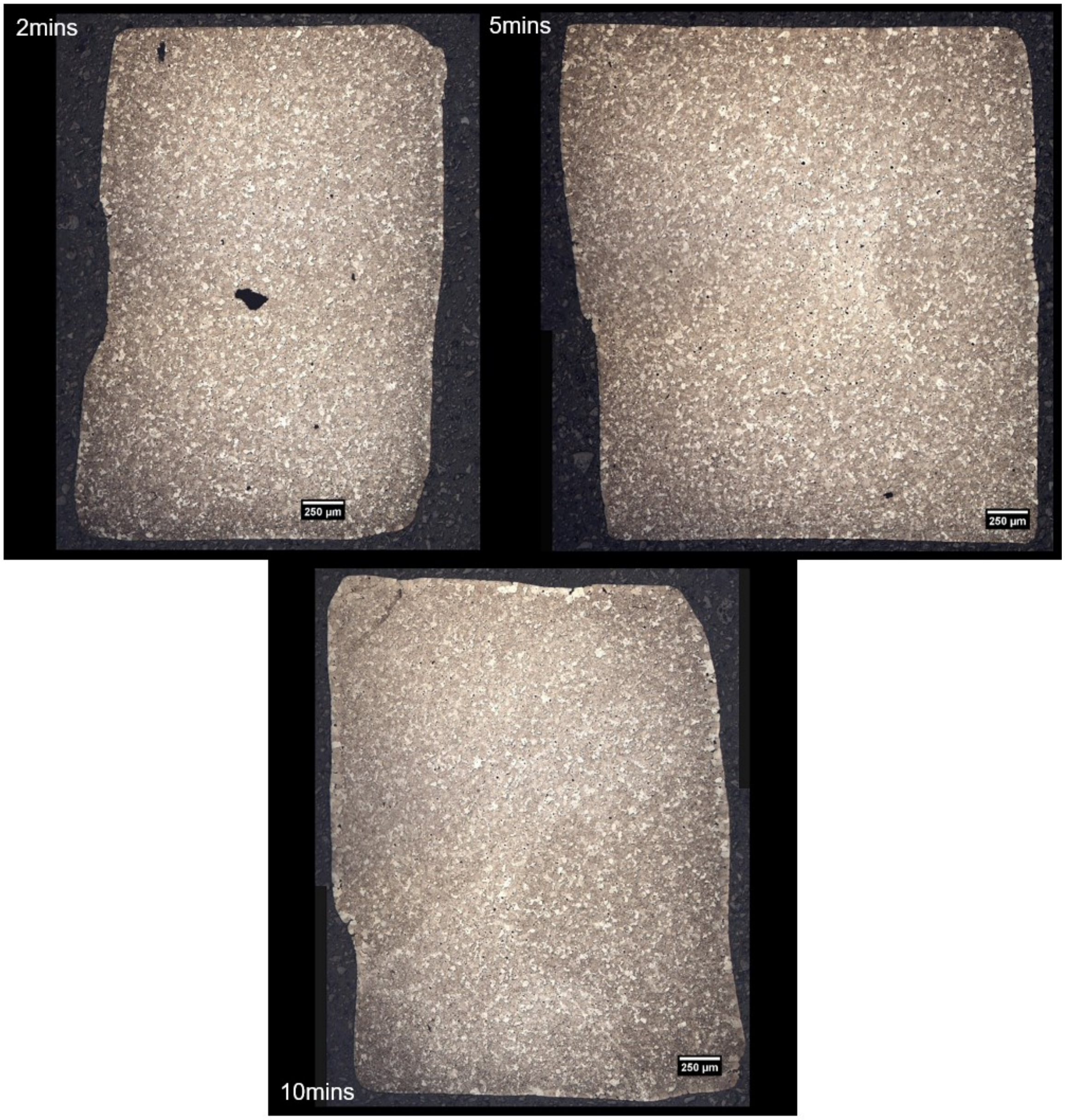

Figure B-3. Etched cross sections of the MIM NiSA SLPS samples sintered at 1345°C for 2-10mins.

Although rather irregular in shape, the 2-10min 1345°C samples, presented in Figure B-3, did not show significant signs of distortion or slumping. Some edge rounding is evident in these samples, but more importantly there is no apparent grain growth in the bulk material. Edge grain growth can be observed after 10mins of hold time.

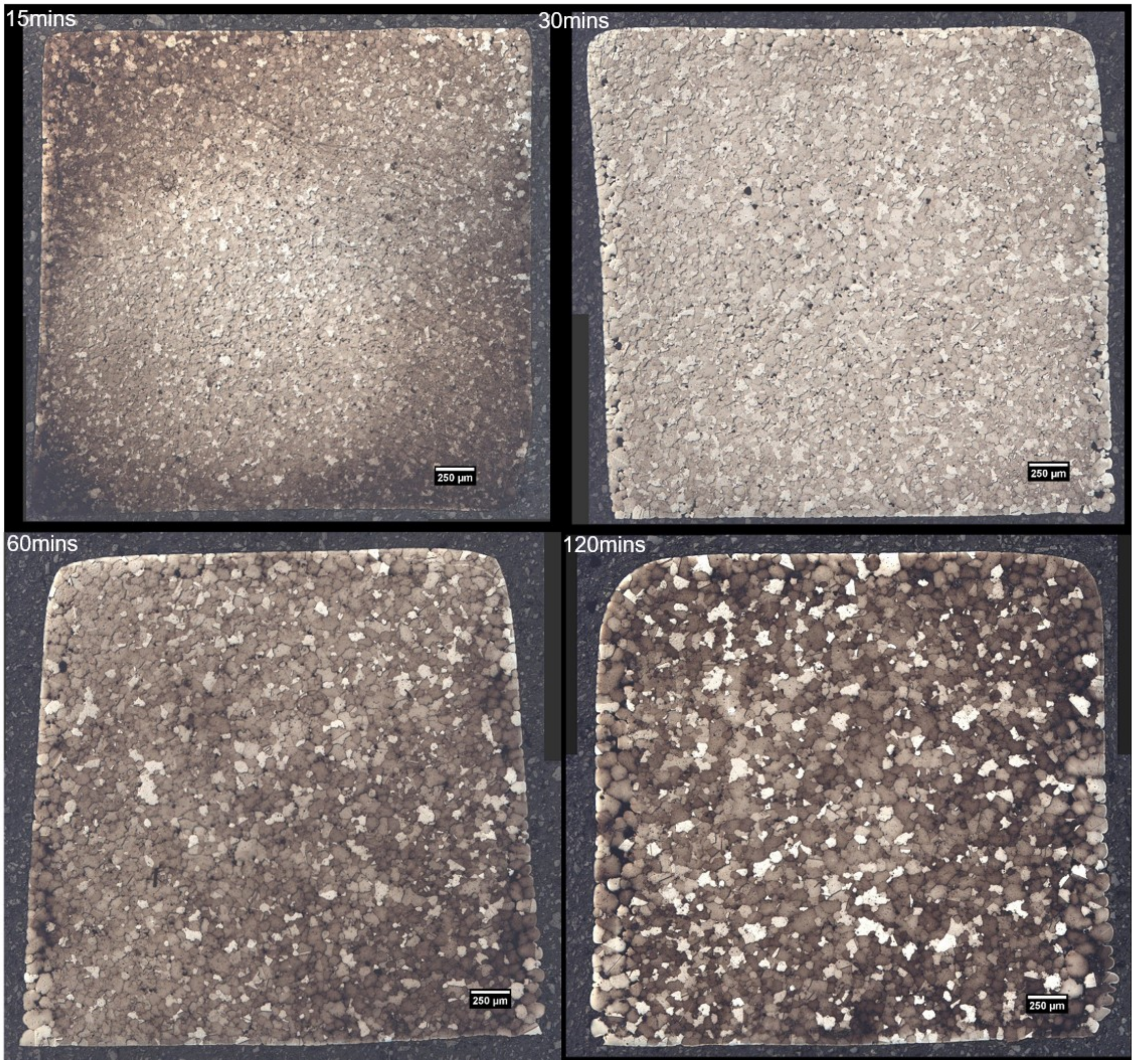

Figure B-4. Etched cross sections of the MIM NiSA SLPS samples sintered at 1345°C for 15-120mins.

In Figure B-4, grain growth has occurred throughout the bulk after 15mins of hold time at 1345°C. Over 120mins of hold time, the grain size increases substantially. The sample height does not decrease over the 120mins either, indicating that the material retains its rigidity during SLPS at this temperature. However, significant edge rounding has occurred by 60mins. Holding at 1345°C for 15-30mins appears to offer the best balance between grain growth and shape retention.

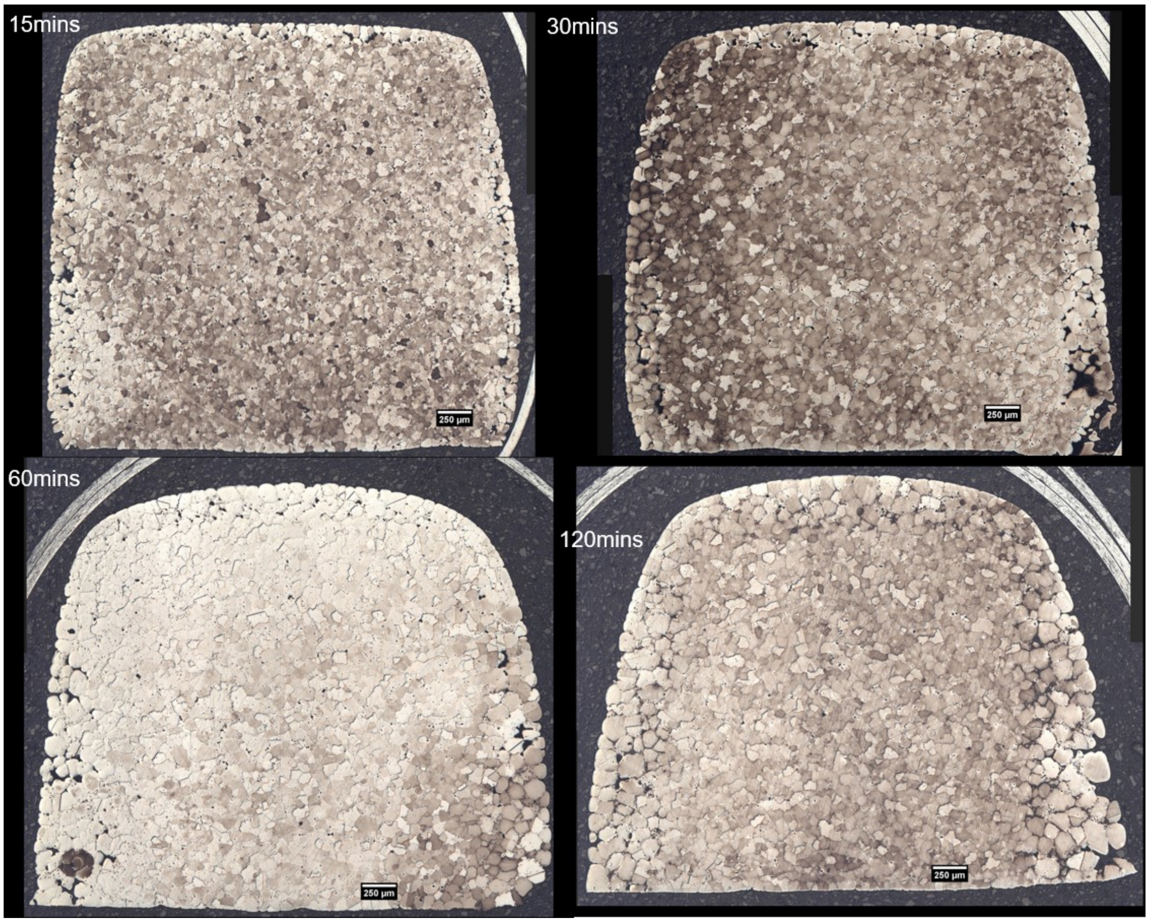

Figure B-5. Etched cross sections of the MIM NiSA SLPS samples sintered at 1350°C for 15-120mins.

In Figure B-5, significant grain growth has occurred throughout the bulk after 15mins of hold time at 1350°C. Grain growth continues over the 120min hold time, however, the sample height has decreased after 15mins, indicating that the material loses rigidity during the early stages of SLPS at this temperature. Significant shape loss and slumping has occurred by 60mins. Although sintering the MIM NiSA at 1350°C provides the largest degree of grain growth, holding at this temperature for any length of time will result in part distortion and slumping.

Cross sections of the 10wt% BNi-2 MIM NiSA LPS samples sintered at 1290°C and held for 15-120mins are presented in Figure B-6.

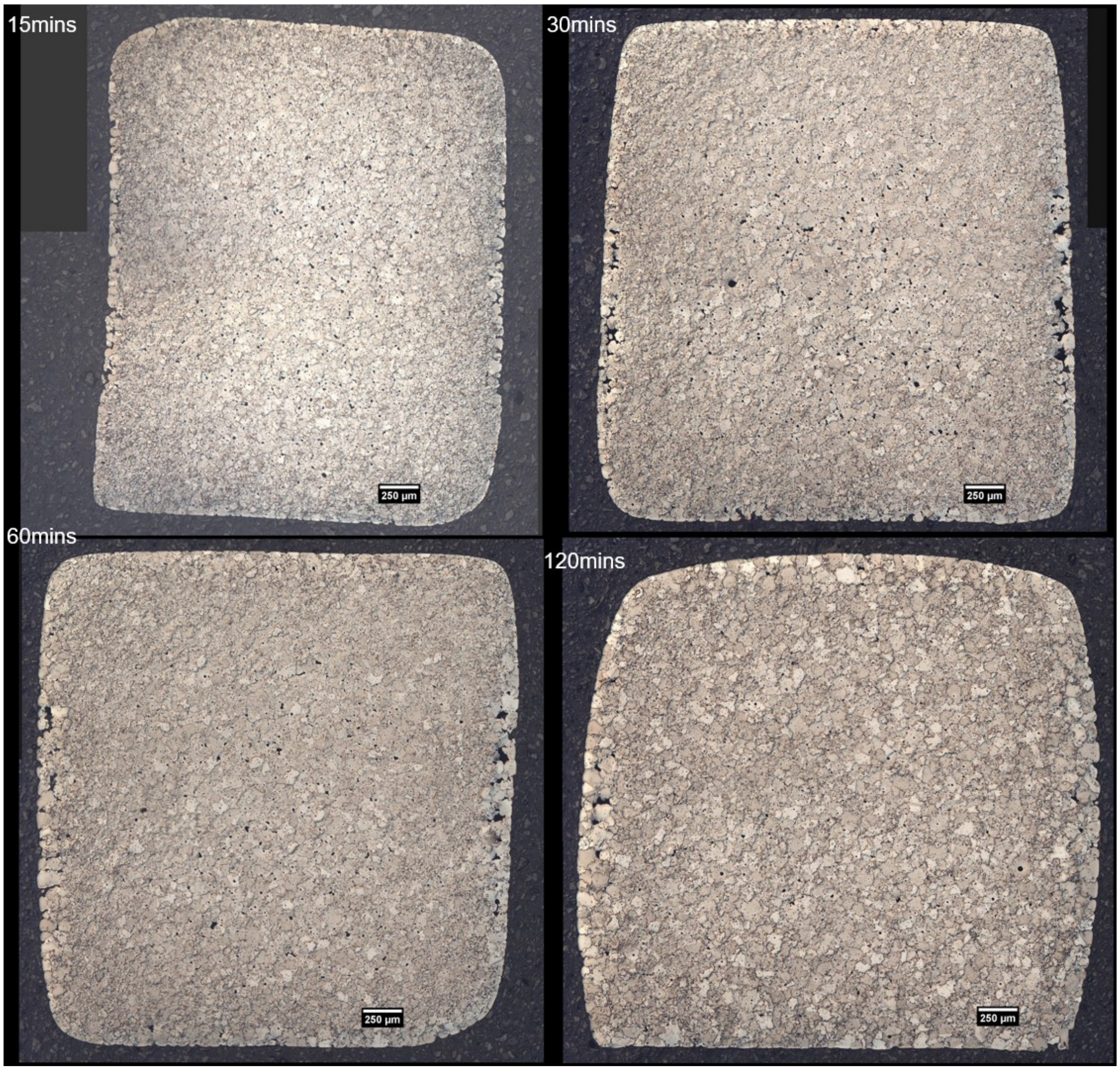

Figure B-6. Etched cross sections of the 10wt% BNi-2 MIM NiSA LPS samples sintered at 1290°C for 15-120mins.

In the 10wt% BNi-2 MIM NiSA, grain growth can be observed in the bulk after 15mins. Edge rounding and sub-surface porosity can also be observed at all hold times. However, after 120mins the sample exhibits swelling instead of slumping. Holding the 10wt% BNi-2 MIM NiSA material at 1290°C for 30-60mins appears to provide the best balance between grain growth and shape loss, though the grain size increase is less substantial than SLPS of the pure MIM NiSA.

B.4. Discussion and Comments

The stitched cross sections of the SLPS MIM NiSA specimens presented in Figures B-1 to B-5 provide a visual reference for the extent of grain growth and material deformation with sintering time and temperature. In terms of grain growth, SLPS at higher temperatures such as 1345°C and 1350°C clearly provide access to coarser grain sizes. Considering shape retention, longer times at these high temperatures are detrimental as they result in edge rounding and an eventual loss of rigidity. If both a coarse grain size and good shape retention are desired, as is the case in this MIM NiSA, the 1335°C temperature is too low and the 1350°C is too high due to the absence of grain growth and shape loss, respectively. At 1340°C, part shape is retained throughout the 120min hold time, so a 60min or 120min hold time is justified to maximize the grain growth response. If 1345°C is selected, a lower hold time between 15-30mins is required to retain the part shape due to the excessive edge rounding at longer hold times. Therefore, from this visual guide of SLPS, the MIM NiSA grain size can be increased by sintering at either 1340°C for 60-120mins or 1345°C for 15-30mins while retaining the part shape.

New SLPS process temperatures and hold times can be selected based on these results. For example, it may be beneficial to evaluate the MIM NiSA at an intermediate temperature between 1340°C and 1345°C to strike an optimal balance between grain growth and shape retention. As well, different hold times may be trialed to minimize the sintering time or to maximize the grain size achieved. It is conceivable that, in an industrial scale MIM operation, a lower target SLPS temperature may be selected to prevent shape loss of the MIM parts in the event of furnace overshoot or localized hot spots. As a result, longer SLPS hold times would be required to obtain the same degree of grain growth that higher process temperatures can achieve at shorter hold times. This component of the SLPS process design largely relies on the temperature control of the sintering furnace. In this study, the DSC and DIL instruments had a temperature accuracy within ±1°C at the sintering temperatures employed. Larger scale industrial furnaces commonly do not have as tight of control over temperature and do not always provide uniform temperature throughout. These realities must be considered while designing and evaluating an SLPS process for the industrial scale production.

In addition, there may be some tolerable degrees of shape loss and edge rounding depending on the benefit of grain coarsening and the specific part in question. For example, if a MIM part requires tight tolerances and no post-processing machining, the 1345°C/15min SLPS process may be an option. However, if there is a significant property benefit to the MIM part having a larger grain size, post-process machining may provide an opportunity to use the 1345°C/120min SLPS process instead.

It is also important to highlight that the MIM NiSA grain size can also be increased at sub-solidus sintering temperatures via the LPS route. Although the BNi-2 additive caused swelling of the MIM NiSA, other additives may be able to enact grain growth while the MIM shape is retained.

B.5. Conclusions

The stitched images provide a useful guide to SLPS of the MIM NiSA. The times and temperatures at which grain growth is enacted are evident while the extent of grain coarsening can also be observed. The influence of time and temperature on the material's shape retention and rigidity can be directly gathered from these images. This visual guide will allow process designers and engineers to quickly reference the general response of the MIM NiSA to various SLPS process parameters.